# Asteroid Deflection Campaign Design Integrating Epistemic Uncertainty

by

Sung Wook Paek

B.S., Korea Advanced Institute of Science and Technology (2010)
S.M., Massachusetts Institute of Technology (2012)

Submitted to the Department of Aeronautics and Astronautics
in partial fulfillment of the requirements for the degree of

Doctor of Philosophy

at the

MASSACHUSETTS INSTITUTE OF TECHNOLOGY

June 2016





Author ..... Signature redacted .....
Department of Aeronautics and Astronautics
May 19, 2016

Certified by ..... Signature redacted .....
Olivier L. de Weck
Professor of Aeronautics and Astronautics and Engineering Systems
Thesis Supervisor

Certified by ..... Signature redacted .....
David W. Miller
Jerome Hunsaker Professor of Aeronautics and Astronautics
Thesis Supervisor

Certified by ..... Signature redacted .....
Jeffrey A. Hoffman
Professor of the Practice of Aerospace Engineering
Thesis Supervisor

Certified by ..... Signature redacted .....
Richard P. Binzel
Professor of Planetary Sciences and Margaret MacVicar Faculty Fellow
Thesis Supervisor

Accepted by ..... Signature redacted .....
Paulo C. Lozano
Associate Professor of Aeronautics and Astronautics
Chair, Graduate Program Committee

# Asteroid Deflection Campaign Design Integrating Epistemic Uncertainty

by

Sung Wook Paek

Submitted to the Department of Aeronautics and Astronautics
on May 19, 2016, in partial fulfillment of the
requirements for the degree of
Doctor of Philosophy

## Abstract

Planetary defense, or asteroid collision avoidance, has been gaining interest with recent meteor or fly-by events, including the Chelyabinsk meteor that entered the Earth's atmosphere and exploded over Russia in 2013. Past or planned robotic missions to near-Earth asteroids are expected to provide an excellent opportunity to demonstrate asteroid deflection techniques.

However, applying a deflection technique to a hazardous asteroid in real-world situations requires extreme care for decision makers due to inherent uncertainty. The forms of uncertainty can be *epistemic* or *aleatoric*. *Epistemic* uncertainty can be reduced by replenishing incomplete information with better observations, whereas *stochastic* uncertainty cannot be reduced owing to its randomness. Although we cannot reduce stochastic uncertainty itself, we can come up with a plan which is robust to random uncertainty, by reducing epistemic uncertainty.

This thesis develops a methodology to design an asteroid deflection campaign that consists of multiple mission stages. The first stage serves as a precursor whose type can achieve different amounts of uncertainty reduction. With this in-situ information obtained by precursors, the follow-up stage may adapt its impactor design. The methodology is implemented in the Asteroid Deflection Integrating Epistemic Uncertainty (ADIEU) framework.

The ADIEU framework is demonstrated in deflection campaigns of select near-Earth asteroids. Generation of campaign solutions over a 15-year period, with different confidence requirements, requires up to 125,000 full-factorial runs and 400 optimization runs per asteroid. Results show that campaigns which consider and reduce epistemic uncertainty can both decrease launch mass and increase robustness. However, there are also cases, under extreme conditions, where a single-stage mission turns out to perform best. The performance envelopes of these different approaches are superposed to generate a *decision map* for use as a visual aid. Finally, this thesis concludes by outlining future work to refine the framework, as well as potential uses of the methodology in terrestrial applications.

Thesis Supervisor: Olivier L. de Weck
Title: Professor of Aeronautics and Astronautics and Engineering Systems

Thesis Supervisor: David W. Miller
Title: Jerome Hunsaker Professor of Aeronautics and Astronautics

Thesis Supervisor: Jeffrey A. Hoffman
Title: Professor of the Practice of Aerospace Engineering

Thesis Supervisor: Richard P. Binzel
Title: Professor of Planetary Science, Joint Professor of Aerospace Engineering

# Acknowledgments

First and foremost, I would like to express my deepest gratitude to my advisor, Prof. Olivier L. de Weck. My graduate program, culminating in this thesis, would never have been completed without his guidance, patience, and confidence in me.

I would also like to expand my appreciation to my committee members, Prof. Jeffery A. Hoffman, Prof. David W. Miller, and Prof. Richard P. Binzel and thesis readers, Prof. Sheila E. Widnall and Dr. Paul W. Chodas (Jet Propulsion Laboratory). Their invaluable advice matured this thesis from the beginning to the end.

It was an amazing experience be at MIT with excellent colleagues - Andrew, Afreen, Chaewoo, Kaushik, Luzius, Marc, Narek, Patricia, Paul, Rany, Roi, Koki, Sam, Sreeja, Sydney, Tak, Tatsuya, Thomas, Vivian, and others. The help of Mr. Robert Irwin in proofreading my thesis as well as the help of Ms. Marilyn Good and Ms. Julia Finn in organizing my trips should be acknowledged.

A number of great friends have been with me during my time at MIT. I would like to thank Andre, Been, Hanbong, Hyosang, Jinwook, Joseph, Jun-Geun, Jeong Hwan, Mina, Mukul, Rezy, Rosa, Sanjay, Soyoung, Sang-Il for sharing thoughts on research, talking about the future, and having fun with me.

Prof. Hyochoong Bang, Prof. Duck-Joo Lee, and Prof. Ju-Jang Lee encouraged and helped me start my graduate Program. Prof. Jaemyung Ahn and Prof. Hanlim Choi also provided advice and supports throughout my Ph.D. program. I am profoundly grateful to them all.

My masters program and the most part of mydoctoral program were supported by the Samsung Fellowship program in Korea. I sincerely appreciate the sponsorship that enabled me to complete this thesis without any financial difficulty.

Gidong, Sukwon, Mr. Hyun-Hee Lee, Ms. Hyo-Jung Kim, Mr. Jae Lee, Mr. Jae Y. Song, and Ms. Yoonjoo Jung in my church community deserve special thanks for their support and concerns. I am grateful to my brother Sung Hoon and cousins, Sung Hwi, Sung Bin, Yeri, Hyeon Woo, and Min Woo in Korea. I truly appreciate my aunt, Ms. Nam Soon Moon (deceased), who took care of me during my undergraduate program when the rest of my family was abroad. I also thank Ms. Akiko Sugimoto for her consideration.

Last but not least, I would like to thank my parents, Mr. Bonghyun Paek and Ms. Bong Sun Moon, for their unconditional love and unwavering support. I dedicate my thesis to them, with my love.

# Contents

# List of Figures

# List of Tables

# Nomenclature

| | |
|---|---|
| $\alpha$ | The irradiation-to-heat conversion ratio of nuclear detonation |
| $\beta$ | (1) The momentum multiplication factor (2) The coefficient of nonlinearity in superposition of gravity in relativity theories |
| $\Delta E$ | The increase in the *internal* energy of an asteroid |
| $\Delta P$ | (1) The change in orbital period (2) The change in pressure |
| $\Delta v$ | The change in velocity |
| $\Delta X$ | Distance of asteroid delection achieved by gravity tractor |
| $\delta$ | Distance of asteroid delection achieved by kinetic impactor |
| $\epsilon$ | The ratio of the final mass (dry mass) to the initial mass (wet mass) |
| $\epsilon_p$ | The ratio of the propellant to the initial mass (wet mass) |
| $\eta$ | The coordinate parallel to the asteroid velocity relative to Earth in the $(\xi, \eta, \zeta)$ frame |
| $\gamma$ | (1) The Grüneisen's coefficient (2) The angle of velocity vector rotation during a close approach (3) The coefficient of space curvature produced by unit rest mass in relativity theories |
| $\lambda$ | (1) Mean longitude (2) The coefficient of thermal expansion |
| $\mathbf{1}_{expr}$ | Indicator function, 1 if *expr* is true and 0 if *expr* is false |

| | |
|---|---|
| $\mathbf{g}$ | The inequality constraint vector in optimization |
| $\mathbf{h}$ | The equality constraint vector in optimization |
| $\mathbf{J}$ | The objective vector to be minimized in optimization |
| $\mathbf{p}$ | The parameter vector in optimization |
| $\mathbf{r}$ | The solar-system-barycentric position |
| $\mathbf{T}$ | The time vector (launch dates and flight timesF) |
| $\mathbf{x}$ | The design vector in optimization |
| $\mathbf{y}$ | The state vector of position and velocity |
| $\mathcal{LN}$ | Log-normal distribution |
| $\mathcal{N}$ | Gaussian distribution |
| $\mu$ | The gravitational parameter of a celestial body |
| $\Omega$ | Longitude of ascending node |
| $\omega$ | Argument of perihelion |
| $\overrightarrow{V_\oplus}$ | The heliocentric velocity vector of Earth |
| $\phi$ | (1) The cant angle of gravity tractor thrusters (2) The azimuth angle in the Earth reference frame (3) The porosity of an asteroid |
| $\psi$ | B-plane azimuth angle |
| $\rho$ | The density of an asteroid |
| $\sigma_{ephem}$ | The position (ephemeris) uncertainty of an asteroid |
| $\theta$ | The rotation angle in the Earth reference frame |
| $\xi$ | The orbit-dependent (MOID) coordinate of the $(\xi, \eta, \zeta)$ frame |

$\zeta$ The time-dependent (phasing) coordinate of the $(\xi, \eta, \zeta)$ frame

$A$ The acceleration of an asteroid by a gravity tractor

$a$ Semi-major axis of the orbit of an asteroid

$b$ Impact parameter

$C$ The (initial) robustness coefficient before impactor mass optimization

$c$ (1) The speed of light (2) The characteristic length of a close approach

$c_p$ The compressional wave velocity

$C_v$ The volume heat capacity

$C_{max}$ The (final) robustness coefficient after impactor mass optimization, used to calculate $J$

$C_X$ The three dimensional rotation matrix about X axis

$D$ The diameter of a Valsecchi circle

$d$ (1) The diameter of an asteroid (2) The distance between an asteroid's center and a gravity tractor

$E$ The *orbital* energy of an asteroid in the heliocentric frame

$e$ (1) Eccentricity of the orbit of an asteroid (2) The coefficient of restitution

$G$ The universal gravitational constant

$g_0$ The Earth's gravity acceleration

$H$ Absolute magnitude

$h$ (1) The number of asteroid revolutions around the Sun (2) The distance between an asteroid's surface and a nuclear explosive or a gravity tractor

$i$ Inclination of the orbit of an asteroid

$I_{sp}$ The specific impulse

$J$ The combined objective of the campaign mass (IMLEO) and the robustness coefficient ($C_{min}$) before time optimization

$J_{min}$ The combined objective of IMLEO $C_{min}$ after time optimization

$K$ The bulk modulus

$k$ The number of Earth revolutions around the Sun

$l$ The total number of spacecraft used in a deflection campaign

$M$ The mass of an asteroid

$m$ The final mass (dry mass) of an impactor or an orbiter

$m_0$ The initial mass (wet mass)

$m_i$ The final mass (dry mass) of an impactor

$m_p$ The propellant mass

$n$ The mean motion of a planet or a satellite

$P$ The orbital period (heliocentric)

$p$ (1) Probability density function (2) The power level of electric propulsion

$p_{th}$ The minimum threshold for the required probability of success

$Q$ The amount of energy per kiloton mass of equivalent TNT

$Q_n$ The number of kilotons of the equivalent charge for a nuclear explosive

$R$ The radius of a Valsecchi circle

$r$ The radius of an asteroid

$s$ The probability of success

$T$ (1) Tisserand's parameter (2) The time between the last impactor's collision and the keyhole passage of an asteroid (3) Trip time in Chebyshev trajectory interpolation (4) Thrust of gravity tractor

$T_n$ The $n$-th Chebyshev polynomial

$V$ The volume of an asteroid

$v_e$ Exhaust velocity

$v_i$ The relative velocity of an impactor

$v_r$ The outward rebounding velocity of ejecta

# Abbreviations

**ADIEU** Asteroid Deflection Integrating Epistemic Uncertainty

**AIDA** Asteroid Impact and Deflection Assessment

**AIDA** Asteroid Impact Mission (part of AIDA)

**ARM** Asteroid Redirect Mission

**AU** Astronomical Unit

**BFGS** Broyden-Fletcher-Goldfarb-Shanno (algorithm)

**CA** Close Approach

**CHEBYTOP** CHEBYshev Trajectory Optimization Program

**CLOMON(2)** CLOse approach MONitoring system (2)

**CTBT** Comprehensive Test Ban Treaty

**DART** Double Asteroid Redirection Test (part of AIDA)

**EIH** Einstein-Infeld-Hoffman (equation of motion)

**ESA** European Space Agency

**GA** Genetic Algorithm

**AU** Gravity Tractor

**IMLEO** Initial Mass in Low-Earth orbit

**JAXA** Japan Aerospace Exploration Agency

**JPL** Jet Propulsion Laboratory

**KI** Kinetic Impactor

**LD** Launch Date

**LOV** Line of Variations

**MOID** Minimum Orbit Intersection Distance

**MPC** Minor Planet Center

**MSDO** Multidisciplinary System Design Optimization

**NASA** National Aeronautics and Space Administration

**NEO** Near-Earth asteroid

**NEO** Near-Earth object

**NEODyS** Near Earth Objects Dynamic Site

**NEP** Nuclear Electric Propulsion

**OSIRIS-REx** Origins, Spectral Interpretation, Resource Identification, Security, Regolith Explorer

**PAT2** Propagator for Asteroid Trajectories Tool

**PHA** Potentially Hazardous Asteroid

**PHA** Potentially Hazardous Object

**POS** Probability of Success

**PTBT** Partial Test Ban Treaty

**SEP** Solar Electric Propulsion

**SQP** Sequential Quadratic Programming (algorithm)

**SRC** Sample Return Capsule

**TNT** TriNitroToluene

**TOF** Time of Flight

**UNCOPUOUS** United Nations Committee on the Peaceful Uses of Outer Space

**VA** Virtual Asteroid

**VC** Valsecchi Circle

# Chapter 1

# Introduction

Since the planetary formation phase ended billions of years ago, our Solar System has been continuing its process of accretion and bombardment [53]. For example, Earth is still accumulating interplanetary materials at a rate of 100 tons every day, most of which are tiny dust or ice particles from comets. Larger objects have a much lower possibility of impacting Earth, but their consequences can be devastating to humanity, as shown in Table 1.1. It is also notable that small-sized objects can have serious consequences in human impact or geographic scope, through high- or low-altitude breakups. The Chelyabinsk meteor (2013) was a high-altitude breakup, and the Tunguska event (1908) was a low-altitude breakup. In Chelyabinsk, 1,500 people were injured by an explosion at a height of around 30 km; in Tunguska, the explosion occurred 5 to 10 km above sparsely populated forests, flattening an area of 2,000 $km^2$.

Table 1.1: Frequencies and consequences of PHO impacts [6, 45, 46].

| Class | Diameter | Potential Fatalities | Frequency | Example |
|---|---|---|---|---|
| High-alt breakup | $<$ 50m | 0 | Annual | Chelyabinsk |
| Low-alt breakup | $>$ 50m | 5,000 | 250-500 yr | Tunguska |
| Regional | $>$ 140m | 50,000 | 5,000 yr | Silverprit |
| Sub-global | $>$ 300m | 500,000 | 25,000 yr | - |
| Low-scale global | $>$ 600m | $>$ 5 million | 70,000 yr | - |
| Medium-scale global | $>$ 1km | $>$ 1 billion | 1 million yr | - |
| High-scale global | $>$ 5km | $>$ 2 billion | 6 million yr | - |
| Extinction | $>$ 10km | 6 billion | 100 million yr | Chicxulub |

Figure 1-1 maps the data of breakup events by small asteroids impacting the Earth atmosphere to create very bright meteors or *bolides*. The size of objects ranges from 1 m to 20 m. The Chelyabinsk meteor had a diameter of 20 m and an estimated mass of 12,000-13,000 metric tonnes, which is heavier than the Eiffel Tower (7,300 metric tonnes) [54]. Combined with a speed of 19 km/s, its kinetic energy before the atmospheric entry was about $1.8 \times 10^{15}$ J,[1] equivalent to 500 kilotons of TNT or 20-30 times greater than the atomic bomb detonated at Hiroshima. The total number of bolides experienced over the 20-year time span from 1994 to 2013 (556), suggests that impacts of small asteroids with Earth are not unusual at all. In fact, several thousand of meteors of fireball magnitude occur in the Earth's atmosphere each day [40].[2]

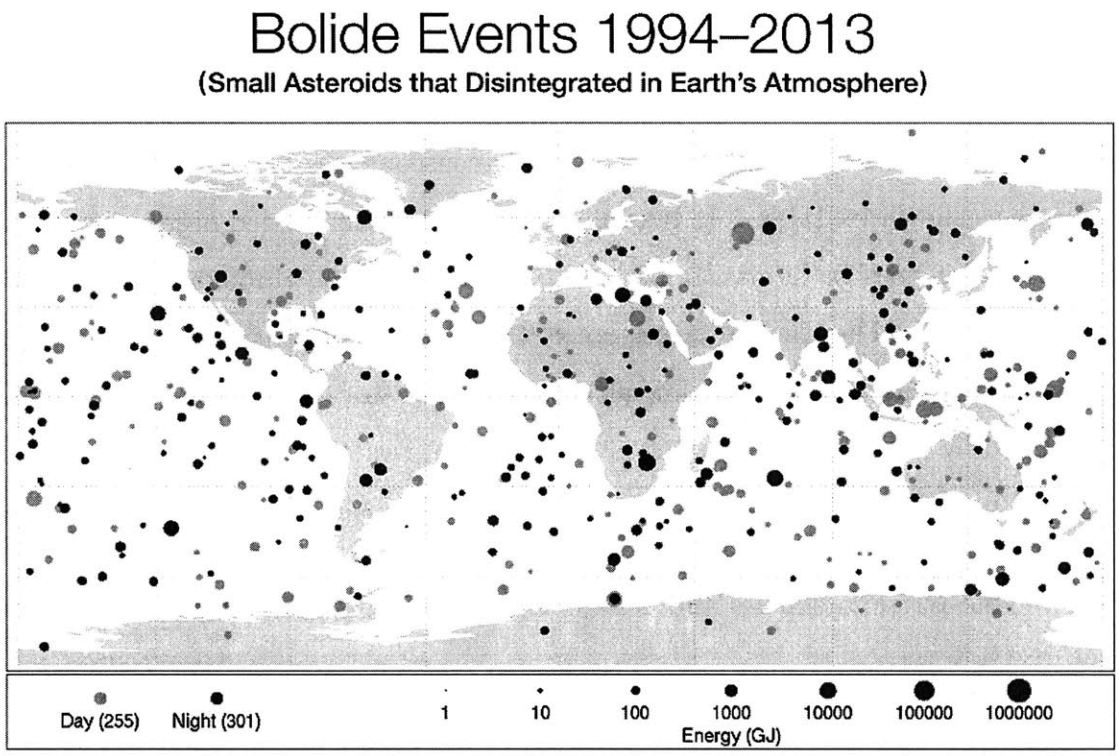


Figure 1-1: Small asteroid strikes between 1994 and 2003 [1]

[1]The amount of the kinetic energy is measured relative to the Earth-centered inertial (ECI) frame. This applies to Fig. 1-1 as well.

[2]For nomenclature, refer to Appendix A.

Of all the natural disasters that could befall us, only an Earth impact by a large comet or asteroid has the potential to end civilization in a single blow [55]. Yet these near-Earth objects also offer tantalizing clues to our solar system's origins, and someday could even serve as stepping-stones for space exploration. Fortunately, our technologies are approaching a level able to discover new asteroids and predict their potential hazards. NASA began an effort in 1998 to catalogue and track 90% of all near-Earth objects larger than 1 km, which was accomplished in 2010. The goal of this effort has been extended to discover 90% of all objects larger than 140 m by 2020. Figure 1-2 shows the cumulative number of discovered potentially hazardous asteroids (PHAs) by end of each year (first of December) [2]. As of August 2015, there were a total of 154 PHAs larger than one kilometer (left) and a total of 1603 PHAs of any size. The number of kilometer-sized asteroids started to saturate in 2010 when the "90%-goal" was met, whereas the total number of any size (includig sub-kilometer) continues increasing as we discover smaller asteroids, which are greater in number and harder to discover. October 7th, 2008 was the first time that we were able to predict an impact before it occurred [56]. The asteroid designated 2008 TC3, approximately 2 to 5 meters in size, struck the Earth's atmosphere. Although the asteroid was only discovered 20 hours before impact, its orbit could be calculated and tracked prior to reaching Earth [57]. Its landing sites in Sudan was less than miles away from predicted, where the errors were mainly due to the J2 effects of Earth [58].

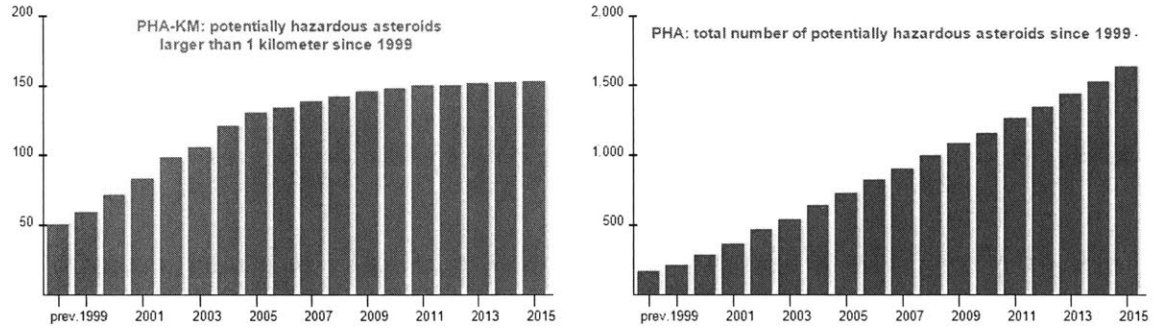


Figure 1-2: Small asteroid strikes between 1994 and 2003 [2]

In contrast with mature technologies for asteroid detection and tracking, no asteroid-deflecting technologies have yet been tested or demonstrated in space. There are two planned missions: the Asteroid Impact & Deflection Assessment (AIDA) mission and the Asteroid Redirection Mission (ARM).

- **AIDA**

The AIDA mission is an international endeavor, which consists of (1) the NASA Double Asteroid Redirection Test (DART) Mission led by the Johns Hopkins Applied Physics Laboratory and (2) the ESA Asteroid Impact Mission (AIM). As part of AIDA, two independent spacecraft would be sent to Didymos: a DART asteroid impactor and an AIM asteroid rendezvous spacecraft. During a close-Earth encounter of the binary asteroid 65803 Didymos (1996 GT) in October 2022, DART will impact Didymos' secondary body, while AIM observes the collision. This would mark the first time humanity has altered the dynamics of a natural Solar System body in a measurable way, seen both from ground observatories and from a rendezvous spacecraft. After the impact, AIM will continue its observation and perform detailed before-and-after comparisons on the structure of the body itself, as well as its orbit. The results will allow small-scale models in laboratories to be calibrated on a large-scale basis, shedding light on the role of the ejecta plume in modifying the asteroid's trajectory.[3] From the lessons learned here, we would hopefully be able to plan future planetary defense strategies and apply the kinetic-energy method if a real threat were to occur.

- **ARM**

The ARM is a mission concept whose goal is robotically returning a multi-ton boulder, typically 2-4 meters in size, from a 100-meter near-Earth asteroid to *cis*-lunar space [59]. Initially, there were two options studied to retrieve a small asteroid, Option A and Option B, as depicted in Fig. 1-4. Option A would deploy a 15-meter

[3]This is a fundamental part of the energy transfer dynamics and has been under scientific debate for over a decade.

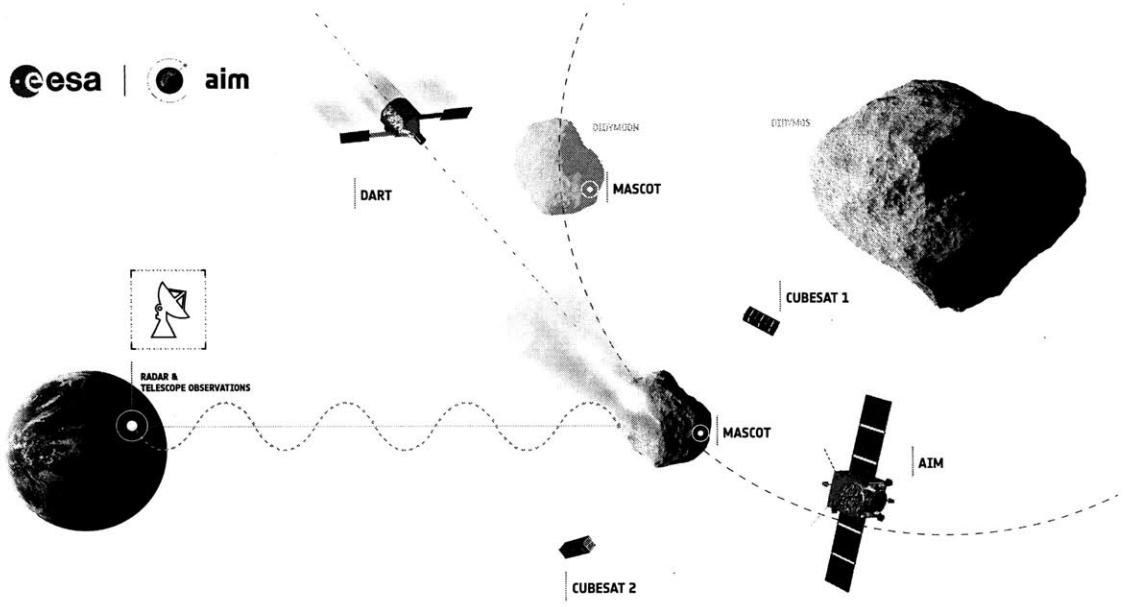


Figure 1-3: The AIDA mission concept [3]

capture bag capable of holding a small asteroid up to 8 m in diameter and 500 tons in mass. Option B, selected in March 2015, would use robotic arms, with micro-spine grippers and drilling anchors at the ends, to grasp a boulder on the asteroid's surface. Upon collection of the boulder, the 50 kW-class Solar Electric Propulsion (SEP) spacecraft will return to a lunar distant retrograde orbit in the mid 2020's, where astronauts could visit the boulder and collect samples. Although measuring changes in the position and speed of the asteroid is not its central objective, the ARM mission will demonstrate key technologies necessary for asteroid deflection. In particular, if the spacecraft with a boulder were to serve as a gravity tractor near the asteroid, its deflection capability would be much greater than the spacecraft itself. Mazanek et al. (2015) predict that using this "enhanced gravity tractor (EGT)" technique could reduce the deflection time by a factor of 10 to 50, from several decades to a few years or less [59]. These missions, along with the Hayabusa mission which will be explained later, inspired the thesis work by raising the following questions: (1) Is it always necessary to use a precursor in asteroid deflection at all? (2) If a precursor is necessary, what kind of precursor should we use? An orbiter such as AIM, or an impactor such as DART?

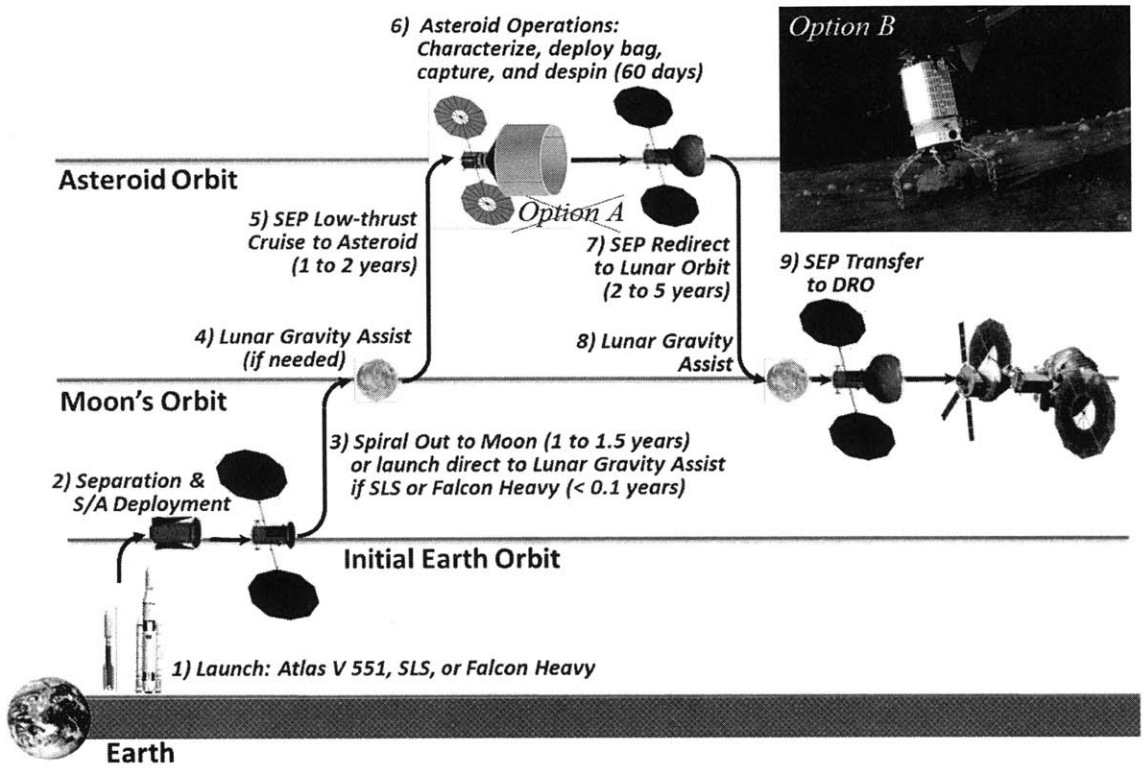


Figure 1-4: The ARM mission concept [4]

## 1.1 Background

To answer aforementioned questions, a framework for asteroid campaign design is necessary. Planning an asteroid deflection campaign under uncertainty is an interdisciplinary topic. Therefore, let us briefly describe some pertinent prior work, as shown in Fig. 1-5. Chapter 1 provides an overview of prior work in (1) astrodynamics and (2) campaign design. Chapter 2 reviews in-depth literature on (3) planetary defense and its subfields, which are more closely related to the proposed framework.

### 1.1.1 Celestial Mechanics/Astrodynamics

Celestial mechanics applies principles of classical mechanics to astronomical objects. As a branch of astronomy, it includes astrodynamics (orbital mechanics) as one of its subfields. Astrodynamics deals with the orbits of rockets, artificial satellites, and spacecraft. Dealing with the orbits of asteroids and spacecraft, this thesis makes heavy use of both disciplines.

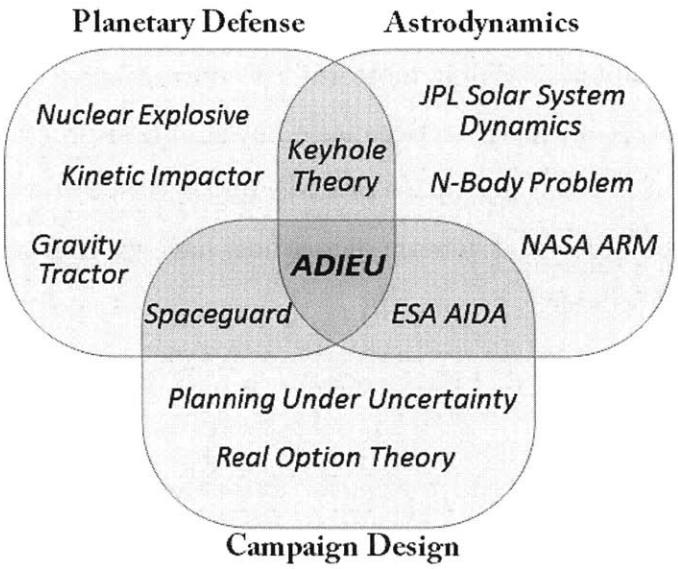


Figure 1-5: Relevant disciplines and literature

- **Astrodynamics**

Astrodynamics focuses on the spacecraft trajectory for space mission design, using Newton's laws of motion and Newton's law of universal gravitation. How to effectively blend orbital maneuvers, orbit plane changes, and interplanetary transfers within a spacecraft propulsion profile has given rise to trajectory optimization problems. Optimal control approaches, which grew out of the calculus of variations, were further developed by Pontryagin and Bryson [60, 61]. Their applications include optimizing the altitude trajectory and thrust profile of early rockets and jet aircraft.

The techniques to solve trajectory or other optimization problems fall into two broad categories: "indirect" techniques and "direct" techniques. The indirect techniques employ analytical[4] or numerical[5] procedures. The direct techniques numerically solve an approximated nonlinear-programming surrogate of the original problem, in order to reduce the problem dimensionality from infinity to a finite number. The former techniques are "indirect" in that they find a solution whose total differential of the performance measure is zero. The latter techniques are "direct" in that they find a solution whose performance measure is greater than that of any other solutions in

[4]The exo-atmospheric guidance algorithm of the Saturn V rocket used an analytic solution [62].
[5]The ascent trajectories of Gemini and Apollo were designed using numerical optimal control.

the neighborhood. In general, nonlinear programming approaches (Newton-Raphson, BFGS, SQP, and Simplex[6]) exhibit more robust convergence to a solution than numerical optimal control approaches. Because many nonlinear programming techniques require continuity in the first derivative of trajectories, such direct sampling methods as hill-climbing algorithms and genetic algorithms have evolved as more computing power has become available.

- **Celestial Mechanics**

Celestial mechanics studies the motions of astronomical objects, including planets and stars. Humanity has continually searched for anomalies contradictory to previous predictions, and discovered new planets as well as new theories, ranging from Kepler's laws to relativity. Space programs have provided an avalanche of planetary data that reveal the dynamical structure of our solar system. Resonance is a perfect example. If simple integer relationships between their orbital periods are satisfied, planets, satellites, or asteroids can become trapped into stable orbits, and thereby protected against close encounters or large perturbations to the orbit. The Moon and other natural satellites have 1:1 *spin-orbit* resonance, where the orbital period equals the rotational period, and the planet Mercury has 3:2 spin-orbit resonance. Two or more bodies may exhibit *orbit-orbit* resonance between their orbital periods. Table 1.2 summarizes two-body or three-body resonances in our Solar System. In a two-body resonance (1st order or 2nd order), perfect synchronization is achieved when the precession of periapsis ($\dot{\omega}$) is taken into account as well as mean motions ($n$). That is, an observer attached to the periapsis would see objects coming into conjunction in the same place every multiple of their periods. In a three-body resonance (0th order), the linear combination of mean longitudes ($\lambda$) equals 180 degrees,[7] preventing all three bodies from ever being in conjunction simultaneously [47–49]. This kind of mean motion resonance (MMR) has also been discovered in extrasolar planets [64].

[6] Quasi-optimum reentry trajectories for the Space Shuttle were determined using a Simplex-based nonlinear programming method [63].

[7] Differentiating this equation with respect to time, the linear combination of mean motions equals 0, which is a mean-motion resonance.

| Solar System Bodies | Definition | Description |
|---|---|---|
| **Planets** | | |
| Neptune and Pluto | $2n_N - 3n_P + \dot{\omega}_P = 0$ | |
| **Asteroids** | | |
| Trojan and Jupiter | $n_{Tr} - n_J = 0$ | 0th order |
| Thule and Jupiter | $3n_{Th} - 4n_J + \dot{\omega}_{Th} = 0$ | 1st order |
| Hilda and Jupiter | $2n_{Hi} - 3n_J + \dot{\omega}_{Hi} = 0$ | 1st order |
| Griqua and Jupiter | $n_{Gr} - 2n_J + \dot{\omega}_{Gr} = 0$ | 1st order |
| Alinda and Jupiter | $n_{Al} - 3n_J + \dot{\omega}_{Al} = 0$ | 2nd order |
| **Jovian satellites** | | |
| Io and Europa | $n_{Io} - 2n_{Eu} + \dot{\omega}_{Io} = 0$ | 1st order |
| Io and Europa | $n_{Io} - 2n_{Eu} + \dot{\omega}_{Eu} = 0$ | 1st order |
| Europa and Ganymede | $n_{Eu} - 2n_{Ga} + \dot{\omega}_{Eu} = 0$ | 1st order |
| Io, Europa and Ganymede | $\lambda_{Io} - 3\lambda_{Eu} + 2\lambda_{Ga} = \pi$ | 0th order |
| **Saturnian satellites** | | |
| Mimas and Tethys | $2\lambda_{Mi} - 4\lambda_{Te} + \dot{\Omega}_{Mi} + \dot{\Omega}_{Te} = 0$ | 2nd order |
| Enceladus and Dione | $n_{En} - 2n_{Di} + \dot{\omega}_{En} = 0$ | 1st order |
| Titan and Hyperion | $3n_{Ti} - 4n_{Hy} + \dot{\omega}_{Hyp} = 0$ | 1st order |
| **Plutonian satellites** | | |
| Styx, Nix and Hydra | $3\lambda_{St} - 5\lambda_{Ni} + 2\lambda_{Hyd} = \pi$ | 1st order |

Table 1.2: Solar system resonances [47–49]

As for small bodies, orbital resonances can destabilize their orbits. There are very few asteroids in the locations where their solar distance causes orbital resonances with Jupiter. This gap in the asteroid distribution is called a Kirkwood gap, as shown in Fig. 1-6. The asteroids in this region collided with Jupiter or other planets over time to create this gap. The orbital elements of the asteroids remaining in Kirkwood gaps vary chaotically, and will eventually evolve onto planet-crossing orbits within a few million years [65]. The latest discoveries include "gravitational keyholes" of near-Earth asteroids, detailed in Chapter 2, which can instead strengthen orbital resonance and increase the impact hazards of an asteroid [66]. Chodas and Yeomans (1999) first discussed this concept, identifying narrow keyholes embedded in the uncertainty regions of several near-Earth asteroids. If an asteroid should pass through one of these keyholes, it can be perturbed onto trajectories that closely approach to or even collide with Earth in a later year [53]. This thesis will focus on deflecting asteroids which have keyholes. Note that not all near-Earth asteroids have gravitational keyholes.

An asteroid trajectory has to pass within 0.15 AU of the Earth to form a keyhole, and only about 20 percent of potential impactor trajectories will have a close approach like this within a 25-year period before potential impact [67].

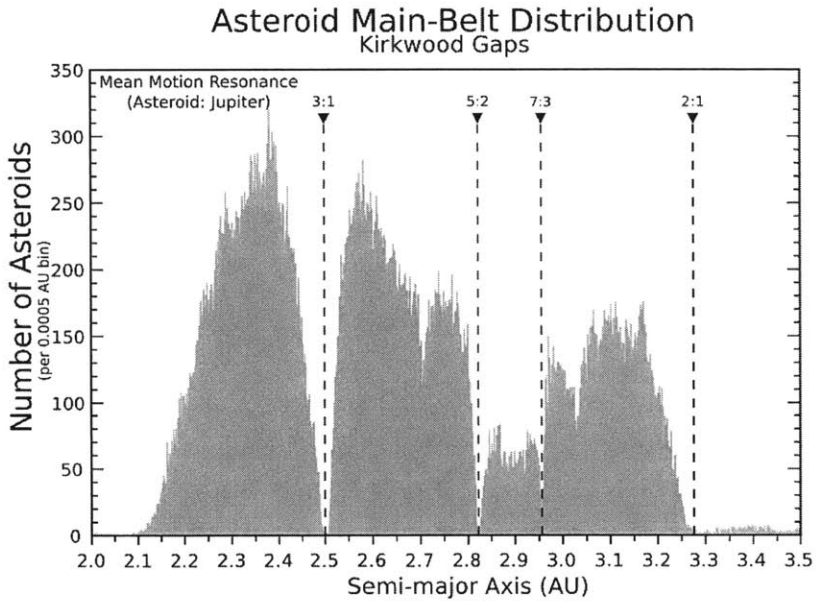


Figure 1-6: Histogram of asteroid population by solar distance, showing the four most prominent Kirkwood gaps [5]

### 1.1.2 Campaign Planning

As the scale of a project increases, its planning becomes more complex, necessitating *campaign*-level optimization. A *Campaign plan* is a plan to achieve an objective, usually of a large scale over an extended period of time [68]. A campaign plan could also have subordinate objectives or intermediate milestones and is often broken down by phases or missions, which share an objective and budget [69]. A budget constraint is imposed on a campaign such that the total cost for missions comprising the campaign cannot exceed the budget. Campaign plans have a wide range of applications such as business marketing, political campaigning, military campaigning, and space exploration. The increased performance of computers has enabled not only static optimization of set points, but also dynamic optimization over longer periods of time [70]. For example, a production optimization problem can be formulated as a

multistage dynamic optimization problem, where the production time is split up into several processing stages. The producer must often satisfy temporally or spatially uncertain demands from consumers. Models which explicitly consider the uncertainty can be expected to generate superior planning decisions compared to models that do not account for the uncertainty. Table 1.3 lists different approaches to cope with uncertainty in planning resource allocation, inventory management, and supply chain coordination [50]. Methods used in this thesis are underlined. *Real options valuation*, often termed *real options analysis*, is used to make budgeting decisions for allocating capital or resources [71]. The real option rule is that one should invest today only if the net present value is high enough to compensate for giving up the value of the option to wait [72]. There are different forms of uncertainty that a budgeting decision should deal with. Market demands or stock prices are *aleatoric* in nature since driven by stochastic processes: the distribution's variance is stochastic. Uncertainties in terrestrial or space exploration are epistemic, however, in that the unknown values are fixed (although unknown), such as the amount of oil reserves or the mass of an asteroid to be deflected [73, 74]. Even if these quantities are changing, they are changing much slower than the decision dynamics of interest.

| **Conceptual models** | **Analytical models** |
|---|---|
| Yield factors | Hierarchy processes |
| Safety stocks | Mathematical programming |
| Safety lead times | Stochastic programming |
| Hedging | Deterministic approximation |
| Over-planning | Laplace transforms |
| Flexibility | Markov decision processes |
| **AI-based models** | **Simulation models** |
| Expert systems | Monte Carlo techniques |
| Reinforcement learning | Probability distributions |
| Fuzzy set theory | Heuristic methods |
| Fuzzy logic | Freezing parameters |
| Neural network | Network modeling |
| Genetic algorithm | Queuing theory |
| Multi-agent systems | Dynamic systems |

Table 1.3: Classification of uncertainty models [50] (methods in this thesis underlined)

### 1.1.3 Planetary Defense

*Planetary defense*, or *asteroid collision avoidance*, consists of techniques to divert an asteroid from its course toward Earth. Its theoretical background and the proposed mitigation methods are explicated in Chapter 2 : Asteroid Impact Hazards. Figure 1-7 illustrates the thesis roadmap, where Chapter 2 is committed to the literature review on planetary defense.

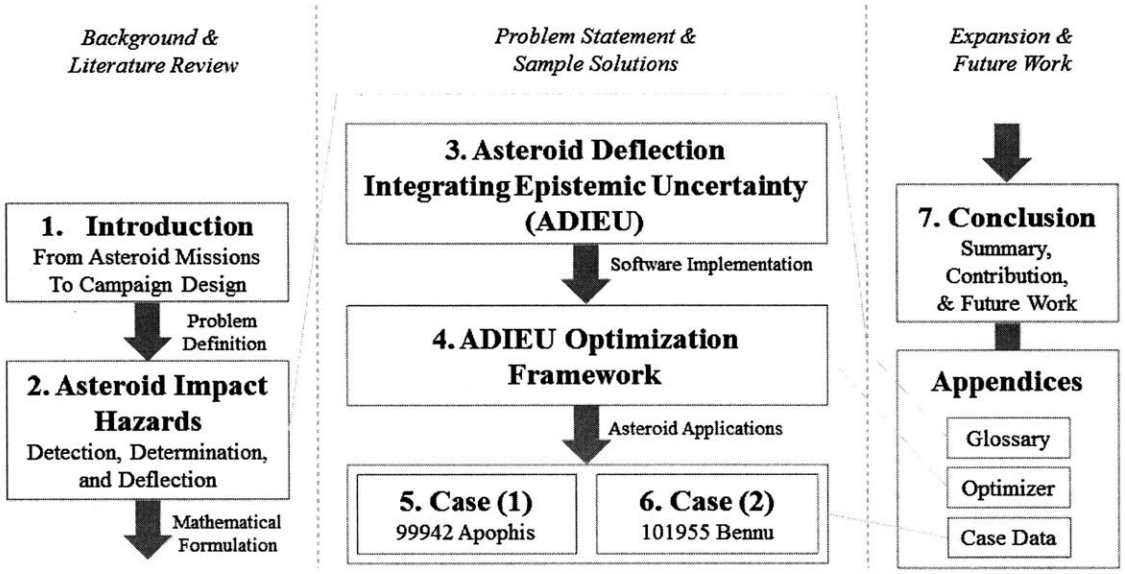


Figure 1-7: Thesis roadmap: seven chapters

## 1.2 Thesis Roadmap

This thesis develops a methodology for deflecting a potentially hazardous asteroid in the presence of uncertainty. The proposed framework, *Asteroid Deflection Under Epistemic Uncertainty*, or ADIEU for short, can be used to design a deflection campaign for any asteroid with gravitational keyholes.[8] With this framework, we want to answer the following two questions:

[8] If an asteroid has a keyhole, deflecting it may be formulated as a double-sided problem that can be solved with this framework. If an asteroid does not have a keyhole, it becomes a one-sided problem that requires a different approach. This difference will be explained along with the "safe harbor" concept in Chapter 3.

- **Q1. Is it always necessary to use a precursor? In other words, should we go with a single mission or a campaign that consists of multiple mission?**

It is intuitive that a campaign with multiple stages, such as AIDA consisting of AIM and DART, would entail more cost than a single stage mission. Also, time is at a premium for asteroid deflection. An early impact can deflect an asteroid more than a later impact. Deploying a precursor first leaves less time for an impactor to change the trajectory of an asteroid. Can the value of information obtained by the precursor compensate for these penalties?

- **Q2. If we need a precursor, what capabilities should it have? In other words, what types of uncertainty should it reduce?**

The capabilities of precursors can vary, as shown in the missions mentioned before. The AIM does not directly contact the asteroid but measures its physical characterictic via remote sensing. The DART collides with the asteroid to deflect it. Other kinds of precursors, such as a lander or a rover, may be conceived, but this thesis will consider a preliminary orbiter (AIM) and a preliminary impactor (DART).

Figure 1-7 graphically depicts the structure of this thesis. Chapter 1 incorporates the idea of campaign design into asteroid missions for hazard mitigation by touching upon relevant prior work. Chapter 2 reviews more literature related to asteroid collision avoidance, whose subfields are explained in detail: (1) detection of near-Earth objects, (2) determination of their impact risks, and (3) deflection (or disruption) methods to lower the risk. Based on the research gaps identified in current literature, Chapter 3 develops a methodology for designing asteroid deflection campaigns that are robust to uncertainty, where a new figure of merit is defined to quantify robustness. Chapter 4 further refines the original research questions into a mathematical optimization problem. The solver is implemented by a genetic algorithm blended with Monte Carlo techniques and probability distributions, as shown in Table 1.3.

The framework is demonstrated for two near-Earth asteroids in Chapters 5 and 6. Chapter 7 summarizes the results and insight obtained in these case studies, suggesting follow-up research directions as well as possible contributions to other disciplines (e.g., terrestrial applications).

# Chapter 2

# Asteroid Impact Hazards

The interest in near-Earth objects (NEOs) was increased when the U.S. Congress requested in 1990 that NASA undertake two workshops [75]: one to study ways of increasing the discovery rate of NEOs and another to study ways for deflecting or destroying an NEO should it pose a danger to life on Earth. The former workshop study culminated in a report which proposed an international NEO survey program called Spaceguard, named after a similar project suggested by Sir Arthur C. Clarke in his novel *Rendezvous with Rama* [76]. The Spaceguard Survey started in 1998, and when its initial objective of locating 90 percent of near-Earth asteroids larger than 1 km was achieved at the end of 2010, the program was extended to locate 90 percent of near-Earth asteroids larger than 140 m [77,78]. The program has drastically increased our knowledge of NEOs and helped scientists refine their theories to predict impact hazards. First, Bowell and Muinonen suggested the use of the minimum orbital intersection distance (MOID) as a criterion to determine the risk of NEO close approaches, such that objects with a MOID less than 0.05AU[1] are classified as potentially hazardous objects (PHOs) [79]. Chodas and Yeomans used linear methods to predict the impact probability of Comet Shoemaker-Levy 9 with Jupiter in 1994; after the collision actually happened, they successfully reenacted the pre-breakup trajectory using a nonlinear method [80–82]. Before long, an automatic collision monitoring system became necessary because (1) the number of discovered NEOs kept increasing and

[1] 4.6 million miles, 7.5 million kilometers, or 19.5 lunar distances

(2) their impact probability continually changed over time. The HORIZONS system operated by NASA/JPL and the CLOMON2 system operated by ESA/University of Pisa are such systems. Both systems have made their database available online, at the Sentry Impact Risks Page and the Near Earth Objects Dynamic Site (NEODyS), respectively. These systems raise alarms if a certain asteroid or comet poses a potential threat to impact Earth.[2] Also, users may query the location and physical characteristics for objects of interest. This chapter is devoted to literature reviews on how these impact-warning systems work to discover near-Earth objects (NEOs) and predict their potential threats in the future. The first section discusses NEO detection, and the second section discusses NEO risk determination. If a NEO turns out to pose a substantial risk to Earth, mitigating actions may be required; thus, the third and last section discusses NEO deflection theories, completing a pipeline of (1) detection, (2) decision (risk determination), and (3) deflection.

## 2.1 Detection

A near-Earth object (NEO) is an object whose trajectory brings it within 1.3 AU from the Sun and hence within 0.3 AU of the Earth's orbit; a NEO is further classified as a potentially hazardous object (PHO) if it passes within 0.05 AU of the Earth's orbit and is large enough to pass through the Earth's atmosphere, about 150 meters in diameter and larger. Objects greater than this minimum threshold can cause regional damage as shown in Table 1.1. Compared to kilometer-sized objects, these smaller ones are more difficult to fully catalogue because of a power law between the size and the number of asteroids, as shown in Fig. 2-1. According to this cumulative chart, the number of NEOs increases by 100 times when the diameter decreases by 10 times; for example, there are 100,000 NEOs whose size is greater than 140 m and 1,000 NEOs

[2]The JPL's system for trajectory calculation actually does not have a name. The term HORIZONS denotes its web interface. The collision monitoring system has its own name, called Sentry. It continually scans the most current asteroid catalog for possibilities of future impact with Earth over the next 100 years. Whenever a potential impact is detected it will be analyzed and the results immediately published in the Sentry Risk Table. Asteroids with the lowest cumulative Palermo Scale is considered to be the most hazardous.

greater than 1 km. The chart also shows the approximate absolute magnitude on the top axis, the average impact interval on the right axis (years), and the approximate impact energy on the bottom axis; a 100-meter-sized asteroid has a greater absolute magnitude and appears darker in the sky, making it harder to detect. Because of this mismatch between the NEO population and its detectability, a specific goal for NEO cataloguing was set in 1992 when a U.S. Congressional study, "Spaceguard Survey Report," mandated that NASA locate 90% of near-Earth asteroids (NEAs) larger than 1 km within 10 years.[3] As shown in Table 1.1, the sizes between 1 km and 140

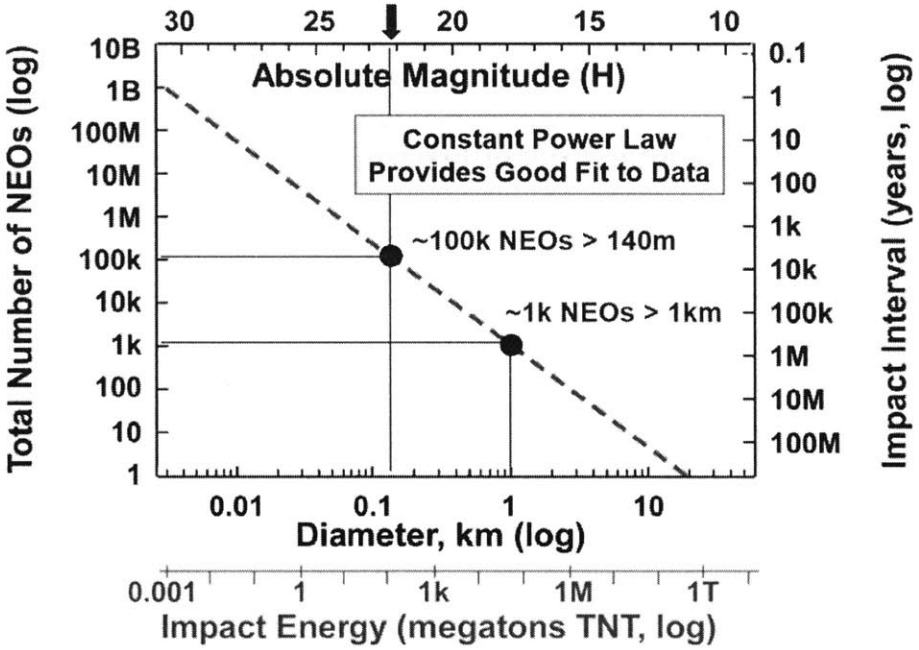


Figure 2-1: Frequency and number of NEOs by size (bottom), impact energy (bottom, second row, in megatons TNT or 4.184 $\times 10^{15}$J), and magnitude (top) [6]

m can cause damage to Earth on a global level and a regional level, respectively. As the program grew, the term Spaceguard now loosely refers to international efforts to discover NEOs, regardless of which organization they are associated with. Among them, the most famous is the Lincoln Near-Earth Asteroid Research (LINEAR), which

[3]Before this goal was set, the Minor Planet Center (MPC) had been cataloging the orbits of asteroids and comets since 1947. "The Minor Planet Center operates at the Smithsonian Astrophysical Observatory (SAO), under the auspices of Division F (formerly Division III and, before that, Commission 20) of the International Astronomical Union (IAU). The Minor Planet Center derives its operating budget from a five-year NASA grant (http://www.minorplanetcenter.net/iau/mpc.html)."

detected 231,082 new objects,[4] of which at least 2,423 were near-Earth asteroids. When the initial Spaceguard goal was achieved, an extension to the project gave NASA the mandate of identifying 90% of near-Earth asteroids as smalls as 140 m by the end of 2020. This was stipulated in the 2005 Budget Authorization Act[5] by the U.S. Congress, which directed the NASA Administrator to comprehensively analyze the ways to detect, track, catalogue, and characterize potentially hazardous near-Earth objects. In light of this background, this section explains technologies we use to find NEOs (subsection 2.1.1), techniques to reduce the orbit uncertainties of a newly discovered asteroid (subsection 2.1.2), and examples in which the asteroid's physical properties were characterized (subsection 2.1.3).

### 2.1.1 Finding Potentially Hazardous Objects

The approaches to finding PHOs can be classified in three categories: ground-based optical systems, space-based optical systems, and spaced-based infrared systems. Ground-based optical systems use large apertures to scan the sky for PHOs at night. Space-based optical systems gather visible light from vantage points near Earth or in Venus-like heliocentric orbits regardless of the time of day or night. Space-based infrared systems operate from similar vantage points, and use passively cooled infrared detectors to find and track objects.

#### (1) Ground-based optical systems

Ground-based optical systems are based on mature technology and cost less than space-based systems. However, ground-based systems (regardless of their spectral region) cannot operate during daylight or twilight. Objects in inner-Earth or Earth-like orbits can be observed only at the beginning and end of the night, so these objects will offer fewer discovery opportunities from the ground. Ground-based systems are also subject to interference from weather, atmospheric turbulence, atmospheric at-

[4] As of September 15, 2011.

[5] Section 321 of the NASA Authorization Act of 2005 (Public Law No. 109-155), also known as the George E. Brown, Jr. Near-Earth Object Survey Act. The Act was signed into law by President Bush on December 30, 2005.

tenuation, and scattering from moonlight. Ground-based systems cannot operate in infrared wavelengths because atmospheric attenuation becomes even more significant in this region, as shown in Fig. 2-2. Ground-based optical systems operating in visible wavelengths cannot determine accurate PHO sizes. Ground-based radar systems require a very large aperture, up to hundreds of meters; the Arecibo radio telescope has a 305 meter (1,001 feet)-sized dish, and the Goldstone network has three 70 meter-sized dish antennas.

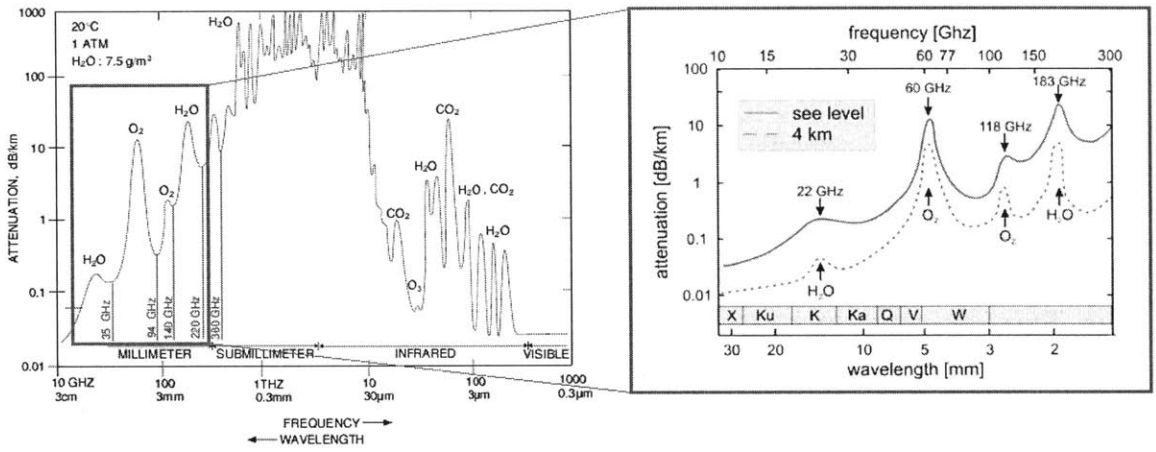


Figure 2-2: Atmospheric attenuation versus frequency and wavelength [7, 8]

### (2) Space-based optical systems

Space-based optical systems use mature technologies obtained from existing spacecraft mission heritage.[6] They can access almost the entire sky at any given time with no interference from weather, daylight, moonlight, or atmospheric attenuation. Also, they can observe objects in inner-Earth or Earth-like orbits easily if they are located at Sun-Earth L1 or in a Venus-like orbit. However, high costs and low maintainability are obstacles for detecting and tracking PHOs for an extended period of time unless the space-based optical system is in low-Earth orbit. Retrieving data from spacecraft to ground may also become challenging as the distance between spacecraft and Earth increases, with higher downlink data rate requirements than infrared detectors.

[6]The Hubble Space Telescope is located in a low-Earth obit, the Kepler Space Observatory is located in an Earth-like orbit (Earth-trailing heliocentric orbit), and Gaia is located in the Sun-Earth L2 which is the farthest Lagrange point from the Sun.

### (3) Space-based infrared systems

Although their technology is not as mature as space-based optical systems, space-based infrared systems have been actively developed and deployed recently.[7] Space-based, passively cooled, infrared systems require smaller apertures than optical systems of equal detection efficiency and provide more accurate estimates of object sizes.[8] Figure 2-3 illustrates why an infrared detector can more easily find an asteroid and more accurately determine its size than a visible detector. The brightness of an asteroid viewed in visible light is the result of both its albedo and size; therefore, a visible detector cannot easily find a dark object (left figure); as for size, a visible detector has difficulty distinguishing a shiny small object from a dark big object (right figure) if the object is millions of miles away. On the other hand, an infrared detector senses the heat of an object, which is more directly related to its size; it can find a dark object as easily as a bright object if two objects have the same size (left figure); the larger objects appear brighter than smaller objects because brightness is not strongly affected by its albedo. However, these heat-sensing detectors must be cooled to cryogenic temperatures for noise reduction, which can be technically challenging.

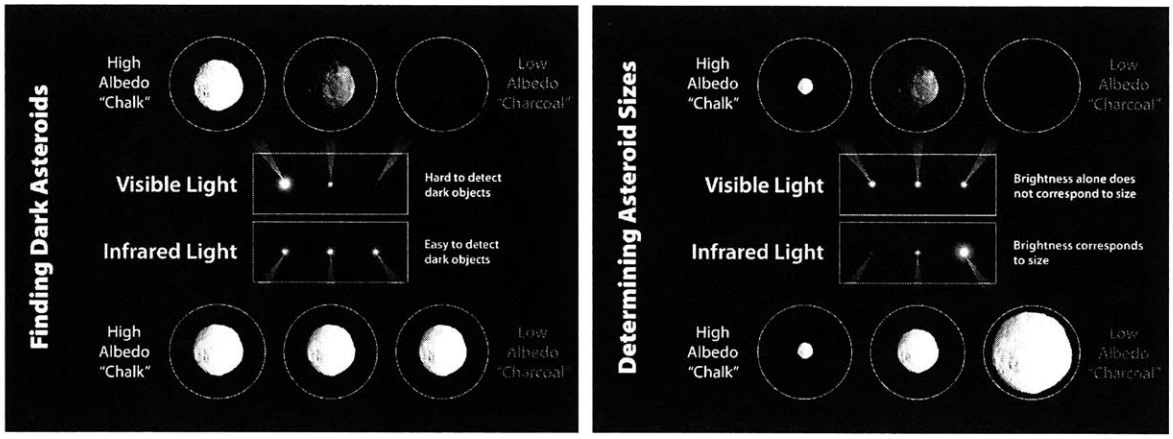


Figure 2-3: Atmospheric attenuation versus frequency and wavelength [9]

[7]The Spitzer Space Telescope is located in an Earth-trailing heliocentric orbit, and the Herschel Space Observatory is located at the Sun-Earth L2 Lagrange point.

[8]The object size uncertainties are less than 50% compared with 230% for visual detectors. A two-band infrared system could lower the size uncertainties to about 20%.

Whichever spectrum is used to detect an asteroid, there is one common principle: subtract static images from a star background. As shown in Fig. 2-4 (left), sub-images are cropped and the static field stars are matched in the star catalogue [10,83]. In the method described in this fugre, sub-images are taken along the predicted trajectory of an asteroid, so the asteroid is on the same location whereas different field stars are in differenct places across sub-images. It is impossible to confirm the presence of the asteroid in the upper right figure (a), whereas the asteroid is bright and no field stars are shown in the lower right figure (b).

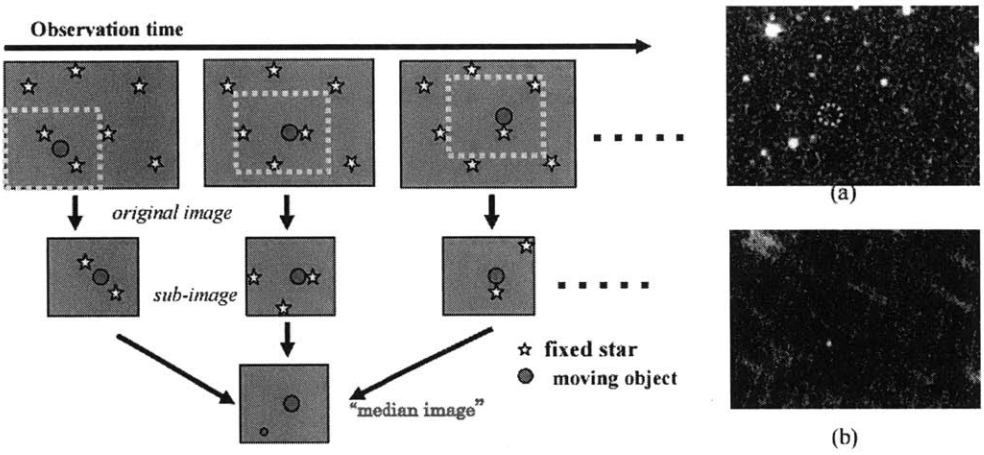


Figure 2-4: Image stacking method (left) and (right) an asteroid detected using this method [10]

### 2.1.2 Orbit Determination

After detecting an asteroid, its orbit should be determined to make informed decisions about mitigation. If decision makers had perfect knowledge of an object's orbit (subsection 2.1.2) and a basic understanding of its size (subsection 2.1.3), mitigation decisions would be much clearer. Orbit uncertainty is relatively small during observations because the measurements constrain the object's position during this period. However, when the object's position is projected into the future, the orbit uncertainties will grow. Figure 2-5 shows how fast the orbit error will grow for a given number of orbits periods observed.

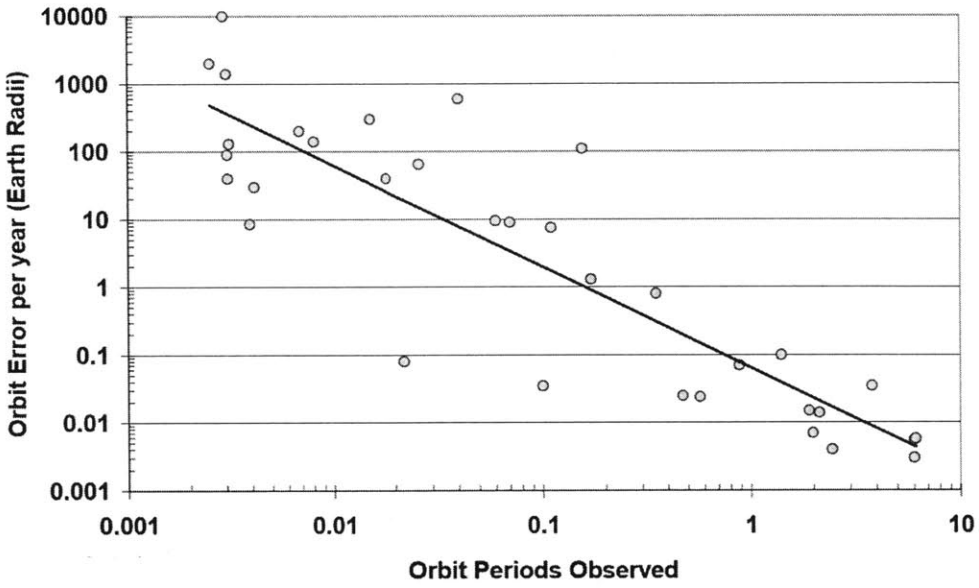


Figure 2-5: Orbit uncertainty growth as a function of observation time [6]

For a single apparition[9] observed by an optical asset, the orbit error per year is 0.1 Earth radii; thus, predictions can be accurate for decades with the uncertainty region constrained to several Earth radii; after that point, the uncertainty region is generally stretched out more than $\pm 0.1$ AU, making the predictions no longer meaningful. Once a full orbit is sampled (two or more apparitions), the error rate drops to 0.01 Earth radii per year, so meaningful predictions can be made up to many centuries, on average. Based on this relationship between error growth and observation time, precise orbit determination can be made with the following ways.

### (1) Radar

Unlike visible detectors, radar can be used in daylight. Radar measurements provide very accurate radial ranging data (8 meters in range, 1 mm/s in range rate) which complements the optical angular data. Therefore, combining the radar data with the optical data can greatly improve the precision in the short term, lowering the coefficient of variation in orbital period by several orders of magnitude. This is

[9] An apparition refers to a period of consecutive days or nights when a particular celestial body may be observed. An apparition begins when it first becomes visible just before sunrise in the eastern sky (heliacal rising), having previously been made invisible by sunlight, and ends when it sets just before sunset in the western sky (heliacal setting).

equivalent to lowering the intercept and the slope of a trend line in Fig. 2-5. Because the optical measurements alone will eventually catch up with the radar-complemented accuracy, the value of radar measurements lies in fast characterization and short-term risk assessment of a newly discovered PHO. Figure 2-6 shows that radar (radio telescopes) can be used both on the ground and in space. However, its usage is limited to only a fraction of the entire PHO population because radar cannot provide active ranging at distances beyond 0.3 AU (45 million kilometers).

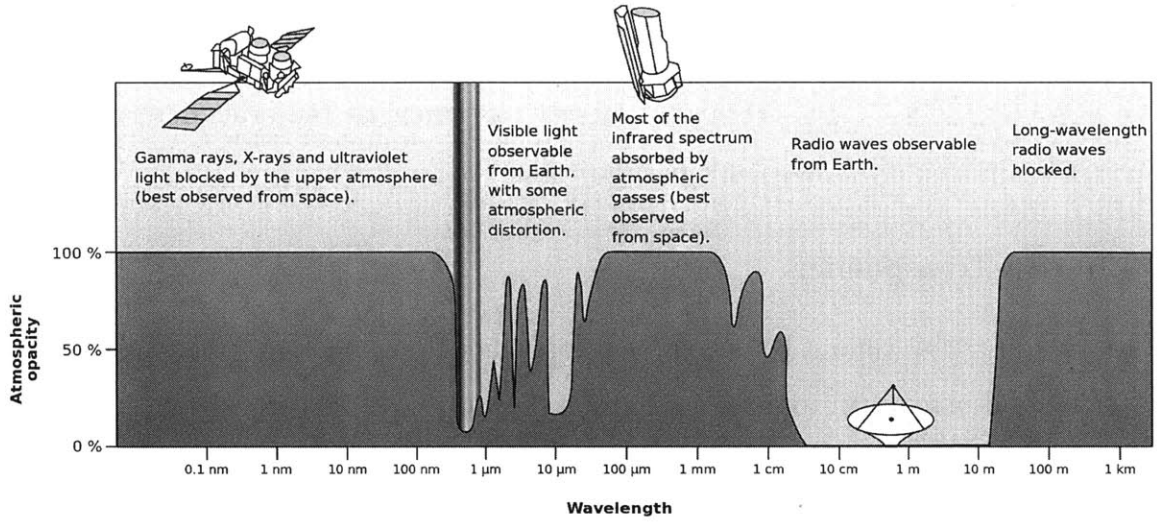


Figure 2-6: Electromagnetic transmittance, or opacity, of the Earth's atmosphere [11]

### (2) Precovery

In astronomy, precovery is short for "pre-discovery recovery," which is a process[10] of revisiting observations of an object that may be found in older archived images. Its purpose is to calculate a more accurate orbit of minor planets that might be asteroids (near-Earth or asteroid-belt), Jupiter-trojans, centaurs, Kuiper belt objects, trans-Neptunian objects, and comets, in a roughly ascending order in distance from the Sun.[11] For a newly discovered object, only a few days or weeks of measurements

[10] Or an image obtained from the process.

[11] For example, the asteroid Pallas (one of the "Big 3" asteroids) was discovered in 1802 and precovered in 1779. Precovery happens most often with minor planets, but dwarf planets, stars, or even exoplanets can be precovered using the same techniques. The dwarf planet Pluto was discovered in 1930 and precovered in 1909.

are available for preliminary orbit calculation with low accuracy. Using the initial information, astronomers can project the motion of the object backward in time and search for it in archived images. Because precovery has the ability to lengthen the observational data interval of a recently discovered object, it often can be used in the orbit-determination process to dramatically improve accuracy. This has an equivalent effect to increasing the number of observed orbit periods in Fig. 2-5).[12] Precovery is particularly useful when a future Earth impact of a particular object cannot be immediately ruled out due to insufficient observation after its discovery. Since the mid-1990s, computers have been used to analyze digital astronomical images and compare them to star catalogues, greatly speeding up the orbit determination process for hundreds of thousands of minor planets.

### (3) In-situ Transponder

If an accurate orbit cannot be determined soon enough by any remote means (including radar and precovery) to make mitigation decisions, a mission to the PHO may be required. Most in-situ orbit estimates are accurate to within 1 km, sufficient to predict a potential impact for many centuries into the future, assuming that a body does not experience planetary encounters or flybys that naturally alter its trajectory. Figure 2-7 illustrates the results from a JPL study. It estimated that tracking the spacecraft orbiting Apophis would reduce the size of a position uncertainty ellipse to $5 \times 0.6$ km after 20 days and to $360 \times 180$m after 65 days[13]. Such an in-situ orbit-determination sensor may be coupled with a spacecraft mission designed to characterize the threat as described later.

[12] An extreme case of precovery involves a near-Earth object which was discovered in 2000 (designated 2000 YK66). Precovery revealed that it had previously been discovered in 1950 and then lost for half a century (provisionally designated 1950DA at that time). This exceptionally long observation period allowed an unusually precise orbit calculation, and the asteroid was determined to have a small chance of colliding with Earth. After an asteroid's orbit is calculated with sufficient precision, it is assigned a number, so it is now called (29075) 1950 DA.

[13] (semi-major axis length) $\times$ (semi-minor axis length)

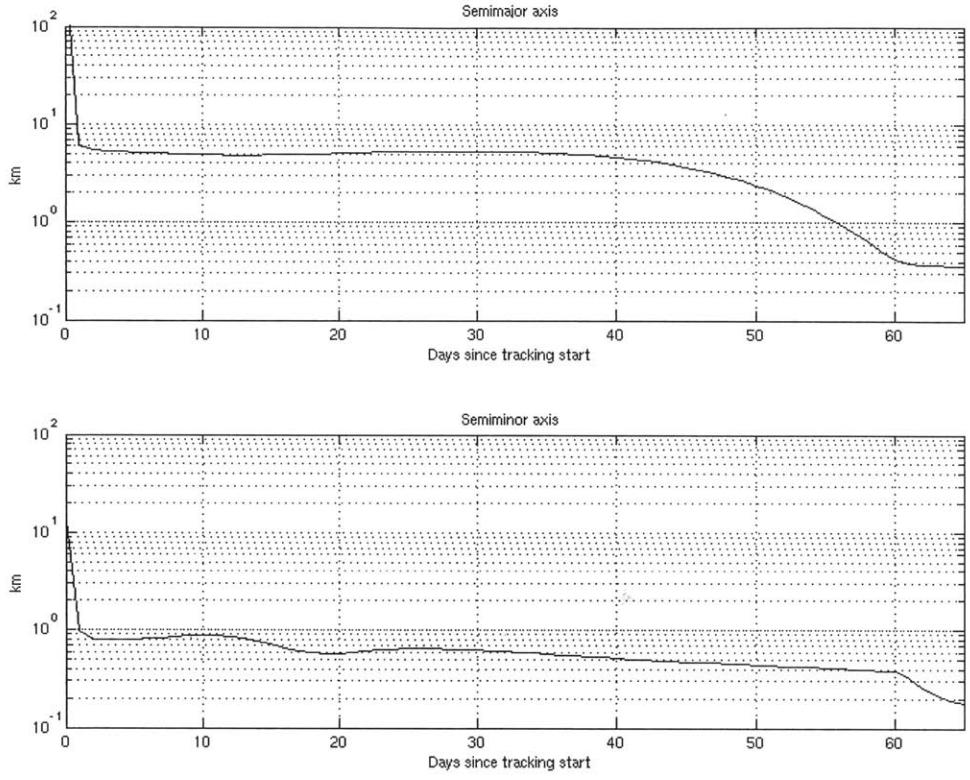


Figure 2-7: Apophis Orbit Uncertainty (1-sigma) at the Earth 2029 B-plane [12]

### 2.1.3 Physical Characterization

The remote sensing techniques discussed so far form a hierarchy in the accuracy of the inferred values for the asteroid's physical parameters. As will be discussed in Section 2.3, one of the key parameters to characterize before deflection is the asteroid's mass. Figure 2-8 shows that optical-intensity measurements of a newly discovered NEO enable an estimate of its mass to within a factor of about 50. If remotely sensed broadband colors are added, rough taxonomic classification of the NEO is possible, improving the mass estimate to within a factor of 8. Adding spectroscopic observations to the mass estimates improves accuracy by a factor of 5 or 6.[14] Polarimetric

[14]This uses a fact that there is a clear correlation between spectral slope and the size of the bodies. For example, smaller objects have larger spectral slopes than bigger objects, possibly owing to space weathering.

observations can improve the accuracy by about a factor of 3, and radar can improve the mass estimate by a factor of 2 by further constraining the asteroid's size and shape. Very accurate mass measurements (from 10% to 1%) can be achieved only by visiting the object; then interior structures and the density distribution can be determined. The following example illustrates the use of various remote sensing techniques from the least accurate (bottom) to the most accurate (the top).

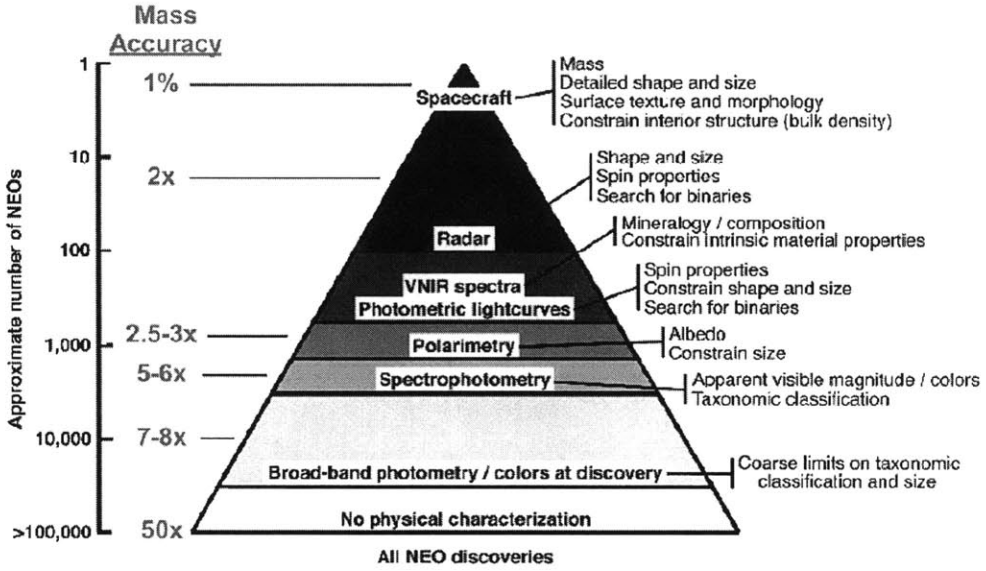


Figure 2-8: Hierarchy of accuracy of remote sensing techniques [6]

### The Hayabusa Mission

The Hayabusa mission by the Japan Aerospace Exploration Agency (JAXA) was the first successful attempt to return an asteroid sample, from 25143 Itokawa to Earth for analysis. Besides the sample return, the mass and topography measurements of the near-Earth asteroid demonstrated how such a mission can greatly improve our knowledge of specific asteroids. Itokawa is classified as a "Mars-crosser" because its aphelion (1.695 AU) is greater than that of Mars (1.67 AU) and its perihelion (0.953 AU) is less than the Martian perihelion (1.3 AU). Itokawa is an Earth-crosser as well for the same reason, where the Earth's aphelion is 1.016 AU and the perihelion is 0.983 AU. See Appendix A for the more detailed definition and other related terms. The

inclination of Itokawa to the ecliptic is 1.6 degrees. Figure 2-9 (left) shows that the orbit of Itokawa has a significantly higher eccentricity than Earth's. The trajectory of Hayabusa spacecraft is shown both in the inertial frame of (Fig. 2-9 left) and in the the rotating frame (2-9 right).

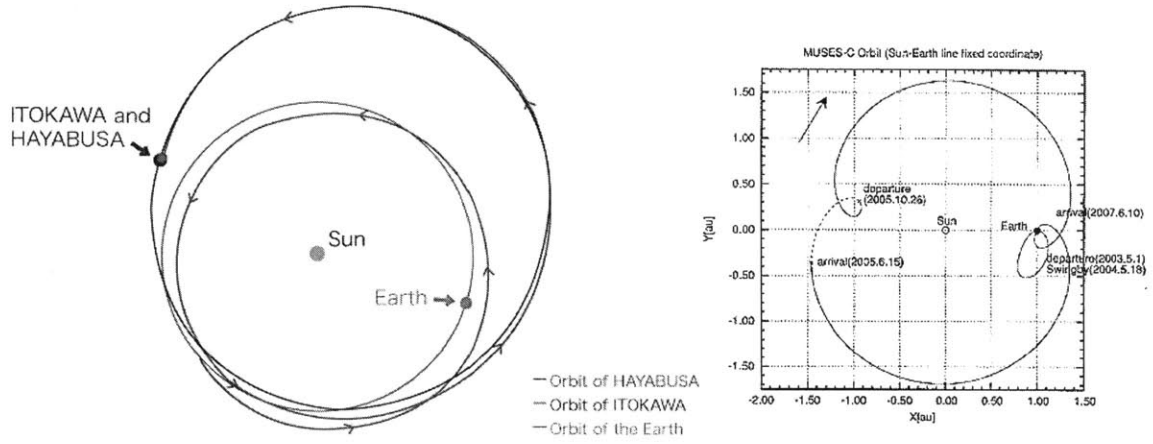


Figure 2-9: The orbits of asteroid Itokawa and Hayabusa spacecraft [13] [14]

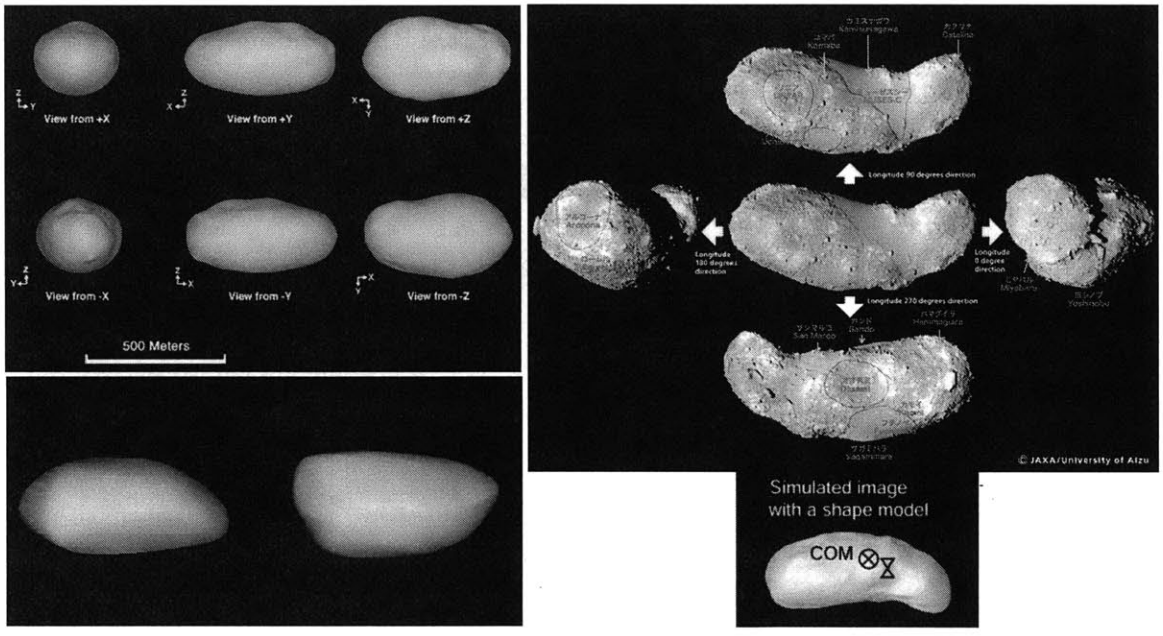


Figure 2-10: Physical models of the asteroid Itokawa before (left) and after (right) the Hayabusa Mission [15–18]

Prior to the Hayabusa mission, ground-based measurements were limited to radar imaging at Arecibo and Goldstone, from which Itokawa's approximate volume and

shape could be found [15]. Itokawa was estimated to be of S-type (stony or siliceous), with the shape of a 630±60-m-long and 250±30-m-wide [84] ellipsoid. Further echo measurements improved this initial ellipsoid model (Fig. 2-10, top-left) to a more irregular shape (Fig. 2-10, bottom-left), but the density, and hence the mass, was still largely unknown [16]. The prior-Hayabusa estimates ranged from $2.7\times10^{10}$ kg to $6.5\times10^{10}$ kg, with an uncertainty level as high as 45% around the nominal value of $4.5\times10^{10}$ kg [84]. The post-Hayabusa data reduced this uncertainty down to 5% around the nominal value of $3.58\times10^{10}$ kg, resulting in a full range of $3.40\times10^{10}$kg to $3.76\times10^{10}$kg [17]. This is a 16-fold improvement from the pre-mission to the post-mission in terms of the coefficient of variation in the asteroid's mass estimate. Note that the true shape of Itokawa (Fig. 2-10, top-right) is significantly different from the initial ellipsoidal model (Fig. 2-10, top-left). Also, the center of mass is slightly off the centroid (bottom-right), implying a heterogeneous density distribution. Onboard measurements from the asteroid multi-band imaging camera (AMICA) and the wide-angle optical navigation camera (ONC-W) were combined with the measurement data from the light detection and ranging instrument (LIDAR), providing accurate knowledge of the spacecraft location relative to the asteroid as well as the asteroid's surface topography [17].

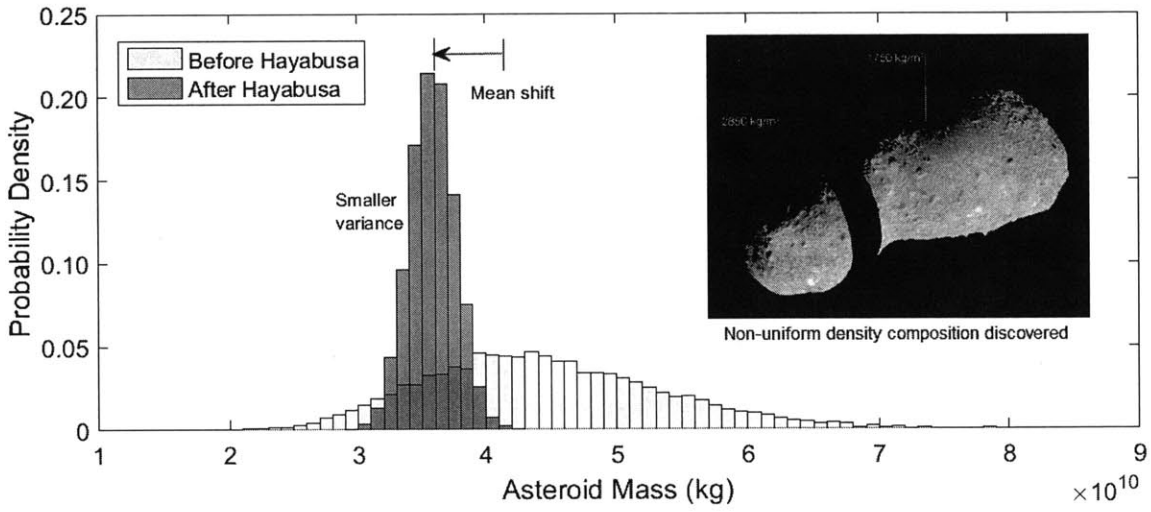


Figure 2-11: Mass distributions of Itokawa before and after Hayabusa Mission [19]

Acceleration of the spacecraft was then calculated from this position data, and after subtracting the contribution of onboard thrusters, the gravity of the asteroid could be obtained. The gravitational coefficient, $\mu = Gm$, defined as the product of the gravity constant and the asteroid mass, was first determined to be (2.39 $\pm$ 0.12) $\times 10^9$ km$^3$/s$^2$, from which the mass of Itokawa was derived to be $3.58 \times 10^{10}$ kg with an uncertainty of $\pm$5%. The shape model of Itokawa constructed with AMICA images indicates a volume of 1.84 $\times 10^7$ m$^3$ within 5% uncertainty, from which the bulk density of 1.95 g/cm$^3$ was determined with 7% uncertainty. The near-infrared spectrometer (NIRS) reported that the Itokawa spectrum near the 1-mm absorption band is similar to those of LL-type chondrites. Considering that the bulk density of LL ordinary chondrites is 3.19 g/cm$^3$, the bulk porosity of Itokawa indicates a high porosity of about 40%, similar to coarse angular (non-round) sands. Itokawa is the first S-type (stony) asteroid showing such a high porosity and the first subkilometer-sized small asteroid showing a rubble-pile structure rather than a solid monolithic structure. The most probable origin of Itokawa is the inner part of the asteroid main belt because a high porosity may be the result of gravitational aggregation of collision fragments.

### 2.1.4 Conclusion

This section discussed several aspects of detecting and tracking PHOs. First, a new PHO is found by using ground-based or space-based assets (2.1.1), and its near-Earth orbit is calculated. Orbit determination further refines this preliminary orbit with a variety of methods (2.1.2). In parallel with orbit determination, physical characterization must be carried out in order to make mitigation decisions 2.1.3. The next section (2.2) is devoted to theories of assessing asteroid hazards. After that, methods for mitiating actual threats are discussed (2.3).

## 2.2 Decision

To determine whether an asteroid is on a likely collision course with Earth, the future approaches of the asteroid must be predicted. Close approaches (CAs), or close encounters, happen periodically with Earth[15]. Periodic approaches can significantly alter an asteroid's trajectory due to accumulation of perturbation effects near the same position in its orbit over multiple periods [25]. This implies that, even if the current pre-CA orbit does not lead to an impact with Earth, altered post-CA orbits might result in an impact. The first part of this section is dedicated to the basic concepts such as b-plane geometry and Öpik's theory to understand the mechanism of close approaches(Subsection 2.2.1). After that, Valsecchi circles and keyhole theories are introduced to explain the repeating patterns of close approaches in the context of orbital resonance (Subsection 2.2.2).

### 2.2.1 B-plane and Öpik's Theory

The b-plane is a classical target plane that has been used in astronomy since the 1960s.[16] Ernst Öpik first introduced the $(\xi, \eta, \zeta)$ coordinate system which is especially useful for a small-body impact analysis. Figure 2-12 illustrates Öpik's notation of $\xi, \eta, \zeta$ axes along with the b-plane comoving with Earth. The b-plane is the plane normal to the unperturbed velocity $\vec{V}_\infty$ of an asteroid, relative to Earth; the b-plane contains the center of the planet (Earth) at the moment when the small body enters the sphere of influence of that planet [21]. The b-plane is named after the impact parameter (or collision parameter) $b$ which is the distance from the target planet to a point in the plane. The impact parameter vector $\vec{b}$ extends from the center of the planet to the intersection of the b-plane and the incoming asymptote; its magnitude is a measure of deflection effects by the planet, as will be explained later in Fig. 2-15. The general planetocentric $(\xi, \eta, \zeta)$ frame, centered at Earth in this case, is defined

[15] or other planets such as Venus or Jupiter if the asteroid has a high orbit eccentricity

[16] The target plane is a plane comoving with the planet and perpendicular to the incoming velocity of the asteroid. The unperturbed, asymptotic velocity of the asteroid is used to calculate its incoming velocity relative to Earth.

as follows. First the positive $\eta$-axis is obtained from the asteroid's geocentric velocity $\overrightarrow{V_\infty}$. Next, the negative $\zeta$-axis is aligned with the b-plane projection of the Earth's heliocentric velocity $\overrightarrow{V_\oplus}$. The positive $\xi$-axis is lastly defined such that the entire coordinate system is right-handed. The same results can be obtained from Eq. 2.1, Eq. 2.2, and Eq. 2.3 [20].

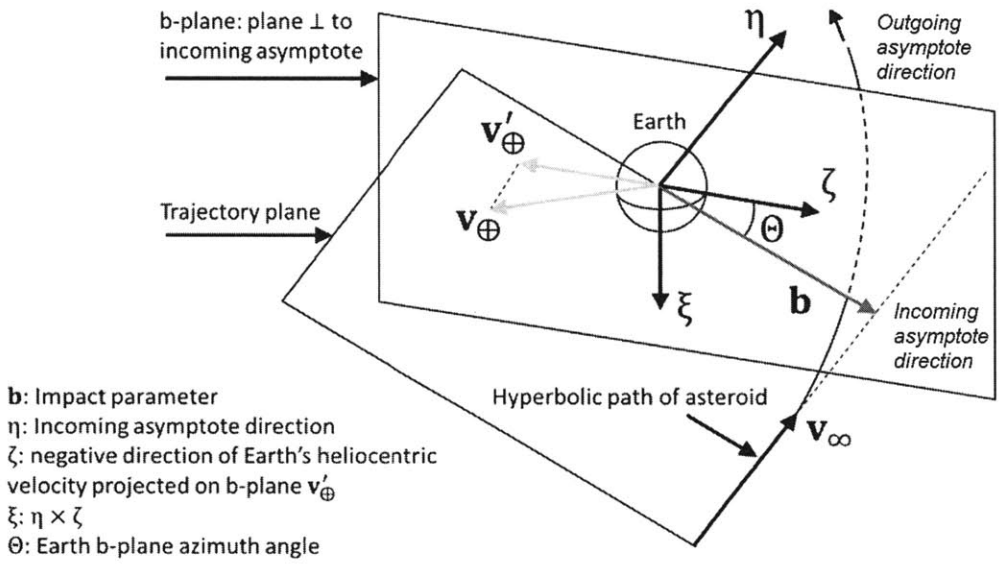


Figure 2-12: Definition of B-plane Axes [20]

$$\vec{\eta} = \overrightarrow{V_\infty} / |\overrightarrow{V_\infty}| \tag{2.1}$$

$$\vec{\xi} = (\overrightarrow{V_\oplus} \times \vec{\eta}) / |\overrightarrow{V_\oplus} \times \vec{\eta}| \tag{2.2}$$

$$\vec{\zeta} = \vec{\xi} \times \vec{\eta} \tag{2.3}$$

This coordinate system has a property which is very important in analyzing the NEO encounters with Earth: Öpik's coordinate system decouples the temporal dimension (time of arrival) and the spatial dimension (MOID) between two celestial bodies [20]. This principle can be demonstrated by approximating the orbits of two bodies as straight lines in a short span of time. To see the effect of changing the time of arrival, suppose that the asteroid arrives at the target planet a few hours later; during that time interval, the planet will have moved linearly with its constant velocity $\overrightarrow{V_\oplus}$, and the origin of the b-plane will also have moved. Because the origin has moved in the

negative $\zeta$ direction according to the sign conventions explained earlier; therfore, the new impact position should be more positive than the old one, translated to the right direction. To see the effect of changing the MOID, we analyze the shortest segment joining two orbits which is the exact definition of MOID. The $\xi$-axis is in parallel with the shortest segment joining the approximately linear orbits of the planet and the small body because the vector $\vec{\xi} = (\overrightarrow{V_\oplus} \times \vec{\eta}) \; / \; |\overrightarrow{V_\oplus} \times |\vec{\eta}$ is orthogonal to both $\overrightarrow{V_\oplus}$ and $\overrightarrow{V_\infty}$. Therefore, the $\xi$ coordinate of the impact point on the b-plane equals the asteroid's MOID. The following statement summarizes our discussion so far:

> In Öpik's frame, the two main factors (spatial and temporal) leading to an impact are decoupled. The proximity between two orbits, measured with MOID, only influences the $\xi$ coordinate of the impact point, whereas the phasing between two bodies, given by time of arrival, only influences the $\zeta$ coordinate. [21]

Öpik's theory models the planetary encounter of a small body as a hyperbolic orbit near Earth. The small body approaches Earth from an incoming asymptote, reaches the minimum approach distance at the b-plane, and leaves Earth towards an outgoing asymptote, as shown in Fig. 2-12. For simplicity, Earth is assumed to have an exactly circular orbit around the Sun, and the Sun's gravity is assumed to be negligibly small compared to the Earth gravity during the CA event. Öpik's theory gives smaller errors for closer approaches, exact only in the limit of the minimum approach distance going to zero. The theory's assumptions work well as long as the gravitational interaction between the planet and the small body can be considered instantaneous in a small region. When the encounter occurs at low planetocentric velocity, with a Tisserand parameter approaching 3, its interaction is no longer "point-like," with increasing errors; for example, Apophis's Tisserand parameter is 2.968, given that $a = 0.922AU$, $e = 0.191$, and $i = 0.0581$ (radians). The analytical theory is inapplicable for a Tisserand parameter exceeding 3 [22], in which case numerical propagation becomes necessary. Except for these limiting cases, Öpik's assumptions provide useful analytic expressions for geometries of pre-CA and post-CA trajectories.

### (1) Pre-CA geometry

The b-plane coordinates can be obtained by multiplying Earth-referenced $(X, Y, Z)$ coordinates by rotation matrices. The Earth reference frame is defined using only the locations of Earth and the Sun, and information about the asteroid[17] is not necessary. The X-axis points radially from the Sun; the Y-axis coincides with the Earth's velocity vector relative to the Sun; and the Z-axis completes the right-handed system, pointing in the direction of Earth's angular momentum vector. The Earth reference frame comoves with Earth and rotates once every year; because the frame orientation is independent of the incoming velocity of the asteroid, the orientation of the asteroid velocity vector will keep changing in the Earth reference frame (Fig. 2-14). By convention, the Sun's gravitational parameter and its distance from Earth are both normalized to 1, and the Earth's period around the Sun will be rescaled to $2\pi$. If an asteroid has semi-major axis $a$,[18] eccentricity $e$, and inclination $i$, then the body's pre-CA velocity components are given by Eq. 2.4, Eq. 2.5, and Eq. 2.6. Note that $\overrightarrow{U}$ means the same as $\overrightarrow{V_\infty}$ in Fig. 2-12. The magnitude of $\overrightarrow{U}$ is $U = 3 - T$ where $T = \frac{1}{a} + 2\sqrt{a(1-e^2)}\cos i$ is Tisserand's parameter[19] with respect to Earth. Because we measure distance in AU and time in $1/(2\pi)$ years, 1U corresponds to a speed of $(1.5 \times 10^8 km)/(60s/min \times 60min/h \times 24h/day \times 365day/yr \times (2\pi)^{-1}yr)$, or $29.87km/s$.

$$U_X = \pm\sqrt{2 - \frac{1}{a} - a(1-e^2)} \tag{2.4}$$

$$U_Y = \sqrt{a(1-e^2)}\cos i - 1 \tag{2.5}$$

$$U_Z = \pm\sqrt{a(1-e^2)}\sin i - 1 \tag{2.6}$$

A more convenient way to visualize this is to use the magnitude and angles. We can define angles $\phi = \tan^{-1}\frac{U_X}{U_Z}$ and $\theta = \tan^{-1}\frac{U_Y}{U}$ in the reference frame, as shown in Fig.

[17] From here onward, the term asteroid will replace the term "small body."

[18] Normalized with respect to the Earth-Sun distance.

[19] Tisserand's parameter (or Tisserand's invariant) is used to distinguish whether an observed small body (comet or asteroid) is a new one or a previously observed one. The value is unique for each orbiting body because it is approximately conserved (Tisserand's relation).

2-13. The components of vector $\vec{U}$ are obtained from $U_X = U\sin\theta\sin\phi$, $U_Y = U\cos\theta$, and $U_Z = U\sin\theta\cos\phi$. The reference coordinates $(X, Y, Z)$ are transformed into the b-plane coordinates $(\xi, \eta, \zeta)$ using Eq. 2.7, and the reverse can be done using Eq. 2.9. Equations 2.8 and 2.10 are expressions with rotation matrices.

$$\begin{bmatrix} \xi \\ \eta \\ \zeta \end{bmatrix} = \begin{bmatrix} 1 & 0 & 0 \\ 0 & \cos\theta & \sin\theta \\ 0 & -\sin\theta & \cos\theta \end{bmatrix} \begin{bmatrix} \cos\phi & 0 & \sin\phi \\ 0 & 1 & 0 \\ -\sin\phi & 0 & \cos\phi \end{bmatrix} \begin{bmatrix} X \\ Y \\ Z \end{bmatrix} \tag{2.7}$$

$$= C_\xi(-\theta)C_Y(-\phi) \begin{bmatrix} X \\ Y \\ Z \end{bmatrix} \tag{2.8}$$

$$\begin{bmatrix} X \\ Y \\ Z \end{bmatrix} = \begin{bmatrix} \cos\phi & 0 & -\sin\phi \\ 0 & 1 & 0 \\ \sin\phi & 0 & \cos\phi \end{bmatrix} \begin{bmatrix} 1 & 0 & 0 \\ 0 & \cos\theta & -\sin\theta \\ 0 & \sin\theta & \cos\theta \end{bmatrix} = \begin{bmatrix} \xi \\ \eta \\ \zeta \end{bmatrix} \tag{2.9}$$

$$= C_Y(\phi)C_\xi(\theta) \begin{bmatrix} \xi \\ \eta \\ \zeta \end{bmatrix} \tag{2.10}$$

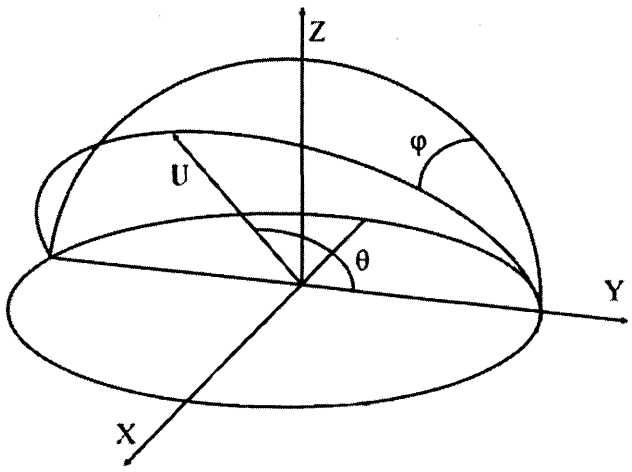


Figure 2-13: Earth reference frame and initial asteroid velocity vector U [21]

Next, the planetocentric velocity vector $(U_X, U_Y, U_Z)$ or $(U, \phi, \theta)$ can be expressed in terms of orbital elements $(a, e, i)$ using Equations 2.11 to 2.13.

$$U = \sqrt{3 - \frac{1}{a} - 2\sqrt{a(1-e^2)}\cos i} \tag{2.11}$$

$$\phi = \tan^{-1}\left[\frac{1}{\sin i}\sqrt{\frac{2a-1}{a(1-e^2)} - 1}\right] \tag{2.12}$$

$$\theta = \cos^{-1}\left[\frac{a(1-U^2)-1}{2aU}\right] = \cos^{-1}\left[\frac{\sqrt{a(1-e^2)} - 1}{\sqrt{3 - \frac{1}{a} - 2\sqrt{a(1-e^2)}\cos i}}\right] \tag{2.13}$$

Conversely, Equations 2.14 through 2.17 transform the velocity vector components into orbital elements.

$$a = \frac{1}{1 - U^2 - 2U_Y} = \frac{1}{1 - U^2 - 2U\cos\theta} \tag{2.14}$$

$$e = \sqrt{U^4 + 4U_Y^2 + U_Z^2(1 - U^2 - 2U_Y) + 4U^2U_Y} \tag{2.15}$$

$$= U\sqrt{(U + 2\cos\theta)^2 + (1 - U^2 - 2U\cos\theta)\sin^2\theta\sin^2\phi} \tag{2.16}$$

$$i = \sin^{-1}\sqrt{\frac{U_Z^2}{U_Z^2 + (1 + U_Y^2)^2}} = \tan^{-1}\frac{U\sin\theta\cos\phi}{1 + U\cos\theta} \tag{2.17}$$

### (2) Post-CA geometry

After the asteroid undergoes a close encounter with Earth, rotation of the velocity vector $\vec{U}$ occurs. To an observer on Earth, this rotation would look like Fig. 2-14, where $\vec{U}$ is rotated by an angle $\gamma$ in the direction $\psi$. In other words, $\gamma$ is the angle between the pre-CA asteroid velocity $\vec{U}$ and the post-CA asteroid velocity $\vec{U}'$. And then, what is $\psi$? The angle $\psi$ is measured counter-clockwise from a meridian containing the $\vec{U}$ vector. In Fig. 2-14, $\psi$ is the angle between the greater arc and $\Delta U = \vec{U}' - \vec{U}$. Denoted interchangeably with $\Theta$ ("Earth b-plane azimuth angle") in 2-12, $\psi$ shows how much an asteroid's CA trajectory plane is tilted with respect to the Earth's ecliptic. In the b-plane, $\psi$ satisfies $\xi = b\sin\psi$ and $\zeta = b\cos\psi$, where $\xi$

and $\zeta$ are related to the MOID and the timing, respectively.[20]

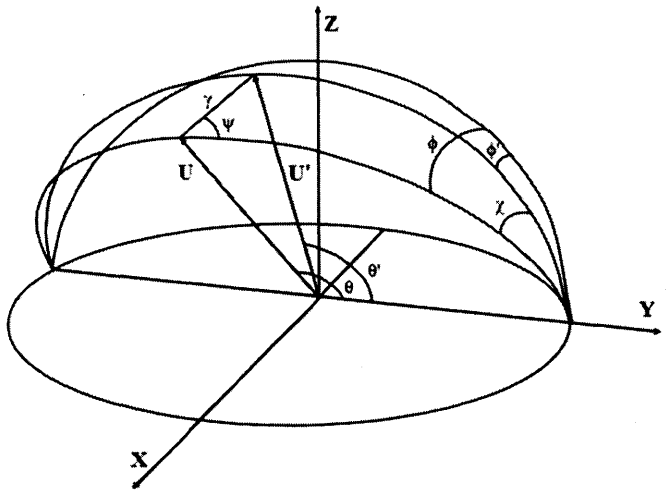


Figure 2-14: Initial and final asteroid velocity vectors (3D represenation) [21]

As shown in Fig. 2-15, $\gamma$ is the magnitude of deflection made during a CA. It can be calculated with the asteroid speed $U$, the planet mass $m$, and the impact parameter $b$. The trajectory of a small body will be deflected more if the planet has larger mass (high $m$) or the small body approaches closer to the planet (low $b$). In Eq. 2.18, we define characteristic length $c = m/U^2$ where $m$ is measured in solar masses and $U$ is normalized. Figure 2-15 illustrates the relationship among impact parameter $b$, characteristic length $c$, and deflection angle $\gamma$.

$$\tan\frac{\gamma}{2} = \frac{m}{bU^2} = \frac{c}{b} \tag{2.18}$$

For $U = 0.5$ (15 km/s), typical for many near-Earth asteroids, the characteristic length becomes (Earth mass in solar masses)$/U^2 = (1/333,000)/(0.5)^2 = 1.2 \times 10^{-5} AU$ or 0.29 Earth radii [22, 85]. An encounter preserves the magnitude of the velocity vector ($U' = U$), but the direction angles will change. The post-encounter angles $\theta'$ and $\phi'$ can be obtained in terms of $\theta, \phi, \gamma$, and $\psi$ using Eqs. 2.19 through

[20]B-plane azimuth angle $\psi$ is different from inclination $i$ in that the former is a tilted angle of a local trajectory near a CA while the latter is a tilted angle of a global trajectory without taking a CA into account.

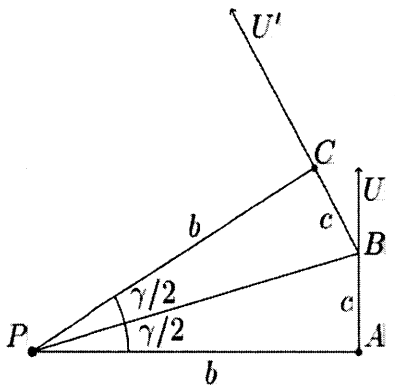


Figure 2-15: Initial and final asteroid velocity vectors (2D representation) [22]

Eq. 2.21 [86].[21] Once $U', \theta'$, and $\psi'$ are all obtained, orbital elements $a'$, $e'$, and $i'$ can be evaluated using Eqs. 2.14 through 2.17.

$$\cos\theta' = \cos\theta\cos\gamma + \sin\theta\sin\gamma\sin\psi \tag{2.19}$$

$$\tan(\phi - \phi') = \frac{\sin\gamma\sin\psi}{\sin\theta\cos\gamma - \cos\theta\sin\gamma\cos\psi} \tag{2.20}$$

$$\tan\phi' = \frac{\tan\phi - \tan(\phi - \phi')}{1 + \tan\phi\tan(\phi - \phi')} \tag{2.21}$$

Potentially hazardous asteroids tend to have multiple encounters with Earth because after establishing the first encounter, they might be deflected into a resonant return orbit in which the orbital periods of Earth and those of an asteroid are synchronized to a ratio of two integers. Therefore, post-encounter analysis from Öpik's theory is useful for identifying resonance orbits and keyholes.

### 2.2.2 Valsecchi Circles and Keyhole Theory

In orbital resonance, the post-encounter semi-major axis determines whether an asteroid will have resonant returns or not. To further extend Öpik's theory, Valsecchi and others developed the analytic theory of resonant returns; while the Öpik theory describes the instantaneous velocity change before and after an encounter, Valsecchi's

[21] First, Eq. 2.19 is used to calculate $\theta'$. Next, the angular difference $\phi - \phi'$ is obtained from Eq. 2.20. Finally, $\phi$ and $\phi - \phi'$ are used in Eq. 2.21 to yield $\phi'$.

theory deals with a much longer time span (orbital period) between successive encounters. Why is the semi-major axis the key parameter in orbital resonance? Using non-dimensionalization, the Earth's orbital period is $2\pi$ and the asteroid's orbital period is $2\pi(a')^{3/2}$, from Kepler's second law of planetary motion. If $a'$ can be represented as the ratio of two integers $k$ and $h$ ($k/h$ or $k$:$h$), a new encounter will happen in $k$ years ($k$ times the orbital period of Earth), by which time the asteroid would have made $h$ revolutions around the Sun ($h$ times the orbital period of the asteroid). In other words, the asteroid is in a resonant return orbit with semi-major axis $a'$ and a period of $k/h$ years. Let's suppose that an asteroid's semi-major axis and theta-angle are $a = a'_0$ and $\theta = \theta'_0$, respectively, after being perturbed by a close encounter. The value of $a'_0$ in AU is obtained from Eq. 2.22, which in turn yields $\theta'_0$ in Eq. 2.23).

$$a'_0 = (\frac{k}{h})^{3/2} \tag{2.22}$$

$$\theta'_0 = \cos^{-1}\frac{1 - U^2 - 1/a'_0}{2U} \tag{2.23}$$

This value of a newly obtained $\theta'_0$ is important in identifying the Valsecchi circles, which will be explained later. To derive an expression for Valsecchi circles, Eq. 2.18 is transformed to two alternative forms: $\cos\gamma = (b^2 - c^2)/(b^2 + c^2)$ and $\sin\gamma = 2bc/(b^2 + c^2)$. The two equations can be used in 2.18 to substitute $\cos\gamma$ and $\sin\gamma$ with $b$ and $c$. Solving the resultant equation for $\zeta$ gives Eq. 2.24.

$$\zeta = \frac{(b^2 + c^2)\cos\theta'_0 - (b^2 - c^2)\cos\theta}{2c\sin\theta} \tag{2.24}$$

Finally, elimination of $b$ in Eq. 2.24 using $b^2 = \xi^2 + \zeta^2$ yields Eq. 2.25.

$$\xi^2 + \zeta^2 - \frac{2c\sin\theta}{\cos\theta'_0 - \cos\theta}\zeta + \frac{c^2(\cos\theta'_0 + \cos\theta)}{\cos\theta'_0 - \cos\theta} = 0 \tag{2.25}$$

This is the equation of a circle $\zeta^2 + \xi^2 - 2D\zeta + D^2 = R^2$ which has a radius R and is centered at (0, D) where:

$$D = \frac{c \sin\theta}{\cos\theta'_0 - \cos\theta} \tag{2.26}$$

$$R = \frac{c \sin\theta'_0}{\cos\theta'_0 - \cos\theta} \tag{2.27}$$

This circle is called a Valsecchi circle. For each $a'_0$ corresponding to a certain specific $k/h$ ratio, the family of possible trajectories form a circle on the b-plane when the intersecting points of all trajectories within the b-plane are joined together. Figure 2-16 plots the radius and center location of the Valsecchi circles of Apophis (2004 MN 4) for various $k/h$ values. A singularity can be seen in both center location and radius near $k/h = 0.9$. The asymptotic velocity of $U = 5.841$ km/s for Apophis's close approach with Earth in 2029 is used to generate this plot.[22]

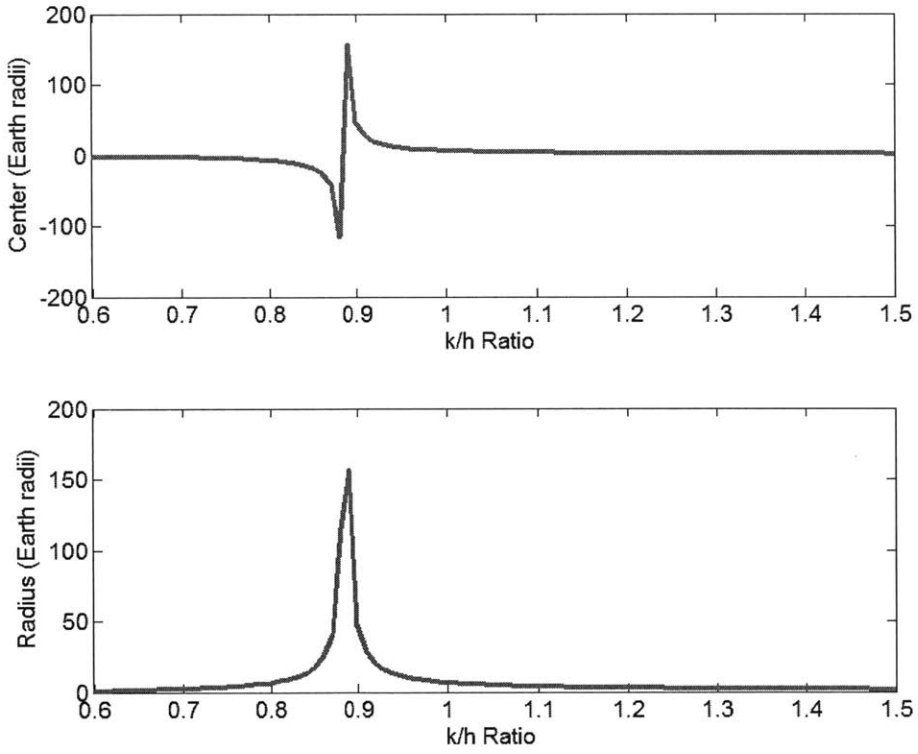


Figure 2-16: Center location and radius of Valsecchi circles for Apophis [22]

[22] The JPL small-body database predicts that this encounter will happen at 21h 46m on April 13th, 2029 [87].

Table 2.1 summarizes the center location and radius of sample Valsecchi circles from Fig. 2-16. Some of these values are drawn in Fig. 2-17. Among the black-lined circles beneath Earth, the largest circle corresponds to $k/h = 7/8$; the second-largest corresponds to $k/h = 6/7$; and the third-largest corresponds to $k/h = 5/6$. The vertical blue line in the figure represents the minimum orbit intersection distance.

Table 2.1: Period ratio, Valsecchi circle radius and center of Apophis

| # Earth Orbits("k") | # Asteroid Orbits("h") | k/h Ratio | VC Radius (Earth radii) | VC Center (Earth radii) |
|---|---|---|---|---|
| 3 | 4 | 0.750 | 4.38 | -5.40 |
| 7 | 9 | 0.777 | 6.09 | -7.00 |
| 4 | 5 | 0.800 | 8.18 | -9.02 |
| 5 | 6 | 0.833 | 14.5 | -15.3 |
| 6 | 7 | 0.857 | 28.0 | -28.7 |
| 7 | 8 | 0.875 | 77.1 | -77.7 |
| 1 | 1 | 1.000 | 8.54 | 8.15 |
| 7 | 6 | 1.167 | 3.93 | 3.78 |
| 6 | 5 | 1.200 | 3.57 | 3.46 |
| 5 | 4 | 1.250 | 3.14 | 3.09 |
| 4 | 3 | 1.333 | 2.62 | 2.65 |

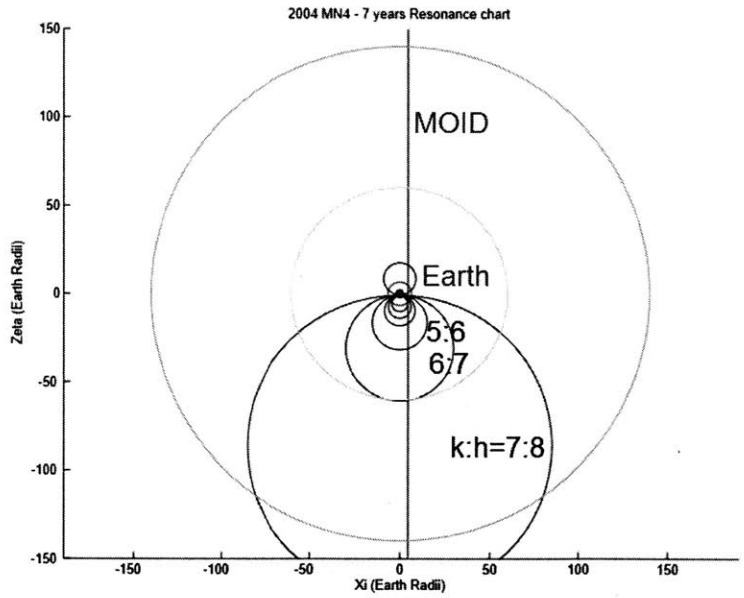


Figure 2-17: Valsecchi circles for Apophis [23]

The term "keyhole" was first introduced by Chodas in 1999. Keyholes are small regions of the b-plane for a specific encounter such that an asteroid will impact Earth at the next resonant return if it passes through one of them. Potential keyhole locations can be estimated by identifying the intersections of Valsecchi circles and the local MOID line. Here, the MOID is the absolute minimum distance that can be achieved in the worst case by altering the timing (phasing) of the encounter between the asteroid and Earth, and the local MOID line is the locus of possible encounters of an asteroid from the Earth perspective in the b-plane. If the MOID is large, the vertical line will move away from Valsecchi circles, leaving no intersections with them.[23] When we have no knowledge of the phasing of the asteroid and Earth and complete knowledge of their orbits, the local MOID has zero width ($\Delta\xi$) and infinite length ($\Delta\zeta$), resulting in a vertical line, as shown in Fig. 2-17. However, this first-hand approximation can be modified: first, the number of Valsecchi circles to consider is greatly reduced by replacing the infinite-length MOID line with an uncertainty region along the line of variations, which will be explained soon; second, a longer-term impact analysis becomes possible by considering the time variability of the MOID.

### (1) Line of Variations (LOV) Approach

The measurement of orbital elements of small bodies is prone to errors due to their small size. The uncertainty region is a relatively small ellipsoid at first, but as time progresses, it is elongated into a tube because the uncertainty grows faster in the along-track direction. To facilitate our understanding, we introduce the notion of virtual asteroids (VAs) whose swarm is bounded by the uncertainty region. There exists only one "true" asteroid in a swarm, but we don't know which one it is; instead, we obtain many possible solutions that all satisfy our measurement reasonably. The position errors of VAs are within the measurement accuracy, but VAs will eventually disperse under differing amounts of perturbing forces. The locus of VAs looks like a straight line when magnified, which is called a line of variations (LOV). Figure

[23] In other words, the distance between the Earth's orbit and the asteroid's orbit is so large that collisions cannot happen under any phasing conditions between Earth and the asteroid.

2-18 illustrates a LOV and other related terms. If a particular VA has a minimum distance of less than 1 Earth radius from Earth, it is known as a virtual impactor (VI). Sigma LOV is a measure of the *along-track* deviation of the VI position relative to the nominal VA; for example, the nominal VA has a sigma LOV of 0 while 99% of the VA swarm has sigma values between -3 and +3 ("3-sigma"). The impact probability decreases as the number of sigmas increase in a normal distribution. Sigma impact, defined as (Distance − Earth's radius)/(Width),[24] is a measure of the impact likelihood in the *cross-track* direction. It is zero when the LOV intersects the Earth and increases as the central axis of the uncertainty region moves away from the Earth. If the numerator is fixed, decreasing width results in a higher sigma impact value.

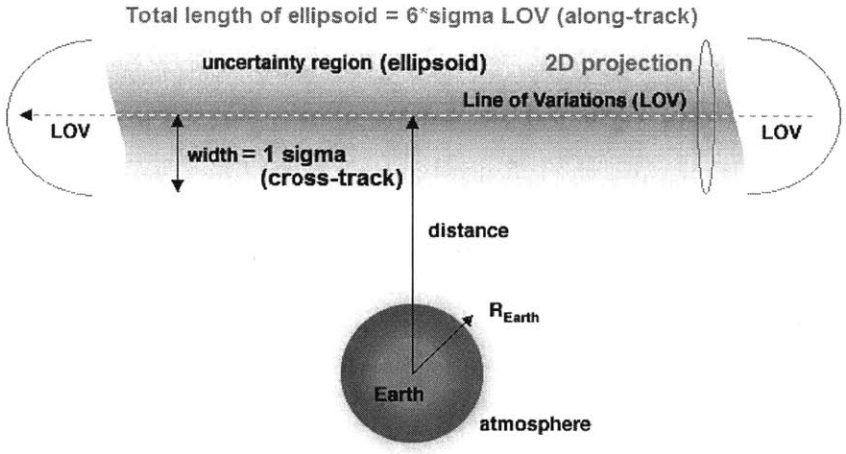


Figure 2-18: Line of variations (LOV) for virtual asteroid (VA) swarm [24]

In our first assumption, the MOID line had an infinite length, so any Valsecchi circles could intersect with it (Fig. 2-19). However, the three-dimensional uncertainty region around the LOV has a finite length and cross-section area, which is now reduced to two-dimensional strips or ellipses when projected onto the b-plane (Fig. 2-20). This implies that (1) only some of the Valsecchi circles can have intersections (keyholes) and (2) the size of keyholes can be determined to be a finite non-zero value.

[24] In the expression, *distance* is measured from the center of Earth to the *along-track* or Sigma-LOV axis, in the *cross-track* direction. The region that spans three times the width (1-sigma, cross-track) from the center line (LOV) away or towards Earth contains 99% of VAs.

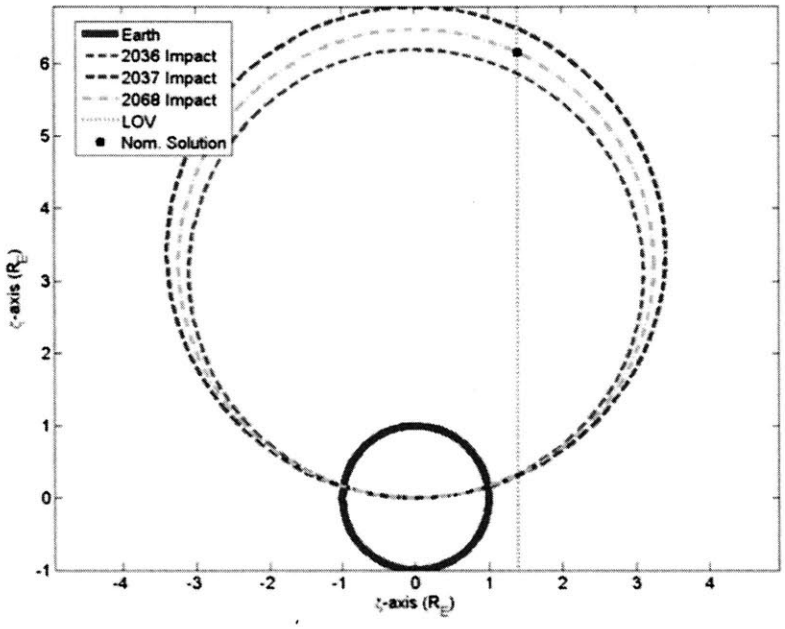


Figure 2-19: Valsecchi circles of Apophis and its line of variations [25]

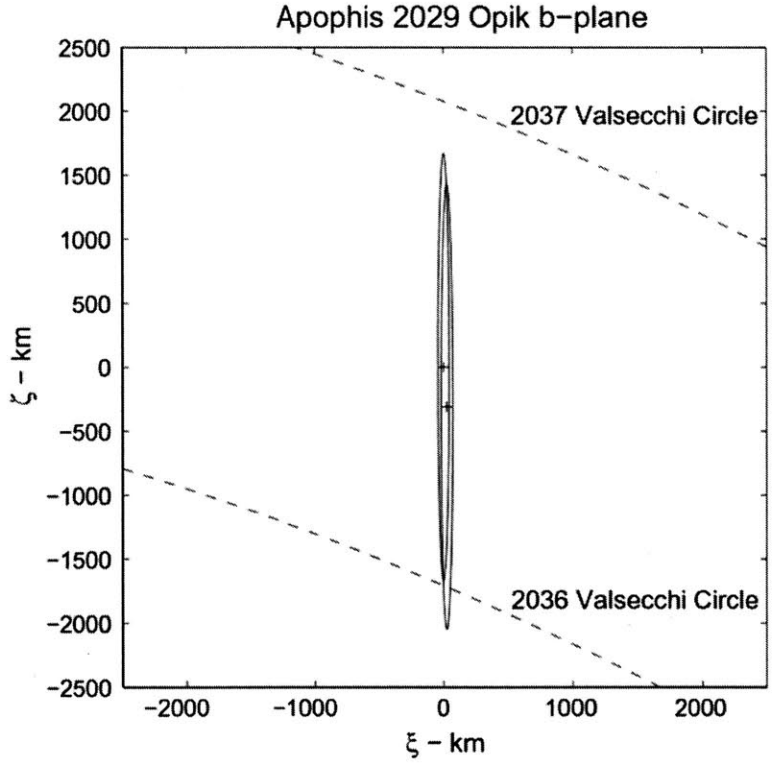


Figure 2-20: Valsecchi circles of Apophis and its line of variations (magnified) [23]

### (2) Drift of Minimum Orbit Intersection Distance (MOID)

In a first-hand impact analysis, it usually suffices to assume that the MOID coordinate ($\xi$) is constant between encounters, only allowing the phasing parameter ($\zeta$) to vary. However, the variation of the MOID may also need to be considered to obtain the precise size or shape of the keyholes. On a very long time scale, secular variations make the MOID slowly evolve through a cycle called the Kozai cycle or $\omega$-cycle. During this precession movement, orbital parameters vary between boundary values, called *proper elements*. Figures 2-21a and 2-21b depict the evolution of eccentricity ($e$) and argument of perihelion ($\omega$) along the iso-Hamiltonian lines of our Solar system. While Apophis follows a circulation trajectory where the $\omega$ value monotonically increases or decreases, 1999 AN 10 follows a libration trajectory where eccentricity and argument of perihelion oscillate in a closed loop.

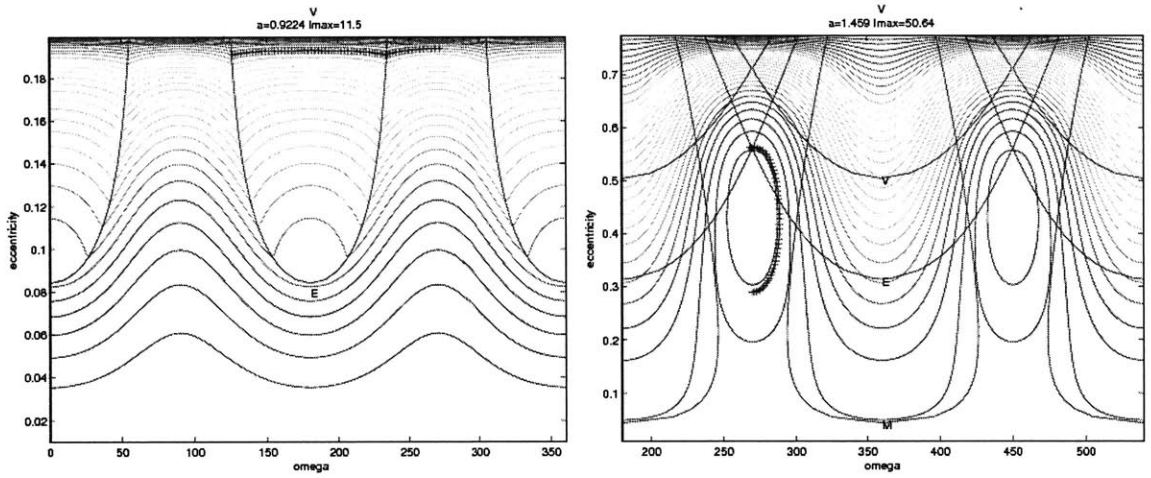


(a) 99942 Apophis (b) 1999 AN 10

Figure 2-21: Long-term drift of orbital parameters [26]

As mentioned at the beginning, changes in orbital elements by Kozai cycles can be neglected except over very long time intervals (thousands of years [88]). On a shorter time scale than Kozai cycles, the MOID can vary because of gravitational perturbation of planets or planet-satellite systems where the barycenter location undergoes changes by alignment of the massive satellites relative to the planet [89]. The secular variation of the MOID may be modeled using simple linear terms for the purpose of obtaining

the keyhole size and locations. For example, the value $\xi''$ at the second encounter will change from $\xi'$ at the first encounter by its first-order derivative multiplied by elapsed time, as shown in Eq. 2.28.

$$\xi'' = \xi' + \frac{d\xi}{dt}(t_0'' - t_0') \tag{2.28}$$

The derivative can be calculated from analytic theory or numerical integration. By setting $\xi''$ to zero (collision at the second encounter), the value of the $\xi'$ can be found for the first encounter.

$$\xi_0 = -\frac{d\xi}{dt}(t_0'' - t_0') \tag{2.29}$$

To compute the other remaining coordinate $\zeta_0'$, we pick two points $(\xi_0', \zeta_{01}')$ and $(\xi_0', \zeta_{02}')$ on the b-plane at the first encounter. After the small body makes $h$ revolutions around the Sun, the two points will be mapped onto $(\xi_1'', \zeta_1'')$ and $(\xi_2'', \zeta_2'')$ on the b-plane at the second encounter with Earth. We then check whether $\zeta_1''\zeta_2'' < 0$; if not, we choose another pair of $\zeta_{01}'$ and $\zeta_{02}' < 0$ until the condition is satisfied. It can be shown that keyholes have lunar crescent (arclet) shapes curved along the associated resonance circles if $c^2 << b^2$, as illustrated in Fig. 2-22. There are two noteworthy facts that can be observed. First, the keyhole is two-dimensional on the b-plane, but this thesis will assume its one-dimensional projection on the $\zeta$ axis for simplicity. Second, Valsecchi's Circles cannot always be used to estimate the keyhole locations. For the case of 1997 XF11 in the figure, Tisserand's parameter $T = \frac{1}{a} + 2\sqrt{a(1-e^2)}\cos i$ is 2.79 from $a$=1.4427 AU, $e$=0.4839, and $i$=4.10 degrees. And the three out of four keyholes overlap with their corresponding Valssecchi circles. On the other hand, Apophis has a Tisserand's parameter of 2.99, much closer to the limiting value of 3, in which case the Valsecchi Circles may not predict the keyhole locations accurately. Because simulating all possible initial conditions to locate keyholes is computationally prohibitive, this thesis will use existing keyhole maps of Apophis and Bennu.

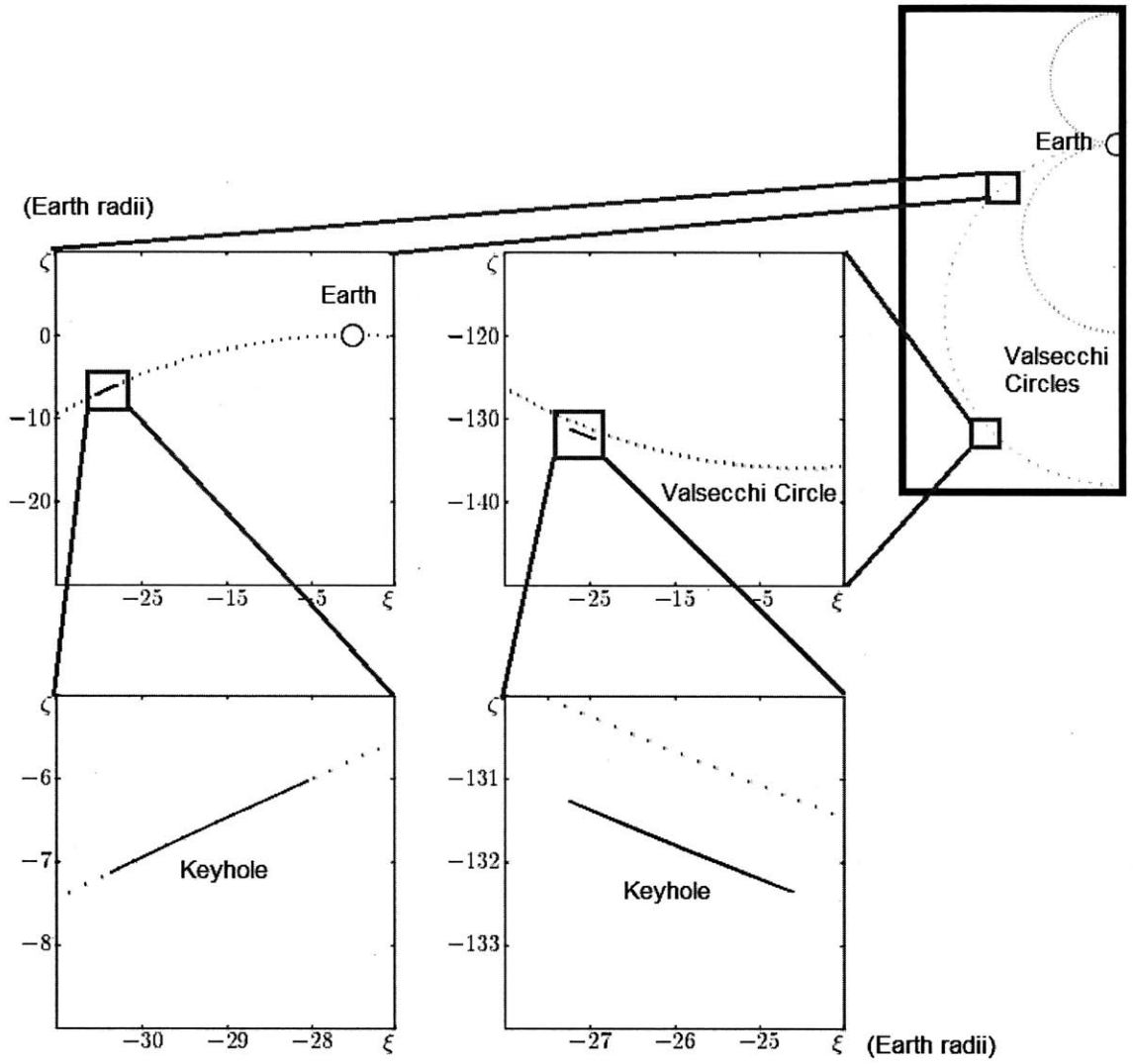


Figure 2-22: Keyholes of 1999 XF 11 in the b-plane of the October 2028 encounter with Earth [22]

It is also visible from Fig. 2-22 that the keyhole farthest from the Earth is somewhat displaced from the resonant circle. This is because the exact resonance correspondsto the circle and the return does not take place at the resonance, but at a slightly dfferent value of semi-major axis to compensate for the non zero value of $\zeta$ at the first encounter [22].

### 2.2.3 Conclusion

This section has covered basic theories behind the close approaches of asteroids. Close approaches (CA) occur periodically if a resonance condition is satisfied between Earth and a near-Earth asteroid (NEA). The minimum distance from Earth varies because (1) the relative phasing between the asteroid and Earth is different in a short term (synodic period) and (2) the asteroid's trajectory itself is perturbed by Earth or other planets.[25] If a close approach happens at one of the gravitational keyholes, an impact may occur at the next resonant return. Therefore, preventing a keyhole passage can eliminate the root cause of a potential future impact. However, this preemtive measure is not applicable to all near-Earth asteroids (NEA). As already remarked, for an asteroid to form a gravitational keyhole, its trajectory has to pass within 0.15 AU of the Earth, and only about 20 percent of potential impactor trajectories will have a subsequent CA within a 25-year period before potential impact [67]. Deflecting NEAs that have keyholes is the focus of this thesis, and deflection of NEAs without keyholes is left as future work.

[25]To clarify, the closest distance from Earth or the minimum CA distance can be changed by Earth. However, the minimum orbit intersection distance (MOID) can only be changed by celestial objects other than Earth.

## 2.3 Deflection

If a substantial impact risk is identified with an asteroid, through the means discussed in the previous section (2.2), mitigation action is required to deflect or even disintegrate it. The first serious study of planetary defense against asteroids was conducted as an interdepartmental student project in systems engineering at the Massachusetts Institute of Technology [90]. This study was conducted in 1967, with a hypothesis that a kilometer-sized asteroid Icarus would collide with Earth in the following year (1968). The study concluded that the asteroid could be deflected or pulverized with six Saturn V rockets carrying 100-Mton warheads [91]. In 1980, Alvarez et al. announced asteroid impact as the putative cause of the Cretaceous-Tertiary extinction [92]. In 1984, Hyde further explored a range of detonation options for nuclear explosives [93]. In 1990, Wood et al. showed that non-nuclear interceptors, such as kinetic energy impactors, could be used for smaller targets [94]. In addition to these direct" (or "impulse") methods, a number of indirect (or "slow-push") methods have subsequently been proposed that utilize gravity, solar/thermal energy, etc. Roughly speaking, strategies for asteroid collision mitigation fall into two basic categories: destruction that disintegrates the asteroid or deflection that delays or advances the asteroid's approach to Earth. Destruction strategies aim at fragmenting the target asteroid and scattering the resultant fragments so that they miss Earth or burn up in the atmosphere. Delay (or advancement) strategies exploit the fact that an impact occurs when both Earth and the asteroid reach the same point in space at the same time. It takes 425 seconds for Earth to travel its diameter (12,750 km) with its orbital speed around the sun, so delaying or advancing the asteroid arrival could avoid the collision in principle [95].

### 2.3.1 Deflecting Direction

Using either a direct or indirect method, this delaying or advancing of an asteroid encounter is done by applying a velocity increment or decrement to change its course towards Earth. In direct deflection where the momentum transfer is impulse-based,

we can calculate the displacement assuming a rectilinear motion, as shown in Eq. 2.30 [27].

$$\delta = \Delta v t \tag{2.30}$$

On a longer time scale, the amount of deflection differs considerably, depending upon in which direction a velocity increment is applied. Figure 2-23 illustrates three possible deflection cases: out-of-plane, radial, and along-track.

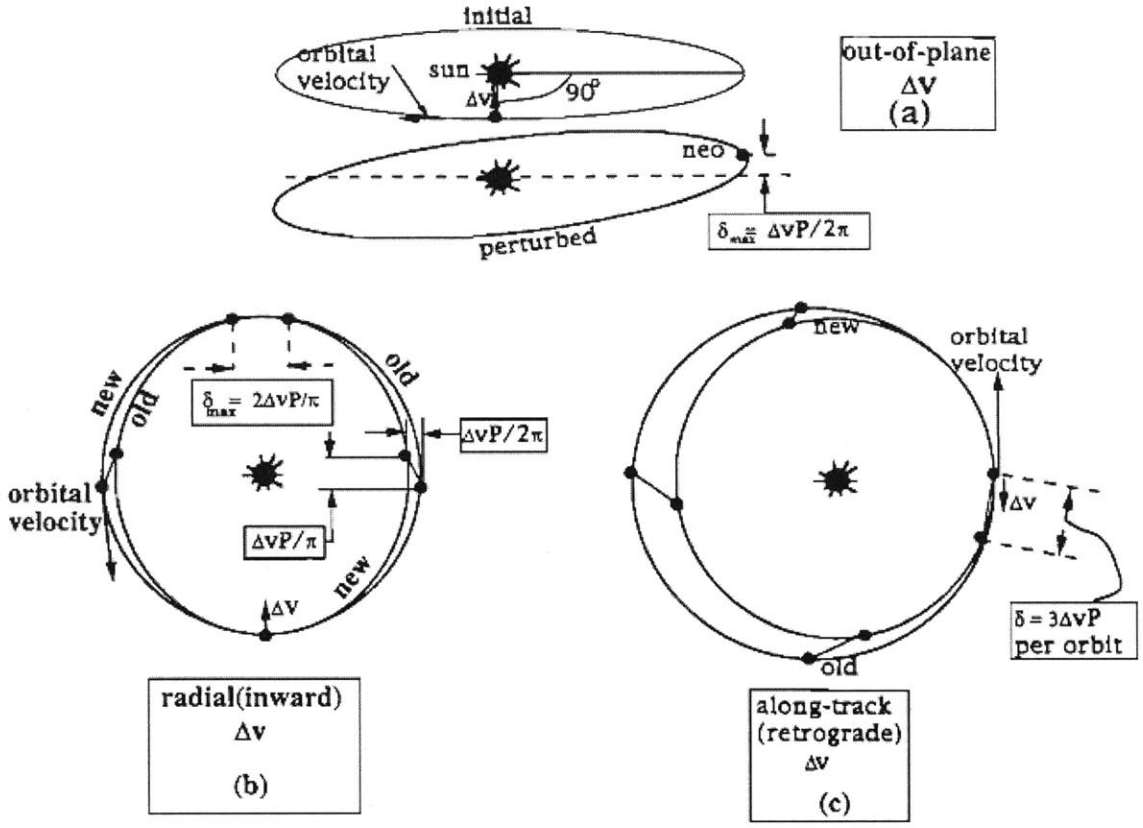


Figure 2-23: Effect on the NEO trajectory upon perturbing the orbital velocity by $\Delta v$: (a) perpendicular to orbital plane; (b) radially in orbital plane; and (c) tangentially in orbital plane [27]

### (1) Perpendicular to orbital plane

An out-of-plane velocity increment, perpendicular to the orbit plane of the NEO, changes only the orbit inclination, as shown in Fig. 2-23(a). Therefore, the original semi-major axis and eccentricity remain unchanged. The maximum displacement

of the NEO ($\delta_{max}$) occurs at 90 degrees from the place in the orbit at which the perturbation was applied, and its magnitude is approximately $\Delta vP/2\pi$.

### (2) Radially in orbital plane

If a velocity increment is applied radially, the eccentricity changes while the semi-major axis is unaffected. The maximum radial displacement occurs at around 90 degrees and the magnitude is still $\Delta vP/2\pi$, the same as before. However, the maximum along-track displacement occurs at around 180 degrees and the distance is bigger, $2\Delta vP/\pi$. Note that the perturbed NEO returns to the starting point at the same time as the unperturbed counterpart because the semimajor axis, and hence the orbit period, was unchanged.

### (3) Tangentially in orbital plane

A delta-v applied along the track of the NEO's motion alters the semi-major axis, and hence orbit period, in addition to a change of eccentricity. The resultant displacement from the original motion is a combination of an oscillatory component (eccentricity change, same as in radial perturbation) and a secular drift (semi-major axis change) that keeps growing over successive orbits. For an elliptical orbit, subtracting the vis-viva equation for the initial orbital energy

$$E = -\frac{GM_s}{2a} = -\frac{GM_s}{r} + \frac{v^2}{2} \tag{2.31}$$

from the equation for the final orbital energy

$$E' = -\frac{GM_s}{2(a+\Delta a)} = -\frac{GM_s}{r} + \frac{(v+\Delta v)^2}{2} \tag{2.32}$$

gives the following relationship:

$$\frac{\Delta a}{a} = 2\frac{\Delta v}{v_0}\sqrt{\frac{2a}{r} - 1} \tag{2.33}$$

where $v_0 = \sqrt{GM_s/a}$ is the mean orbital velocity. The semi-major axis change $\frac{\Delta a}{a}$ can be approximated by $\frac{2}{3}\frac{\Delta P}{P}$ from Kepler's third law, and the mean position in the new orbit diverges by a distance $-2\pi a\frac{\Delta P}{P}$. The the mean velocity of divergence is

$$\Delta v' = \frac{2\pi a}{P}\frac{\Delta P}{P} = v_0\frac{\Delta P}{P} = 3v_0\sqrt{\frac{2a}{r} - 1} \tag{2.34}$$

For a circular orbit, $r = a$, the maximum deflection is

$$\delta = |\Delta v' t| = 3\Delta v t \tag{2.35}$$

given that $t$ is much greater than the orbital period $P$. The same result holds for a nearly circular orbit with low eccentricity. The greatest deflection effect is achieved at perihelion because of the smallest $r$. This tangential in-plane velocity change has the larger effect on deflection distance than radial in-plane or out-of-plane directions.

### 2.3.2 Deflecting Methods

In the 2005 Budget Authorization Act, the U.S. Congress, for the first time, directed the NASA Administrator to provide an analysis of alternatives (methods) to detect or divert an object on a likely collision course with Earth. The report to Congress considered a wide range of deflection alternatives, either impulse-based or slow-push-based. It concluded that (1) nuclear detonation is the most effective alternative of all and that (2) kinetic impactor is the second most effective (or the most effective non-nuclear alternative). Slow-push methods ranked low in both effectiveness and technology readiness as a whole, but amongst them (3) gravity tractor had a relatively high potential compared to the others.[26] The report also discussed characterization requirements of each method to maximize the efficacy of each method. For example, Fig. 2-24 and Fig. 2-25 show qualitative assessments of characterization requirements for impulse deflection and slow-push deflection, respectively. Mass always receives the top priority for characterization. Density and material properties also need to be

[26] Other slow-push methods considered in this report include Yarkovsky effect enhancement, focused solar beam, mass driver, pulsed laser, and space tug. [96]

characterized in impulse methods, but not in slow push methods.

| | Mass | Spin | Density | Material Properties | Size & Shape | Surface Properties |
|---|---|---|---|---|---|---|
| Conventional Expl. Surface - Contact | Yes | No | Helpful | Helpful | Helpful | Helpful |
| Conventional Expl. Subsurface | Yes | No | Helpful | Helpful | No | No |
| Kinetic Impactor | Yes | No | Helpful | Helpful | Helpful | No |
| Nuclear (Contact) | Yes | No | Helpful | Helpful | Helpful | No |
| Nuclear (Standoff) | Yes | No | No | No | No | No |
| Nuclear Explosive (Sub-Surface) | Yes | No | Helpful | Helpful | No | No |
| Nuclear Explosive (Surface Delayed) | Yes | Yes | Helpful | Helpful | No | Helpful |

Figure 2-24: Characterization required for Impulse Methods [6]

| | Mass | Spin | Density | Material Properties | Size & Shape | Surface Properties |
|---|---|---|---|---|---|---|
| Yarkovsky | Yes | Yes | No | No | Yes | Yes |
| Focused Solar | Yes | Helpful | No | No | No | Yes |
| Gravity Tractor | Yes | Yes | No | No | Yes | No |
| Mass Driver | Yes | Yes | Yes | Yes | Helpful | Helpful |
| Pulsed Laser | Yes | Helpful | No | No | No | Yes |
| Space Tug | Yes | Yes | No | No | Yes | Yes |

Figure 2-25: Characterization required for Slow Push Methods [6]

### (1) Kinetic Energy Impactor

The kinetic impactor method uses a hypervelocity collision, which transfers linear momentum from a projectile (impactor) to a target asteroid. The amount of delta-v achieved is proportional to the impactor momentum ($m_i v_i$) and inversely proportional to the asteroid mass ($m$), as shown in Eq. 2.36. The coefficient $\beta$ is called a momentum transfer (multiplication) efficiency or simply a "beta" factor.

$$\Delta v = \beta \frac{m_i v_i}{M} \tag{2.36}$$

The beta factor is the ratio of the asteroid momentum change (output after collision) and the impactor momentum (input before collision); by definition, $\beta - 1$ equals the coefficient of restitution (COR) $e$ which is the ratio of the post-collision relative speed to the pre-collision relative speed.[27] Fig. 2-26 describes the possible values of $\beta$ with corresponding examples. **Subplastic** collision occurs when a small, dense object (a bullet for example) passes through a large, less dense object; it is also called a "perforating" collision. The beta factor is less than unity ($\beta < 1$), and the coefficient of restitution is less than zero ($e < 0$). In a **perfectly inelastic (plastic)** collision, two objects coalesce and do not separate from each other; kinetic energy is dissipated as heat or work done in deforming the objects ($\beta = 1$ and $e = 0$). Most collisions on Earth we usually see fall into imperfect inelastic collisions ($1 < \beta < 2$, $0 < e < 1$), between perfectly inelastic and perfectly elastic. **Perfectly elastic** collisions conserve kinetic energy because the objects rebound from one another with the same relative speed with the pre-collision speed ($\beta = 2$ and $e = 1$). In special cases, kinetic energy may increase during exoergic reactions [97]. These kinds of collisions are called **superelastic** where energy or mass is released as a result of explosion.[28]

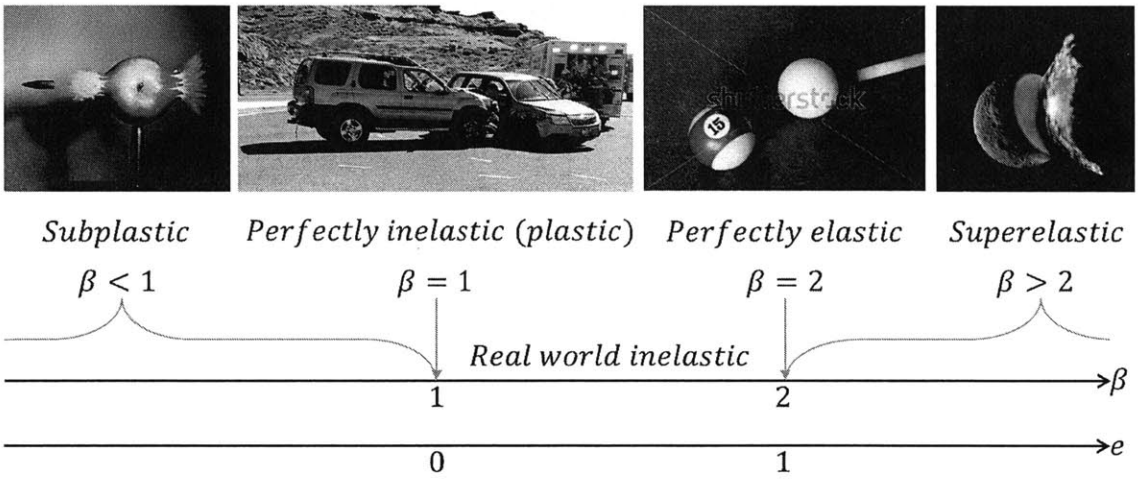


Figure 2-26: Momentum multiplication factor and coefficient of restitution [28, 29]

When an impactor collides with a target asteroid, it is expected that the hypervelocity collision scatters ejecta from a crater newly created on the surface. Some of the

[27] alternatively, the speed of separation divided by the speed of approach

[28] It is possible that e=$\infty$ for a perfect explosion of a rigid system.

ejecta returns to the asteroid, while ejecta with a higher speed will eventually escape the asteroid's gravity. This back-scattering effect, analogous to the exhaust plume of a rocket, magnifies the amount of transferred momentum. Figure 2-27 presents empirical results on how the momentum exchange depends on the relative speed of the impacting bodies and the properties of the target. The linear trend on the log-log plot implies a power law; river rock (green), basalt (red), and aluminum (blue) have a slope of $2/3$ while sand has a shallower slope of 0.4. River rock, basalt, and aluminum are all non-porous, so their variation in $\beta$ comes from different material strengths. Porous materials are expected to have low ejecta velocities and correspondingly small values of $\beta$, as shown in sand and pumice. Kinetic impact methods may be quite effective in diverting rocky bodies, but this may not be true for more porous targets.

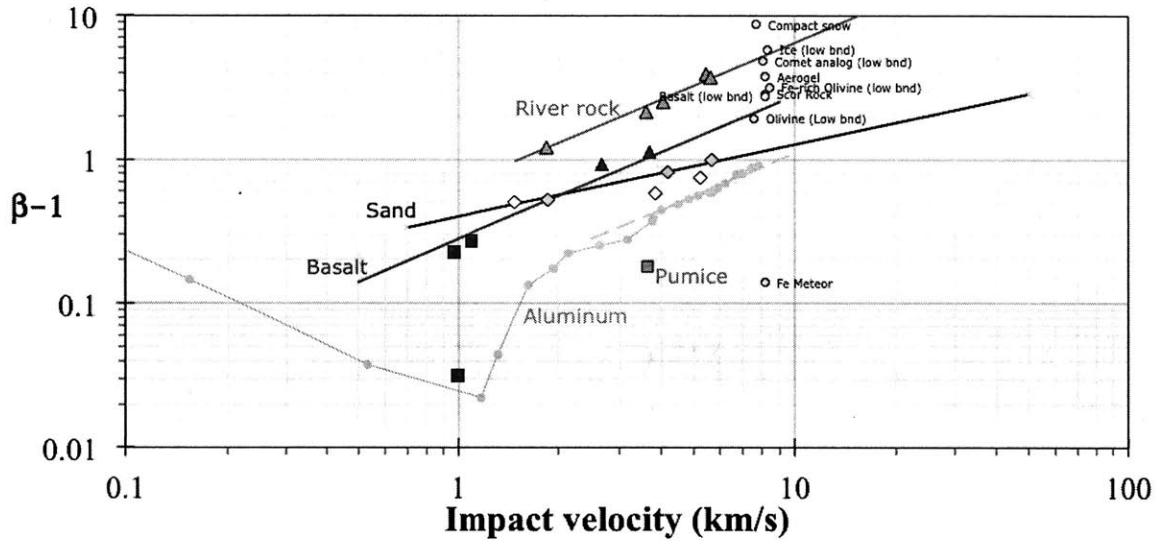


Figure 2-27: Power law between $\beta$ and impact velocity for various materials [28, 29]

### (2) Nuclear Explosives

Nuclear explosives deliver energy to a target asteroid quickly and compactly by either deflecting its collision course or fragmenting and dispersing it [93]. The most straightforward energy-coupling scheme is a "surface burst," which produces a shock-wave beneath the surface propagating through inner structures of the asteroid. This

process excavates a crater and produces ejecta whose momentum is analogous to that of a rocket's thrust. However, this scheme is likely to shatter the asteroid due to a direct impulse concentrated in a narrow area. In order to deliver a gentler push, a "standoff burst" can be used with neutron, X-ray, or gamma-ray coupling. Heat generated from these sources evaporates part of an asteroid. The volume of the blown-up part depends on the penetration depth and the burst height, or equivalently the line-of-sight exposed surface area. For example, if a charge is detonated at a height of $h = (\sqrt{2} - 1)R = 0.414R$ (Fig. 2-28a), a maximum dose of $f_{max} = 0.27$ times the total radiative yield is delivered to 0.296 times the asteroid surface area (Fig. 2-28b). Neutrons penetrate this irradiated area as deep as 20 cm for stony ("S-type") asteroids, assuming a mean neutron cross-section of $10^{-24}$ cm$^{-2}$ and mean atomic weight of 25. This yields a "shell" mass of $3.7 \times 10^9$ g if the asteroid has a density of 2 g cm$^{-3}$ and a diameter of 50 m.

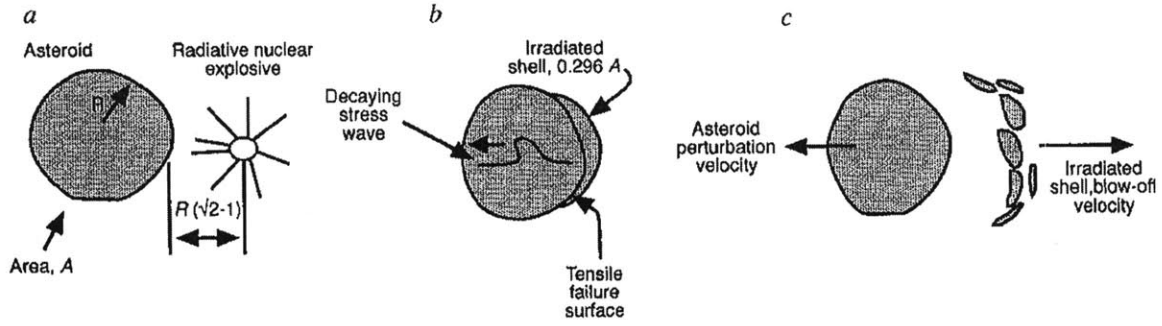


Figure 2-28: Standoff burst of nuclear explosive [30]

Further assuming that the fraction, $\alpha = 0.3$, of the irradiation energy is converted to internal energy, $\Delta E$, it follows that

$$\Delta E = f_{max} \alpha Q \tag{2.37}$$

where $Q = 4 \times 10^{12}$ J is the amount of energy per kiloton mass of equivalent TNT. This increase in internal energy induces a temperature rise as much as 100 K. At the same time, the thermodynamic pressure increases because the irradiated shell has constant volume while the interntal energy increases. In Eq. 2.38, the coefficient $\gamma$

is the thermodynamic Grüneisen ratio, which is assumed to be unity here [98].[29] For example, one kiloton of nuclear explosive will cause a pressure rise up to 1.7 kbar, which accelerates the irradiated shell to the right in Fig. 2-28.

$$\Delta P = \gamma \rho \Delta E \tag{2.38}$$

At the same time, a stress wave pulse is propagated to the left within the asteroid. This relative movement breaks away the shell from the asteroid, by conservation of momentum. The outward rebouding velocity of shell material is given by

$$v_r = \Delta P \rho c_p \tag{2.39}$$

where $c_p$ is the compressional wave velocity, assumed to be 2 km/s through the asteroid material. The velocity of the rebounding shell is 31 m/s/kton in the direction between the explosive and the asteroid's center of mass. Because a 50 meter-sized asteroid has an escape velocity of 5.3 cm/s, most of the shell material exceeding this velocity will escape the asteroid's gravity field. From conservation of momentum, the shell velocity of 31 m/s/kton causes an asteroid velocity perturbation of 11 cm/s/kton.[30] An alternative approach involving a nuclear explosive is to detonate a charge on the surface. This "surface burst" induces cratering on the asteroid. The thrown-off material perturbs the asteroid velocity. The empirical formulas of surface detonation are based on a limited number of reduced-scale experiments. This method contains more uncertainty than radiative stand-off detonation because the asteroid would behave differently whether its ejecta production is limited by gravity recapture or material strength.

[29] Grüneisen ratio describes the effect that changing temperature has on the size of a crystal lattice. It is defined by $\gamma = V \frac{dP}{dE}_V$, and solving this equation for $dP$ yields Eq. 2.38. Grüneisen's parameter relates thermal expansion, heat absorption, and volume strain: $\lambda = 3\gamma \frac{C_v}{K}$ where $\lambda$ is the coefficient of thermal expansion, $C_v$ is volume heat capacity, and $K$ is bulk modulus (Grüneisen's law).

[30] As the size of an asteroid grows to 1 km and 10 km, the perturbation velocity decreases to $11 \times 10^{-3}$ cm/s and $11 \times 10^{-6}$ cm/s. Also, the energy coupling efficiency, $e$, is largely unknown. If its value ranges from 0.03 to 0.3, velocity perturbation of 1 cm/s requires 0.01-0.1 Mton and 0.01-0.1 Gton of nuclear explosives for diameters of 1 km and 10 km, respectively. The degree of coupling depends on the scaled depth $r/Q_n^3$ as well as the asteroid material [27].

If the asteroid is huge (>100m) and the possibility of fragmentation is low, then a subsurface burst could be used to maximize the energy coupling. Conversely, we may purposefully induce fragmentation, if the warning time is too short and a collision with Earth is inevitable. In that case, dispersing the asteroid fragment would be the only option to lower casualties. Only a completely coupled (buried) nuclear charge would be able to fracture a well consolidated asteroid. Empirical relations suggest a power law between the shock-induced particle velocity and the energy scaled radius, as shown in Eq. 2.40 for hard (igneous) terrestrial rocks and Eq. 2.41 for soft rocks [30].

$$\log v_r(m/s) = 5.233 - 2\log(r/Q_n^{1/3}) \tag{2.40}$$

The shock-wave energy per unit mass, $v^2$, should exceed the fracture limit, $E_{frac}$, for the asteroid to disintegrate. Assuming $E_{frac} = 1000J/kg$, and hence for $v_r = 32$ m/s, an explosive charge of $Q_n = 1$ (kton) will generate a 74-m-spherical fragment. Similarly, a 1-Mton charge and a 1-Gton charge are expected to fragment 740 m and 7.4 km of the asteroid, respectively.

$$\log v_r(m/s) = 4.590 - 2\log(r/Q^{1/3}) \tag{2.41}$$

Softer rocks can be fragmented into smaller fragments with the same amount of charge: 34 m from a 1 kton charge, 340 m from a 1 Mton charge, and 3.4 km from a 1 Gton charge. Burying an explosive charge at an optimal depth would require the use of smaller explosives for excavation. The required extra explosives would be minimal compared to the fragmentation explosive (up to 1/3000 of explosives for deflection) for a 100-m-diameter asteroid, but may be significant (up to 1/4 of explosives for deflection) for a 10-km-diameter asteroid.[31] A NASA report submitted to the U.S. Congress in 2007, concluded:

> Nuclear standoff explosions are assessed to be 10-100 times more effective than the non-nuclear alternatives analyzed in this study. Other techniques involving the surface or subsurface use of nuclear explosives

[31] Drilling may also be used, depending on our knowledge of inner structures of the asteroid.

may be more efficient, but they run an increased risk of fracturing the target NEO. They also carry higher development and operations risks.

Despite its projected effectiveness, the use of nuclear explosive devices in space is internationally controversial, and the United Nations Committee on the Peaceful Uses of Outer Space (UNCOPUOUS) will need to address this issue. The 1963 Partial Test Ban Treaty (PTBT) banned nuclear weapon tests in the atmosphere, in outer space, and underwater. The PTBT became redundant with the signing of the Comprehensive Test Ban Treaty (CTBT) in September 1996.

### (3) Gravity Tractor

A gravitational tractor, or simply a gravity tractor, is a concept proposed by Lu and Love, which can alter an asteroid's trajectory using gravity as a virtual towline [30,31]. The spacecraft hovers near the asteroid with its ion thrusters angled outwards so that the exhaust does not impinge on the asteroid's surface. As can be seen in Fig. 2-29, a plume angle of $\phi_p = 20$ deg and a cant angle of $\phi_c = 60$ deg yields the hovering distance of $d = 1/\cos(\phi_c - \phi_p/2)$=1.556 $r$.

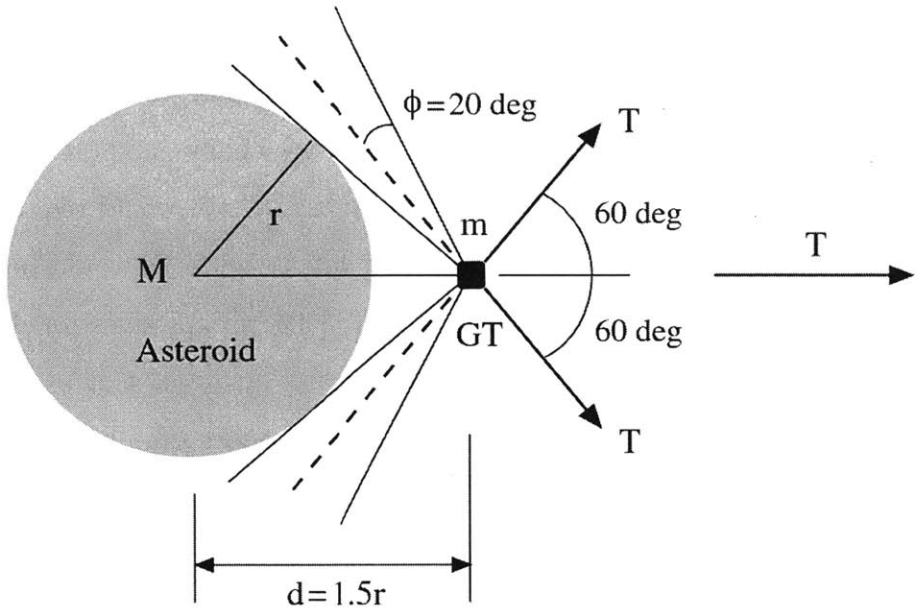


Figure 2-29: Gravity tractor geometry with angled thrusters [31]

The two ion thrusters, each with a towing thrust $T$, produce a total thrust $T$.

Equation 2.42 yields a total thrust of 0.05326 N, provided that $G = 6.6695\times10^{-11}$ $Nm^{-2}kg^{-2}$, $M = 4\times10^{10}$ kg, $m = 1000$ kg, $r = 160$ m, and $d = 240$ m (or a hovering altitude of 240 m − 160 m = 80 m). This translates into acceleration of $A = 1.1579 \times 10^{-9}$ $mm/s^2$, as shown in Eq. 2.43.

$$T = M\frac{\Delta V}{\Delta t} = \frac{GMm}{d^2} \tag{2.42}$$

$$A = \frac{\Delta V}{\Delta t} = \frac{Gm}{d^2} = \frac{T}{M} \tag{2.43}$$

The resulting velocity and position changes over a towing period of $\Delta t$ are $\Delta V = A\Delta t$ and $\Delta X = \frac{1}{2}A(\Delta t)^2$, respectively. One year of towing can achieve $\Delta V = 0.036$ mm/s and $\Delta X = 575$ m. It can be shown that actual changes in velocity and position are tripled by orbital amplification effects[32] Therefore, $\Delta V = 3A\Delta t = 0.11$ mm/s and $\Delta X = \frac{3}{2}A(\Delta t)^2 = 1.7$ km. After the propellant runs out, the accumulated velocity change until then can still achieve additional deflection distance over the coasting time. For an accelerating time of $\Delta t$ and coasting time of $t_c$, we obtain a total position change

$$\Delta X = \Delta X_a + \Delta X_c = \frac{3}{2}A(\Delta t)^2 + \Delta V t_c = \frac{3}{2}A\Delta t(\Delta t + 2t_c) \tag{2.44}$$

The second term $\Delta X_c$ is proportional to coasting time $t_c$, and $\Delta X_c = 10.3$ km if $t_c = 3$ years. As $t_c$ grows, the coasting deflection term will surpass the accelerating deflection term, $\Delta X \approx \Delta X_c = \Delta V t_c$. This is less efficient than kinetic energy deflection in the tangential direction ($\delta = 3\Delta vt$), but more efficient than kinetic energy deflection in out-of-plane direction ($\delta = \frac{1}{2\pi}\Delta vt$) or radial direction ($\delta = \frac{2}{\pi}\Delta vP$), as illustrated in Fig. 2-23 . [33] The propellant consumption can be estimated from

$$\Delta m_f = \frac{2T\Delta t}{g_0 I_{sp}} \tag{2.45}$$

[32] Clohessy-Wiltshire-Hill equations

[33] Radial acceleration does not affect the semi-major axis, so the position change does not grow anymore beyond $\frac{2}{\pi}\Delta vP$ after an orbit period.

where $g_0 = 9.8$ m/s$^2$ and we assume $I_{sp} = 3000$ s for typical ion engines. Using the thrust value of $T = 0.053$ N before, the propellant consumption rate is 0.3 kg per day or 114 kg per year. Despite its small deflection ability, a gravity tractor is still a feasible method if an asteroid has a small keyhole and is of relatively small size and mass [99].[34] This method is insensitive to the structure, surface properties, and rotation state of the asteroid because it does not require anchoring to provide physical connections between the spacecraft and the asteroid. For example, "rubble pile" asteroids, loosely held together by gravity, could best be dealt with using a gravity tractor; while a kinetic energy impactor or nuclear explosive might just break up the pile without sufficiently adjusting its course [100].

## 2.4 Chapter Summary

This chapter provides a literature review pertinent to asteroid impact avoidance. When an asteroid with potential impact hazards is first discovered, the actual risk is evaluated to determine whether an action of deflection or disruption is necessary. This *pipeline* of detection(discovery)-determination-deflection(disruption) represents the chronological order as well as the decreasing order of technology readiness levels. The following chapters propose a methodology for designing deflection campaigns to overcome the lack of deflection technology demonstration in space and the lack of our knowledge on specific asteroids.

[34] For example, the primary 2029 keyhole of Apophis has a 700 m diameter. If there are no other uncertainties, this is the minimum deflection requirement.

# Chapter 3

# The ADIEU Framework

This chapter introduces a new framework for asteroid deflection integrating *epistemic* uncertainties (ADIEU). The purpose of this framework is to make an asteroid deflection campaign more robust to *stochastic* uncertainties, by reducing epistemic uncertainties. *Epistemic* uncertainties arise from incomplete information or knowledge; therefore, measurements or surveys can reduce these uncertainties. On the other hand, *stochastic* uncertainties cannot be reduced because they are inherently random.[1] The ADIEU framework is implemented as a software package. It is written mostly in MATLAB and is also connected with a NASA open-source tool, consisting of Excel macros, that optimizes low-thrust trajectories powered with electric propulsion.[2] Figure 3-1 illustrates key modules and data flows, which together enable tradespace exploration and optimization. First, this chapter describes the user interface and simulation model. The next chapter explains how the software package's optimizer optimizes outputs (Chapter 4). After basic parameters are set for a specific asteroid (3.1), inputs (3.2) are transformed into outputs (3.3) through a simulation model (3.4). We consider a scenario of deflecting the asteroid Apophis with a kinetic energy impactor. After we interpret the results and obtain insights from this case (Chapter 5), ADIEU is applied to other asteroids.

[1] Thunnissen (2003) classifies uncertainty into four categories: ambiguity, aleatoric (stochastic), epistemic, and interaction [73]. Möller and Beer (2004) use the three categories of stochastic, informal, and lexical uncertainties [101].

[2] Excel macros are written in the VBA languate, which stands for Visual Basic for Applications.

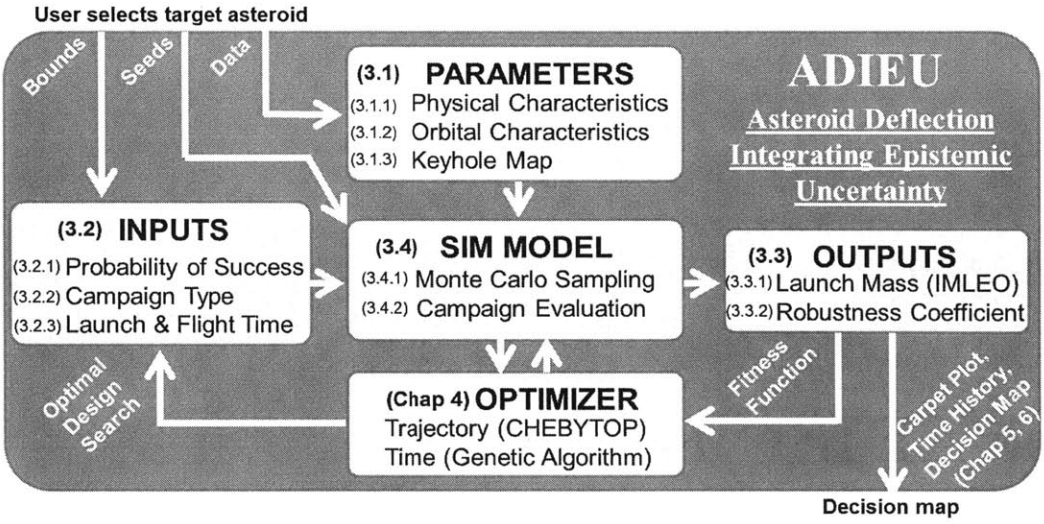


Figure 3-1: The ADIEU Framework and Chapter 3 Organization

## 3.1 Parameters

The ADIEU framework requires three kinds of parameters about the target asteroid: (1) physical characteristics, (2) orbital characteristics, and (3) a keyhole map. Each subsection in this section discusses a category of parameters in more detail.

### 3.1.1 Physical Characteristics

Mass $m$ and the $\beta$ factor are the two most important characteristics governing the deflection results using a kinetic impactor. The velocity change of the target asteroid is proportional to $\beta$ and inversely proportional to the asteroid's mass (Eq. 2.36). Based on only ground measurements, these parameters usually contain large amounts of uncertainty. The mean and the standard deviation of each parameter is needed.

#### Mass Uncertainty

The mass of an asteroid can be approximated as the product of spherical volume, density, and solidity. The solidity is obtained by subtracting the total porosity[3] from unity.

$$m \approx \frac{4\pi r^3 \rho}{3}[1 - \phi_{total}] = \frac{\pi d^3 \rho}{6}[1 - (\phi_{macro} + \phi_{micro})] \tag{3.1}$$

[3]Sum of micro-porosity and macro-porosity.

In this formula, the uncertainty of each variable is propagated into the mass uncertainty. The formula below is easily extendable to an ellipsoid if $r^3$ is replaced by the product of the lengths of three semi-major axes. However, a spherical assumption will be used because we do not have any shape information about Apophis. Table 3.1 summarizes the data relevant to calculating the mass of Apophis. Two datasets are presented for the diameter; new data in the second row has a lower standard deviation (15 meters) than new data in the first row (60 meters), reducing the mass uncertainty from 160% to 60%. Because the diameter uncertainty is propagated, old data has a skewed distribution with a long tail in the higher mass range (Fig. 3-2 left); new data has an almost symmetric distribution due to a smaller standard deviation (Fig. 3-2 right). As a result, the right tail of the new data extends less ($< 10 \times 10^{10} kg$) than the tail of the old data ($> 10 \times 10^{10} kg$), even though the new data has a higher average diameter (325 meters) or volume than the old data has (270 meters).

Table 3.1: Range of physical parameters for Apophis [51]

| Parameter | Min | Avg | Max | S.D. | C.O.V. |
|---|---|---|---|---|---|
| Diameter (m) | 210<br>(310) | 270<br>(325) | 330<br>(340) | 60<br>(15) | 0.222<br>(0.046) |
| Bulk density (g/cm$^3$) | 3.0 | 3.2 | 3.4 | 0.2 | 0.063 |
| Solidity (%) | 37.9 | 72.1 | 96.3 | 29.2 | 0.405 |
| Micro-porosity (%) | 3.7 | 7.9 | 12.1 | - | - |
| Macro-porosity (%) | 0 | 20 | 50 | - | - |
| Mass ($10^{10}$ kg) | 0.6<br>(1.8) | 2.4<br>(4.1) | 6.2<br>(6.7) | - | - |
| Kinetic energy (Mt TNT) | 105 | 450 | 1100 | - | - |

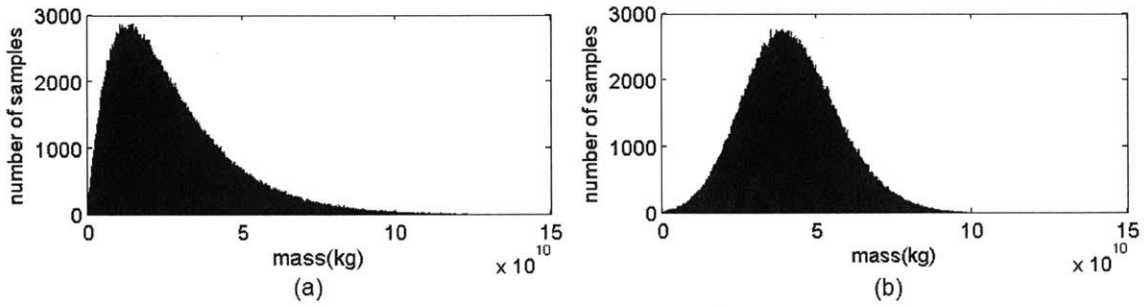


Figure 3-2: Mass distribution

The best estimates of Apophis's mass contain an error of around 40% from ground measurements. This uncertainty can be reduced below 10% if a precursor spacecraft orbiting or hovering over the asteroid would make in-situ measurements. This is in analogy to Itokasa's mass estimate improvement described in section 2.1.3.

#### Beta Uncertainty

For Apophis, the initial distribution of $\beta$ is assumed to be a Gaussian distribution $\beta_i \sim \mathcal{N}(2, 0.3)$ such that its 3-sigma interval is approximately within an interval [1,3]. If a preliminary impactor is used during the precursor stage, the final distribution is assumed to be $\beta_f \sim \mathcal{N}(2, 0.1)$. The specifics of $\beta$ distributions are detailed in Chapter 6, with graphical descriptions in Fig. 6-2 and Fig. 6-3.

#### Campaign Types

Provided with mass uncertainty and $\beta$ uncertainty, we can take the following courses of action before launching a kinetic impactor mission.

- Reduce no uncertainty at all (no precursor stage)
- Reduce only mass uncertainty with a preliminary orbiter
- Reduce both mass uncertainty and $\beta$ uncertainty with a preliminary orbiter and a preliminary impactor

A preliminary orbiter and a preliminary impactor in the precursor stage can be modeled after past missions or planned missions in Table 3.2 and Fig. 3-3. The dry mass of a preliminary orbiter and the dry mass of a preliminary impactor, arriving at the asteroid, are set to be 400 kg and 500 kg, respectively.

### 3.1.2 Orbital Characteristics

The ADIEU framework needs two categories of orbit information: ephemeris uncertainty and deflection curve. The deflection curve shows how much an asteroid *will* be deflected assuming no uncertainties are involved; superposing physical uncertainties on this curve (nominal solution) will generate a range of curves (probability density

Table 3.2: Datails of past or planned missions to asteroids [32–34, 52]

| | Hayabusa (JAXA) | OSIRIS-REx (NASA) | AIDA (ESA) |
|---|---|---|---|
| Configuration | Orbiter + SRC | Orbiter + SRC | Orbiter + Impactor |
| Propellant | Xenon | Hydrazine | - |
| Dry Mass | 380 kg | 750 kg | 395 kg + 532 kg |
| Wet Mass | 510 kg | 1529 kg | 491 kg + 1694 kg |
| Target Asteroid | 25143 Itokawa (1998 SF36) | 101955 Bennu (1999 RQ36) | 65803 Didymos (1996 GT) |
| Delta-V from LEO | 4.632 km/s | 5.087 km/s | 5.098 km/s |

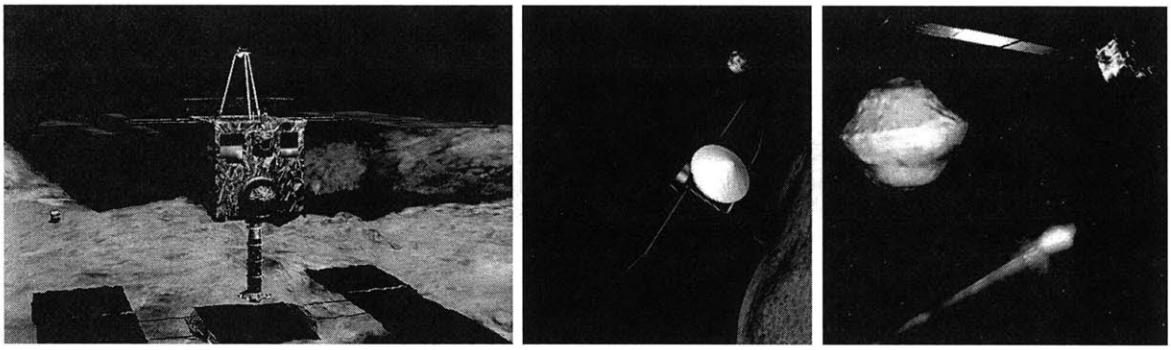

Figure 3-3: Artist concept of asteroid exploration missions (Hayabusa, OSIRIS-REx, AIDA) [32–34]

function) which cover all possible cases. Ephemeris uncertainty is used to define how much an asteroid *should* be deflected for safety.

### Orbit Uncertainty

Ephemeris uncertainty levels vary among asteroids because each asteroid has a unique observation history. Apophis has been observed hundreds of times and tracked over a decade, so it has a very low ephemeris uncertainty level. However, other less studied asteroids may have much larger ephemeris uncertainties.[4] The spacecraft orbiting or hovering over an asteroid can track the asteroid position (transponder) in addition to measuring the asteroid mass (remote-sensor). Therefore, the possibilities of uncertainty reduction for physical characteristics and ephemeris are:

[4]The uncertainty of an asteroid can also change over time. Apophis also used to have large uncertainties; its uncertainty ellipse had a size of $580 \times 15$ km on its impact plane (b-plane). However, the size has shrunk to $47 \times 6$ km when new measurements became available in 2013.

- Reduce no uncertainty at all
- Reduce uncertainties in mass and ephemeris
- Reduce uncertainties in mass, $\beta$, and ephemeris

These three options correspond to Type 0, Type 1, and Type 2 campaigns. The type number tells how many precursors each type has: Type 0 has no precursor, Type 1 has one precursor, and Type 2 has two precursors. Therefore, the no-precursor option (Type 0 campaign) does not reduce any uncertainty before deflecting an asteroid. The orbiter-only option (Type 1 campaign) sends a remote-sensing precursor that measures the asteroid mass and tracks the asteroid position. The orbiter-impactor option (Type 2 campaign) sends an orbiter and an impactor as a combined package during the precursor stage; the orbiter observes the impactor's collision with the asteroid, through which a better estimate of $\beta$ can be obtained. Table 3.3 summarizes the architectures of Type 0, Type 1, and Type 2 campaigns and their uncertainty-reducing capabilities.

Table 3.3: Campaign Types and Their Capabilities

| Campaign Type | Type 0 (Single-mission-like) | Type 1 (Hayabusa-like) | Type 2 (AIDA-like) |
|---|---|---|---|
| Configuration | Main-impactor | Pre-orbiter<br>Main impactor | Pre-orbiter<br>Pre-impactor<br>Main-impactor |
| Orbit Uncertainty Reduced? | No | Yes | Yes |
| Mass Uncertainty Reduced? | No | Yes | Yes |
| Beta Uncertainty Reduced? | No | No | Yes |

### Deflection Curve

The deflection curve of an asteroid plots deflection capability (deflected distance) as a function of the deflection epoch (impact time). Figure 3-4 shows how much Apophis may be deflected on the 2029 b-plane, if a velocity change of 0.37 mm/s is imparted along the asteroid's velocity vector. As can be seen from the curve, the same amount of velocity change can have significantly different effects depending on several variables. First, an impulse delta-v applied earlier will have more deflecting effects than the same amount of delta-v applied later, which is demonstrated by an increasing overall trend. There are also local, oscillatory behaviors because the deflecting effect will vary according to the position of an asteroid in its orbit. For a constant along-track delta-v, we get the largest b-plane deflection if we apply it at perihelion, and the smallest at aphelion. The deflection curve, a chacteristic of an asteroid, is obtained assuming perfect knowlege for the physical characteristics of the asteroid, so the curve may be considered as a nominal solution. In order to obtain a deflection curve, the equations of motion for a given asteroid should be solved twice. Solving the equations without deflection gives a natural ballistic trajectory, and solving the equations with deflection gives a post-deflection trajectory. The two trajectories are then compared to calculate the net deflected distance.

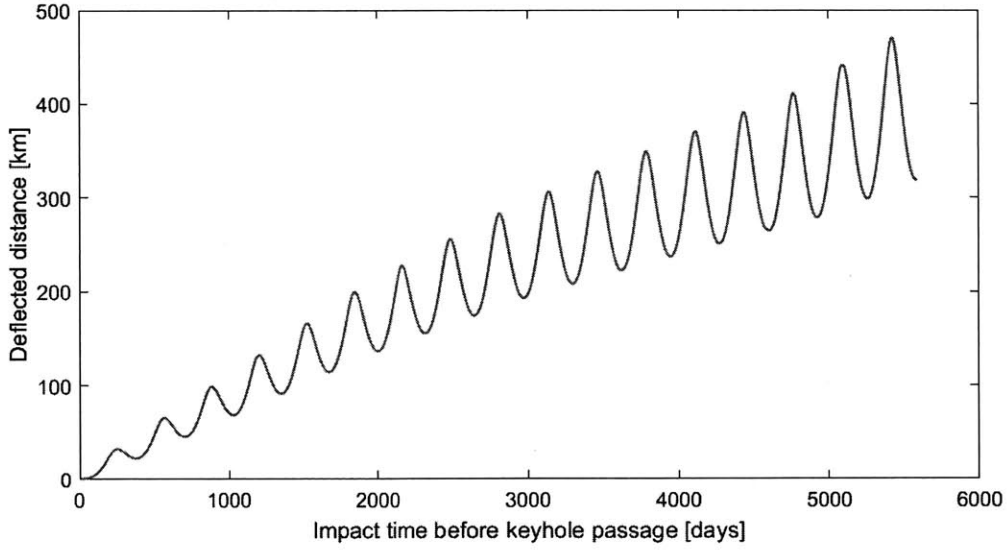


Figure 3-4: Calculated deflection curve of Apophis (Delta-v = 0.37 mm/s)

One of the physical models for trajectory calculation is a modified form of the Einstein-Infeld-Hoffmann (EIH) equation, as described in Eq. 3.2. This involves the mutual Newtonian gravitational accelerations as well as their relativistic corrections. Due to the high speeds of solar system bodies, not considering relativistic correction would result in propagation errors as much as millions of kilometers over decades. Excluded in this model are solar radiation pressures, Yarkovsky effects, the $J_2$ effects of the Sun, Earth, and other planets. The framework uses a solver called PAT2, short for Propagator for Asteroid Trajectories Tool, to solve this equation [102].

$$\begin{aligned}\ddot{\mathbf{r}}_i = \sum_{j\neq i} \frac{\mu_j(\mathbf{r}_j - \mathbf{r}_i)}{r_{ij}^3}\Bigg\{1 &- \frac{2(\beta+\gamma)}{c^2}\sum_{k\neq i}\frac{\mu_k}{r_{ik}} - \frac{2\beta-1}{c^2}\sum_{k\neq j}\frac{\mu_k}{r_{jk}} \\ &+\gamma\left(\frac{v_i}{c}\right)^2 + (1+\gamma)\left(\frac{v_j}{c}\right)^2 - \frac{2(1+\gamma)}{c^2}\dot{\mathbf{r}}_i\cdot\dot{\mathbf{r}}_j \\ &- \frac{3}{2c^2}\left[\frac{(\mathbf{r}_i-\mathbf{r}_j)\cdot\dot{\mathbf{r}}_j}{r_{ij}^3}\right]^2 + \frac{1}{2c^2}(\mathbf{r}_j-\mathbf{r}_i)\cdot\ddot{\mathbf{r}}_j\Bigg\} \\ &+\frac{1}{c^2}\sum_{j\neq i}\frac{\mu_j}{r_{ij}^3}\left\{[\mathbf{r}_i-\mathbf{r}_j]\cdot[(2+2\gamma)\dot{\mathbf{r}}_i - (1+2\gamma)\dot{\mathbf{r}}_j]\right\}(\dot{\mathbf{r}}_i-\dot{\mathbf{r}}_j) \\ &+\frac{(3+4\gamma)}{2c^2}\sum_{j\neq i}\frac{\mu_j\ddot{\mathbf{r}}_j}{r_{ij}},\end{aligned} \tag{3.2}$$

Here, $\mathbf{r}_i$, $\dot{\mathbf{r}}_i$, and $\ddot{\mathbf{r}}_i$ are the solar-system-barycentric position, velocity, and acceleration vectors of body $i$.[5] They are measured with respect to the center of mass of the solar system. Also, $r_{ij} = |\mathbf{r}_j - \mathbf{r}_i|$ is the distance between bodies $i$ and $j$. The constant $c$ is the speed of light, and $\mu_i = Gm_i$ where $G$ is the gravitational constant and $m_i$ is the mass of body $i$. This equation is in fact an expansion of a Newtonian equation of motion (black part) with relativistic terms containing $c^2$ (gray part). In the relativistic part, $\beta$ and $\gamma$ are parametric post-Newtonian parameters.[6] In general relativity, both $\beta$ and $\gamma$ are 1. Because $\ddot{\mathbf{r}}$ terms appear both on the right- and left-hand side of equation, this problem is implicit. With the following state vector

[5] It follows that $v_i = |\dot{\mathbf{r}}_i|$.

[6] More specifically, $\beta$ measures the nonlinearity in superposition of gravity, and $\gamma$ measures the space curvature produced by unit rest mass. This $\beta$ has a different meaning from the momentum multiplication factor.

$$\mathbf{y} = \begin{bmatrix} \mathbf{r}_1 \\ \vdots \\ \mathbf{r}_N \\ \dot{\mathbf{r}}_1 \\ \vdots \\ \dot{\mathbf{r}}_N \end{bmatrix} \tag{3.3}$$

for the $N$ bodies considered, the EIH equation can be formulated as

$$f(t, \mathbf{y}, \mathbf{y}') = 0 \tag{3.4}$$

This implicit expression can be turned into an explicit one, $\mathbf{M}(\mathbf{y})\mathbf{y}' = f(t, \mathbf{y})$,[7] if we drop the last term in Eq. 3.2 containing the $\ddot{\mathbf{r}}_j$ terms. We finally obtain $\mathbf{y}' = f(t, \mathbf{y})$ by replacing $f(t, \mathbf{y})$ with $\mathbf{M}(\mathbf{y})^{-1} f(t, \mathbf{y})$. In order to obtain the position of each body at a given time $t > t_0$, we integrate $\mathbf{y}'(t)$ with an initial condition of $\mathbf{y}_0 = \mathbf{y}(0)$. We propagate two initial state vectors, $\mathbf{y}_{01}$ for the nominal case *without* $\Delta v$ (nominal, Fig. 3.5 left) and $\mathbf{y}_{02}$ for the deflected case *with* $\Delta v$ (deflected, Fig. 3.5 right), using the EIH equation. Propagation for a given time interval, until keyhole passage, will produce two different final states $\mathbf{y}_1$ and $\mathbf{y}_2$. The deflected distances may be measured on the b-plane after a coordinates transformation. This approach using a discrete delta-v is applicable only to "impulse-based" deflection methods, among which kinetic impactor (KI) deflection is considered in this thesis. It should also be noted that imparting a velocity change exactly on the along-track direction may not be always physically possible or economically desirable. If an oblique collision occurs, all the other components other than the along-track component of the velocity change will not contribute to secular deflection [58]. Reference [102] contains details about orbit propagation using the EIH equation, and Appendix B explains how to convert deflected distances into the b-plane coordinates.

[7] $M$ is a mass matrix, a symmetric matrix which connects the generalized coordinate vector $\dot{\mathbf{q}}$ of a system and the kinetic energy $T = \frac{1}{2}\dot{\mathbf{q}}\mathbf{M}\dot{\mathbf{q}}^T$. The mass matrix $M$ usually depends on the state $\mathbf{q}$, therefore varying with time(https://en.wikipedia.org/wiki/Mass_matrix).

$$\mathbf{y}_{01} = \begin{bmatrix} \mathbf{r}_1(0) \\ \vdots \\ \mathbf{r}_N(0) \\ \dot{\mathbf{r}}_1(0) \\ \vdots \\ \dot{\mathbf{r}}_{ast}(0) \\ \vdots \\ \dot{\mathbf{r}}_N(0) \end{bmatrix} \qquad \mathbf{y}_{02} = \begin{bmatrix} \mathbf{r}_1(0) \\ \vdots \\ \mathbf{r}_N(0) \\ \dot{\mathbf{r}}_1(0) \\ \vdots \\ \dot{\mathbf{r}}_{ast}(0) + \Delta v \\ \vdots \\ \dot{\mathbf{r}}_N(0) \end{bmatrix} \tag{3.5}$$

Kinetic impactor (KI) deflection, considered in this thesis, is very non-symmetrical, unlike gravity tractor (GT) deflection. KI deflection is always much easier to remove orbital energy than to increase, but there is not much difference for GT deflection [58]. As shown in Fig. 3-5, even though increasing energy (positive delta-v) and decreasing it (negative delta-v) achieves the nearly same deflection, the former requires much more propellant to accelerate an impactor than the latter.

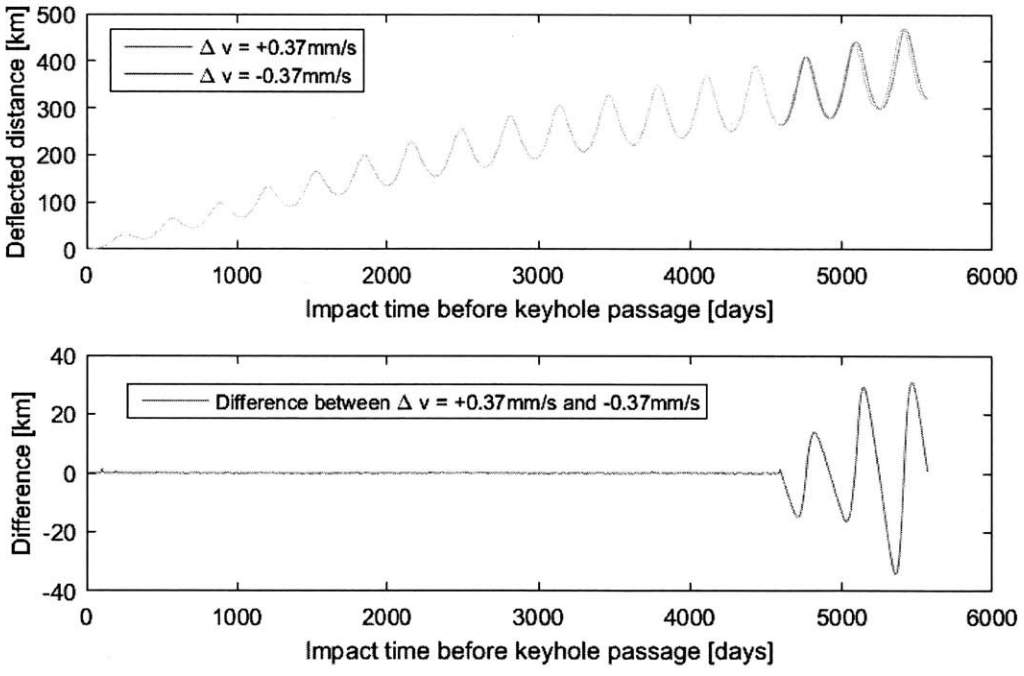


Figure 3-5: Calculated deflection curves of Apophis (Delta-v = $\pm 0.37$ mm/s, upper) and their difference (lower)

### 3.1.3 Keyhole Map

A keyhole map contains detailed information about gravitational keyholes. Usually, one axis shows $\zeta$ coordinates, which points in the negative direction of Earth's heliocentric velocity projected on to the b-plane (refer to Fig. 2-12); the other axis could be $\xi$ coordinates, impact probability, or minimum approach distance. Any keyhole maps used in this thesis will look like Fig. 3-6 where the horizontal axis is the $\zeta$ coordinate and the vertical axis is the minimum distance. The valley in the middle ($\zeta = 0$) marked by '2036' means that Apophis will pass through this keyhole in 2029[8], assuming the asteroid is not deflected; there is going to be an impact at a future encounter in 2036 because the post-encounter minimum distance is less than 1 Earth radius($R_\oplus$) on the y-axis.

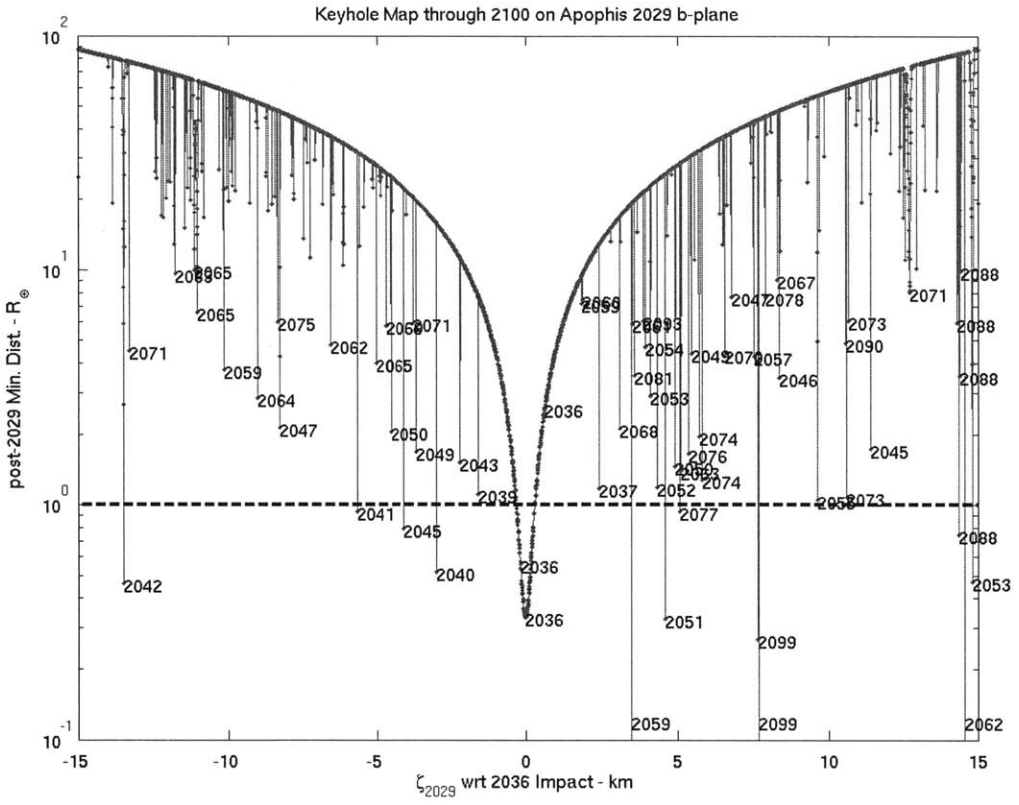


Figure 3-6: Keyhole map of Apophis in the 2029 impact plane [12]

[8] as shown by the subscript in $\zeta_{2029}$ in the label of the horizontal axis

A gravitational keyhole refers to a small region of space near a planet through which an asteroid must pass in order to achieve an orbital resonance structure. The term 'resonance' here means that the orbital period of a planet and that of an asteroid are synchronized with a ratio of two integers, $k/h$. For example, Apophis has an orbit period of 324 days and has a 9:8 periodic resonance relative to Earth (365 days). Generally speaking, once an asteroid passes through a keyhole near a planet, the planet will alter the orbit of the passing asteroid such that it would collide with that planet after a given number of orbital passes defined by the resonance structure. Apophis's current $k$:$h$=9:8 resonance structure was once suspected to be altered to a 7:6 resonance, with a new period of 312 days, should it pass through the 2036-keyhole in 2029 (Fig. 3-6).[9] Apophis will come close to Earth every 6 years instead of every 8 years, making it even more hazardous. Therefore, preventing a keyhole passage would be a good strategy to eliminate the prerequisite condition of a future impact. Deflecting by hundreds of kilometers to avoid gravitational keyholes prior to keyhole passage is easier to achieve than deflecting by several Earth radii to avoid Earth after keyhole passage. Furthermore, as an asteroid passes through a gravitational keyhole, its orbital resonance with Earth becomes stronger, making post-keyhole deflection much less effective than any pre-keyhole deflection efforts. In the case of Apophis, the difference in deflection efficiency could be dozens of multiples; this is because passing through the 2036-keyhole in 2029 changes both the orbit of Apophis and its deflection characteristics (as discussed in section 3.1.2 regarding the deflection curve). Although this is potentially a very effective mitigation strategy to prevent an asteroid from passing through keyholes, its implementation requires thorough knowledge of the location of gravitational keyholes and their sizes. The width of the 2036-keyhole is only 700 meters, so Apophis must be deflected at least by this amount; otherwise, the asteroid will still pass through the same keyhole. However, deflecting Apophis by exactly 700 meters (neither more than that nor less than that) is infeasible due to orbit uncertainty and mass uncertainty. The possible range of deflection distance

[9]The possibility of this keyhole passage and the corresponding impact scenario was eliminated in 2013 when additional ground observations enabled more precise orbit determination. However, this case will still be used as a case study in this thesis.

may span over hundreds of kilometers or tens of kilometers in the best cases. Figure 3-6 shows that the vicinity of the 'primary' 2036-keyhole is very crowded with much narrower 'secondary' keyholes; among them, keyholes marked with 2042, 2041, 2045, 2040, 2059, 2051, 2099, 2088, 2053, and 2062 are below the $10^0(=1)R_\oplus$, showing potential future impact risks. We should look farther away for keyhole-free regions.

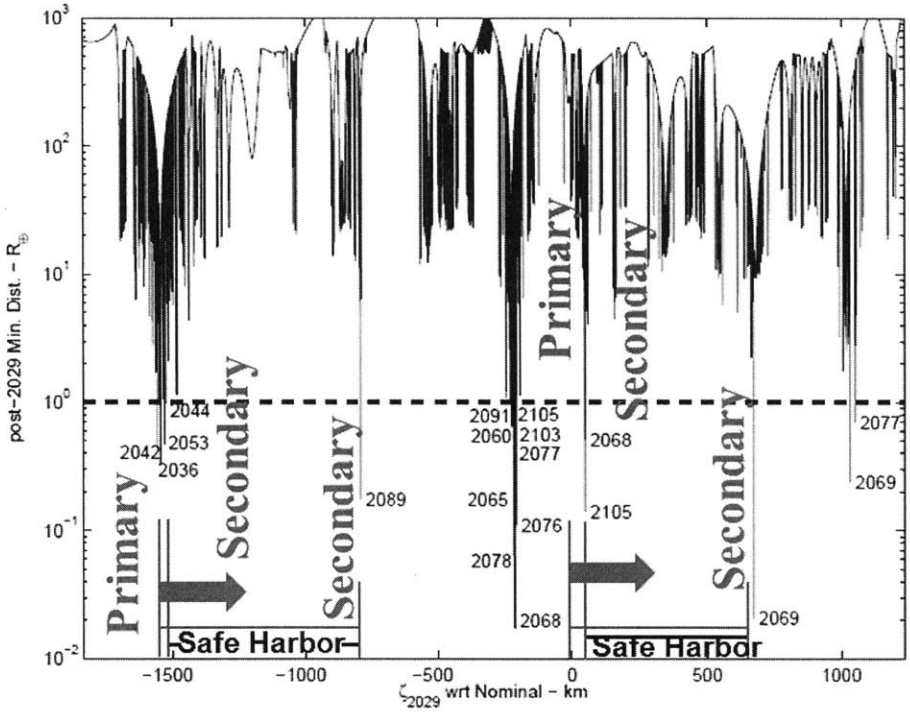


Figure 3-7: Keyhole map of Apophis and safe harbor [35]

Figure 3-7 is a zoom-out version of Fig. 3-6, with an increased horizontal axis range of -1500 km to +1000 km compared to -15 km to +15 km before. The hypothetical scenario of preventing the 2036-keyhole passage has a safe harbor approximately from +20 km to +800 km relative to the 2036-keyhole.[10] This 'raw' range is used to derive the 'effective' safe harbor that accounts for uncertainties in Apophis's orbit and physical characteristics. As shown in Fig. 3-8, the effective safe harbor (allowed

[10] After the possibility of Apophis passing through the 2036-keyhole has been eliminated, the latest estimate shows that it will elude the 2068-keyhole by a small margin of 200 kilometers, which is the distance measured between the '2068' label and the origin ($\zeta = 0$) in Fig. 3-7. Although Apophis, without deflection, will not pass through the 2068-keyhole, the margin provided by doing nothing may not be large enough if deflection uncertainty is considered. If we want to deflect Apophis to a more keyhole-free region, beyond the 2105-keyhole and before the 2069-keyhole, the ideal deflection distance should be between +50 km and +700 km.

region) is obtained by subtracting the orbit (ephemeris) uncertainty and the numerical propagation uncertainty from the two ends. In other words, the minimum deflection requirement is obtained by adding the uncertainty terms to the raw lower boundary, and the maximum deflection requirement is obtained by subtracting the uncertainty terms from the raw upper boundary. In Eq. 3.6 and Eq. 3.7, $\Delta\zeta_{eff}$ is deflection distance for passing into the effective safe harbor, and $\Delta\zeta$ is for the raw safe harbor; $\sigma_{ephem}$ and $\sigma_{prop}$ are the orbit uncertainty and the physical uncertainty, respectively.

$$\Delta\zeta_{min,eff} = \Delta\zeta_{min} + \sigma_{ephem} + \sigma_{prop} \tag{3.6}$$

$$\Delta\zeta_{max,eff} = \Delta\zeta_{max} - \sigma_{ephem} - \sigma_{prop} \tag{3.7}$$

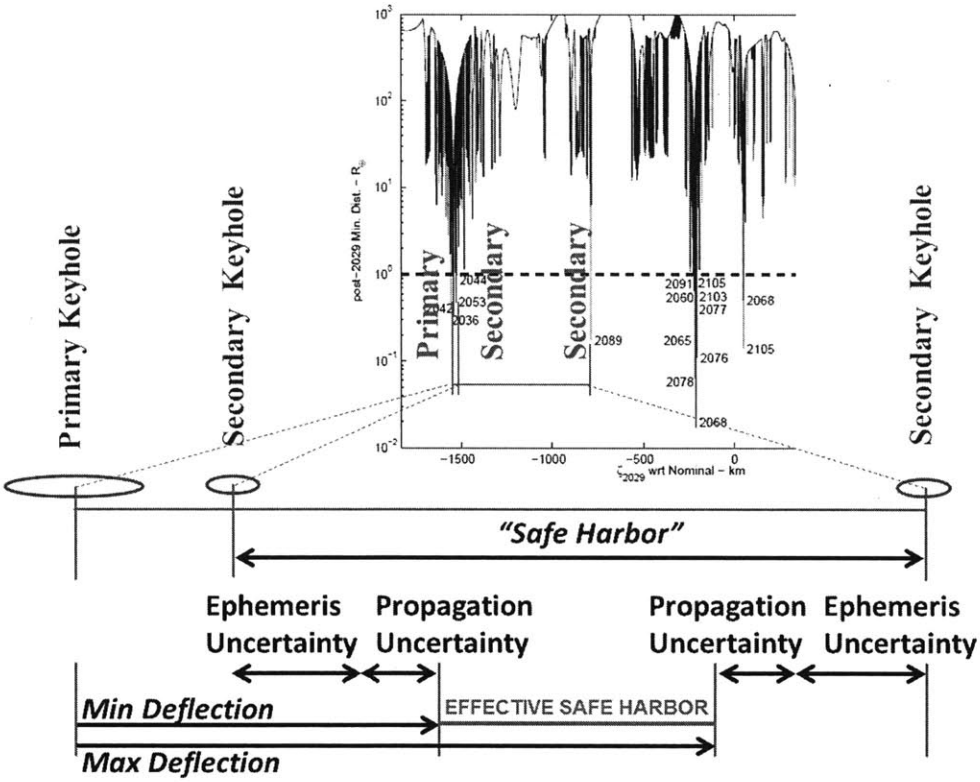


Figure 3-8: *Effective* safe harbor (outside-in derivation) [35]

While Fig. 3-8 clearly illustrates the concept of an effective safe harbor, Fig. 3-9 provides an alternative way of understanding Eq. 3.6 and Eq. 3.7. Suppose that the asteroid will pass through the primary keyhole if no deflecting action is applied to it; however, because this nominal estimate contains orbit uncertainties within itself, it is possible the asteroid passes through any point, unknown a priori, between (primary keyhole) - (ephemeris uncertainty) and (primary keyhole) + (ephemeris uncertainty). We want to account for the propagation uncertainties as well, so that the asteroid *must* land onto the (raw) safe harbor for any point of passage between (primary keyhole) - (ephemeris uncertainty) - (propagation uncertainty) and (primary keyhole) + (ephemeris uncertainty) + (propagation uncertainty). This requirement can be satisfied if the deflected distance is greater than Eq. 3.6 and less than Eq. 3.7.

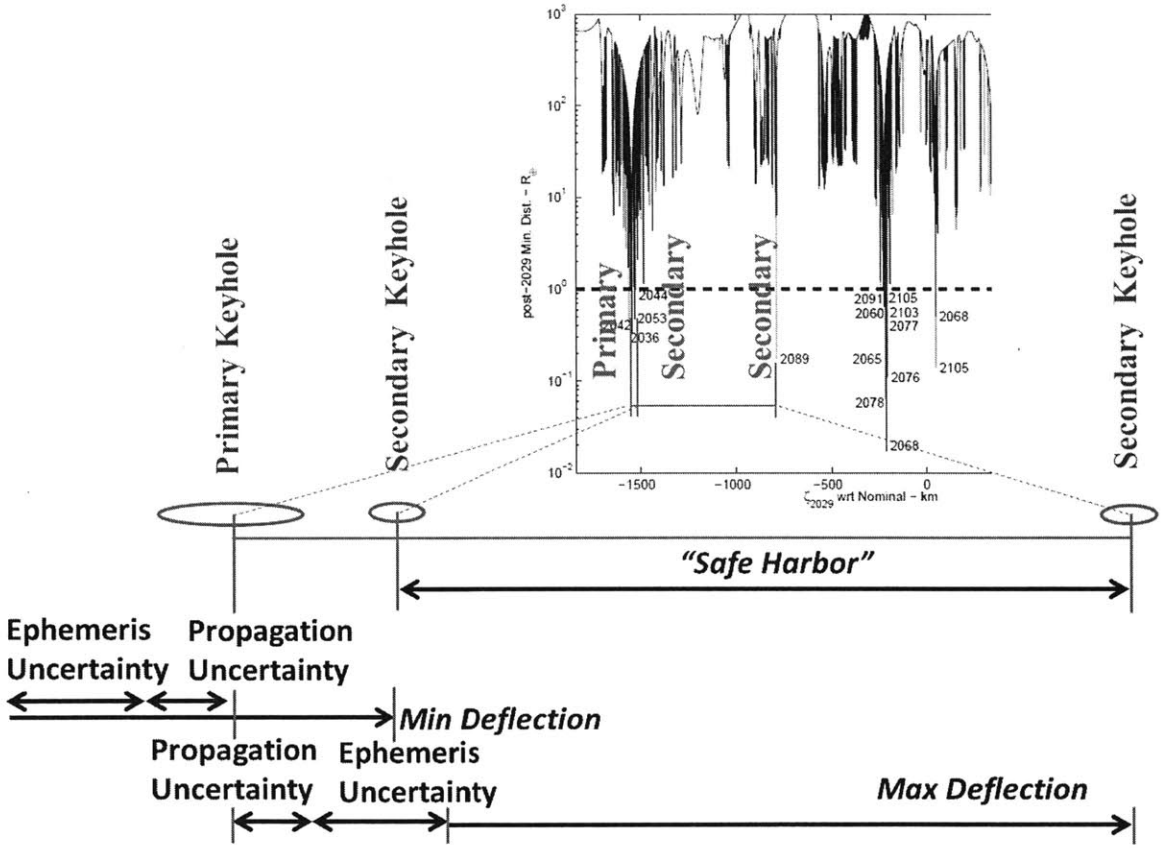


Figure 3-9: *Effective* safe harbor (inside-out Derivation) [35]

With this definition of an effective safe harbor, the probability of success is defined by Eq. 3.8. The numerator is the area of the probability density function for deflected distance, integrated from the lower boundary of the effective safe harbor to the upper boundary. The denominator is the area of the same function, but this time it is integrated over the entire range of real numbers, equal to unity by the definition of a probability density function. As shown in Fig. 3-10, a deflected distance distribution with a low uncertainty level (right) will squeeze more area within the effective safe harbor than a distribution with a high uncertainty level (left). The key idea here is that deflecting an asteroid too much could push it into a neighboring keyhole and increase rather than decrease the likelihood of a future impact.

$$s = \frac{\int_{\Delta\zeta_{min,eff}}^{\Delta\zeta_{max,eff}} p(\Delta\zeta)\Delta\zeta}{\int_{-\infty}^{\infty} p(\Delta\zeta)\Delta\zeta} = \int_{\Delta\zeta_{min,eff}}^{\Delta\zeta_{max,eff}} p(\Delta\zeta)\Delta\zeta \tag{3.8}$$

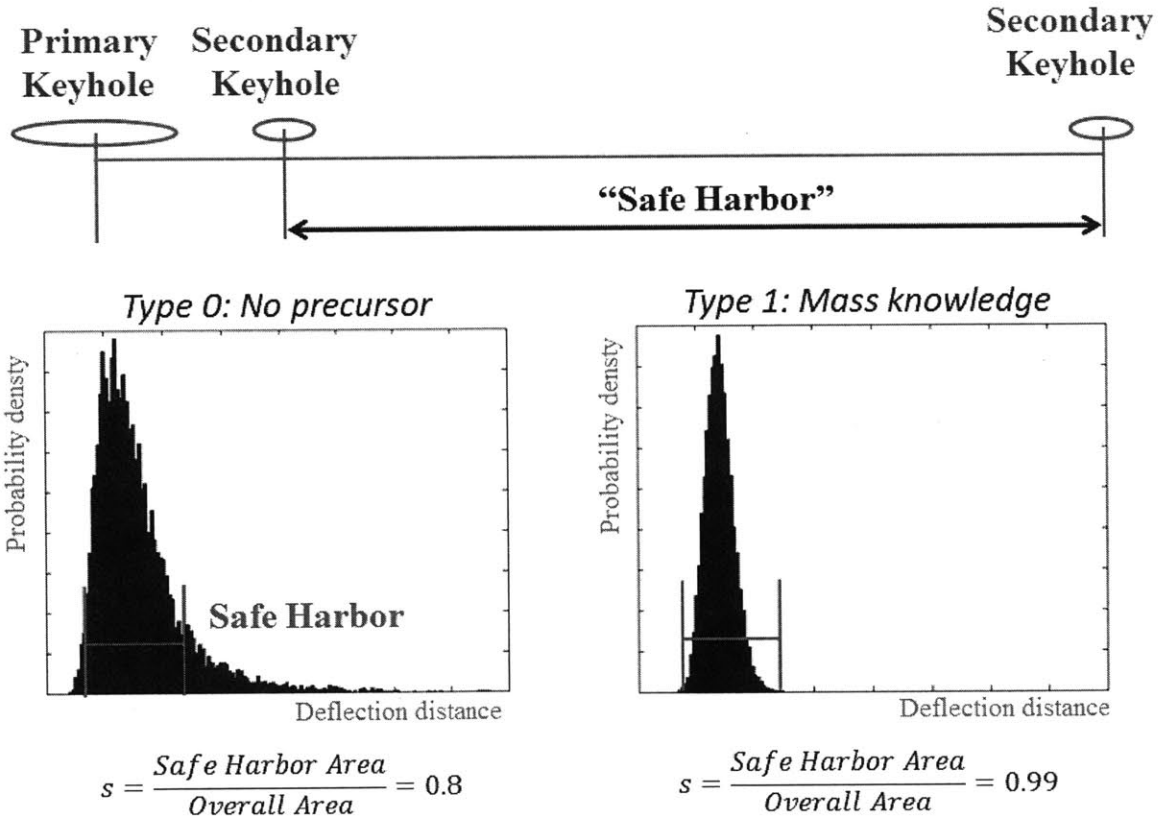


Figure 3-10: Keyhole map of Apophis and deflection safe harbor

### 3.1.4 Conclusion

This subsection introduced orbital parameters and physical parameters that affect asteroid deflection results. This collective information is summarized into two major inputs: deflection curve and keyhole map. The deflecton curve, which is basically a time series of deflected distances, tells us when to deflect an asteroid. The keyhole map provides guidelines on where an asteroid should go (or by how much we should deflect it). As remarked earlier, KI deflection is very non-symmetrical in that it's always much easier to remove orbital energy than to increase it. That means that KI deflection will decrease zeta, moving an asteroid left on the keyhole map. Therefore, the safe harbor region we looked at so far must be mirrored, as shown in Fig. 3-11

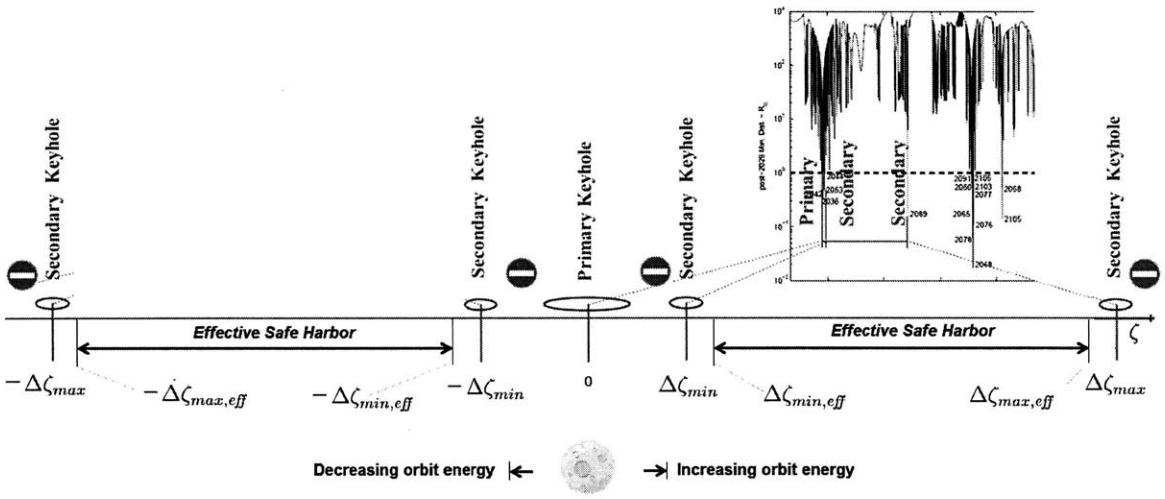


Figure 3-11: *Effective* safe harbor (double-sided)

For simplification, we assume here that the keyhole distribution is symmetric around the primary keyhole. Given two choices between +20 km to +800 km and -20 km to -800 km, a trajectory optimizer will mostly opt for the second choice because the optimization goal is to save fuel.

## 3.2 Inputs

There are three inputs to the ADIEU simulation model: (1) the required probability of success, (2) the campaign type, and (3) the start date of a campaign. When a minimum requirement is set for the probability of success, the simulation model finds a deflection campaign with a specified type and a start date, such that their probability of success exceeds this threshold.

### 3.2.1 Probability of Success

The user can define a minimum threshold for the probability of success. That is, all campaign designs generated by ADIEU must satisfy

$$s = \int_{\Delta\zeta_{min,eff}}^{\Delta\zeta_{max,eff}} p(\Delta\zeta)\Delta\zeta \geq p_{threshold} \tag{3.9}$$

The probability of failure is obtained by subtracting the probability of success from unity or 100%. Therefore, the probability of failure decreases by a factor of ten as shown in $10\% \rightarrow 1\% \rightarrow 0.1\% \rightarrow 0.01\%$, while the probability of success is approaching an asymptote of $90\% \rightarrow 99\% \rightarrow 99.9\% \rightarrow 99.99\%$.

### 3.2.2 Campaign Type

The user can also specify the type of deflection campaign: Type 0 with no uncertainty reduction, Type 1 for reducing mass uncertainty only, and Type 2 for reducing uncertainty in mass and $\beta$. A tradeoff exists where reducing more uncertainties requires investing more time and cost, leading to higher campaign complexity.

### 3.2.3 Campaign Start Date

The campaign start date is the date when the first stage of an overall campaign starts, equal to the launch date. For a Type 0 campaign, the one and only stage starts on this date. There are multiple stages in a Type 1 or Type 2 campaign; because the user provides only the start date of the first stage, start dates of the remaining stages

are optimized by the optimizer. By fixing only one or two of three inputs, the user can perform a wide variety of tradespace explorations. For example, fixing two input variables enables us to perform the following tasks.

- **Provided a campaign start date and a campaign type**: find the maximum probability of success, i.e., the upper limit of reliability that a given type of deflection campaign can achieve on that date.
- **Provided a campaign start date and a probability threshold**: find campaign types that are feasible under these conditions. If there is more than one type available, we can rank them according to a figure of merit.
- **Provided a probability threshold and a campaign type**: find optimal start dates of that deflection campaign. Similarly, if there are multiple launch windows available, we can rank them.

If we fix one input variable and let the other two variables vary, then more complicated behaviors can be observed, as follows:

- **Provided a campaign start date**: we can observe transition of optimal campaign types as we increase a threshold for the minimum probability of success.
- **Provided a probability threshold**: we can observe transition of optimal campaign types as we progress in time, i.e., delay the launch date or reduce available time until the asteroid passes through a keyhole.
- **Provided a campaign type**: we can plot a figure of merit (e.g., launch mass) as a function of start date and probability of success[11].

The last item gives rise to the notion of *decision maps* for asteroid deflection strategies.

[11] $F \leftarrow f(p_{threshold}, t_{start})$

## 3.3 Outputs

One of the main objectives of this thesis has been to make an asteroid deflection campaign more robust to stochastic uncertainty by reducing epistemic uncertainty. Therefore, it would be beneficial to first explain a measure for quantifying how robust a campaign is. The robustness coefficient ($C_{max}$) captures the maximum amount of variability that can be tolerated while keeping the probability of success above a given threshold ($p_{threshold}$).

### 3.3.1 Robustness Coefficient

Robustness is defined as the ability to tolerate or resist perturbations, which are usually random or stochastic. In asteroid deflection, small-body effects are difficult to quantify, even with precursor missions, and subject to randomness. Also, the momentum multiplication factor ($\beta$ factor) is hard to characterize, even with a dedicated precursor. This is because $\beta$ depends on an asteroid's internal structures. The mismatch between the actual $\beta$ and the predicted $\beta$ may also occur if an impctor collides with an asteroid at an oblique angle, as shown in Fig. 3-12, where the along-track velocity component is less than desired. In any case, a wrong $\beta$ value would cause propagation errors, which grow over time. For simplicity, it will be assumed that this propagation error is linearly proportional with time. The propagation terms in Eq. 3.6 and Eq. 3.7 can be rewritten as in Eq. 3.10 and Eq. 3.11, where $C$ is a propagation coefficient.

$$\Delta\zeta_{min,eff} = \Delta\zeta_{min} + \sigma_{ephem} + CT \tag{3.10}$$

$$\Delta\zeta_{max,eff} = \Delta\zeta_{max} - \sigma_{ephem} - CT \tag{3.11}$$

Because the safe harbor parameters such as its size $\zeta_{SH} = \Delta\zeta_{min,eff} - \Delta\zeta_{min,eff}$ and its aspect ratio $AR_{SH} = \Delta\zeta_{min,eff}/\Delta\zeta_{min,eff}$ have critical impacts on the robustness coefficient values, a safe harbor must be carefully selected and defined.

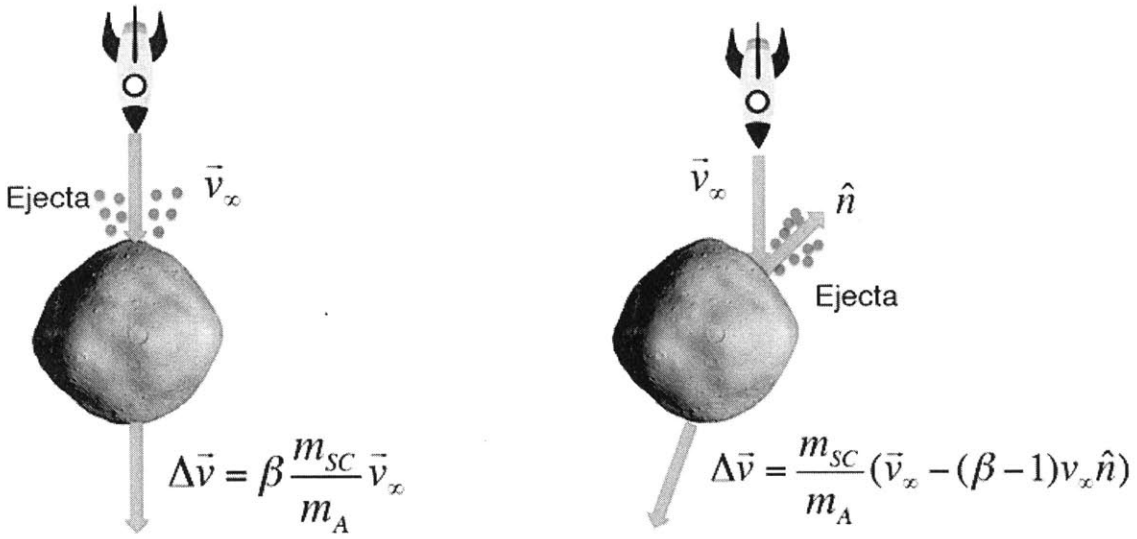


Figure 3-12: Difference in the desired $\beta$ and the actual $\beta$ [36]

As shown in Fig. 3-13, the propagation uncertainty is zero ($C \times 0$) at the time of keyhole passage ($D - 0yr$); as we go backwards in time, uncertainty grows linearly, $C \times T$. If we wait until keyhole passage, we cannot achieve deflection at all, because the asteroid is already passing the keyhole.[12] On the other hand, if we attempt deflection too early, propagation uncertainty will be just too large to guarantee successful deflection. The effective safe harbor will get narrower as $C \times T$ increases, and at some point the harbor will vanish when $\Delta\zeta_{min,eff} = \Delta\zeta_{max,eff}$. These two extremes imply that there is an optimal time when the impactor should hit an asteroid. Figure 3-13 also compares different values of $C$. Let's suppose that a Type 0 campaign is used to deflect an asteroid. Because its deflection distribution is spread so widely, we cannot guarantee a success if the dynamic range of stochastic uncertainty grows at a rate higher than $C_1$. Now, suppose that a Type 1 campaign is used. The deflection distribution is much narrower, so the deflection campaign will succeed even with an uncertainty growth rate as large as $C_2$ ($C_1$). Because we want the maximum tolerable $C$ ($C_{max}$) to be as large as possible, a Type 1 campaign ($C_{max} = C_2$) is more prefer

[12]This can also be shown from a deflection curve where deflection is zero when impact time before keyhole passage is zero. In other words, the effectiveness of deflection is zero this case. When the impact time is very close to keyhole passage, deflection is not zero, but its effectiveness will be too low to enable deflection with a reasonable amount of impactor mass.

able than a Type 0 campaign ($C_{max} = C_1$), given that $C_2 > C_1$. Because $C_{max}$ is a measure of how robust a campaign is against stochastic uncertainties, we will hereafter call it the "robustness coefficient." By rewriting the integral bounds, Eq. 3.8 now looks like

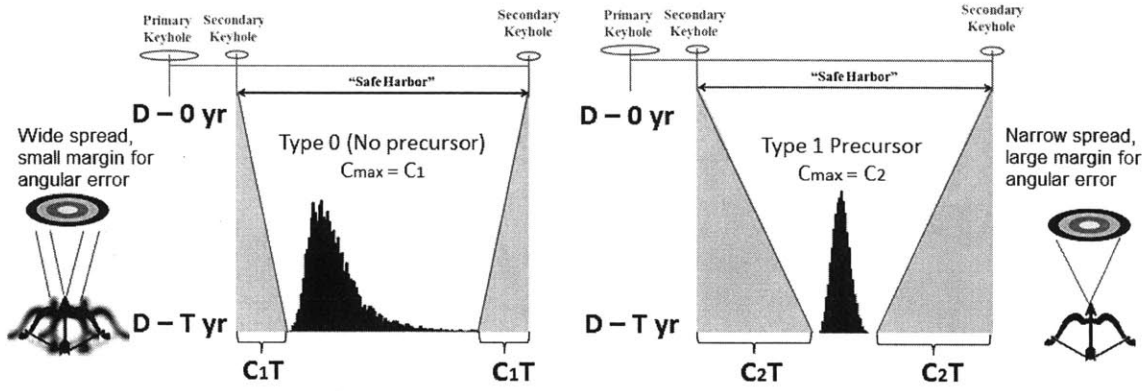


Figure 3-13: Safe harbors with varying amounts of propagation uncertainty

$$s(m, C, \mathbf{T}) = \int_{\Delta\zeta_{min}+\sigma_{ephem}+C(t_{keyhole}-t^l_{arrival})}^{\Delta\zeta_{max}-\sigma_{ephem}-C(t_{keyhole}-t^l_{arrival})} p(\frac{\Delta\zeta}{m})\Delta\zeta \tag{3.12}$$

where $\frac{\Delta\zeta}{m}$ in $p(\frac{\Delta\zeta}{m})$ means that the deflection distribution is stretched from the original deflection distribution of a unit impactor-mass by a factor of $m$. This linear assumption is based on Eq. 2.36, where the velocity change is proportional to the impactor mass ($\Delta v \propto m_i$). The probability of success $s(m, C, \mathbf{T})$ is a function of $m$, $C$, and $\mathbf{T}$; the last argument $\mathbf{T}$ is a "time vector" that contains the start date and the end date of each stage.

$$\mathbf{T} = \begin{bmatrix} t^1_{departure} & t^1_{arrival} & \cdots & t^l_{departure} & t^l_{arrival} \end{bmatrix}^T \tag{3.13}$$

The arrival date of the last stage ($t^l_{arrival}$) is plugged into Eq. 3.10 and Eq. 3.11 to yield Eq. 3.12. More details about the probability of success function and the robustness coefficient will be discussed in the simulation model section (3.4).

### 3.3.2 System Mass

The system mass is obtained by summing up the initial mass in low-Earth orbit (IMLEO) for each stage in a deflection campaign.[13] For a Type 0 campaign, the system mass equals the impactor mass and all supporting subsystems including propulsion. For a given set of dates ($\mathbf{T}$) and an initial robustness coefficient ($C = 0$), the arrival mass of an impactor is set to maximize the probability of success. Notice that it is equivalent to minimizing the negative of probability, as shown below.

$$\left\{m_{arrival}^{impactor}(0, \mathbf{T})\right\}^{type0} = \underset{m}{\text{argmin}} \left\{-s^{type0}(m, 0, \mathbf{T})\right\} \tag{3.14}$$

Next, we increase the robustness coefficient by increments until the maximized probability of success is less than the provided probability threshold, which is assumed to be 0.9. In other words, we find the maximum value of the robustness coefficient which satisfies the probability of success requirement. In the equation below, $\mathbf{1}$ is an indicator function. The value of $\mathbf{1}_{expression}$ is 1 if the expression is true and 0 if the expression is false. We want to maximize (minimize the negative of) the indicator function, so $C$ should satisfy $s{>}0.9$ such that the indicator function is unity. The probability threshold $p_{threshold}$, which is 0.9 here, can be varied to other values: 0.99, 0.999, and 0.9999.

$$C^* = \max \underset{C}{\text{argmin}} \left\{-\mathbf{1}_{s^{type0}(m(C,\mathbf{T}),C,\mathbf{T})>0.9}\right\} \tag{3.15}$$

Through these iterations, the impactor arrival mass and the robustness coefficient can be obtained at the same time. The final step is to convert the mass of an impactor at the asteroid arrival into the initial mass in low-Earth orbits (IMLEO). From now on, $m_0$'s refer to the "wet mass" with propellant, while $m$'s stand for the "dry mass" without propellant. The dry mass is divided by the mass ratio $\epsilon = m/m_0$ to yield

[13] The IMLEO is often used as a rough measure of the cost of a space mission. This is because the amount of cargo that should be transported to LEO is a major determinant of the cost. The IMLEO is the total mass initially in LEO, but it does not specify how this total mass is partitioned into individual launch vehicles [103].

the wet mass.[14] The mass ratio depends on the launch date and duration of flight (elements of $\mathbf{T}$); $m$, $C$, and $p_{threshold}$ are irrelevant.

$$(IMLEO)^{type0} = (m_0)^{impactor}_{departure} = (m)^{impactor}_{arrival}/\epsilon(\mathbf{T}) \tag{3.16}$$

The system mass of a Type 1 campaign is the sum of a preliminary orbiter and an impactor. We have to consider the mass ratio of a preliminary orbiter and the mass ratio of an impactor separately, because they are usually different. Unlike the impactor whose mass is adjusted, the orbiter mass is always 400 kg. This is because the mass of an asteroid orbiter, with the same number of instruments, is insensitive to asteroid mass.

$$(IMLEO)^{type1} = (m_0)^{orbiter}_{departure} + (m_0)^{impactor}_{departure} = \left\{\frac{m}{\epsilon(\mathbf{T})}\right\}_{orbiter} + \left\{\frac{m}{\epsilon(\mathbf{T})}\right\}_{impactor} \tag{3.17}$$

The system mass of a Type 2 campaign is obtained by adding masses of a preliminary orbiter, a preliminary impactor, and a main impactor. The orbiter arrival mass is 400 kg, and the pre-impactor arrival mass is 500 kg. The arrival mass of a main impactor is also 500 kg, the same as a preliminary impactor, to ensure repeatable deflection results. The impact velocity is always constant at 10 km/s.

$$(IMLEO)^{type2} = (m_0)^{pre-orbiter}_{departure} + (m_0)^{pre-impactor}_{departure} + (m_0)^{impactor}_{departure} \tag{3.18}$$

The IMLEO sum of mission phases is used as a proxy of campaign cost because IMLEO can be estimated to a certain degree. However, the actual cost is rather difficult to estimate due to the lack of any analogous missions. Thus, modeling the campaign cost is left as future work.

[14] This is equivalent to unity subtracted by propellant ratio. That is, $\epsilon = 1 - \epsilon_p = 1 - m_p/m_0$.

## 3.4 Simulation Model

The simulation model has two central parts: the Monte Carlo module and the campaign simulator, as shown in Fig. 3-14. The figure below graphically depicts these parts and their sub-parts, in relation to the overall framework illustrated in Fig. 3-1.

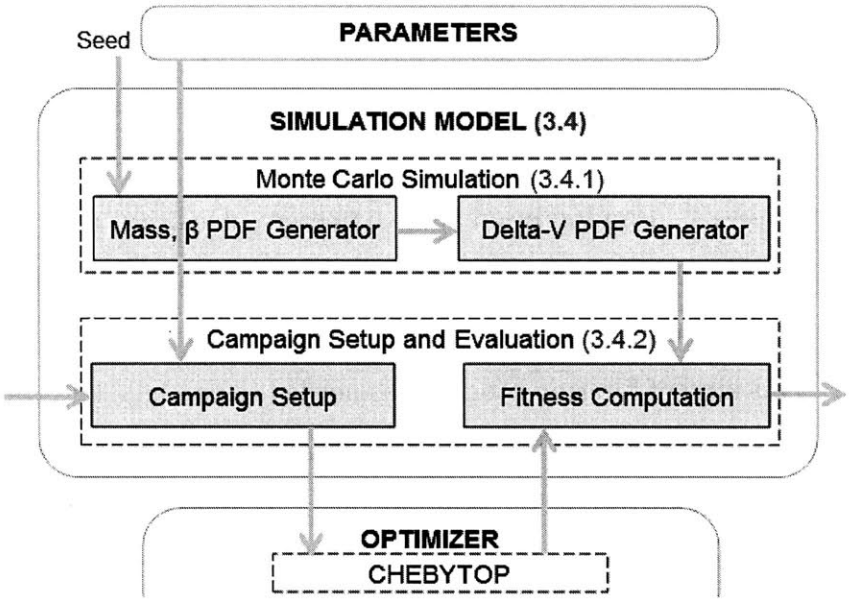


Figure 3-14: Simulation Model Breakdown

First, the Monte Carlo module sets up the probability density functions of asteroid mass and $\beta$ factor. By picking random values from these two distributions, a delta-v[15] distribution is obtained using Eq. 2.36. The delta-v distribution is saved and repeatedly used throughout simulations, after scaling,[16] in order to save computation time. The campaign module sets up basic parameters for the Chebyshev Trajectory Optimization Program (CHEBYTOP), which constitutes an inner optimization loop within the optimizer module, as will be explained in Chapter 4. After the CHEBYTOP is run, the simulation module retrieves the results and evaluates the fitness of the given campaign configuration.

[15] A delta-v per unit impactor mass, to be exact. See the footnote below.

[16] For reusability, we calculate the delta-v per unit impactor mass, $\frac{\Delta v}{m_i} = \beta \frac{v_i}{m}$, which is multiplied by impactor mass ($m_i$) to yield delta-v.

### 3.4.1 Monte Carlo Simulation

The Monte-Carlo simulator uses a default pseudorandom number generator in MATLAB, called the Mersenne Twister. Its name comes from the period of the random numbers, which is a Mersenne prime or $2^n - 1$. The most common version uses $n = 19937$, corresponding to a repetition period of $2^{19937} - 1$ or $4.3 \times 10^{6001}$, so it can pass several stringent tests for statistical randomness [104]. Algorithm 1 details the procedures used in the Monte Carlo module, which are repeated for three campaign types and sampling indexes ranging from 1 to 10,000, which is the total number of simulation samples.[17] Randomly created diameters, densities, and porosities are examined to see whether the resulting asteroid mass is higher than the minimum threshold. If not, this set of variables is rejected and a new set of variables is randomly chosen. This kind of filtering process was needed to preclude lower-end outliers. The low-end outliers are more problematic than high-end outliers because the calculation of delta-v requires division by asteroid mass. If the asteroid mass sample is significantly lower than the average asteroid mass, or even close to zero, then the corresponding delta-v would be too high from a numerical perspective. The target asteroids, Apophis and Bennu, have nominal mass around 40 to 60 billion kilograms, and the minimum acceptable mass is set to be 10 billion kilograms.

[17] Because 10,000 samples are used, 0.01% is the minimum non-zero probability of failure that can be be detected in simulations, corresponding to the probability of success 99.99%.

**Algorithm 1** Create delta-v distribution

```
1: procedure CREATE–ΔV–DISTRIBUTION
2:     for all campaign types do
3:         for all sampling indexes do
4:             Initialize asteroid mass to zero
5:             while asteroid mass is less than minimum mass do
6:                 Create diameter variable randomly
7:                 Create density variable randomly
8:                 Create porosity variable randomly
9:                 Calculate asteroid mass
10:            end while
11:            Initialize asteroid β to zero
12:            while asteroid β is less than minimum β do
13:                Create asteroid β randomly
14:            end while
15:            Calculate delta-v per impactor mass
16:        end for
17:    end for
18:    Save delta-v-per-impactor-mass distribution to archive
19: end procedure
```

We also restrict the minimum value of $\beta$ to be unity, but the reason behind this is slightly different. The value of $\beta$ cannot be less than unity unless the impactor penetrates the asteroid. Penetration is physically impossible for the target asteroids we consider in our case studies, so $\beta$ should be sampled again if its value is below unity. Once the number of acceptable samples reaches our preset number, the module calculates the delta-v per impactor mass and saves its distribution to an archive.

### 3.4.2 Campaign Evaluation

The campaign module sets up a deflection campaign and evaluates how well it achieves the set aims. To enable evaluation, we have to define a fitness function or objective function, which summarizes the design solution into a figure of merit. It is the role of an optimizer to minimize or maximize the figure of merit by finding an optimal set of design variables. The fitness function to be minimized in the ADIEU framework is defined as the ratio of the total system mass and $(C_{max} + 1)$. Algorithm 2 illustrates how the fitness of a campaign is evaluated.

**Algorithm 2** Fitness computation routine

1: **procedure** COMPUTE–FITNESS
2: Initialize probability of success $s$ to 1
3: Initialize robustness coefficient $C$ to 0
4: Initialize mass $m$ and $m_{prev}$ to $m_{max}$
5: **while** $s > p_{threshold}$ **do**
6: Find $m$ that maximizes $s(m, C, \mathbf{T})$ (Algorithms 3 & 4)
7: Set $s \leftarrow s(m, C, \mathbf{T})$
8: Increment $C \leftarrow C + \Delta C$
9: **if** $s > p_{threshold}$ **then**
10: Update $m_{prev} \leftarrow m$
11: **end if**
12: **end while**
13: Get the final value of $C$, which is equal to $C_{max}$+1
14: Calcuate initial impactor mass $m_0 \leftarrow m_{prev}/\epsilon(\mathbf{T})$
15: Add precursor mass (if applicable) $m_0 \leftarrow m_0 + m_{precursor}$
16: **end procedure**

As can be seen above, the fitness computation routine keeps incrementing $C$ until the "best" case fails to meet the minimum requirement for the probability of success. When this happens and the loop is terminated, the *compute-fitness* routine returns the optimal impactor mass upon asteroid arrival. Then how can the best case be found that maximizes the likelihood of success? There are two possible ways, as described in Algorithms 3 and 4. The first routine evaluates all pairs of the impactor mass and the likelihood of success. The mass is found using MATLAB's built-in function *max*. This algorithm is used as a baseline in evaluating Type 0 campaigns.

**Algorithm 3** Optimal impactor mass computation routine-1 (maximum detection)

1: **procedure** FIND–IMPACTOR –MASS–1
2: **for** all $m$ in delta-v-per-impactor-mass distribution **do**
3: Calculate delta-v
4: Calculate deflection distance
5: Calculate likelihood of success
6: Save ($m$,$s$) pair
7: **end for**
8: Read ($m$,$s$) pair
9: Return $m$ that maximizes $s$
10: **end procedure**

The second routine uses a different approach, which detects a "knee" point instead of the maximum point. This routine detects a point where the nonzero likelihood does not increase anymore. Figure 3-15 (left) clearly illustrates this difference. The first routine (red) finds the impactor mass that maximizes the likelihood of success, whereas the second routine (blue) finds the impactor mass beyond which the likelihood does not increase anymore.

**Algorithm 4** Optimal impactor mass computation routine-2 ("knee" detection)

1: **procedure** FIND–IMPACTOR–MASS–2
2: Initialize $m$ and $m_{prev}$ to the minimum value in delta-v-per-impactor-mass distribution
3: Initialize $s_{prev}$ to 0
4: **while** $m$ is not the maximum value in distribution **do**
5: Calculate delta-v
6: Calculate deflection distance
7: Calculate likelihood of success $s$
8: Update $m_{prev} \leftarrow m$
9: **if** $s$ is nonzero and not greater than $s_{prev}$ **then**
10: Break out of while loop
11: **end if**
12: **end while**
13: Assign $m \leftarrow m_{prev}$
14: Return $m$
15: **end procedure**

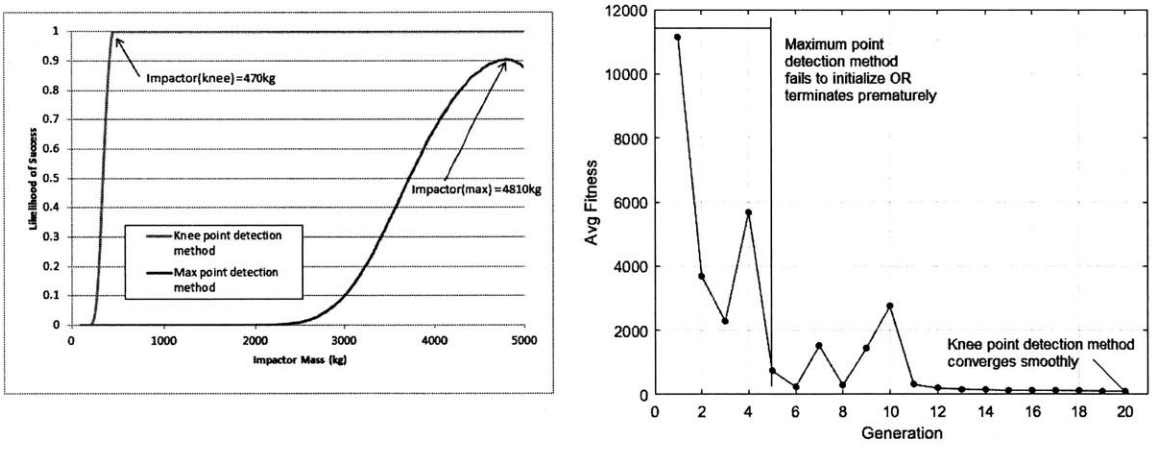


Figure 3-15: Maximum detection vs. knee detection: comparison of optimal solutions and convergence histories

The idea of maximum detection (first routine) is logically correct, and it is used for Type 0 campaign evaluation where all possible cases have already been pre-calculated. If knee detection (second routine) is used to evaluate Type 0 campaigns, it will stop at the first local maximum and return it as an answer, which is incorrect. Therefore, evaluation of Type 0 campaigns only uses a maximum detection method.

However, the two methods behave quite differently when evaluating Type 1 and Type 2 campaigns. Because the number of possible cases is too large to calculate, an optimization approach is preferred to a full-factorial approach. As an optimizer manipulates the impactor mass value, the shape of the likelihood-of-success function changes dynamically. The maximum detection method caused the optimizing process to terminate prematurely, as shown in Fig. 3-15 (right). In the few cases where optimization did converge, the impactor mass was close to the maximum limit (5,000 kg) because the mass-likelihood graph is skewed to the right, as shown in Fig. 3-15 (left). In contrast, using the knee detection method, the solution converges smoothly until the end (right). Furthermore, the converged value of the impactor mass tends to be much lower (left). By virtue of its benign behaviors when used with a genetic algorithm, the knee detection scheme is used throughout the remainder of this thesis.

## 3.5 Chapter Summary

This chapter introduces a proposed framework for designing asteroid deflection campaigns under uncertainty. From a user perspective, the interfaces of this framework are first explained to facilitate its use: (1) how to set up parameters; (2) what are inputs (design vector) and outputs (objective vector). The last section discusses the simulation model. This completes the pipeline of a *forward problem* or one-time simulation. The path from a design to its objective is iterated by an optimizer to improve the performance, as shown in Fig. 3-16. This generalized simulation module can be implemented as Fig. 3-17 and integrated into the ADIEU framework.

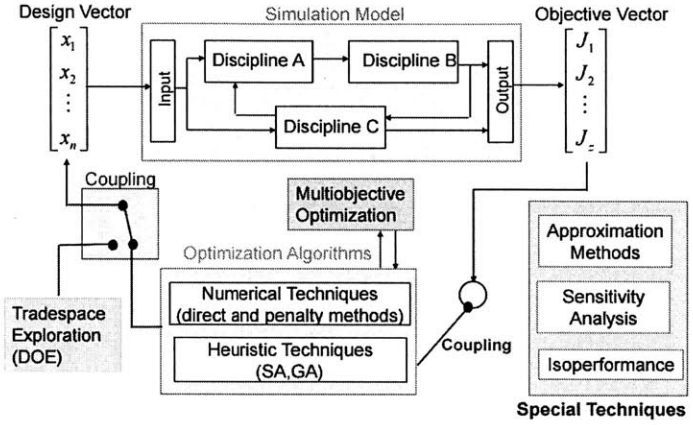


Figure 3-16: Multidisciplinary system design optimization (MSDO) framework

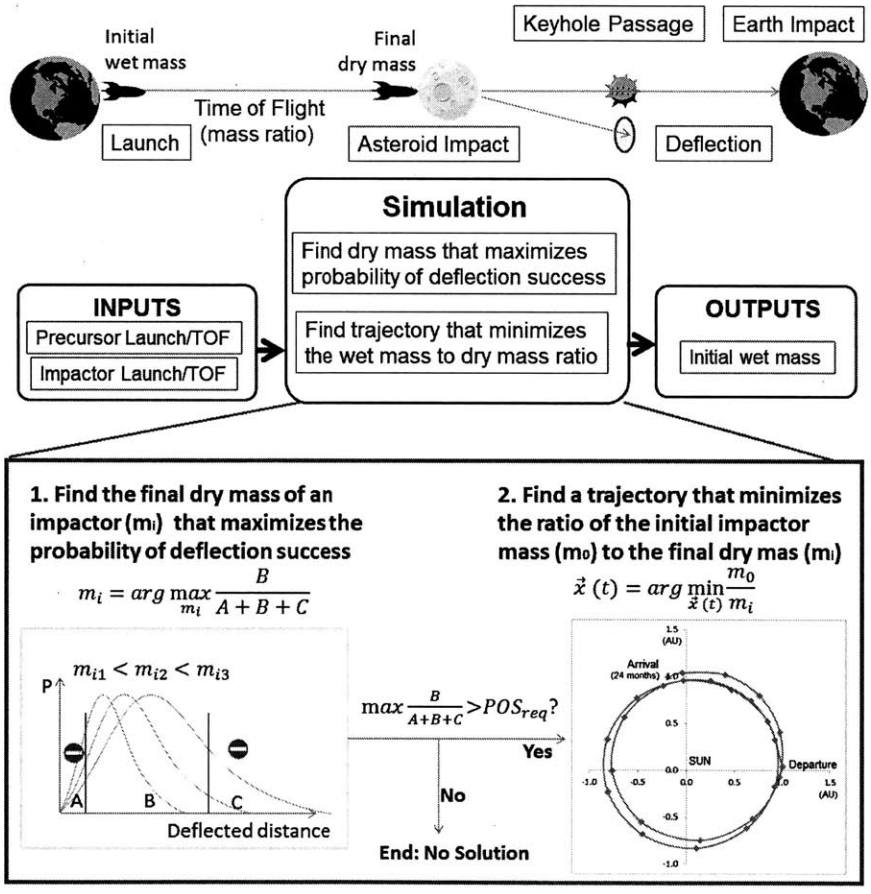


Figure 3-17: The simulation module in ADIEU framework

# Chapter 4

# Optimization Algorithm in ADIEU

Based on our previous discussion on how ADIEU interfaces with the user, we will see how ADIEU actually works. This chapter will construct a mathematical formulation of the asteroid deflection problem. This chapter also explains how a genetic algorithm is connected to a user interface to generate optimal campaign designs. The last part of this chapter discusses how Chebyshev optimization works internally.

## 4.1 Mathematical Formulation

The formal multi-objective problem can be formulated as:

$$\begin{aligned} \min_{\mathbf{x}} \quad & \mathbf{J}(\mathbf{x},\mathbf{p}) \\ \text{subject to:} \quad & \mathbf{g}(\mathbf{x},\mathbf{p}) \leq 0 \\ & \mathbf{h}(\mathbf{x},\mathbf{p}) = 0 \\ & x_{i,LB} \leq x_i \leq x_{i,UB} \qquad (i = 1,...,n) \end{aligned} \tag{4.1}$$

In this expression, $\mathbf{x}$ is the design vector of design variables $x_i$ with lower bound $x_{i,LB}$ and upper bound $x_{i,UB}$ where $i = 1,...,n$; $\mathbf{p}$ is the parameter vector of fixed parameters $p_j$ where $j = 1,...,m$; $\mathbf{J}$ is the objective vector with objectives $J_k$ to be minimized where $k = 1,...,z$; $\mathbf{g}$ is the inequality constraint vector with $g_{i_1}$ where $i_1 = 1,...,m_1$; $\mathbf{h}$ is the equality constraint vector with $h_{i_2}$ where $i_2 = 1,...,m_2$.

### 4.1.1 Objectives

The objective of the asteroid deflection problem is to minimize the initial mass in low-Earth orbit (IMLEO) while maximizing the robustness margin coefficient ($C_{max}$).

$$\mathbf{J} = \begin{bmatrix} m_{IMLEO} \\ -C_{max} \end{bmatrix} \tag{4.2}$$

To simplify the problem into a single objective optimization, the objective vector is transformed into a scalar. One way to do this is by dividing the initial mass by the robustness coefficient plus one.[1] (One is added to prevent the denominator from becoming zero.)

$$J_{scalar} = \frac{m_{IMLEO}}{C_{max} + 1} \tag{4.3}$$

The analysis of different campaign types consists of the following two steps. First, we will compare the $J_{scalar}$ objectives of campaign types and rank them. Second, we will reconstruct IMLEO and C from each $J_{scalar}$ to compare the campaign types on the basis of Pareto optimality (non-dominance). Thus two versions of decision maps (single-option and multiple-options) will be created, which will be explained in the following chapters.

### 4.1.2 Design Vector

The main deliverable of this thesis work is a "decision map" that can be used to choose the best deflection campaign under different combinations of a reliability requirement and scheduling constraints. Therefore, the design vector consists of two parts. The first part defines a minimum threshold for the probability of success ($p_{threshld}$) as a measure of reliability. The second part defines the departure date and the arrival date of each stage; the departure date is when the spacecraft leaves a low-Earth orbit and the arrival date is when the spacecraft either performs a rendezvous or collides

[1] Division is used here because linear combination may have issues with interpreting whether it makes sense to add different units (dimensions). Nondimensionalization can avoid this problem, but the final nondimensionalized value depends on anchor points. Anchor points are two extreme cases corresponding to the best case and the worst case, which is hard to define in asteroid deflection.

with the asteroid. This design vector will have a varying number of design variables depending on the number of stages in a specific campaign design. A generalized expression for the design vector would look like

$$\mathbf{x} = \begin{bmatrix} p_{threshold} & \mathbf{T}^T \end{bmatrix}^T = \begin{bmatrix} p_{threshold} & t^1_{departure} & t^1_{arrival} & \cdots & t^l_{departure} & t^l_{arrival} \end{bmatrix}^T \tag{4.4}$$

The simplest case is a Type 0 campaign where there is only one stage (main impactor).

$$\mathbf{x} = \begin{bmatrix} p_{threshold} & t^1_{departure} & t^1_{arrival} \end{bmatrix}^T \tag{4.5}$$

A Type 1 campaign has two stages: the first stage for a preliminary remote-sensing orbiter and the second stage for a main impactor.

$$\mathbf{x} = \begin{bmatrix} p_{threshold} & t^1_{departure} & t^1_{arrival} & t^2_{departure} & t^2_{arrival} \end{bmatrix}^T \tag{4.6}$$

A Type 2 campaign has two precursor stages and one main stage, with a total of three stages: the first stage for a preliminary remote-sensing orbiter, the second stage for a preliminary impactor, and the third stage for a main impactor.

$$\mathbf{x} = \begin{bmatrix} p_{threshold} & t^1_{departure} & t^1_{arrival} & t^2_{departure} & t^2_{arrival} & t^3_{departure} & t^3_{arrival} \end{bmatrix}^T \tag{4.7}$$

In the equations above, the duration of flight $\Delta t^l = t^l_{arrival} - t^l_{departure}$ may be used interchangeably instead of $t^l_{departure}$. In this case, a general design vector can be re-written as

$$\mathbf{x} = \begin{bmatrix} p_{threshold} & t^i_{departure} & \Delta t^i \end{bmatrix}^T (i = 1, 2, .., l) \tag{4.8}$$

### 4.1.3 Constraints

In order to avoid unnecessarily constraining the optimization problem, the number of inequality constraints is minimized and no equality constraint is used. Equation 4.9 shows that there are three kinds of inequality constraints: probability of success, milestone dates for each stage, and initial mass in low-Earth orbit. The first row, $p_{threshold} - s \leq 0$, states that the probability of success obtained from Eq.3.8 must be greater than or equal to the provided threshold. The even-numbered (2nd, 4th, ..., $(2l)$-th) rows after that, $t^i_{departure} - t^i_{arrival} \leq 0 (i = 1, 2, ..., l)$, are trivial causality statements that enforce that the spacecraft in each stage must arrive at the asteroid after it has departed fdom an orbit around Earth.[2] The odd-numbered rows (3rd, 5th, ..., $(2l+1)$-th) with $t^{i+1}_{arrival} - t^i_{departure} \leq 0 (i = 1, 2, ..., l-1)$ state that the subsequent stage must start after the previous stage ended so that later stages can benefit from information obtained in earlier stages. The $(2l+2)$-th row, $t^l_{arrival} - t_{keyhole} \leq 0$, states that the spacecraft in the final stage (which will always be an impactor) must arrive at an asteroid before the asteroid passes through a keyhole. The bottom-most row, $m_{IMLEO} - 5000kg \leq 0$, requires that initial mass in low-Earth orbit be less than or equal to 5,000 kilograms. This is used as a maximum IMLEO launch mass constraint and can be changed if heavier lift capability is available.

$$\mathbf{g} = \begin{bmatrix} p_{threshold} - s \\ t^1_{departure} - t^1_{arrival} \\ t^1_{arrival} - t^2_{departure} \\ t^2_{departure} - t^2_{arrival} \\ \cdots \\ t^l_{departure} - t^l_{arrival} \\ t^l_{arrival} - t_{keyhole} \\ m_{impactor} - 5000kg \end{bmatrix} \leq 0 \tag{4.9}$$

[2] Alternatively, $\Delta t^i = t^i_{arrival} - t^i_{departure} \geq 0 \forall j \in \{1, 2, ..., l\}$

Based on our discussion, the constraint vector can be re-written as

$$\mathbf{g} = \begin{bmatrix} p_{threshold} - s \\ -\Delta t^i \\ t^{j+1}_{arrival} - t^j_{departure} \\ t^l_{arrival} - t_{keyhole} \\ m_{impactor} - (m_j)_{UB} \end{bmatrix} \leq 0 \tag{4.10}$$

where $i \in \{1, 2, ..., l\}$, $j \in \{1, 2, ..., l-1\}$, and $\Delta t^j$ means $t^j_{arrival} - t^j_{departure}$. There is usually no equality constraint, except for Type 2 campaigns. In a Type 2 campaign, it is assumed that a preliminary orbiter and a preliminary impactor are launched together, on the same date. Therefore, we need the following equality constraint:

$$\mathbf{h} = \begin{bmatrix} t^1_{departure} - t^2_{departure} \end{bmatrix} = \mathbf{0} \tag{4.11}$$

### 4.1.4 Parameters

Table 4.1 summarizes the mission parameters used in campaign optimization. If the terminal velocity relative to an asteroid is set to be zero ($|\dot{r}_{s/c} - \dot{r}_{ast}| = 0$), the spacecraft matches the velocity of the asteroid ($\dot{r}_{s/c} = \dot{r}_{ast}$), moving together in the heliocentric frame. For a nonzero relative velocity of the impactor ($|\dot{r}_{s/c} - \dot{r}_{ast}| = v_{rel}$), the collision does not always occur in a tangential direction, especially if $v_{rel}$ is several dozens of kilometers per second. However, for $v_{rel} = 10$ km/s, the collision is nearly parallel with the asteroid velocity. Therefore, the $\Delta v$ loss in the non-tangential directions would be negligible. Now that the asteroid velocity and the impactor velocity are collinear, there can be two possible cases where $v_{rel} = 10$ km/s. First, the impactor may catch up the asteroid, with $v_{s/c} = v_{ast} + 10km/s$. Second, the impactor is caught up by the asteroid, with $v_{s/c} = v_{ast} - 10km/s$. The trajectory optimizer always chooses the latter, which consumes less fuel. Consequently, the asteroid will be deflected to the left ($-\zeta$) on the keyhole map. To consider both directions ($\pm\zeta$), the safe harbor is defined to be (20km $< |\Delta\zeta| <$ 800km).

Table 4.1: Master table of parameters used in ADIEU framework

| Parameters | Symbol | Value | Units |
|---|---|---|---|
| **Spacecraft Common Parameters** | | | |
| Earth parking orbit altitude | $h_P$ | 1000 | $km$ |
| Specific impulse | $I_{sp}$ | 3000 | $s$ |
| Initial vehicle power | $P_0$ | 2.6 | $kW$ |
| **Type 0 Campaign Parameters** | | | |
| Upper bound of impactor mass | $(m_1)_{UB}$ | 5000 | $kg$ |
| Excess velocity | $v_1$ | 10 | $km/s$ |
| Launch date lower bound | $(t_1)_{LB}$ | 0 | $day$ |
| Launch date lower bound | $(t_1)_{UB}$ | 5000 | $day$ |
| TOF lower bound | $(\Delta t_1)_{LB}$ | 100 | $day$ |
| TOF upper bound | $(\Delta t_1)_{UB}$ | 5000 - $t_1$ | $day$ |
| **Type 1 Campaign Parameters** | | | |
| Preliminary orbiter mass | $m_1$ | 400 | $kg$ |
| Excess velocity of preliminary orbiter | $v_1$ | 0 | $km/s$ |
| Main impactor mass | $(m_2)_{UB}$ | 500 | $kg$ |
| Excess velocity of impactor | $v_2$ | 10 | $km/s$ |
| **Type 2 Campaign Parameters** | | | |
| Preliminary orbiter mass | $m_1$ | 400 | $kg$ |
| Excess velocity of preliminary orbiter | $v_1$ | 0 | $km/s$ |
| TOF lower bound | $(\Delta t_1)_{LB}$ | 100 | $day$ |
| TOF upper bound | $(\Delta t_1)_{UB}$ | 800 | $day$ |
| Preliminary impactor mass | $m_2$ | 500 | $kg$ |
| Excess velocity of preliminary impactor | $v_2$ | 10 | $km/s$ |
| TOF lower bound | $(\Delta t_2)_{LB}$ | 800 | $day$ |
| TOF upper bound | $(\Delta t_2)_{UB}$ | 1000 | $day$ |
| Main impactor mass | $m_3$ | 500 | $kg$ |
| Excess velocity of impactor | $v_3$ | 10 | $km/s$ |
| TOF lower bound | $(\Delta t_3)_{LB}$ | 100 | $day$ |
| TOF upper bound | $(\Delta t_3)_{UB}$ | 1000 | $day$ |

Because all masses are constraints at the asteroid, rather than constraints in low-Earth orbits, the masses should be converted to the corresponding IMLEO values. As discussed in 3.3.2, each stage has a distinct conversion factor (mass ratios) because the relative velocity and the launch date of each spacecraft are different. By adding the masses of all stages are added, we obtain the campaign mass (system mass) that is one of outputs of this framework. Finally, these constraints are assumed to be fixed in the problem and can be modified during sensitivity analysis. For instance, the maximum impactor mass can be increases per launch vechicle capabilities.

## 4.2 Genetic Algorithm

Designing an asteroid deflection campaign presents a challenging optimization problem for several reasons, which favors the use of heuristics over gradient-based methods or local brach prediction [105].

- **Objective**: The objective space is discontinuous and non-linear, such as launch windows which are necessary to estimate the system mass.[3]
- **Input**: The input design vector contains continuous, integer, and discrete (categorical) variables. A threshold for the probability of success is continuous, the launch date is considered to be an integer, and the campaign type is categorical.
- **Output**: Functional evaluations are computationally expensive. Each evaluation has communication overheads between different programs (MATLAB and Excel macros). Also, the number of evaluations necessary increases as the number of design variables increases.

A heuristic refers to a technique or procedure contributing to "reduction in the search for a satisfactory solution" (Newell, Shaw, and Simon 1967) [106]. It can be viewed as a shortcut which enables us to quickly find a good-enough solution instead of endlessly searching for an exact solution. Although heuristics without a theoretical background fall into a rule-of-thumb that makes no guarantees (Perkins 1981), heuristics defined by exact procedures form a branch of computer science called evolutionary algorithms.[4] Among a wide variety of evolutionary algorithms[5], genetic algorithms (GAs) are the most popular in solving optimization problems. GAs mimic the process of natural selection. Individuals with differing genes fight for survival in the population, but only the "fittest" can survive and reproduce. This selection process improves the entire population over generations.

[3]This can be best illustrated with Fig. 5-2.

[4]Evolutionary algorithms are the central characteristic of evolutionary computing, which is a subfield of artificial intelligence (computational intelligence).

[5]Other types of evolution algorithms include genetic programming, evolution strategy, and differential evolution. Also closely related are swarm-based algorithms (e.g. particle swarm algorithm and learning classifier system (LCS).

**Algorithm 5** Implementation of genetic algorithm

```
procedure EVOLUTIONARY–ALGORITHM
    Generate the initial population of individuals randomly
    Evaluate the fitness of each individual in that population
    while termination condition not reached do
        Select the best-fit individuals as "parents" for reproduction
        Breed parents through crossover and mutation to give birth to "offspring"
        Evaluate the individual fitness of new individuals.
        Replace least-fit population with new individuals.
    end while
end procedure
```

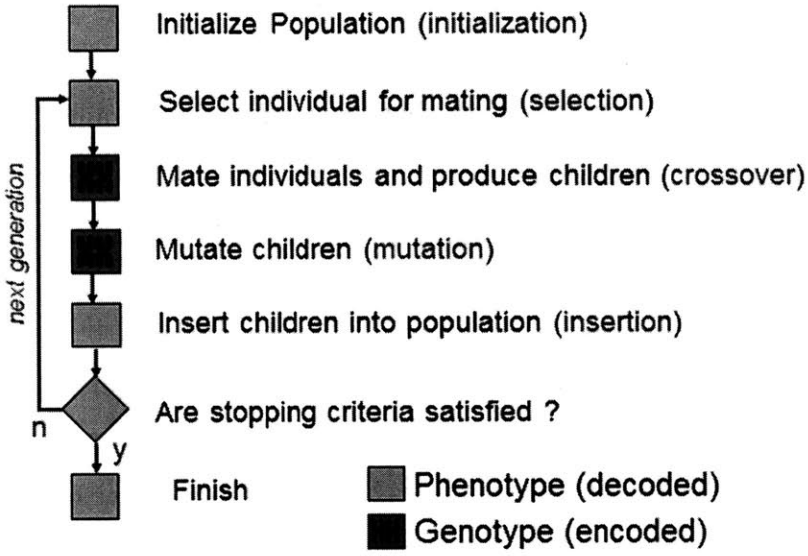


Figure 4-1: Genetic Algorithm [37]

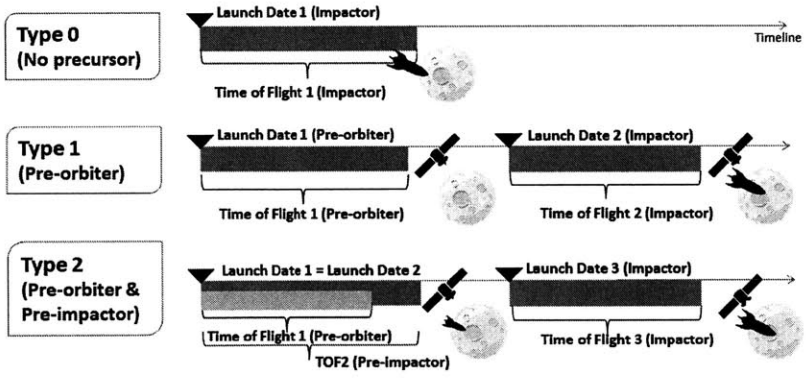


Figure 4-2: Time variables optimized by GA [74]

## 4.3 CHEBYTOP

CHEBYTOP is an acronym for Chebyshev Trajectory Optimization Program which is an analysis tool to optimize one-way trajectories between planetary bodies. It is a preliminary design tool for missions using electric propulsion, and the user can obtain results with minimal setup and execution time. The tool was originally programmed in FORTRAN in the late 1960's by The Boeing Company under contract to the NASA Ames Research Center. A later version uses .dll files and the user can run the same program with an Excel interface instead of using a DOS prompt.

### 4.3.1 Trajectory Optimization

The equation of motion for interplanetary flight can be described as a two-body problem. Adding an acceleration term from the onboard propulsion of a vehicle,

$$\ddot{\mathbf{r}}(t) + \frac{\mu \mathbf{r}(t)}{|\mathbf{r}(t)|^3} = \mathbf{a}(t), 0 \leq t \leq T \tag{4.12}$$

where $\mathbf{r}(t)$ is the position vector of the vehicle, $\mathbf{a}(t)$ is the applied acceleration vector, and $\mu$ is the gravitational constant of the Sun. The basic problem then is to minimize

$$J = \int_0^T |\mathbf{a}(t)|^2 dt = \int_0^T \left| \ddot{\mathbf{r}}(t) + \mu \frac{\mathbf{r}(t)}{|\mathbf{r}(t)|^3} \right|^2 dt \tag{4.13}$$

subject to boundary conditions on $\mathbf{r}$ and the thrust history of $\mathbf{a}$. These constraints are imposed on $T, \mathbf{a}(t)$, $\mathbf{x}(0)$, $\dot{\mathbf{r}}(0)$, $\mathbf{r}(T)$, and $\dot{\mathbf{r}}(T)$. The trip time, $T$, is always assumed to be fixed. The end points, $\mathbf{r}(0)$ and $\mathbf{r}(T)$, can be fixed or allowed to vary in a prescribed orbit to determine optimum launch or arrival times. The acceleration, $\mathbf{a}$, may be completely unconstrained (variable thrust) or exhibit on/off behaviors (constant thrust). For an ion engine with a constant specific impulse ($I_{sp}$), we have

$$\mathbf{a}(t) = \frac{a_0}{\epsilon(t)} \frac{p(r,t)}{p_0} \mathbf{u}(t) \tag{4.14}$$

In this equation, $a_0$ and $p_0$ are the initial acceleration and the power level, respectively of the vehicle at a distance of 1 AU from the Sun, assuming solar electric propulsion (SEP). A generalized power level at solar distance $r$ and time $t$ is expressed as $p = p(r,t)$, and it follows that $p_0 = p(1,0)$.[6] The on/off switching behavior can be described with a unit direction vector $\mathbf{u}(t)$ that is parallel with an acceleration vector with unit magnitude during an accelerating phase and is a zero vector during a coasting phase. Finally, $\epsilon(t)$ is the mass fraction of the vehicle relative to the initial mass, which follows

$$\frac{d\epsilon(t)}{dt} = \frac{a_0}{v_e}\frac{p(r,t)}{p_0}\sigma(t) \tag{4.15}$$

where $v_e$ is exhaust velocity and $\sigma(t) = |\mathbf{u}(t)|$ takes 0 or 1 as its value. The program solves the variable thrust optimization problem in exact fashion. The constrained thrust solution, on the other hand, is achieved using approximations to the original problem. Going back to our trajectory optimization problem, the time duration can be normalized by setting $s = t/T$. Then we obtain

$$J = T\int_0^1 \left|\frac{\ddot{\mathbf{r}}(s)}{T^2} + \mu\frac{\mathbf{r}(s)}{|\mathbf{r}(s)|^3}\right|^2 ds \tag{4.16}$$

where the boundary conditions are now $\mathbf{r}(0)$, $\dot{\mathbf{r}}(0)$, $\mathbf{r}(1)$, and $\dot{\mathbf{r}}(1)$ for the same problem. For convenience, we make a final substitution of $J = 2P/T^3$ and get

$$P = \frac{1}{2}\int_0^1 \left|\ddot{\mathbf{r}}(s) + \mu T^2\frac{\mathbf{r}(s)}{|\mathbf{r}(s)|^3}\right|^2 ds \tag{4.17}$$

such that minimization of $P$ solves the original problem. We also note that the quadratic form of the integrand, $\left|\ddot{\mathbf{r}}(s) + \mu T^2\mathbf{r}(s)/|\mathbf{r}(s)|^3\right|^2$, is simple enough to allow for approximation of $x(s)$ by a polynomial. The CHEBYTOP program approximates state time histories by a Chebyshev polynomial. This enables us to (1) perform integration and differentiation in a closed form, and (2) reduce the number of optimized parameters to a finite number.

[6] In nuclear electric propulsion (NEP), the power level is constant regardless of the distance from the Sun ($p = p(r,t) = p_0$).

### 4.3.2 Chebyshev Polynomials

In some cases, it is desirable to replace a function with an approximating surrogate, possibly because the *true* function is unavailable or computationally expensive to evaluate. One approach to deal with such cases is to use an "interpolant" $\hat{f} = \hat{f}(x)$, which agrees with a particular function $f = f(x)$ at a set of known points $x_0, x_1, ..., x_n$ [107]. The interpolant can then be used to compute values of $f(x)$ at other points $x \neq x_i$ $(i = 0, 1, ..., n)$. In approximation theory, Chebshev polynomials or other methods based on non-equispaced points (or grids) are preferred to equispaced methods when using polynomial interpolation. This is because polynomial interpolation using equispaced points suffer from Runge's phenomenon, oscillations at the boundaries, which is similar to the Gibb's phenomenon when using Fourier interpolation.

Let's suppose we want to represent an arbitrary scalar function $f(s)$ continuous on [0,1] by a polynomial $\hat{f}(s)$ of degree less than $n$. Because the degree of a polynomial is limited, there is in general no combination of coefficients which enables $\hat{f}(s) = f(s)$ at every possible $s$ in [0,1].[7] A more realistic goal is to minimize the error by choosing appropriate coefficients of $\hat{f}(s)$. There can be many ways to measure how closely $\hat{f}(s)$ approximates $f(s)$: one can define the norm $||\hat{f}(s) - f(s)||$ using integrals, sums, suprema, derivatives, nonlinear functions, etc. Choosing the coefficients of $\hat{f}(s)$ such that it equals $f(s)$ at certain points $s = s_\nu$ $(\nu = 1, 2, ..., n)$ is known to achieve "close" approximations for a wide range of definitions. There points are called Chebyshev points (nodes) of the given interval.

$$s = s_\nu = \frac{1}{2}(1 - \frac{\cos \pi(\nu - 1)}{n - 1}) \tag{4.18}$$

The non-uniform linear spacing is actually obtained from the uniform angular spacing of the points on the circumference of a circle. The circle has a radius of 1/2, and its center is at (1/2, 0) such that it passes through two points (0,0) and (1,0). We mark points on the circumference whose central angles are multiples of $\pi/n$. The Chebyshev points are obtained by projecting these points onto the segment connecting points

[7] The few exceptions to this are when $f(s)$ itself is a polynomial of degree less than $n$.

(0,0) and (1,0). Although Chebyshev interpolation in the CHEBYTOP program uses an interval [0,1], Chebyshev polynomials are usually defined on an interval [-1,1]. More details about their original derivation and properties are provided in Appendix C. Using Chebyshev polynomials, finite-thrust optimization becomes an interpolation problem, where the approximated trajectory is expressed as a weighted sum of Chebyshev polynomials:

$$\hat{f}(s) = \sum_{k=1}^{n} \Phi^k T_{k-1}(s) \tag{4.19}$$

where $T_k$ is the $k$th Chebyshev polynomial$T_k(s) = \cos \pi k\sigma$, $\sigma = \nu/(n-1)$, and $s$ is a set of $s_\nu$ defined in Eq. 4.18($\nu = 1, 2, ..., n$). The requirement that $\hat{f}(s_\nu) = f(s_\nu)$ at $\nu = 1, 2, ..., n$ leads to $n$ linear equations with $n$ unknown coefficients $\Phi^k$. If we let $F$ denote the column matrix of $n$ known quantities of the original function such that

$$\mathbf{F} = \begin{bmatrix} f(s_1) & f(s_2) & \dots & f(s_n) \end{bmatrix}^T \tag{4.20}$$

Similarly, if we let $\Phi$ denote a column vector whose elements are $\Phi^1$ through $\Phi^n$, the solution of the linear equations may be written as $\Phi = \mathbf{AF}$ for some n-by-n matrix $\mathbf{A}$. If $T(s)$ denotes a n-by-1 column vector whose elements are Chebyshev polynomials $T_0(s)$ through $T_{n-1}(s)$, Eq. 4.19 may be rewritten as Eq. 4.21. Differentiating this equation twice $\ddot{\hat{f}}(s) = \ddot{\mathbf{T}}(s)^T\mathbf{AF} = \mathbf{T}(s)^T\mathbf{BAF}$ for some n-by-n upper triangular matrix $\mathbf{B}$ because the trigonometric terms of Chebyshev polynomials repeat themselves during differentiation.

$$\hat{f}(s) = \mathbf{T}(s)^T\mathbf{AF} \tag{4.21}$$

Going back to the minimization problem in Eq. 4.17, $P$ can be approximated as

$$P = \frac{1}{2}\sum_{m=1}^{nd}\int_0^1 \ddot{x}(m,s)^2 ds + \sum_{m=1}^{nd}\int_0^1 \ddot{x}(m,s)y(m,s)ds + \frac{1}{2}\sum_{m=1}^{nd}\int_0^1 w(s)^2 ds \tag{4.22}$$

where $nd$ is the number of timestamps (dimensions) for the position vector, $x(m,s)$ is the $m$th Cartesian coordinate of $x(s)$, and $r(s) = \left[\sum_{m=1}^{nd} x(m,s)^2\right]^{1/2}$, $y(m,s) = \mu\tau^2 x(m,s)/r(s)^3$, $w(s) = \mu\tau^2/r(s)^2$. To further rearrange this expression into a more computation-friendly form, we let $\mathbf{X}(m)$ and $\mathbf{Y}(m)$ be the $m$th n-by-1 vectors with elements $[\mathbf{X}(m)]_\nu = x(m,s_\nu)$ and $[\mathbf{Y}(m)]_\nu = y(m,s_\nu)$. Note that $\mathbf{W}$ with elements $w(s_\nu)$ is independent of index $m$. Also, letting $\hat{x}(m,s)$, $\hat{y}(m,s)$ and $\hat{w}(s)$ be the polynomials that interpolate $x(m,s)$, $y(m,s)$, and $w(s)$ at $s_\nu$ satisfies, from our discussions so far, that $\ddot{\hat{x}}(m,s) = \mathbf{T}(s)^T\mathbf{BAX}(m)$, $\hat{x}(m,s) = \mathbf{T}(s)^T\mathbf{AY}(m)$, and $\hat{w}(s) = \mathbf{T}(s)^T\mathbf{AW}$. Substituting these expressions yields

$$P = \frac{1}{2}\sum_{m=1}^{nd} \mathbf{X}(m)^T\mathbf{DX}(m) + \sum_{m=1}^{nd} \mathbf{X}(m)^T\mathbf{EY}(m) + \frac{1}{2}\mathbf{W}^T\mathbf{FW} \tag{4.23}$$

where $\mathbf{C} = \int_0^1 \mathbf{T}(s)\mathbf{T}(s)^T ds$, $\mathbf{D} = \mathbf{A}^T\mathbf{B}^T\mathbf{CBA}$, $\mathbf{E} = \mathbf{A}^T\mathbf{B}^T\mathbf{CA}$, and $\mathbf{F} = \mathbf{A}^T\mathbf{CA}$. The n-by-n matrices $\mathbf{C}$, $\mathbf{D}$, $\mathbf{E}$. $\mathbf{F}$ may be pre-calculated, stored, and used repeatedly. Now that the objective function has been interpolated, optimization techniques may be applied to find its minimum. Reference [38] explicates how to obtain partial derivatives of the above expression such that optimization techniques which require the second-order derivatives may be applied.

Figure 4-3 compares the optimum values of $J$ generated by the CHEBYTOP program with existing solutions for Earth-to-Mars low-thrust rendezvous trajectories, which shows a good agreement for a two-dimensional case and a three-dimensional case. Figure 4-4 demonstrates how to use the CHEBYTOP's Excel interface for an asteroid deflection mission. The mass ratio and an Earth-to-asteroid trajectory are generated when a user provides the time variables and the impact velocity. The process of entering inputs and retrieving outputs can be automatically performed by MATLAB.

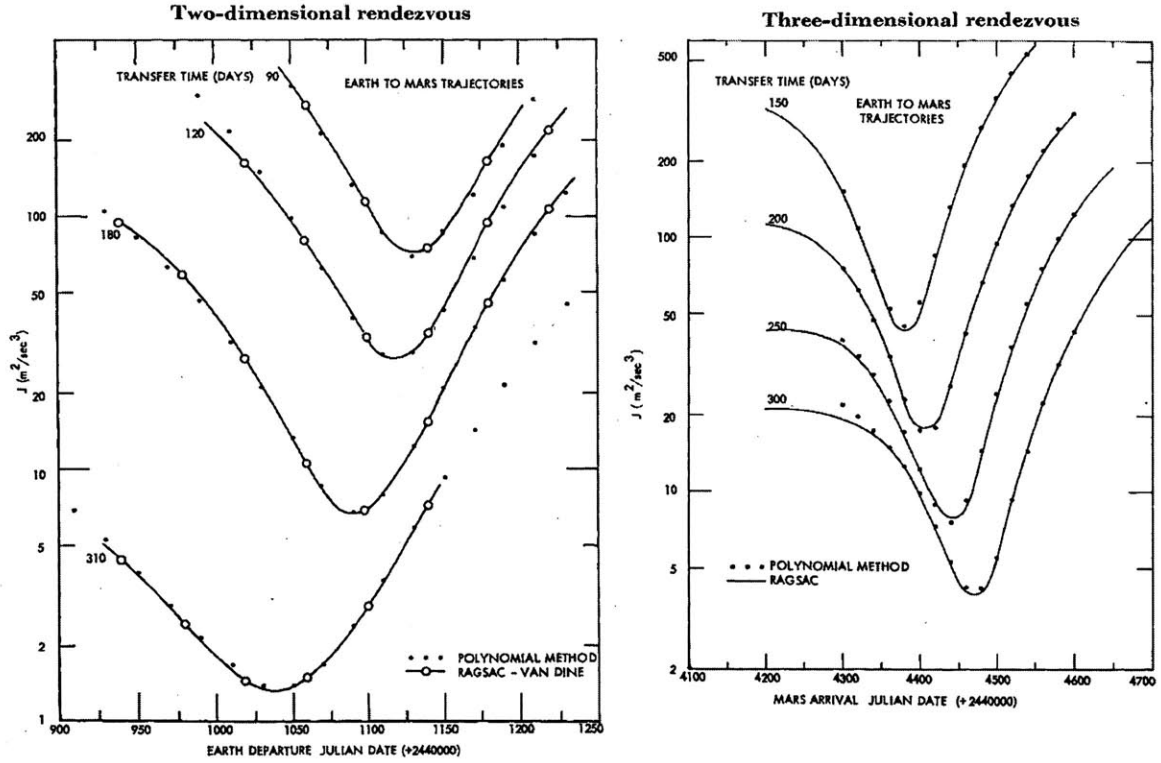


Figure 4-3: Chebyshev Interpolation Performance [38]

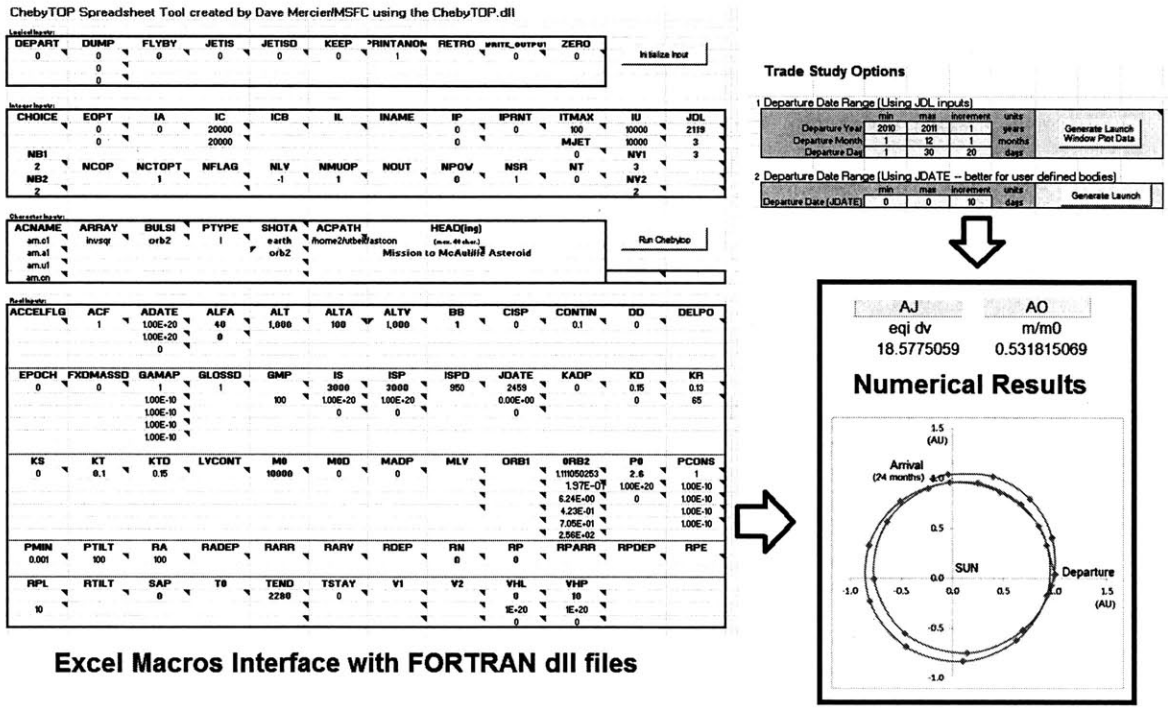


Figure 4-4: CHEBYTOP Program GUI

## 4.4 Chapter Summary

This chapter formulated asteroid deflection campaigns as a mathematical optimization problem. Genetic algorithm is used to optimize the launch date and the time of flight. Trajectory optimization uses two tiers of solvers. First, the CHEBYTOP program, a NASA open-source tool, optimizes a low-thrust spacecraft trajectory from Earth to asteroid with a two-body assupmtion. Second, the PAT2 written by Egger [102] calculates a post-deflection asteroid trajectory by solving an N-body problem.

# Chapter 5

# Case 1: Apophis Results

This chapter presents the results of applying the proposed framework to the asteroid 99942 Apophis. Figure 5-1 presents the overall organization of this chapter, in connection with previous chapters.

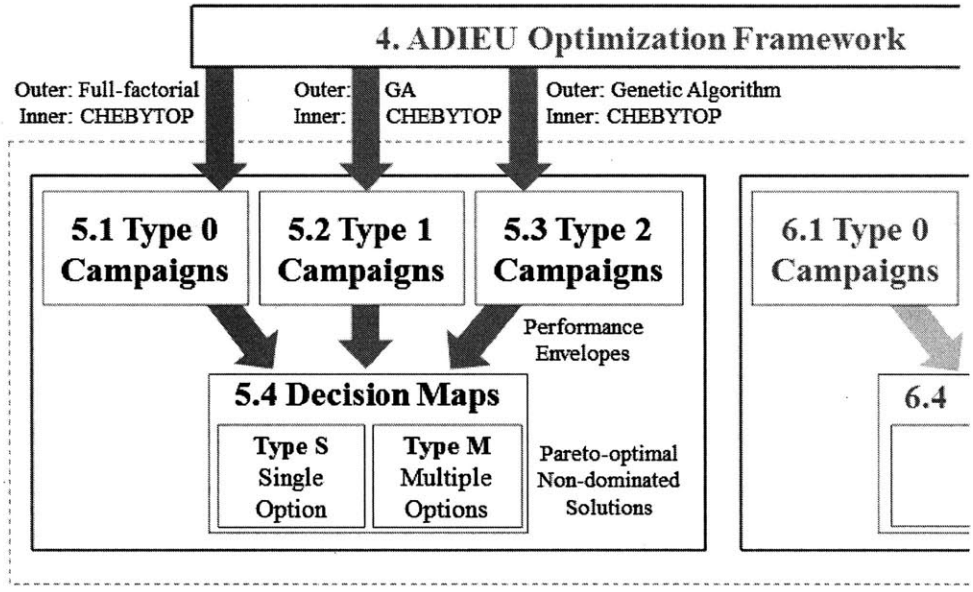


Figure 5-1: Organization of the results presented in Chapter 5

The ADIEU framework developed in Chapters 3 and 4 is applied to Apophis (Chapter 5) and Bennu (Chapter 6). For each asteroid, three types of campaigns are considered. Type 0 campaigns have only one variable to optimize (duration of flight) and do not require a genetic algorithm. Therefore, a full-factorial search is

performed, which requires around 125,000 CHEBYTOP runs.[1] Type 1 or Type 2 campaigns have multiple variables to optimize, which necessitates the use of a genetic algorithm (GA). Each campaign requires 50 GA runs,[2] each of which requires 400 to 4,000 CHEBYTOP runs plus routines specific to GAs such as encoding, decoding, and selection. These numbers of evaluations for Type 0, Type 1, and Type 2 are required for each level of probability of success. Because we consider 4 levels of probability of success (90%, 99%, 99.9%, 99.99%), the numbers of evaluations presented above should all be multiplied by 4. After the optimization runs are complete, the results are compared to each other. Two kinds of decision maps are presented: Type S with a single option and Type M with multiple options. A Type S decision map compares the optimization objectives, IMLEO/$(C_{max}+1)$, to decide the best campaign option. Alternatively, a Type M decision map considers the IMLEO and $C_{max}$ separately, and if two or more campaign types are superior in one aspect, they are considered equally good. This notion of *Pareto-optimal, non-dominated* solutions enables us to consider a set of options and perform trade-off analysis.

## 5.1 Type 0 Campaign

Figure 5-2 plots the initial mass in low-Earth orbit (IMLEO) for Type 0 (no precursor) campaigns for Apophis. A threshold of 90% is used as the threshold for the probability of success. The horizontal axis is the time of flight (duration of flight) in Earth days. The vertical axis is the launch date, in days elapsed since January 1, 2014. This plot is similar to a pork-chop plot in that both plots are used to visualize the required amount of energy for reaching a target body, with a time-of-flight axis and a launch date axis. However, the porkchop plots have sparse "islands of feasible solutions," whereas Fig. 5-2 shows a large connected region of all feasible solutions, which is

[1] For a 5000-day (approximately 15 years) time interval, the CHEBYTOP is evaluated every 10 days. Because the arrival must happen before keyhole passage, the maximum duration of flight decreases linearly as the launch is delayed. This gives an estimate of (5000/10) $\times$ (5000/10)/2 = 125,000 runs.

[2] Type 1 and Type 2 campaigns use a coarser granularity of 100 days, instead of the 10 days used in Type 0 campaigns. Therefore, there are (5000/100)=50 launch dates to evaluate.

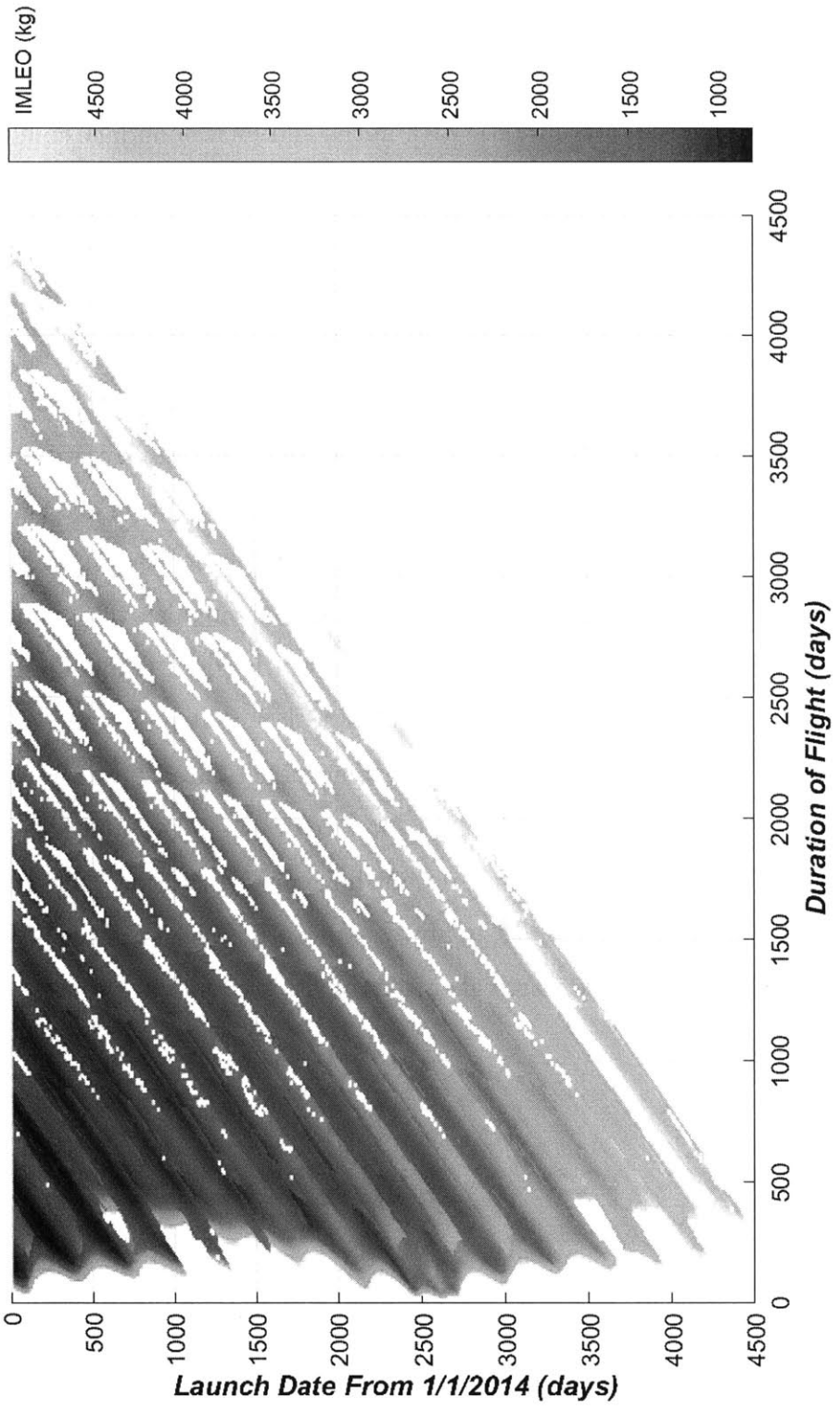


Figure 5-2: Mass (IMLEO[kg]) of Type 0 campaigns (PoS=90%)

interspersed with small blank patterns where no solution is available. When drawing a porkchop plot, one usually assumes that the spacecraft uses chemical propellant. It is obtained by solving Lambert's problem, which is basically a differential equation (Newton's law of mutual attraction), with initial and final boundary conditions for an interplanetary flight. The spacecraft makes an impulse burn (delta-v) at the starting point and does not make additional maneuvers until it reaches the destination. At the destination, the spacecraft makes a final impulse burn to rendezvous with the target body or to be captured[3] into an orbit around it. The duration of thrust is instantaneous, negligible compared to the total duration of flight. If electric propulsion is used, on the other hand, the spacecraft accelerates continuously over the thrusting arcs of its trajectory. Although there could be intervals (coasting arcs) during which the propulsion system is turned off, the overall duration of thrust is not negligible at all, compared to the total duration of flight. To distinguish the plots in this thesis from porkchop plots, the term "carpet plot" will be used throughout this thesis. Named after its appearance, a *carpet plot* has "holes" that represent cases where an interplanetary flight is impossible with a given launch date, duration of flight, and propulsion system requirements. *Carpet plots* are drawn only on one diagonal half of the plane, unlike *porkchop plots* that do not have any restriction. The (lower) triangular part (lower) of a *carpet plot* is always empty because that part is a keep-out zone corresponding to *too late* arrivals after the asteroid passes through a keyhole.

[3] aero-captured if the planet has its atmosphere

As shown in Fig. 5-3, the holes inside the admissible region have slopes related to the Earth's orbital period, Apophis' orbital period, and their algebraic combinations. First, the alignment of multiple patterns is governed by two slopes. One is the Earth's orbital period (1 year), and the other is the synodic period of the Earth's orbit and Apophis' orbit. The synodic period is a minimum time interval for two co-orbiting objects to have successive alignments [108]. It is also the time for an object to reappear on the same side with respect to the other object. The synodic period of Apophis and Earth is 2,838 days (7.8 years).[4] Inside each pattern, there are three edges whose slopes are also related to the orbital periods.

- **Earth's period** = 1 year
- **Apophis' period** = 0.89 year
- **Harmonic of synodic period** = $1/2 \times 7.8 = 3.9$ years

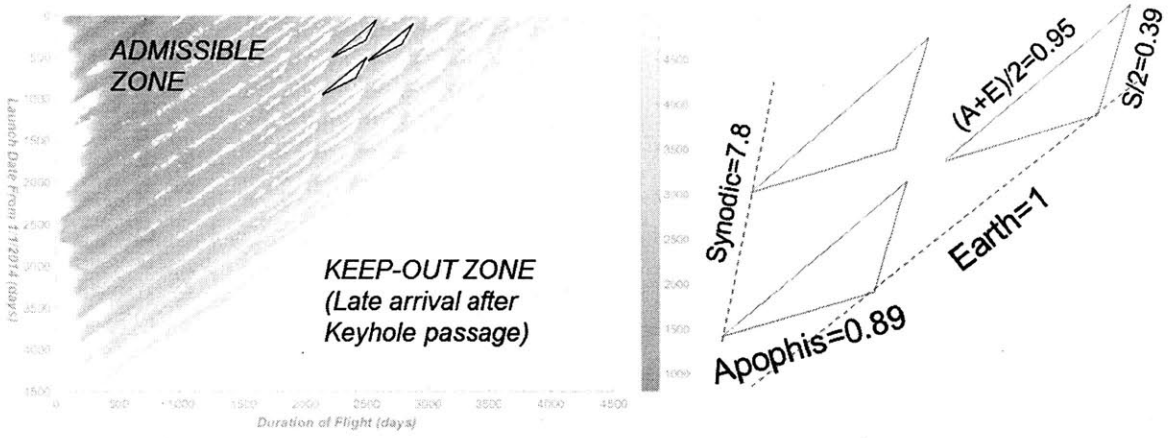


Figure 5-3: Admissible region and periodic patterns

The robustness coefficient ($C_{max}$) and the combined (balanced) performance measure (IMLEO/($C_{max}$+1)) are only calculated when an orbital transfer from Earth to Apophis is possible. Therefore, their plots have exactly the same admissible regions, as illustrated in Fig. 5-4 and Fig. 5-5.

[4]This is obtained by $1/|1/P_A - 1/P_E|$ where $P_A$ is the asteroid's orbit period and $P_E$ is the Earth's orbit period.

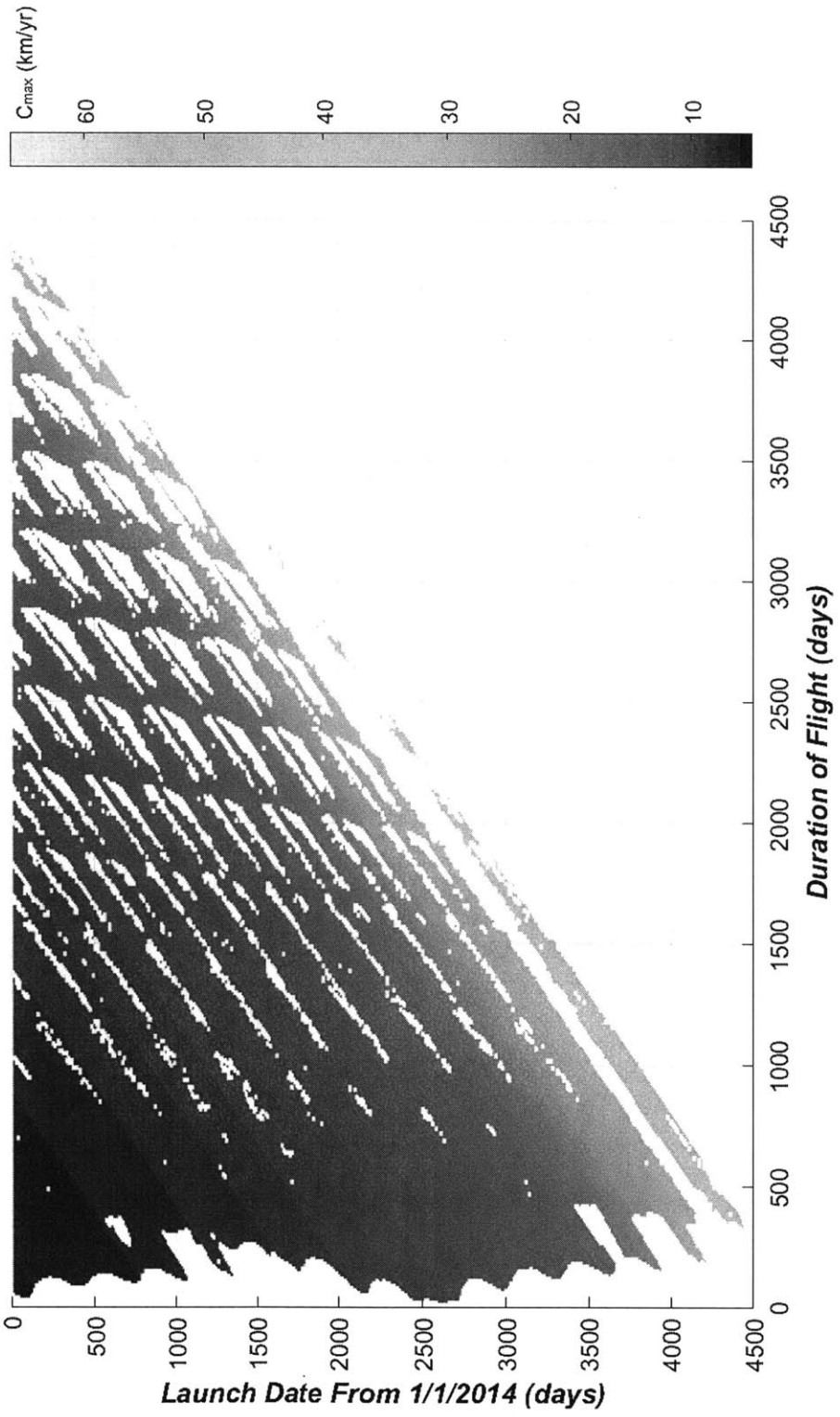


Figure 5-4: Robustness coefficient ($C_{max}$) of Type 0 campaigns (PoS=90%)

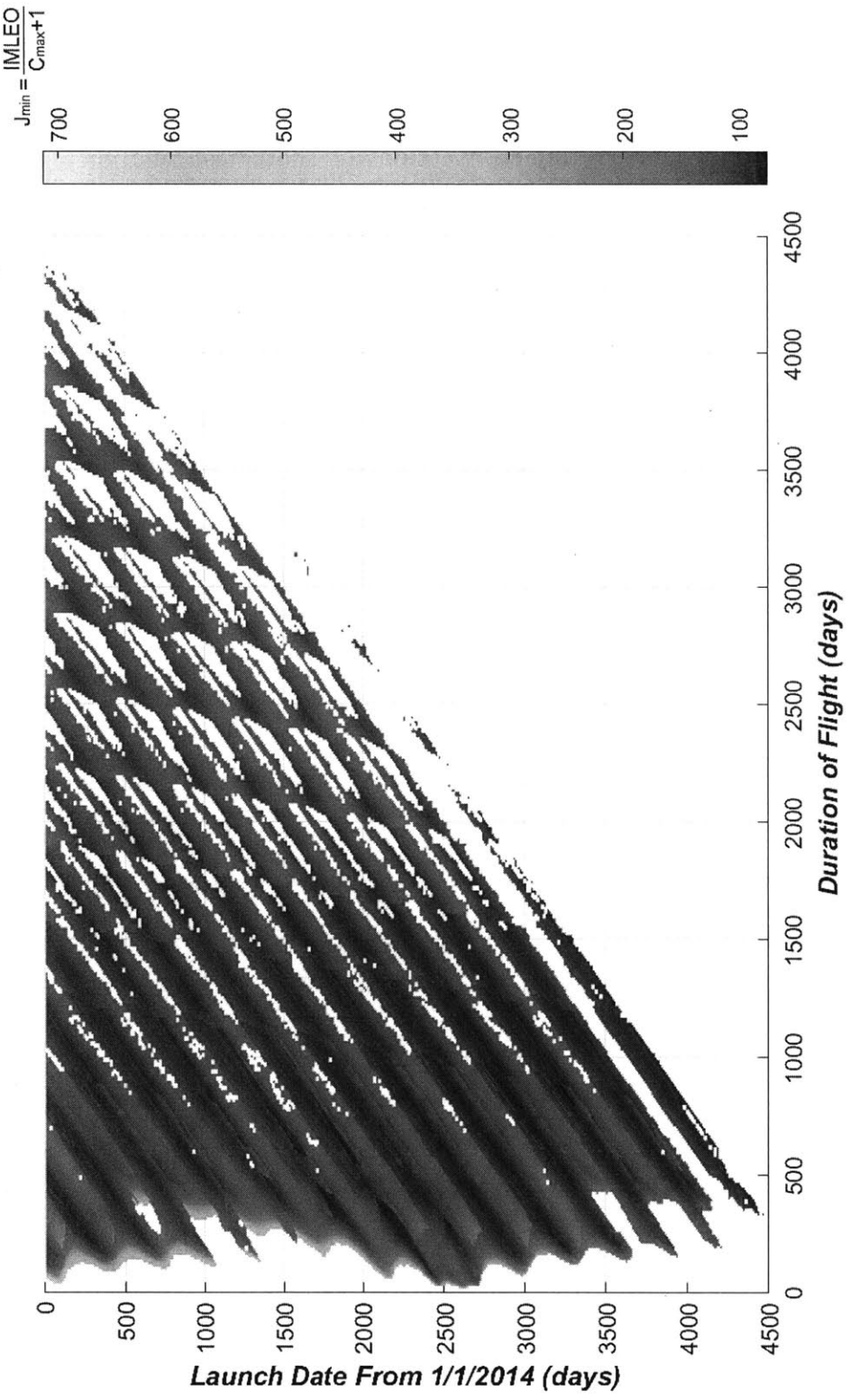


Figure 5-5: Balanced objective ($\frac{IMLEO}{C_{max}+1}$) of Type 0 campaigns (PoS=90%)

Before performing any post-processing, let's pick five representative architectures, as shown in Fig. 5-6. The details of these architecture solutions are summarized in Table 5.1. Solution A, located at (LD, TOF) = (0, 840) [day], represents a low-mass architecture benefitted from early action and short trip. Solution B also departs early, but its extremely long flight requires a large amount of propellant. Because of such a lengthy trip, the actual impact for deflection is rather delayed, requirng a larger impactor mass. This again increases the mass limit further, pushing very close to the 5,000 kg limit. Solution C is exactly opposite to Solution B in that its flight time is extremely short, only 130 days. This increases the IMLEO also, because more propellant is burnt at a higher rate in order to expedite the trip. Consequently, the mass ratio is the lowest amongst the five case, meaning the worst fuel efficiency. Solution E is very late and massive, due to the low deflection-per-unit-mass efficiency when there is not much time left for deflection to take effects. Solution D is the "sweet spot" or a global optimum whose $J_{min}$ is the lowest. Its mass is in the mid-range, and the $C_{max}$ value is fairly high, successfully achieving two goals (minimize mass and maximize robustness) the same time. However, there are many other local minima that may equaly work well compared to this global minimum. In fact, locating multiple "sweet spots," instead of one, helps make the campaign robust to program uncertainty such as launch delays or mission failures. Therefore, we need to interpret these carpet plots to generate a family of solutions for each date, or a time history of solutions. How can we do this?

Table 5.1: Five campaign architectures (POS = 90%)

| Point | $t^1_{start}$ *days* | $IMLEO$ *kg* | $C_{max}+1$ *km/yr* | $\frac{IMLEO}{C_{max}+1}$ *kg yr/km* | $\Delta t^1$ *days* | $\frac{m_{impactor}}{IMLEO}$ - | $m_{impactor}$ *kg* |
|---|---|---|---|---|---|---|---|
| A | 0 | 840 | 7 | 120.0 | 180 | 0.5805 | 488 |
| B | 0 | 4990 | 29 | 172.1 | 4300 | 0.4821 | 2406 |
| C | 490 | 4830 | 8 | 603.8 | 130 | 0.1583 | 765 |
| D | 3290 | 2150 | 25 | 86.0 | 790 | 0.6930 | 2280 |
| E | 4450 | 2810 | 16 | 175.6 | 330 | 0.6201 | 2760 |

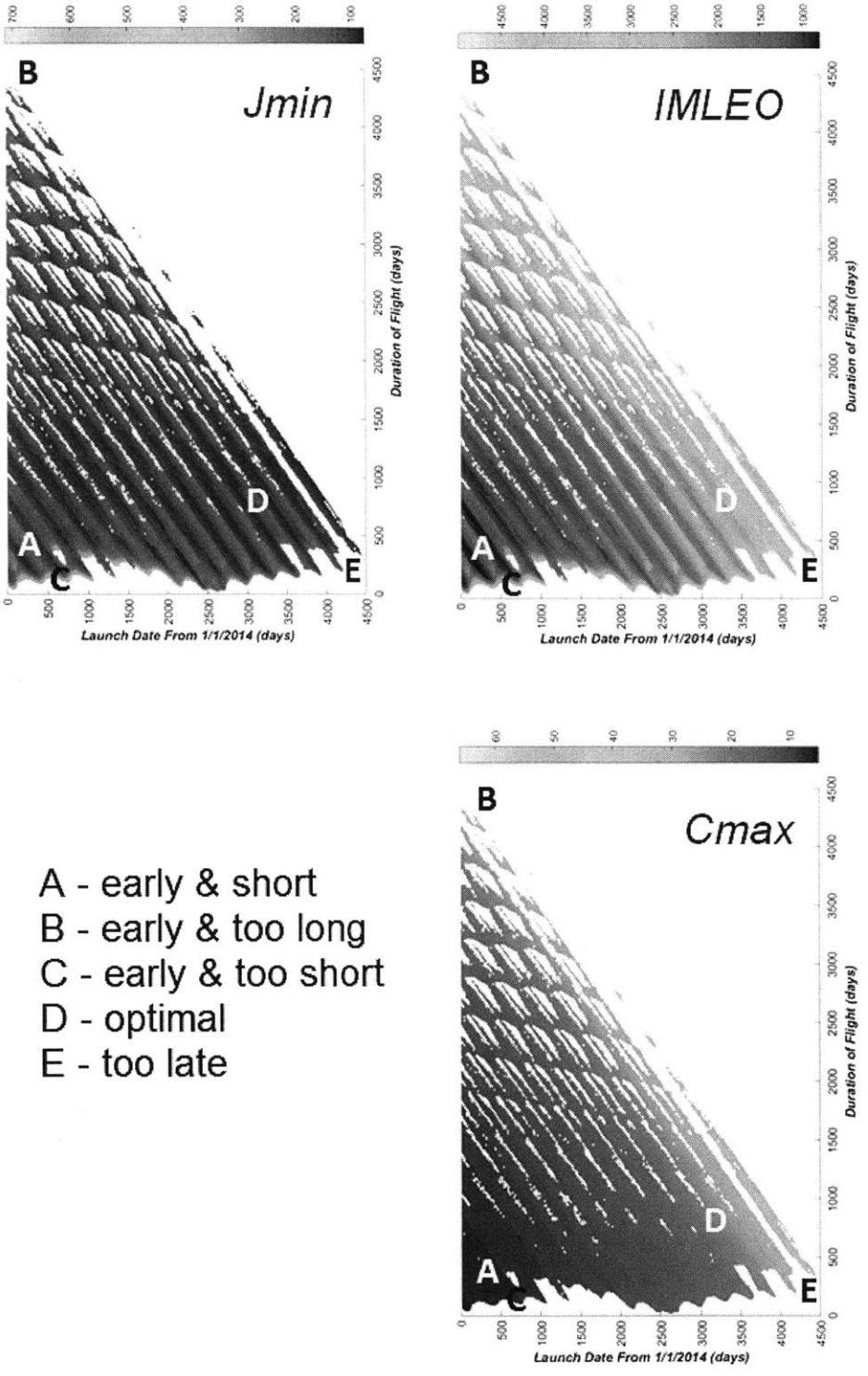


Figure 5-6: Location of five campaign architectures on carpet plots

Figure 5-7 illustrates a recommended procedures for interpreting these carpet plots. In the objective space, as depicted in Fig. 5-5 or the left bottom of Fig. 5-7, we first fix a launch date (1st arrow) and then identify the optimal duration of flight for the date (2nd arrow). By repeating this for each date, the objective can be plotted as a function of launch date, as shown in the left top of Fig. 5-7. The optimal flight time for each date is also used in the IMLEO space (Fig. 5-2 or Fig. 5-7 right bottom) as well as the $C_{max}$ space (Fig. 5-4 or Fig. 5-7 middle bottom) to plot the time history of the initial mass (middle top) and the robustness coefficient (right top). For the IMLEO, the longer we wait, the mass increases more. For robustness, the longer we wait, robustness increases also. The globally optimal $J$ is to wait about 3/4 of time, 3300 days since the epoch.

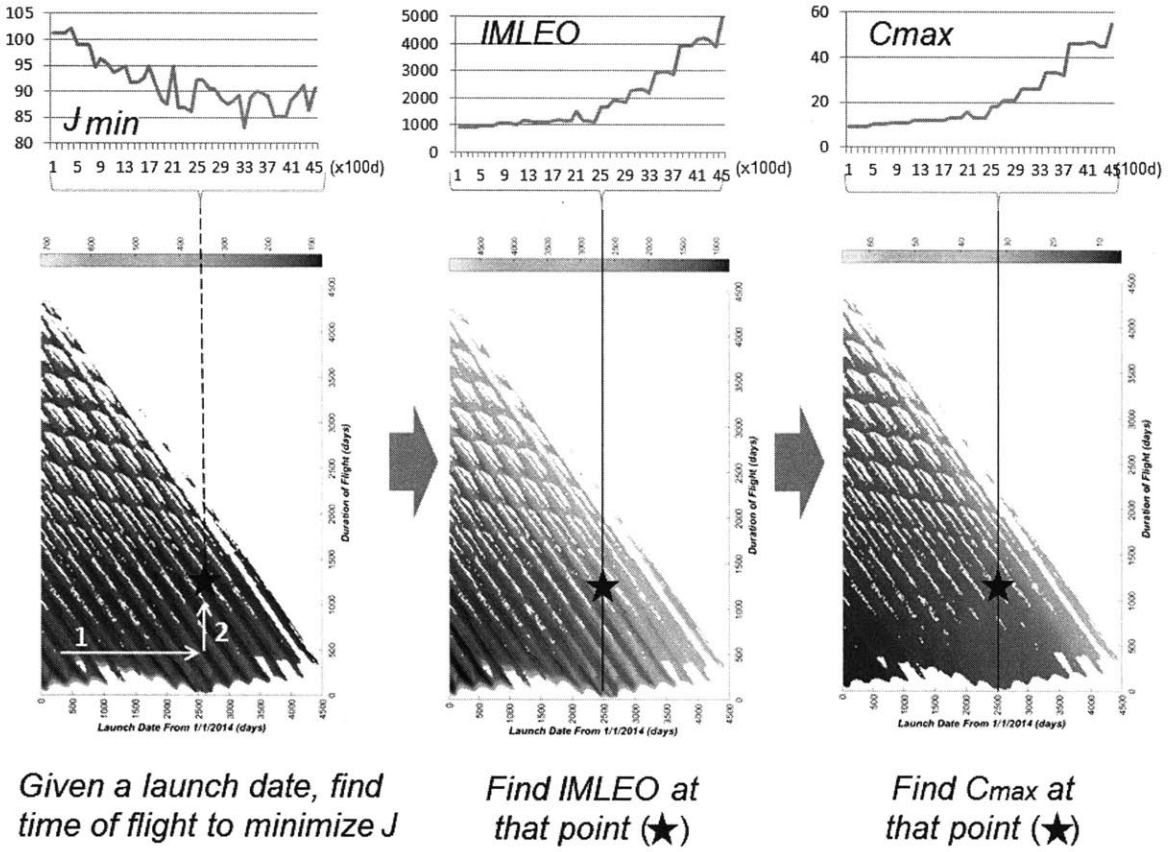


Figure 5-7: Interpretation of carpet plots for Type 0 campaigns

Algorithm 6 explains, once again, how to generate these plots and interpret them. For each launch date, we evaluate the objective $J$ for all possible time-of-flight values.[5] The results obtained from full-factorial combinations are saved in (launch date, time of flight, $J$) tuples, which are implemented as a two-dimensional array (matrix) in MATLAB.[6] After that, we find the minimum $J$ ($J_{min}$) and the corresponding duration of flight ($TOF_{min}$) for each launch date. By repeating this for every date, the time history of $J_{min}$ can be obtained, as shown in Fig. 5-8.

**Algorithm 6** Get time histories for $J$, IMLEO, and $C_{max}$

**procedure** CREATE–TIME–HISTORY
  **for** all launch dates ($\leftrightarrow$) **do**
    **for** all possible values for time (duration) of flight ($\updownarrow$) **do**
      Evaluate IMLEO and $C_{max}$
      Save (launch date, time of flight, IMLEO) tuple
      Save (launch date, time of flight, $C_{max}$) tuple
      Evaluate scalar objective $J$ =IMLEO/($C_{max}$+1)
      Save (launch date, time of flight, $J$) tuple
    **end for**
    Find the minimum $J$, $J_{min}$
    Find the time of flight that gives the minimum $J$, $TOF_{min}$
    Save (launch date, $J_{min}$) pair
    Find the IMLEO for $J_{min}$ from the (launch date, time of flight, IMLEO) tuple by substituting (time of flight) = $TOF_{min}$
    Save (launch date, IMLEO for $J_{min}$) pair
    Find the $C_{max}$ for $J_{min}$ from the (launch date, time of flight, $C_{max}$) tuple by substituting (time of flight) = $TOF_{min}$
    Save (launch date, $C_{max}$ for $J_{min}$) pair
  **end for**
**end procedure**

In this figure, the objective is minimized for each date, so the vertical axis is labeled as $J_{min}$ instead of $J$. The smallest of all $J_{min}$'s is the global minimum. If the launch date for the global optimum has not changed, we can wait for this most

[5]The maximum duration of flight decreases for later departures because the impactor must arrive before the set date of a keyhole passage.

[6]For example, the two-dimensional array can be represented as $J_{i,j}$ where $i$-th launch date is when $10i$ days have elapsed since an epoch of January 1, 2014 and the $j$-th time of flight has a duration of $10j$ days in this case. The tuple representation, used in other programming languages, is more generally defined using set theories. In ordered pairs notation, (launch date, time of flight) is associated with a corresponding $J$, generating an augmented pair or nested set, (launch date, time of flight, $J$).

optimal timing to initiate a deflection campaign. If the optimal launch date has already passed, there are still other promising dates with local minima, before the end of the overall time window. After the end of all solutions, there are no Type 0 campaign solutions, and we must resort to other types of campaigns.

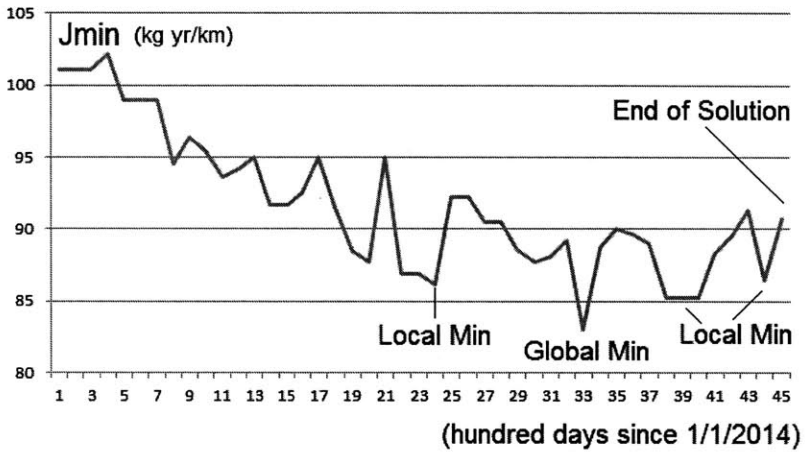


Figure 5-8: Time history of $J_{min}$ for Type 0 campaign (Apophis)

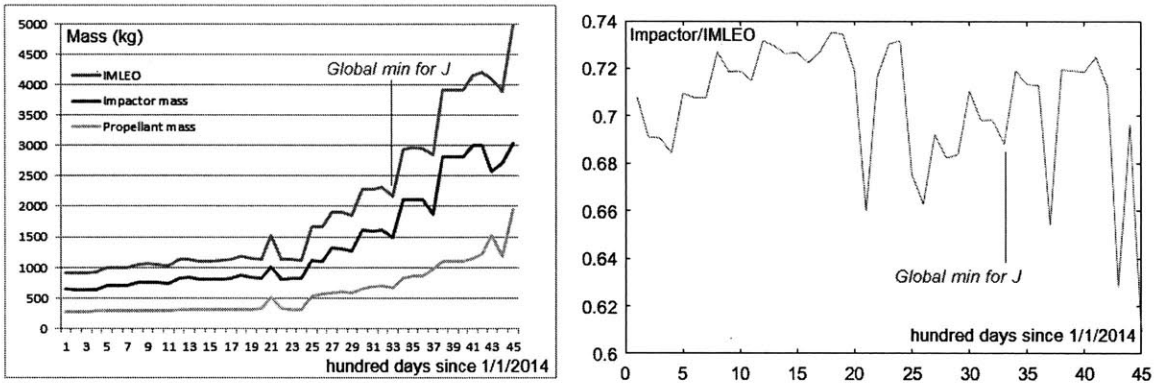


Figure 5-9: Time history of IMLEO, impactor mass, and their ratio corresponding to $J_{min}$ on each launch date

Similarly, we can generate the time histories of IMLEO and $C_{max}$ that give an optimal $J_{min}$ when combined. That is, $TOF_{min}$ may not minimize the IMLEO or maximize $C_{max}$ for a given launch date, but it does minimize their ratio in a balancing way. Figure 5-9 further breaks down the IMLEO into the impactor mass and the propellant mass. The ratio of the two shows a declining trend over time, requiring more propellant per impactor mass. This is because (1) faster trajectories are needed

for the closer we get to keyhole passage and (2) a heavier impactor is needed for a late impact than an early impact to achieve the same amount of deflection. It is also notable that the global minimum $J_{min}$ does not correspond to the minimum propellant mass. If the optimal launch date for the global minimum has not passed, we can simply wait until the optimal date to start a deflection campaign. What should be done if the optimal date has already passed? The next launch date corresponding to one of the local minima may be selected. However, this ad-hoc approach, starting from available design parameters (time vector), would produce a wide range of performance metrics. Is it possible to set our desired goals and derive the enabling designs backward?

- **Iso-performance**

One use of the previous plots and time histories is to identify "iso-performance" solutions that achieve the same level of performance (probability of success in this case) despite differing design details. Iso-performance is an inverse design method that starts from a desired vector of performance requirements and works backwards to identify acceptable solutions in the design space [109]. Figure 5-10 illustrates an example of iso-performing campaign configurations. In this figure, three configurations that have similar objective values (around 91) are presented. Therefore, they have iso-performance in their combined objective $J_{min}$ in addition to their probability of success. These configurations have different time-of-flight (TOF) values and varying numbers of revolutions around the Sun, leading to variation in their propellant mass ratios. Their impactor mass and IMLEO both increase as later launch dates (LD) are selected. Because their robustness coefficient values increase over time, the objective, which is the ratio between IMLEO and $(C_{max} + 1)$, remains constant.

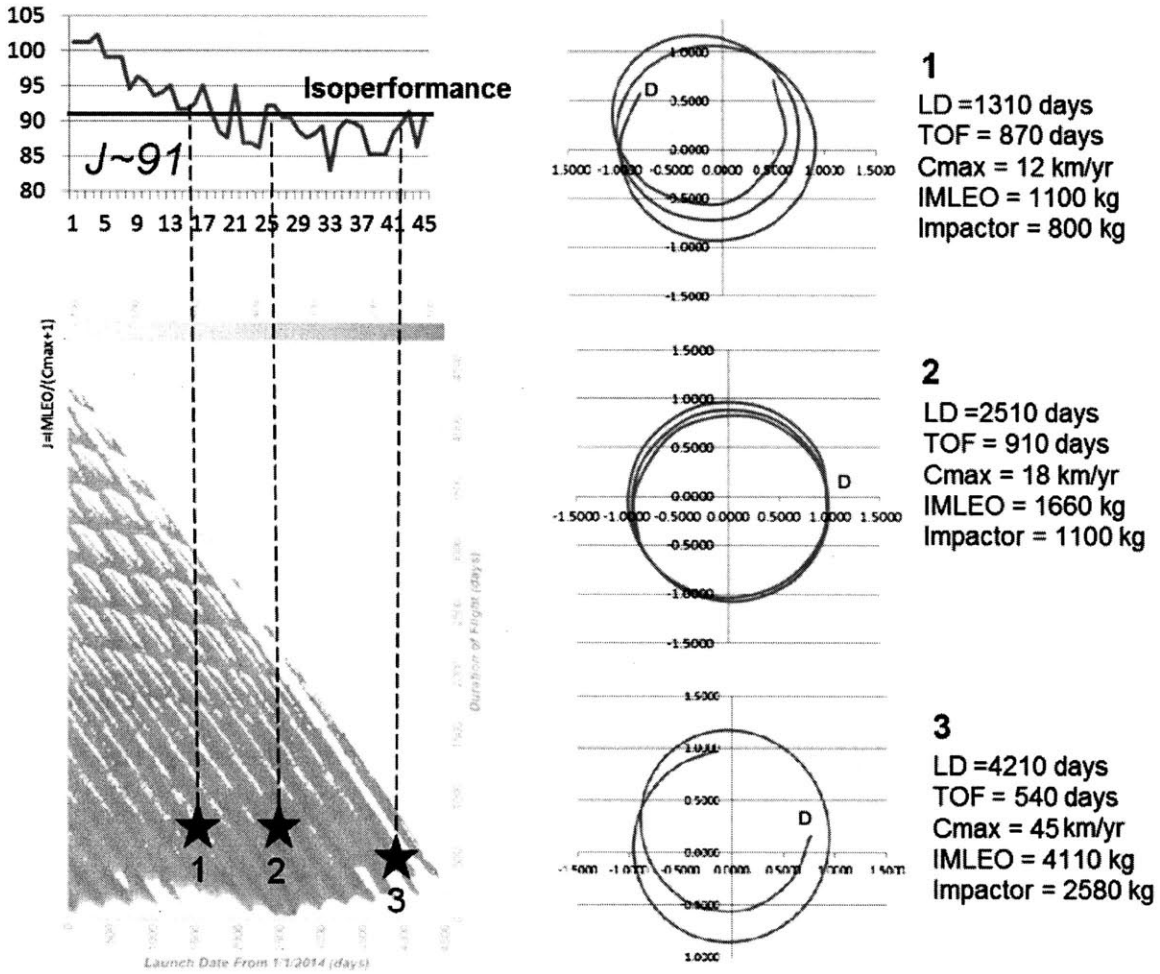


Figure 5-10: Iso-performance in Type 0 campaigns for Apophis 2029 keyhole deflection (Probability of Success = 0.9)

## 5.2 Type 1 Campaign

For a Type 1 campaign, a *carpet plot* cannot be obtained due to a higher dimensionality. In a Type 0 campaign, there is only one flight leg with an impactor. The launch date and the duration of flight can be drawn on a two-dimensional plot. However, a Type 1 campaign has a precursor and an impactor, and each of the two flight legs has its own launch date and duration of flight, resulting in a total of four variables. In a similar manner, a Type 2 campaign requires a total of six time variables. Generating two-dimmensional carpet plots for Type 1 and Type 2 campaigns is left for future work. Instead of the carpet plot, a genetic algorithm is used to find an optimal combination of variables. By searching for a set of optimal variations at each time step, a time history of the performance metric can be obtained, as shown in Fig. 5-11.

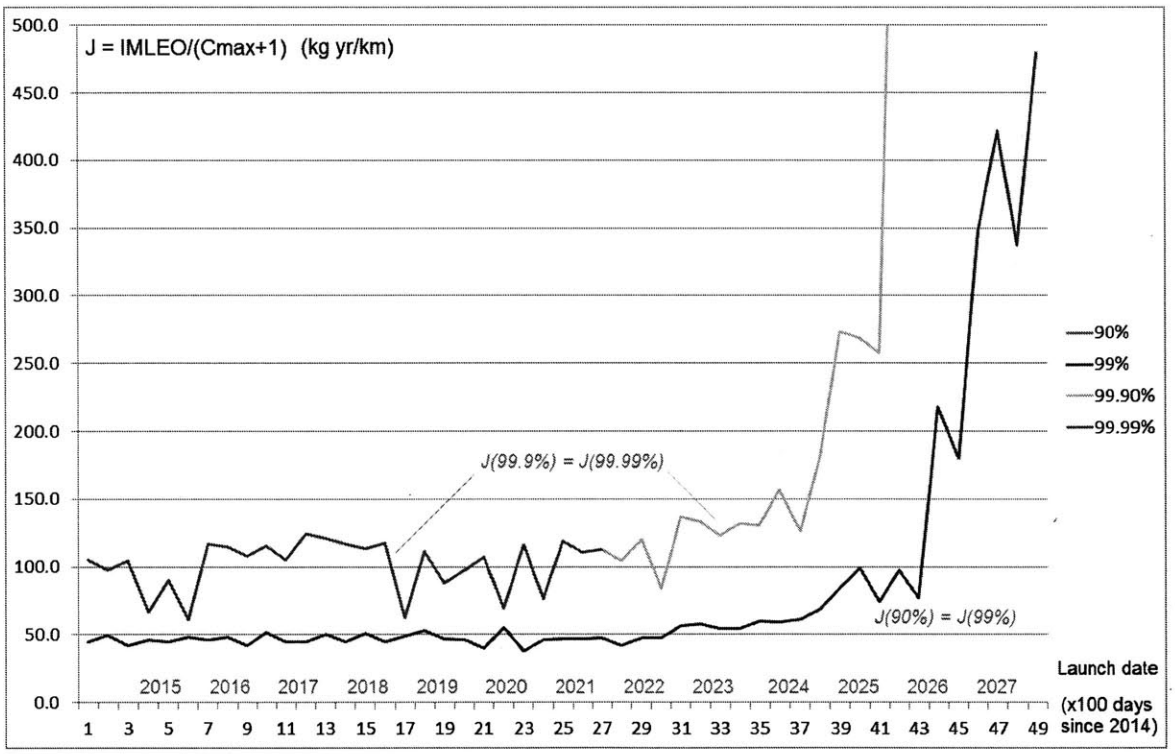


Figure 5-11: Type 1 performance for various reliability levels

In the figure above, the 90% graph and the 99% graph overlap on one another, and so do the 99.9% graph and the 99.99% graph. There are two possible explanations for this phenomenon. First, this could be an artifact of granularity parameters used in

Monte Carlo simulations. The volume of samples (10,000) may not be large enough to differentiate small differences in thresholds. However, because this is not the case for Type 2 campaigns, as will be shown later, the number of samples (resolution) does not explain everything. The second explanation to complement the first explanation is that the mechanism of how Type 1 campaigns work limits the reaction to small changes in the threshold. In a Type 1 campaign, only mass uncertainty is reduced, with $\beta$ uncertainty still remaining. This limits the ability of a Type 1 campaign to adjust its configuration, so its likelihood of success cannot easily follow the small changes in thresholds.

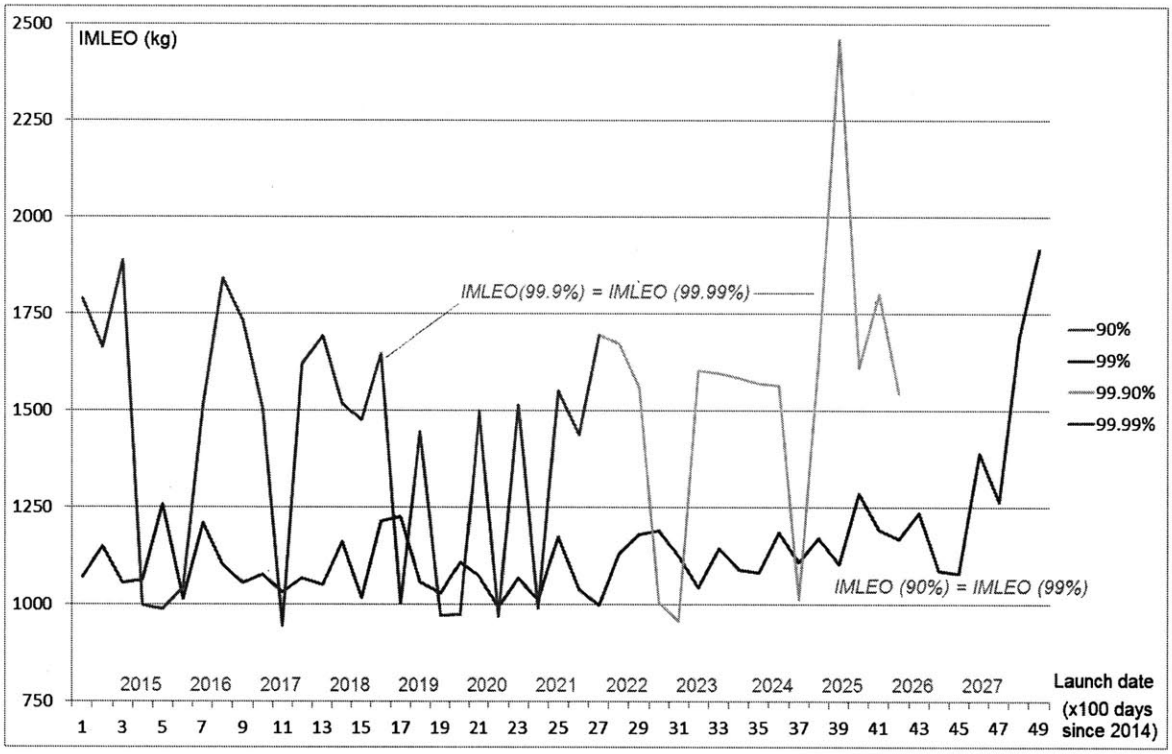


Figure 5-12: Type 1 IMLEO requirement for various reliability levels

Figure 5-12 shows how the IMLEO changes over time for different reliability requirements. As shown in the previous plot, the 90% IMLEO and the 99% IMLEO are identical, and the 99% IMLEO and the 99.99% IMLEO are the same. The IMLEO for achieving higher success probabilities is usually considerably higher mass than the IMLEO for lower success probabilities. However, there exist a few dates when this trend is reversed. However, these cases with lower IMLEO values should not be

misinterpreted as better-performing cases because the corresponding $C_{max}$ values are much smaller, resulting in higher overall ratios in the end. Figure 5-13 confirms the fact that $C_{max}$ values for higher thresholds are much smaller than $C_{max}$ values for lower thresholds, at least by a factor of two. The $C_{max}$ value for the thresholds of 99.9% and 99.99% reaches zero earlier than those for 90% and 99%. The robustness coefficient of zero means that the campaign cannot have a likelihood of success greater than the provided threshold. Therefore, the last launch date when 99.9% or 99.99% campaigns are feasible is earlier than the last date for 90% or 99%. In other words, we can guarantee a 99.99% success at a maximum until around 2028, but this guaranteed value decreases to 99% afterwards. After 2028, the 99% class campaigns also become impossible because the maximum possible likelihood of success goes below 90%. This is a "last minute" mission, only one year before keyhole passage.

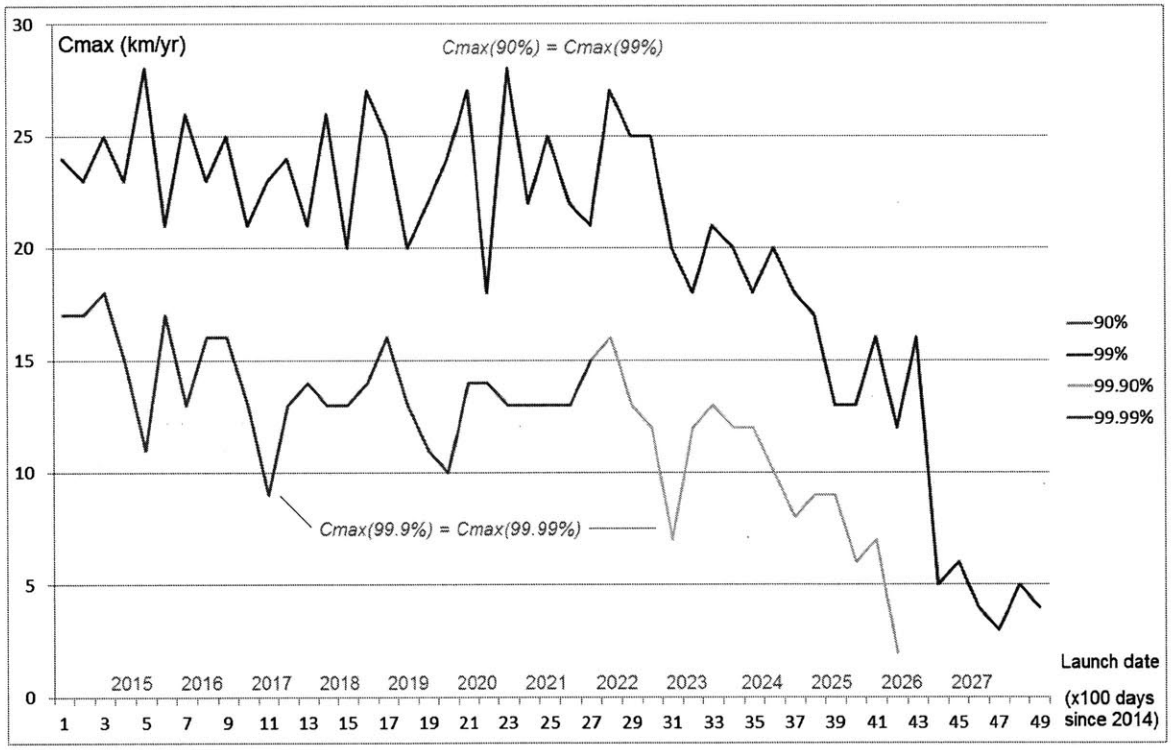


Figure 5-13: Type 1 robustness coefficient ($C_{max}$) for various reliability levels

To obtain a campaign solution after 2028, at least one of the following requirements should be relaxed: (1) the maximum limit for the impactor and or propulsion system capability mass and/or (2) the minimum threshold for the likelihood of success. The

former is set to be 5,000 kg, so the launch date for a Type 0 campaign may be extended if this limit is increased. Otherwise, we would have to accept the decreased likelihood of success, which is below the threshold requirement.

## 5.3 Type 2 Campaign

Similar to a Type 1 case, a *carpet plot* cannot be obtained for a Type 2 campaign. Therefore, we minimize the objective ($J$) at each launch date to obtain the time histories of the minimum objective ($J_{min}$), the system mass (IMLEO), and the robustness coefficient ($C_{max}$). The time histories for Type 2 campaigns are presented in the same order as Type 1 campaigns: $J_{min} \rightarrow$ IMLEO $\rightarrow C_{max}$. Figure 5-14 illustrates the time history of $J_{min}$. When compared with the robustness coefficient for Type 1 campaigns (Fig. 5-11), two main differences can be observed.

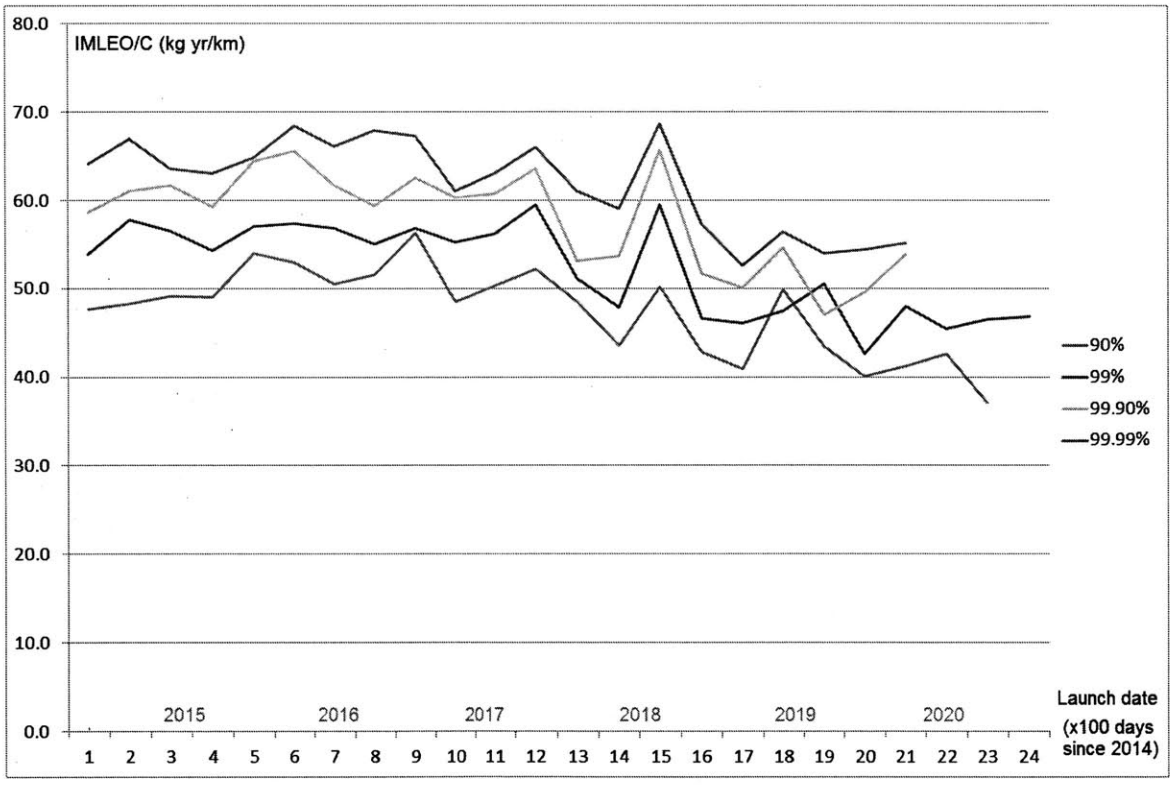


Figure 5-14: Type 2 objective ($J_{min}$) for various reliability levels

First, the $J_{min}$ values for Type 2 exhibit a decreasing trend over time, contrary to the $J_{min}$ values for Type 1 that increase over time. In Type 1 campaigns, the $\beta$ uncertainty is unchanged after the mass uncertainty is reduced, so the robustness coefficient decreases for later launch dates as the safe harbor gets narrower. Furthermore, the system mass increases as the impactor mass increases for later launch dates. Figure 5-15 illustrates how (1) the growth of impactor mass (numerator) and (2) the decline of robustness coefficient (denominator) work together in increasing their ratios. In fact, the former effect is small, if not zero, as demonstrated in the magnitude of slope in the impactor mass plot. However, even this small growth of impactor mass does decrease the remaining width margin of the safe harbor that was small to begin with; i.e., small decrements in a small entirety can yield a non-negligible decreasing trend. When the system mass sharply increases later (Fig. 5-12, red), the robustness coefficient drops to near zero (Fig. 5-13, red), marking the end of feasible campaign solutions. Mathematically, the time derivative of the objective function $J_{min}$ is expressed by

$$\frac{dJ_{min}}{dt} = \frac{d}{dt}\left(\frac{m}{C+1}\right) = \frac{(C+1)\frac{dm}{dt} - m\frac{d(C+1)}{dt}}{(C+1)^2} \tag{5.1}$$

where $m$ signifies the IMLEO and $C$ is short for $C_{max}$. As the impact mass increases slowly, $\frac{dm}{dt}$ will have a small positive value. The value of $\frac{d(C+1)}{dt} = \frac{dC}{dt}$ will be non-positive, making the numerator of Eq. 5.1, and hence the overall fraction, always positive. Then, what happens in Type 2 campaigns? As can be seen in Fig. 5-16, unlike Type 1, the reinforcements between the system mass and $C_{max}$ in Type 2 work in such a way that $J_{min}$ improves over time. The main impactor mass is not adjustable but fixed to a value that is the same as the preliminary impactor mass. In future work, the main impactor mass could be chosen by the optimizer. The current framework uses a constant impactor mass (500 kg), so the system mass fluctuates, depending upon the mass ratio, which is governed by trajectory conditions at a given launch date. Figure 5-17 illustrates that the system mass decreases from mid-2017 on and flattens out towards the end.

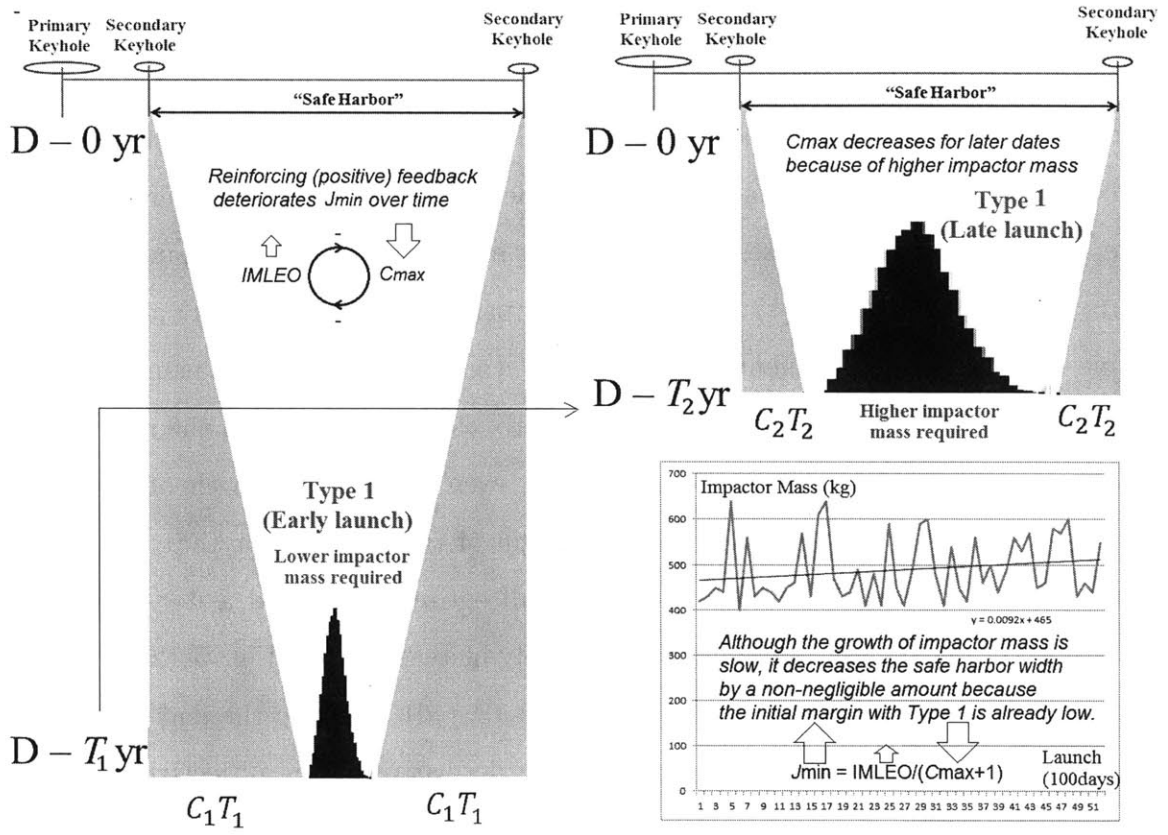


Figure 5-15: Behavior of Type "1" campaigns, revisited (not to scale)

As for $C_{max}$, it increases over time, which is a completely opposite trend compared to Type 1 campaigns. Because the deflection distribution of Type 2 is much narrower than the distribution of Type 1, the safe harbor has an ample width margin when a Type 2 campaign is used. The improvement of $J_{min}$ in Type 2 campaigns over time is accomplished by the optimizer, which delays the arrival date of the main impactor as late (close to keyhole passage) as possible, for each launch date. However, if the main impactor's arrival at a target asteroid is too late and close to its keyhole passage, that campaign solution has to be discarded for the following reasons. A Type 2 campaign determines the asteroid's $\beta$ by conducting multiple collision experiments (each with a 500 kg impactor) to collect sample values and reduce statistical variations. It takes time to determine the $\beta$ value after the main impactor's collision, so there should be a time buffer between the main impactor's collision and the keyhole passage. If the final $\beta$ value, inferred from the preliminary impactor's collision and the main impactor's

collision, suggests that the asteroid cannot make it into a safe harbor, an additional fine-tuning stage might also be required. Due to these reasons, the solutions whose main impact date is less than 5 years away from the keyhole passage are filtered out during post-processing. This time buffer for assimilating information and handling contingencies is required only in Type 2 campaigns, whose impactor mass cannot be adjusted. Type 1 campaigns do not require sampling of $\beta$ values and are able to adjust the impactor mass in accordance with the results from a one-time asteroid mass measurement, so this kind of "cooling time" is unnecessary. This duration (5 years) may be changed in future work for sensitivity analysis.

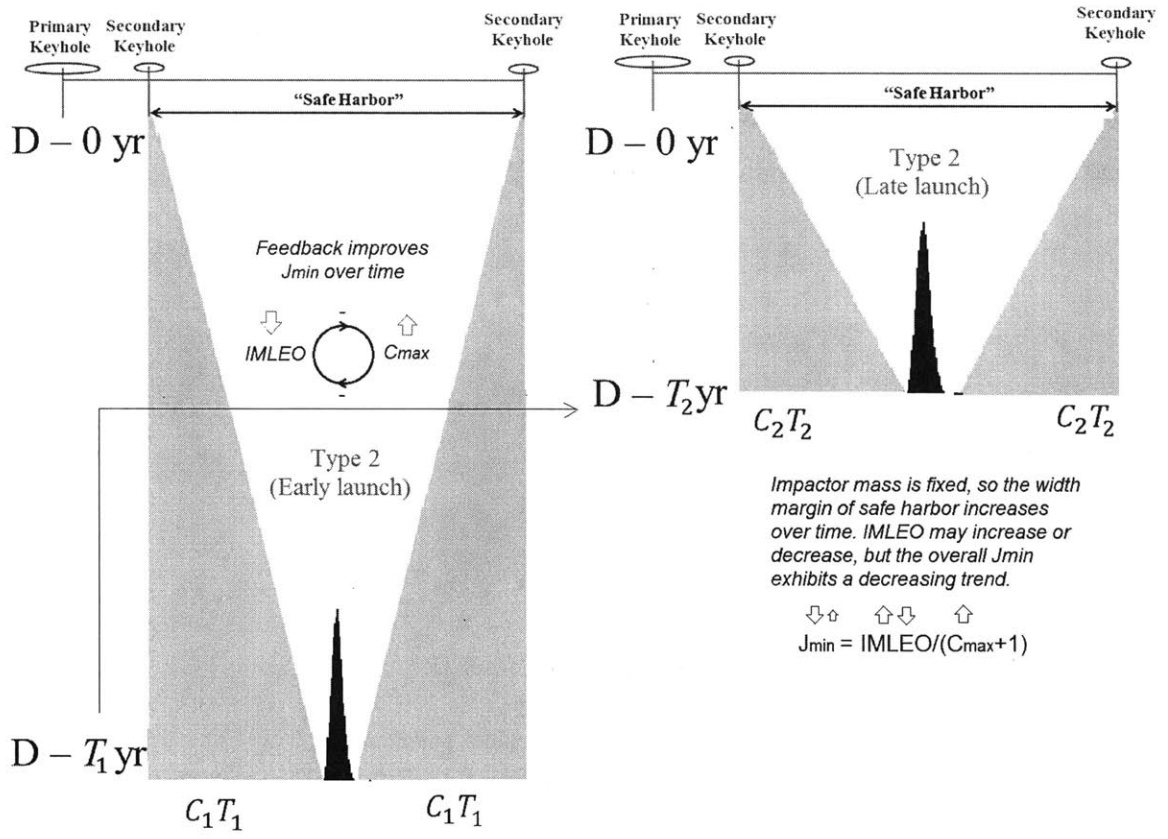


Figure 5-16: Behavior of Type 2 campaigns (not to scale)

Figure 5-17 depicts how the system mass of Type 2 campaigns varies over time. Different reliability thresholds separate the IMLEO curves well, which are clustered and move together. They all increase at the beginning of 2014, hit a maximum in 2015 or 2016, and start decreasing in mid-2017, and then plateau afterwards. Because the preliminary impactor mass and the main impactor mass are both fixed, this IMLEO variation is purely due to the changing of a mass ratio (epsilon), which divides the impactor mass in IMLEO=$m_{impactor}/\epsilon$. The robustness coefficient curves, illustrated in Fig. 5-18, show a much clearer stratification according to the reliability threshold levels, where the value of $C_{max}$ is higher when the threshold level is lower. The sign of $\frac{dC}{dt}$ is mostly positive, and the sign of $\frac{dm}{dt}$ is undetermined in Eq. 5.1, but its numerator $(C+1)\frac{dm}{dt} - m\frac{d(C+1)}{dt}$ is mostly negative. This is because the changes in $C$, multiplied by $m$ (several thousand [kg]), have much larger effects than the changes in $m$ that are weighted with $C$ (several dozen [km/yr]).

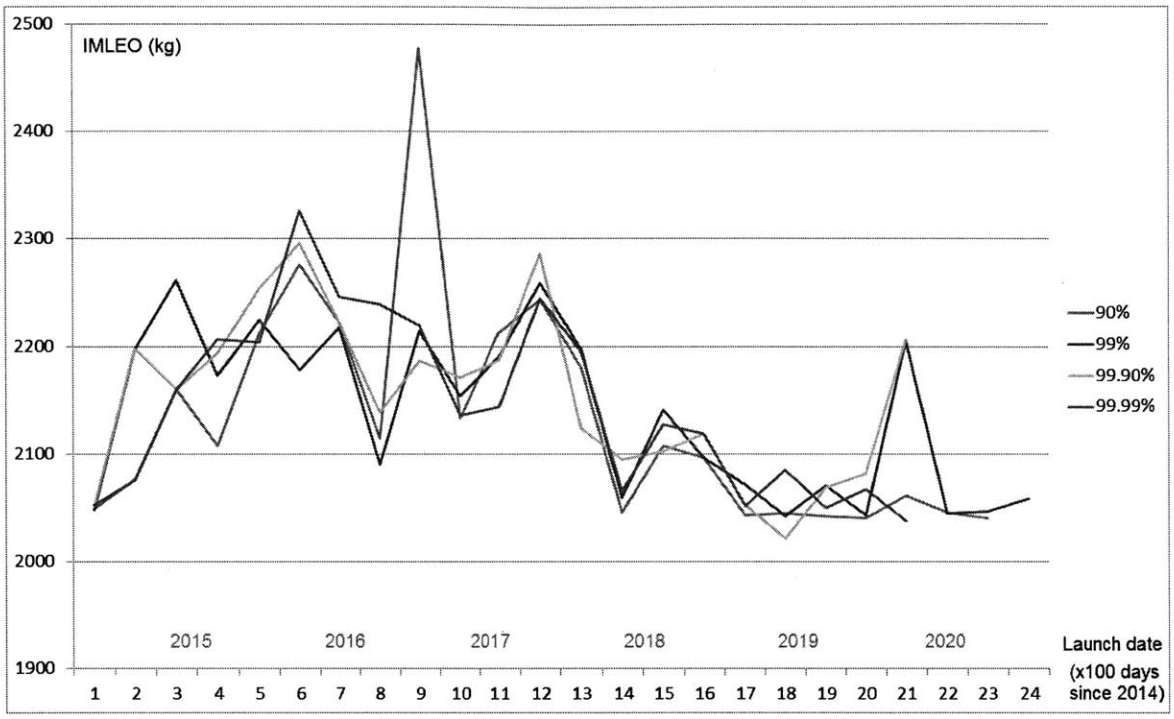


Figure 5-17: Type 2 mass (IMLEO) for various reliability levels

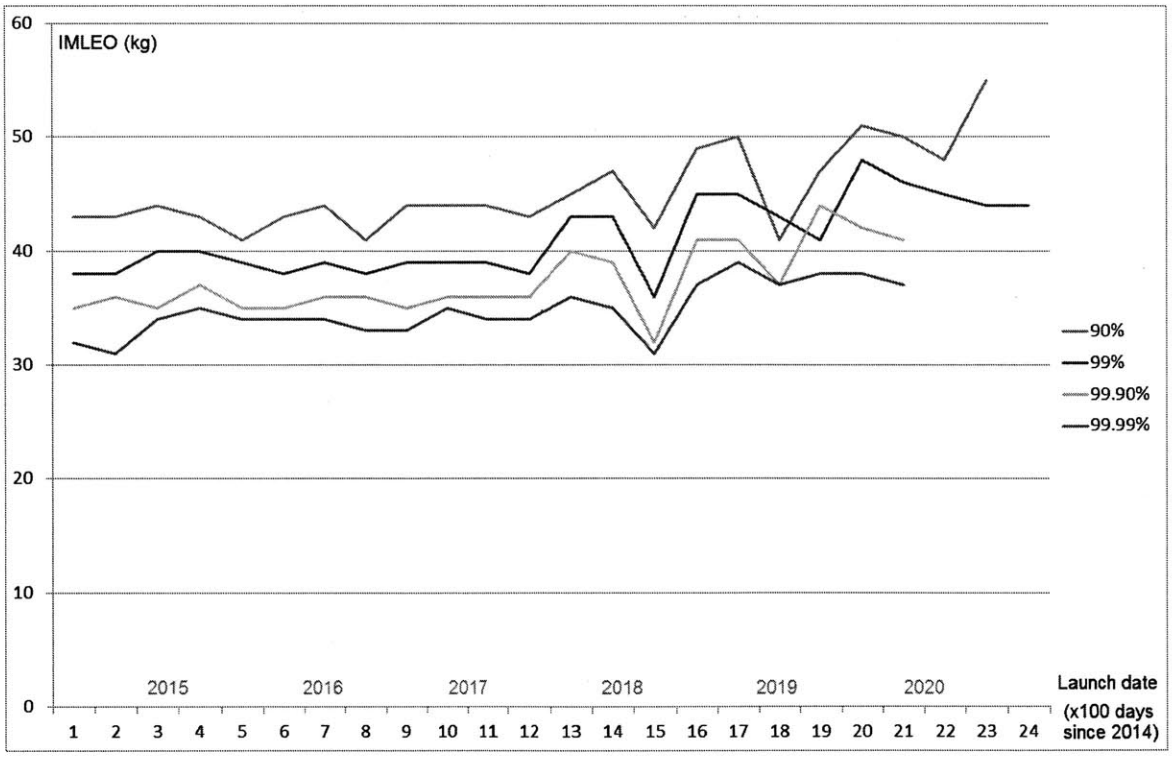


Figure 5-18: Type 2 robustness coefficient ($C_{max}$) for various reliability levels

## 5.4 Decision Map

Decision maps, the final deliverable of the ADIEU framework, are created by assimilating information obtained from carpet plots and time histories. To meet a wide variety of decision-making requirements, two types of decision maps are proposed: Type S for a single option and Type M for multiple options. As will be shown in this chapter and the next chapter, decision maps can look considerably different even between asteroids with relatively similar parameters. Decision maps are powerful visualization tools for its user to (1) understand the uncertainty characteristics of an asteroid and (2) communicate single/multiple strategies with stakeholders.

### 5.4.1 Type S Map

Figure 5-19 summarizes the optimization results of all types of campaigns. The horizontal axis shows launch dates in terms of how many days have elapsed since January 1, 2014. The time span of 5500 days is analyzed before the keyhole passage on Apr 13, 2029: with 100 day intervals, 55 grid points are generated. The vertical axis shows different levels for the likelihood of success. As the likelihood threshold increases, the greater portion of a deflected distance distribution must be included within the safe harbor, which is more difficult to satisfy and may necessitate campaign planning with more sophisticated precursors.

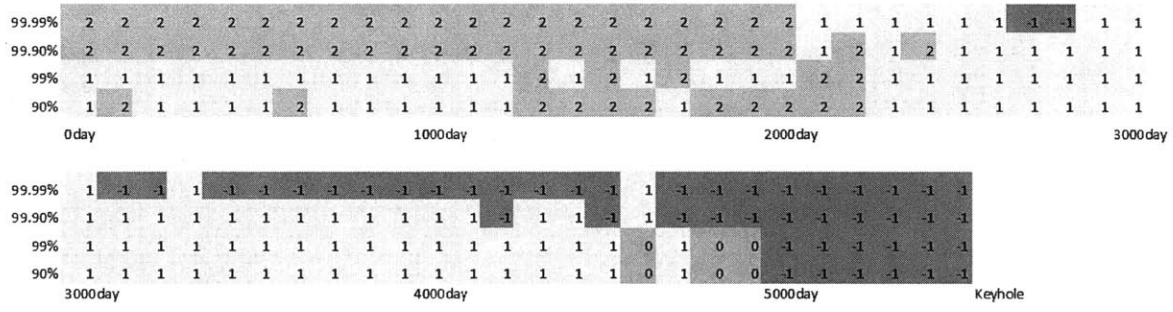


Figure 5-19: "S-Type" decision map of Apophis (single option with the lowest $J_{min}$)

Therefore, it is intuitive that Type 2 campaigns are dominant for higher thresholds that require more robustness. Indeed, a Type 2 strategy is required to meet the highest POS requirement for early launches, as demonstrated by green region marked

with "2" at 99.9% and 99.99%, from day 0 to day 2,000. For lower thresholds, Type 1 campaigns with a fewer precursor number and low precursor mass are cost-effective solutions (yellow region marked with "1"). This suggests that for lower levels of mssion success (90% and 99%), Type 1 campaigns (a "Hayabusa"-like remote sensing first, followed by a main impactor using precursor information) are optimal up to about launch daty 4,500. As time passes, Type 1 campaigns take over all range of threshold levels because Type 2 campaigns are only feasible for earlier launch dates. After 5,000 days there is no feasible solution (red region marked with "-1"). This infeasible region begins earlier for the highest POS reqruiement (99.99%), as early as fom 3,000 days. Type 0 campaigns have a very small window of application during the transition between Type 1 campaigns and no feasible solution (between 4,500 days and 5,000 days) but cannot achieve high POS due to their "single-shot" nature.

### 5.4.2 Type M Map

A Type M map graphically depicts *multiple* campaign options ($\mathbf{x}$) that yield non-dominated performance in criterion space ($\mathbf{J}$). Let $\mathbf{J^1} = \mathbf{J}(\mathbf{x_1})$ and $\mathbf{J^2} = \mathbf{J}(\mathbf{x_2})$ be two objective (criterion) vectors for a minimization problem, $min_{\mathbf{x}}\mathbf{J}(\mathbf{x})$, where $\mathbf{J} = \begin{bmatrix} J_1 & J_2 & \dots & J_n \end{bmatrix}^T$. Then $\mathbf{J^1}$ *weakly dominates* $\mathbf{J^2}$ if and only if $\mathbf{J^1} \leq \mathbf{J^2}$ and $\mathbf{J^1} \neq \mathbf{J^2}$.[7] Also, $\mathbf{J^1}$ *strongly dominates* $\mathbf{J^2}$ if and only if $\mathbf{J^1} < \mathbf{J^2}$.[8] As shown in Fig. 5-20, the objective vector $\mathbf{J}$ has two elements, $J_1$ and $J_2$. In the ADIEU framework, we want to minimize IMLEO and maximize $C_{max}$, which yields $J_1$ = IMLEO and $J_2 = -C_{max}$.

If we have multiple objective vectors, $\mathbf{J^1} = \mathbf{J}(\mathbf{x_1})$ through $\mathbf{J^n} = \mathbf{J}(\mathbf{x_n})$, we can determine whether any one of them strongly (weakly) dominates the others by examining the following extended condition:

$$\mathbf{J^i} < \mathbf{J^j} (or \mathbf{J^i} \leq \mathbf{J^j}), j \in \{1, ..., n\}, j \neq i \tag{5.2}$$

[7] More precisely, $J_i^1 \leq J_i^2 \ \forall i$ and $J_i^1 < J_i^2$ for at least one $i$.
[8] More precisely, $J_i^1 < J_i^2 \ \forall i$.

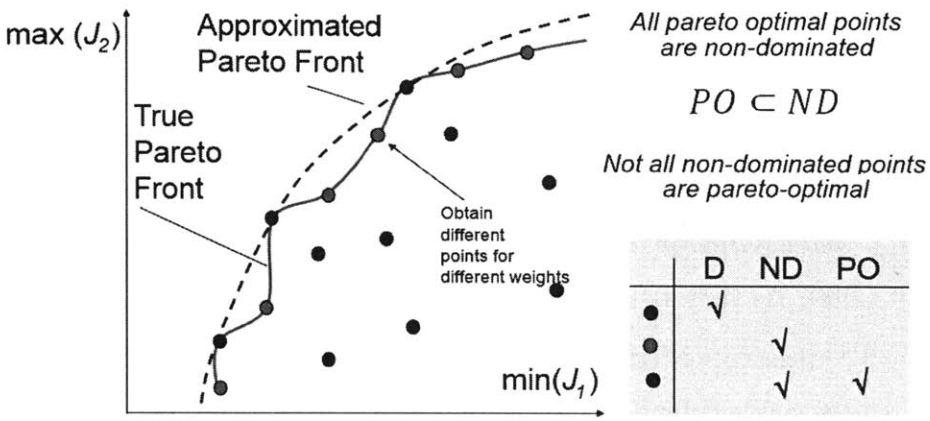


Figure 5-20: Pareto optimality and non-dominance [39]

These vectors are usually generated with a *weighted sum* approach, where the vector **J** is scalarized into $J_{scalar} = \lambda J_1 + (1 - \lambda)J_2$ $(0 \leq \lambda \leq 1)$ for a bi-objective optimization problem. By non-dimensionalizing J elements in terms of their upper and lower bounds and imposing extra constraints, we can obtain a smoother Pareto front. This technique is called adaptive weighted sum (AWS) [110], whose application is beyond the scope of this thesis. We pick only one solution per campaign type, so at most three solutions will be compared against one another in each case (cell) in Fig. 5-21.

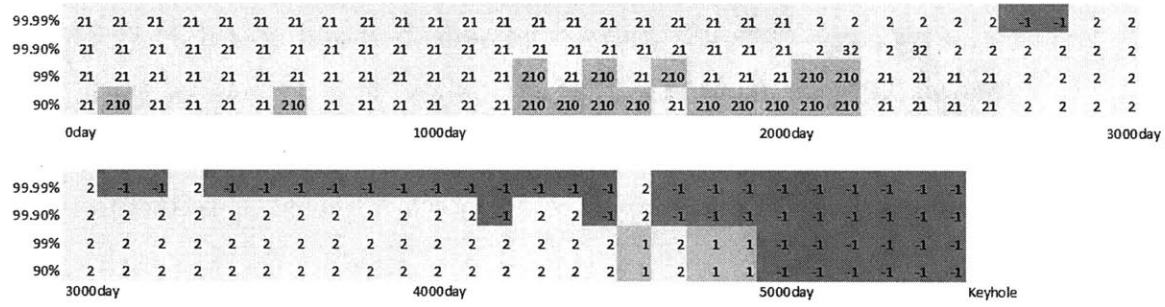


Figure 5-21: "M-Type" decision map of apophis (multiple non-dominated options)

For early launch dates, Type 1 and Type 2 are non-dominated. There are some cases between 1,000 days and 2,000 days when all three campaign types are non-dominated. After that, the map is identical with a single-option map as the number of available options decreases. Figure 5-22 shows a transposed (upright) version of the Type S decision map (left) and the Type M decision map (right).

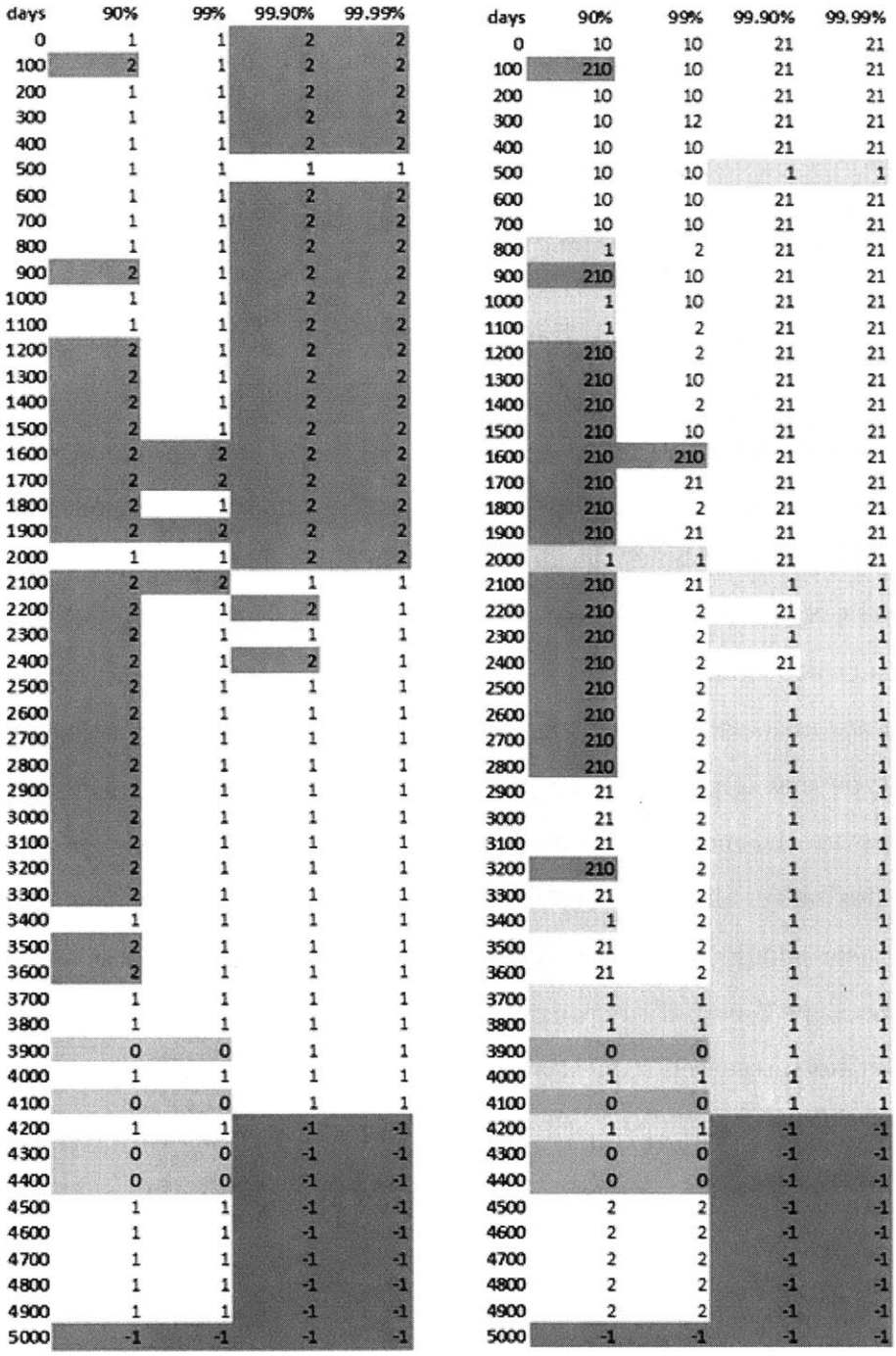

| days | 90% | 99% | 99.90% | 99.99% |
|---|---|---|---|---|
| 0 | 1 | 1 | 2 | 2 |
| 100 | 2 | 1 | 2 | 2 |
| 200 | 1 | 1 | 2 | 2 |
| 300 | 1 | 1 | 2 | 2 |
| 400 | 1 | 1 | 2 | 2 |
| 500 | 1 | 1 | 1 | 1 |
| 600 | 1 | 1 | 2 | 2 |
| 700 | 1 | 1 | 2 | 2 |
| 800 | 1 | 1 | 2 | 2 |
| 900 | 2 | 1 | 2 | 2 |
| 1000 | 1 | 1 | 2 | 2 |
| 1100 | 1 | 1 | 2 | 2 |
| 1200 | 2 | 1 | 2 | 2 |
| 1300 | 2 | 1 | 2 | 2 |
| 1400 | 2 | 1 | 2 | 2 |
| 1500 | 2 | 1 | 2 | 2 |
| 1600 | 2 | 2 | 2 | 2 |
| 1700 | 2 | 2 | 2 | 2 |
| 1800 | 2 | 1 | 2 | 2 |
| 1900 | 2 | 2 | 2 | 2 |
| 2000 | 1 | 1 | 2 | 2 |
| 2100 | 2 | 2 | 1 | 1 |
| 2200 | 2 | 1 | 2 | 1 |
| 2300 | 2 | 1 | 1 | 1 |
| 2400 | 2 | 1 | 2 | 1 |
| 2500 | 2 | 1 | 1 | 1 |
| 2600 | 2 | 1 | 1 | 1 |
| 2700 | 2 | 1 | 1 | 1 |
| 2800 | 2 | 1 | 1 | 1 |
| 2900 | 2 | 1 | 1 | 1 |
| 3000 | 2 | 1 | 1 | 1 |
| 3100 | 2 | 1 | 1 | 1 |
| 3200 | 2 | 1 | 1 | 1 |
| 3300 | 2 | 1 | 1 | 1 |
| 3400 | 1 | 1 | 1 | 1 |
| 3500 | 2 | 1 | 1 | 1 |
| 3600 | 2 | 1 | 1 | 1 |
| 3700 | 1 | 1 | 1 | 1 |
| 3800 | 1 | 1 | 1 | 1 |
| 3900 | 0 | 0 | 1 | 1 |
| 4000 | 1 | 1 | 1 | 1 |
| 4100 | 0 | 0 | 1 | 1 |
| 4200 | 1 | 1 | -1 | -1 |
| 4300 | 0 | 0 | -1 | -1 |
| 4400 | 0 | 0 | -1 | -1 |
| 4500 | 1 | 1 | -1 | -1 |
| 4600 | 1 | 1 | -1 | -1 |
| 4700 | 1 | 1 | -1 | -1 |
| 4800 | 1 | 1 | -1 | -1 |
| 4900 | 1 | 1 | -1 | -1 |
| 5000 | -1 | -1 | -1 | -1 |

| days | 90% | 99% | 99.90% | 99.99% |
|---|---|---|---|---|
| 0 | 10 | 10 | 21 | 21 |
| 100 | 210 | 10 | 21 | 21 |
| 200 | 10 | 10 | 21 | 21 |
| 300 | 10 | 12 | 21 | 21 |
| 400 | 10 | 10 | 21 | 21 |
| 500 | 10 | 10 | 1 | 1 |
| 600 | 10 | 10 | 21 | 21 |
| 700 | 10 | 10 | 21 | 21 |
| 800 | 1 | 2 | 21 | 21 |
| 900 | 210 | 10 | 21 | 21 |
| 1000 | 1 | 10 | 21 | 21 |
| 1100 | 1 | 2 | 21 | 21 |
| 1200 | 210 | 2 | 21 | 21 |
| 1300 | 210 | 10 | 21 | 21 |
| 1400 | 210 | 2 | 21 | 21 |
| 1500 | 210 | 10 | 21 | 21 |
| 1600 | 210 | 210 | 21 | 21 |
| 1700 | 210 | 21 | 21 | 21 |
| 1800 | 210 | 2 | 21 | 21 |
| 1900 | 210 | 21 | 21 | 21 |
| 2000 | 1 | 1 | 21 | 21 |
| 2100 | 210 | 21 | 1 | 1 |
| 2200 | 210 | 2 | 21 | 1 |
| 2300 | 210 | 2 | 1 | 1 |
| 2400 | 210 | 2 | 21 | 1 |
| 2500 | 210 | 2 | 1 | 1 |
| 2600 | 210 | 2 | 1 | 1 |
| 2700 | 210 | 2 | 1 | 1 |
| 2800 | 210 | 2 | 1 | 1 |
| 2900 | 21 | 2 | 1 | 1 |
| 3000 | 21 | 2 | 1 | 1 |
| 3100 | 21 | 2 | 1 | 1 |
| 3200 | 210 | 2 | 1 | 1 |
| 3300 | 21 | 2 | 1 | 1 |
| 3400 | 1 | 2 | 1 | 1 |
| 3500 | 21 | 2 | 1 | 1 |
| 3600 | 21 | 2 | 1 | 1 |
| 3700 | 1 | 1 | 1 | 1 |
| 3800 | 1 | 1 | 1 | 1 |
| 3900 | 0 | 0 | 1 | 1 |
| 4000 | 1 | 1 | 1 | 1 |
| 4100 | 0 | 0 | 1 | 1 |
| 4200 | 1 | 1 | -1 | -1 |
| 4300 | 0 | 0 | -1 | -1 |
| 4400 | 0 | 0 | -1 | -1 |
| 4500 | 2 | 2 | -1 | -1 |
| 4600 | 2 | 2 | -1 | -1 |
| 4700 | 2 | 2 | -1 | -1 |
| 4800 | 2 | 2 | -1 | -1 |
| 4900 | 2 | 2 | -1 | -1 |
| 5000 | -1 | -1 | -1 | -1 |

Figure 5-22: Decision Maps of Apophis (Single Option and Multiple Options)

The M-type decision map shows which set of asteroid deflection campaigns (Type 0, 1, 2, or -1 for none) are available for each combination of POS and initial launch date. A general trend is that the longer we wait, the fewer non-dominated campaign options make sense. Also, the more strongest the POS level, the fewer options are available.

## 5.5 Chapter Summary

This chapter applied the ADIEU framework to asteroid Apophis, whose keyhole passage in 2029 should be avoided. Although the possiblity of 2029 keyhole passage has been ruled out in reality, considering this virtual problem provides much insight. Type S and Type M decision maps can be used in different situations. If we have clear-cut requirements about the deflection schedules and the required probability of success (POS) level, reading out the corresponding cell in a Type S map would give the exact solution. On the other hand, if the program schedule and the POS requirment are uncertain, Type M can be used to identify the most widely applicable campaign type that appears the most frequently across the table. For example, Type 1 campaigns are the most prevalent in the Type M map and should be used for the maximum flexibility, although Type 2 campaigns are equally prevalent in the Type S map. A user should confer the Type M map if the programmatic uncertainty is high and the Type S map if the programmatic uncertainty is low. These two decision maps answer both research requestions raised in the introduction: (1) Should we use a precursor? (Type 0 vs Type 1/2); (2) Which precursor should we use? (Type 1 vs Type 2).

# Chapter 6

# Case 2: Bennu Results

Following the previous chapter, this chapter presents the results obtained by applying the ADIEU framework to deflection campaigns for the asteroid 101795 Bennu (1999 $RQ_{36}$). On the Sentry List, 99942 Apophis and 101955 Bennu are among the highest-ranked in the Palermo Technical Impact Hazard Scale: Apophis is the 6th highest and Bennu is the 2nd highest, as of March 15th 2016. They belong to different minor planet categories in terms of orbit classification. Apophis is an Aten asteroid with a semi-major axis less than 1 AU, and Bennu is an Apollo asteroid with a semi-major axis greater than 1 AU.[1] Other orbital elements in the heliocentric frame, excluding the semi-major axis, are rather similar: Bennu has a slightly higher inclination than Apophis, but both have similar eccentricity values. As shown in Table 6.1, their mass and physical characteristics are very similar, which generate similar-looking deflection curves in combination with commonalities in orbit parameters, as seen in Fig. 6-1. These deflection characteristic curves illustrate how much an asteroid can be deflected with a unit mass (kg) of an impactor capable of imparting set values of delta-v.[2] For comparison, the curve for 2011 AG5 is also plotted, which depicts how its large eccentricity (0.4) breaks the sinusoidal symmetry and causes upward-pointing spikes. This probably means that a carpet plot for 2011 AG5 would have more irregular features, which is left for future work.

[1] Both categories cross the Earth's orbit. See Appendix A for more categories.

[2] For the velocity change of an asteroid, a value of dv=0.37 $\mu$ m/s is used in this thesis.

| Parameter | Symbol | Apophis | Bennu | Unit |
|---|---|---|---|---|
| **Orbital Characteristics** | | | | |
| Semi-major axis | $a$ | 0.92228 | 1.1264 | AU |
| Eccentricity | $e$ | 0.19108 | 0.20375 | - |
| Inclination | $i$ | 3.33129 | 6.0349 | deg |
| Longitude of ascending node | $\Omega$ | 204.45719 | 2.0609 | deg |
| Mean anomaly | $M$ | 215.53998 | 101.7039 | deg |
| Argument of perihelion | $\omega$ | 126.39364 | 66.2231 | deg |
| Orbital period | $P$ | 323.513 | 436.649 | days |
| | | (0.89) | (1.20) | (yr) |
| Earth MOID | | 0.00066 | 0.00322 | AU |
| | | (99,000) | (482,000) | km |
| **Physical Characteristics** | | | | |
| Mean diameter | | 325±15 | 490±20 | m |
| Equatorial diameter | | | 550±20 | m |
| Bulk density | | 3.2±0.2 | | $g/cm^3$ |
| Solidity | | 0.72±0.24 | | |
| Mean density | | 2.30 | 1.26±0.07 | $g/cm^3$ |
| Mean Mass | | $4\times10^{10}$ | $6\times10^{10}$ | kg |
| Rotation period | | 30.4 | 4.29 | h |
| Albedo | | 0.23 | 0.046 | |
| Temperature | | 270 | 259 | K |
| Absolute magnitude | $H$ | 19.7 | 20.9 | |

Table 6.1: Estimated Properties of Apophis and Bennu

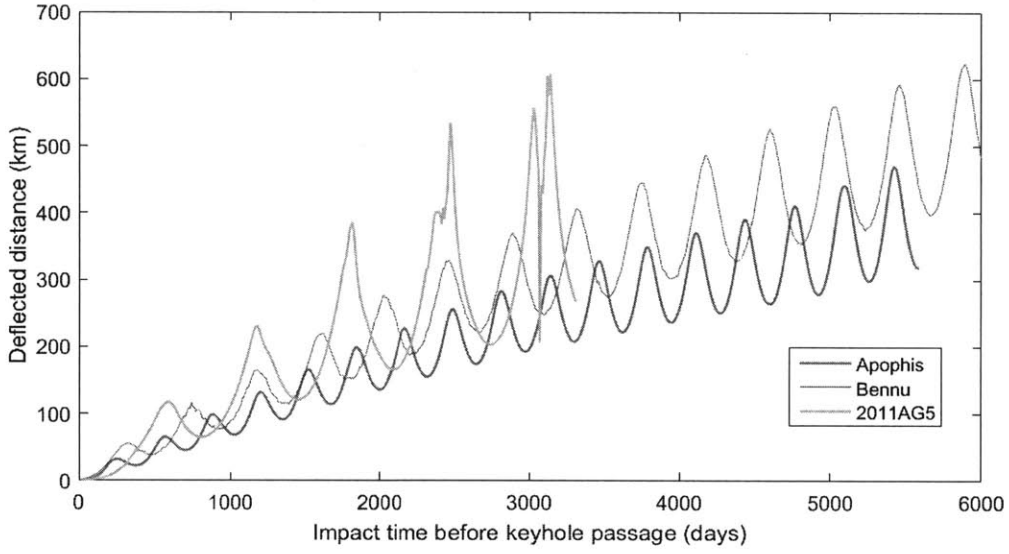


Figure 6-1: Deflection characteristic curves of Apophis, Bennu, and 2011AG5 per unit impactor mass

Going back to the comparison of Apophis and Bennu, their major physical difference is in their assumed $\beta$ distributions. Apophis is an S-type (silicaceous or stony) asteroid, which is expected to produce greater plume effects than C-type (carbonaceous) Bennu, which has a higher porosity level. For Apophis, the initial $\beta$ is assumed to follow a Gaussian distribution $\beta_{ai} \sim \mathcal{N}(2, 0.3)$ such that its 3-sigma interval is approximately within an interval [1,3] as seen in Fig. 6-2. The $\beta$ distribution of Bennu is assumed to follow a log-normal distribution $\beta_{bi} \sim \mathcal{LN}(2.5, 1.8)$ that occupies the left half of the interval [1,3].

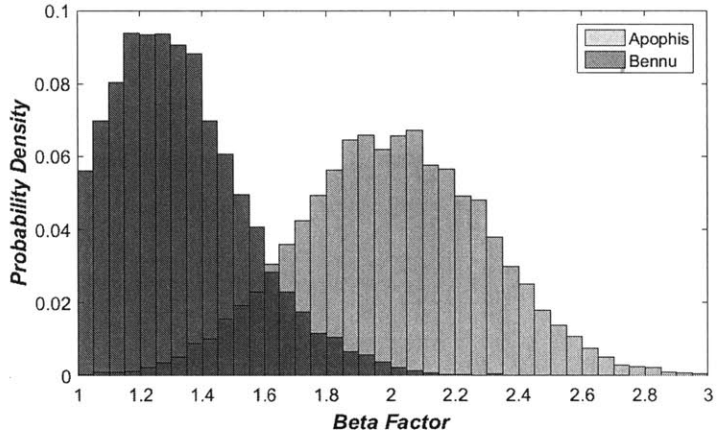


Figure 6-2: Initial $\beta$ distributions assumed for Apophis and Bennu

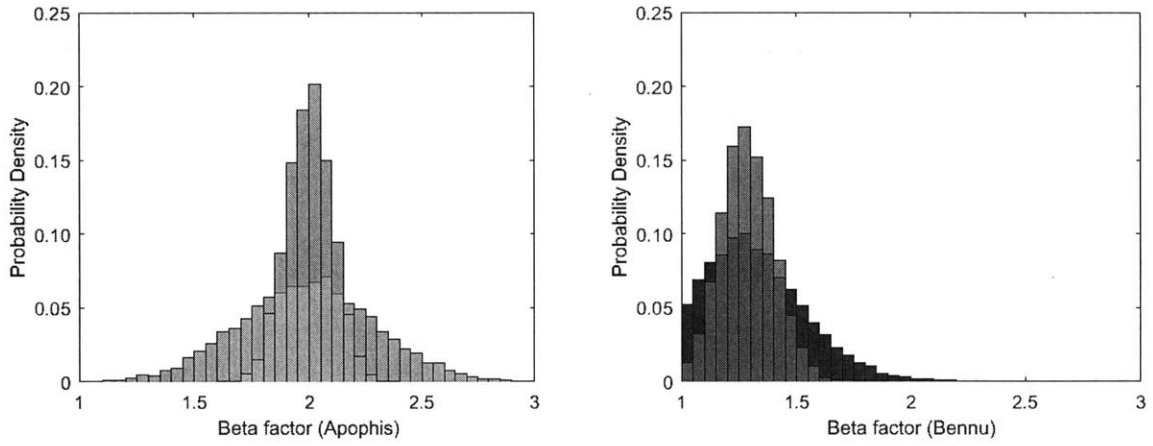


Figure 6-3: Primary and secondary keyholes for Bennu in 2135

After a precursor stage of a Type 2 campaign, the final $\beta$ distribution of Apophis is assumed to follow a narrower Gaussian distribution $\beta_{af} \sim \mathcal{N}(2, 0.1)$ in Fig. 6-3 (left). Similarly, the final $\beta$ distribution of Bennu is assumed to be $\beta_{af} \sim \mathcal{LN}(2.5, 0.09)$. In the previous chapter, the safe harbor location of [20km, 800km] relative to the primary keyhole was used for Apophis. The same safe harbor size is assumed for Bennu. Figure 6-4 (right) illustrates one of Bennu's keyholes that has a similar harbor size with the keyhole used in Apophis' case. Because the masses of the two asteroids are of the same orders of magnitude, by using the same safe harbor sizes we can exclude the effects of differences in their keyhole maps and investigate the effects of physical parameters only.

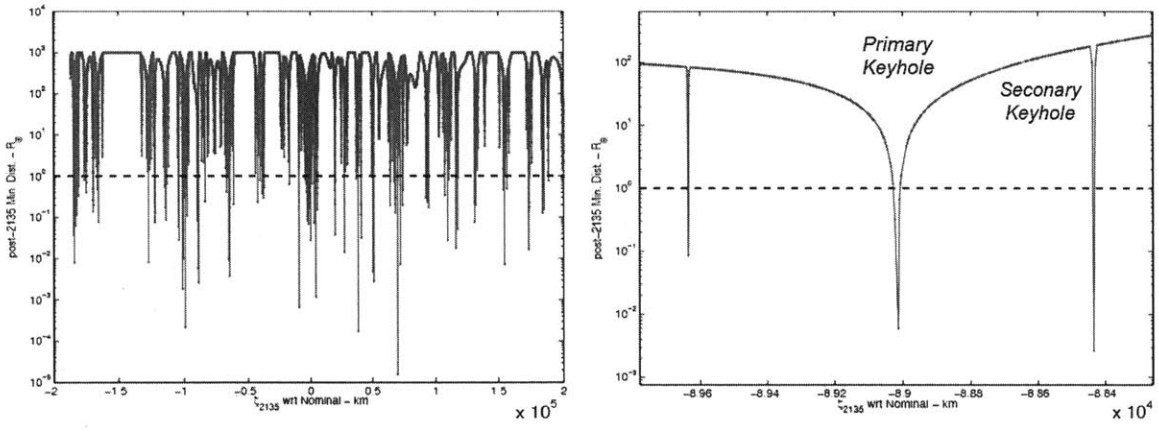


Figure 6-4: Changes in $\beta$ distributions for Apophis (left) and Bennu (right) [36]

## 6.1 Type 0 Campaign

The position uncertainty of Bennu is nonzero in a Type 0 campaign, which does not include a precursor stage to measure the position prior to an impact. Without literature available on the position uncertainty levels of Bennu, a value of 100 km (3-sigma) is assumed, which is about twice the uncertainty level of Apophis. Therefore, the width of an *effective* safe harbor for Bennu is narrower than that of Apophis. However, as shown in Fig. 6-2 and Fig. 6-3, the $\beta$ values for Bennu are more compactly distributed than those for Apophis. As a result, it becomes easier to

deflect Bennu into its effective safe harbor than to deflect Apophis into its effective safe harbor. In Apophis' case, Type 0 campaigns can achieve a maximum of 99% likelihood of success.[3] Type 0 campaigns for Bennu further reduce the failure rate, achieving the 99.99% POS. This is because the deflected distance distribution of Bennu is less widely spread than that of Apophis. When the deflected distance is calculated from the *beta* factor and the asteroid mass, the uncertainties in their distributions are propagated. Bennu has a narrower spread in the $\beta$ factor distribution as well as the mass distribution than Apophis. Hence, the results of the Bennu deflection campaigns are more sensitive to the likelihood-of-success thresholds than those of Apophis deflection campaigns (Type 0) that did not differ in the 90% threshold case and the 99% threshold case. Bennu, on the other hand, has different Type 0 campaign designs for each threshold level: 90%, 99%, 99.9%, and 99.99%. Figures 6-6 through 6-17 (a total of 12 plots) delineate *carpet plots* of the optimization objective ($J_{min}$), the system mass (IMLEO), and the robustness coefficient ($C_{max}$) at four POS threshold levels. This is to show that selecting a particular probability-of-success level has a large impact on the result. As the POS increases, mission opportunities are becoming fewer. The carpet plots of Bennu exhibit periodic patterns in retrograde direction due to its orbit period longer than 1 Earth year.

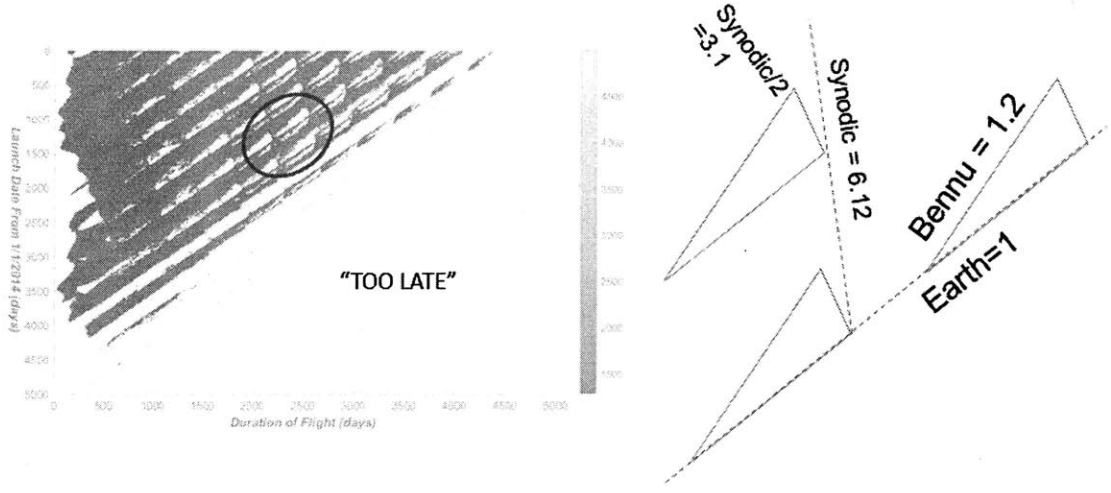


Figure 6-5: Admissible region and periodic patterns

[3]The *carpetplots* were identical for 90% and 99% for Apophis deflection campaigns.

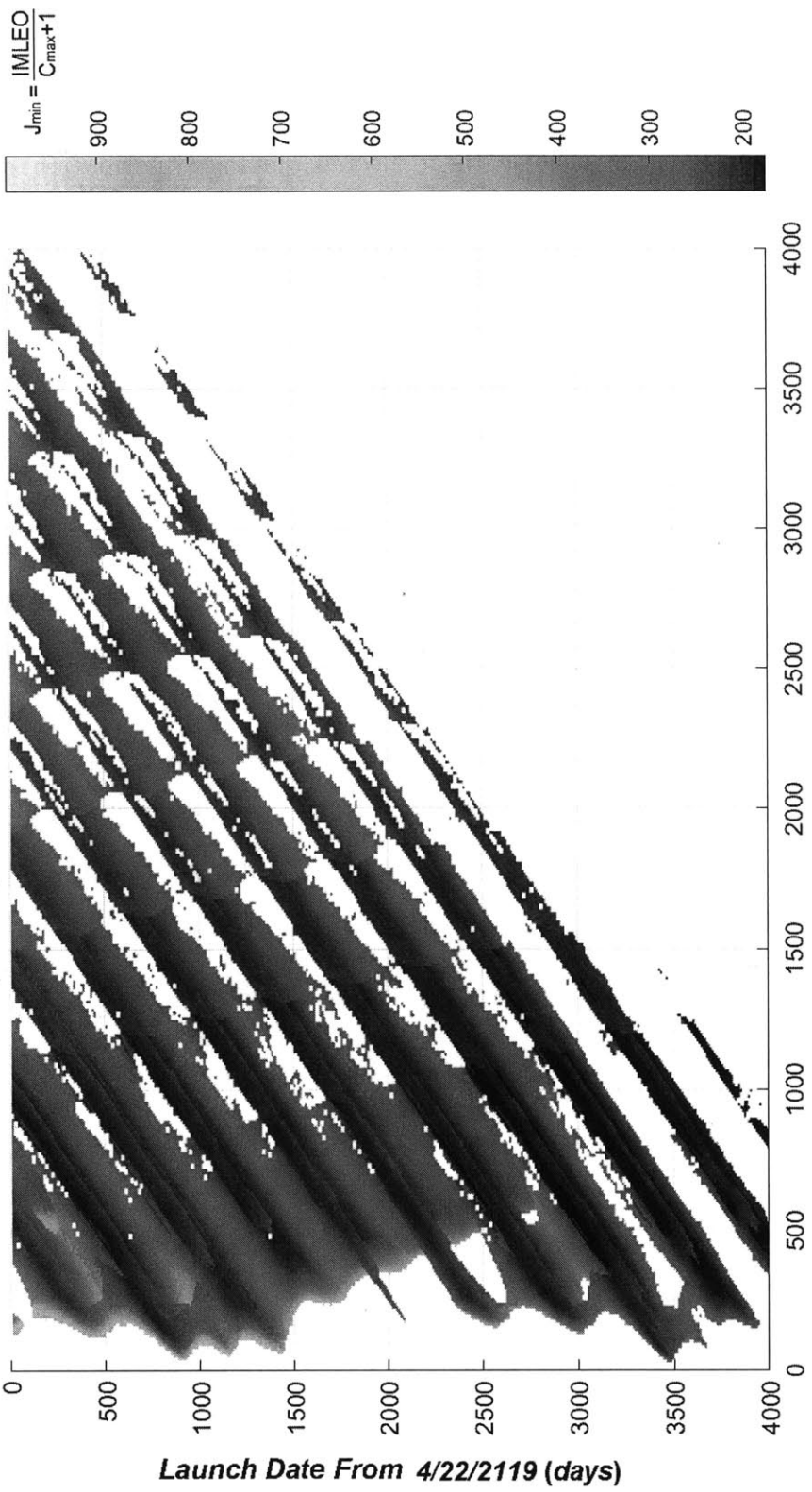


Figure 6-6: Balanced objective ($\frac{IMLEO}{C_{max}+1}$) of Type 0 campaigns (PoS = 90%)

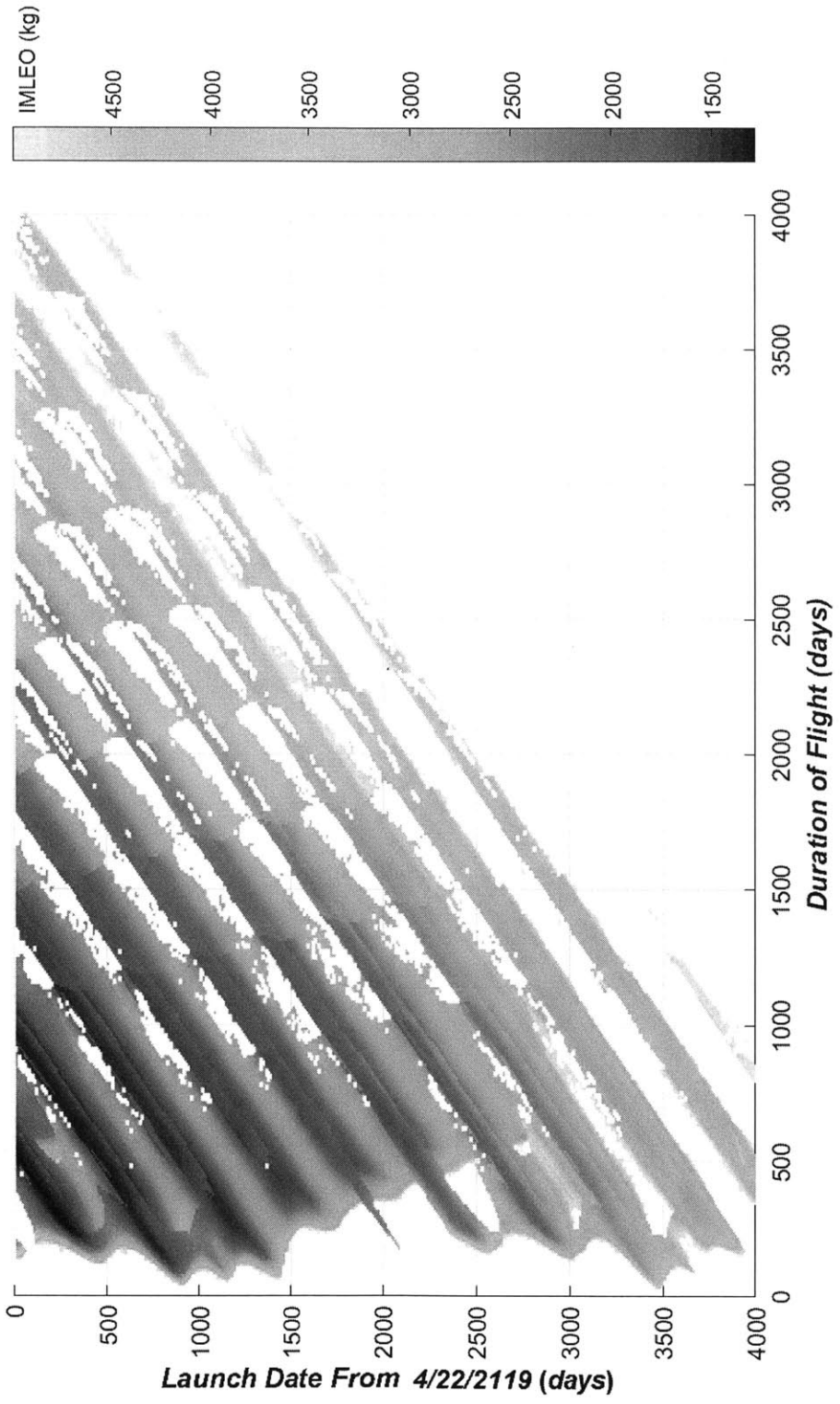


Figure 6-7: Mass (IMLEO[kg]) of Type 0 campaigns (PoS = 90%)

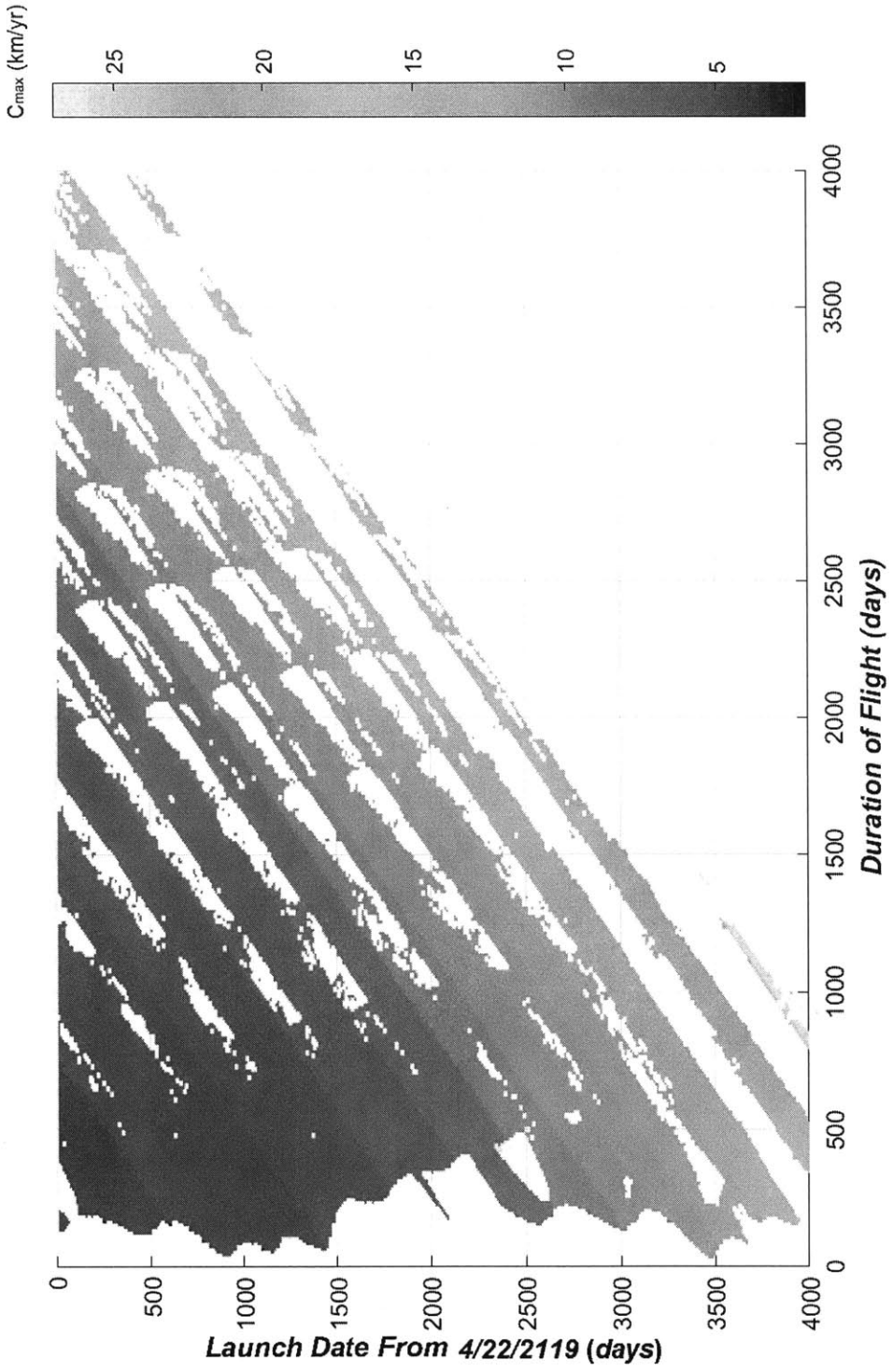


Figure 6-8: Robustness coefficient ($C_{max}$) of Type 0 campaigns (PoS = 90%)

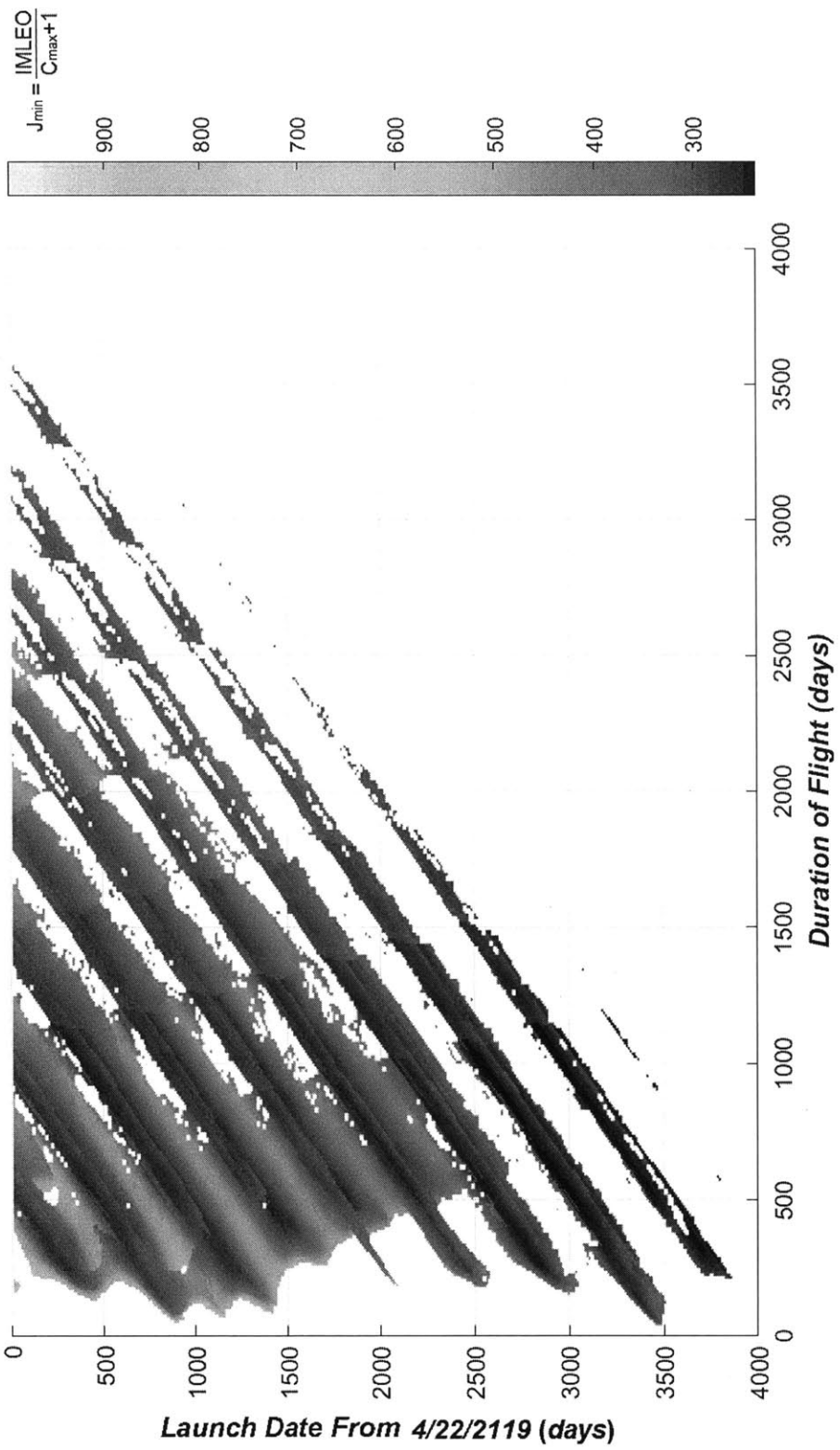


Figure 6-9: Balanced objective ($\frac{IMLEO}{C_{max}+1}$) of Type 0 campaigns (PoS = 99%)

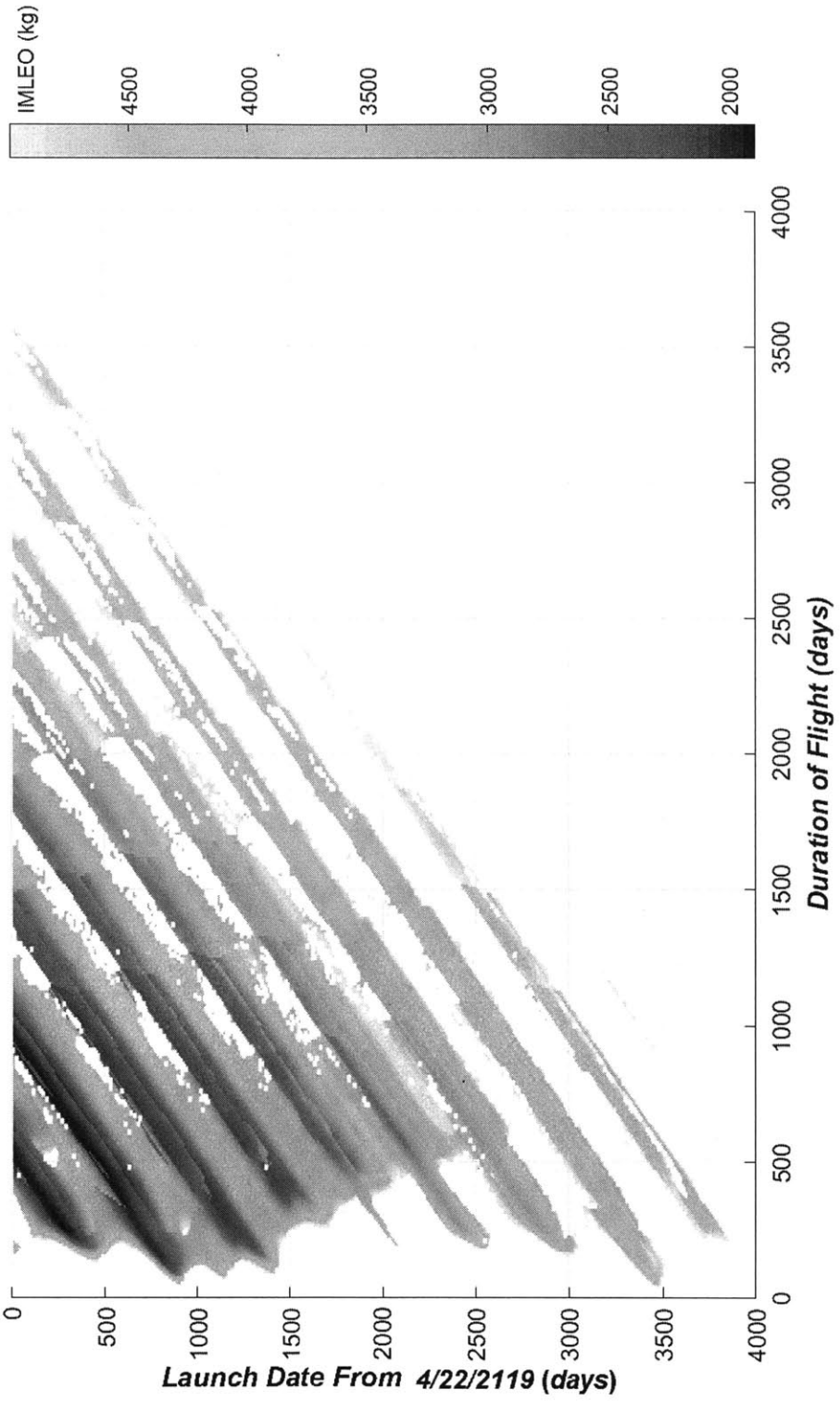


Figure 6-10: Mass (IMLEO[kg]) of Type 0 campaigns (PoS=99%)

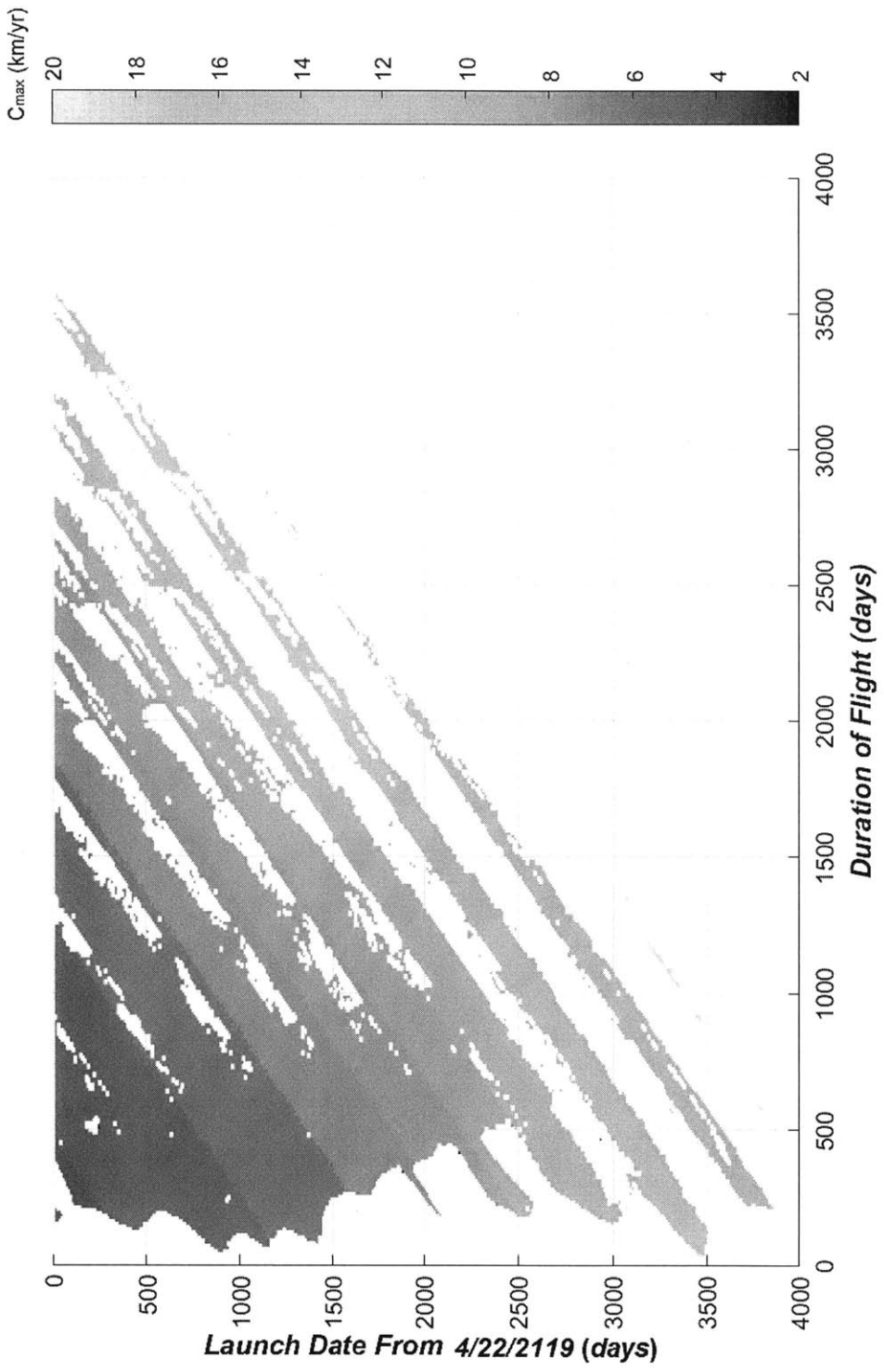


Figure 6-11: Robustness coefficient ($C_{max}$) of Type 0 campaigns (PoS=99%)

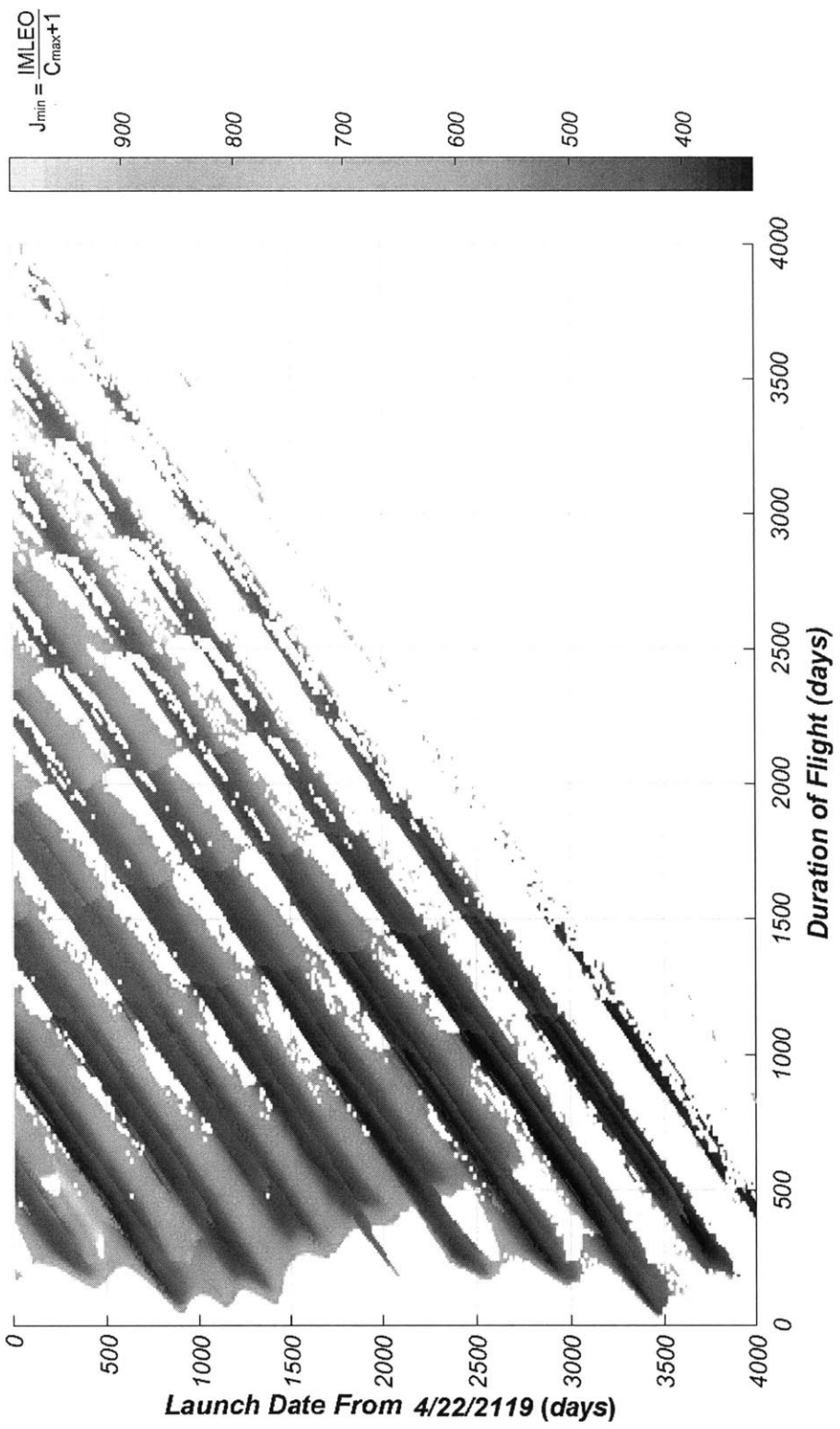


Figure 6-12: Balanced objective ($\frac{IMLEO}{C_{max}+1}$) of Type 0 campaigns (PoS=99.9%)

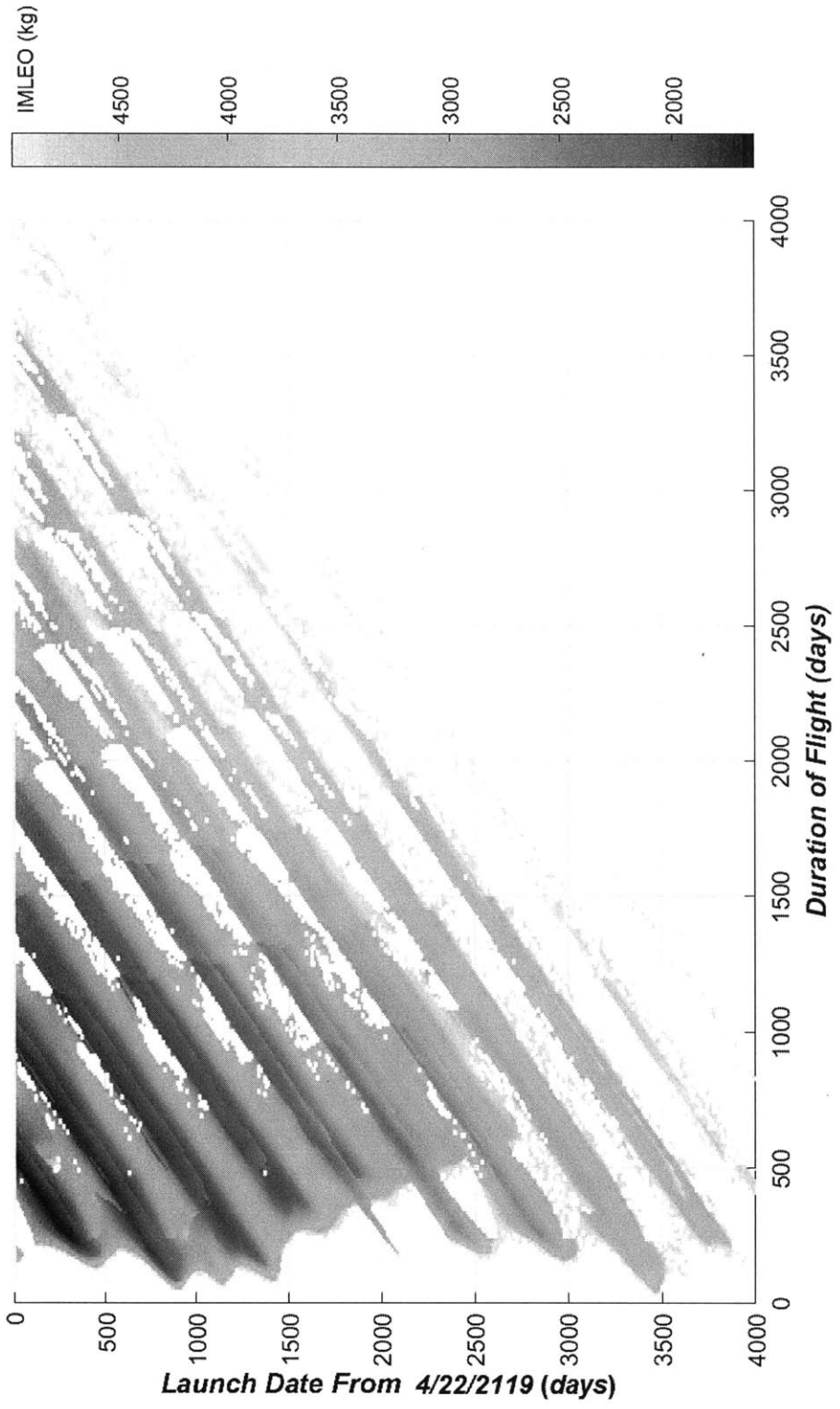


Figure 6-13: Mass (IMLEO[kg]) of Type 0 campaigns (PoS=99.9%)

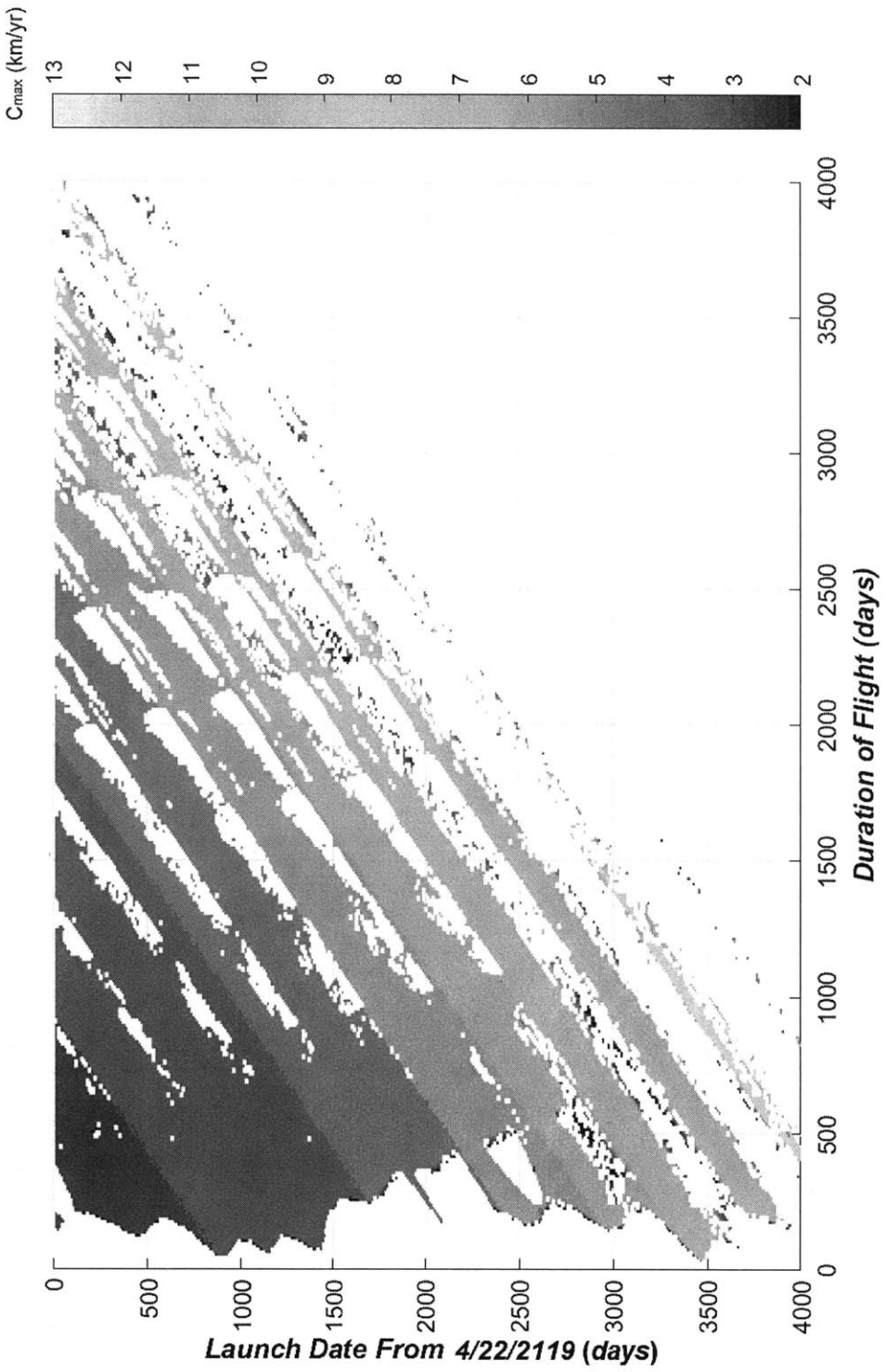


Figure 6-14: Robustness coefficient ($C_{max}$) of Type 0 campaigns (PoS=99.9%)

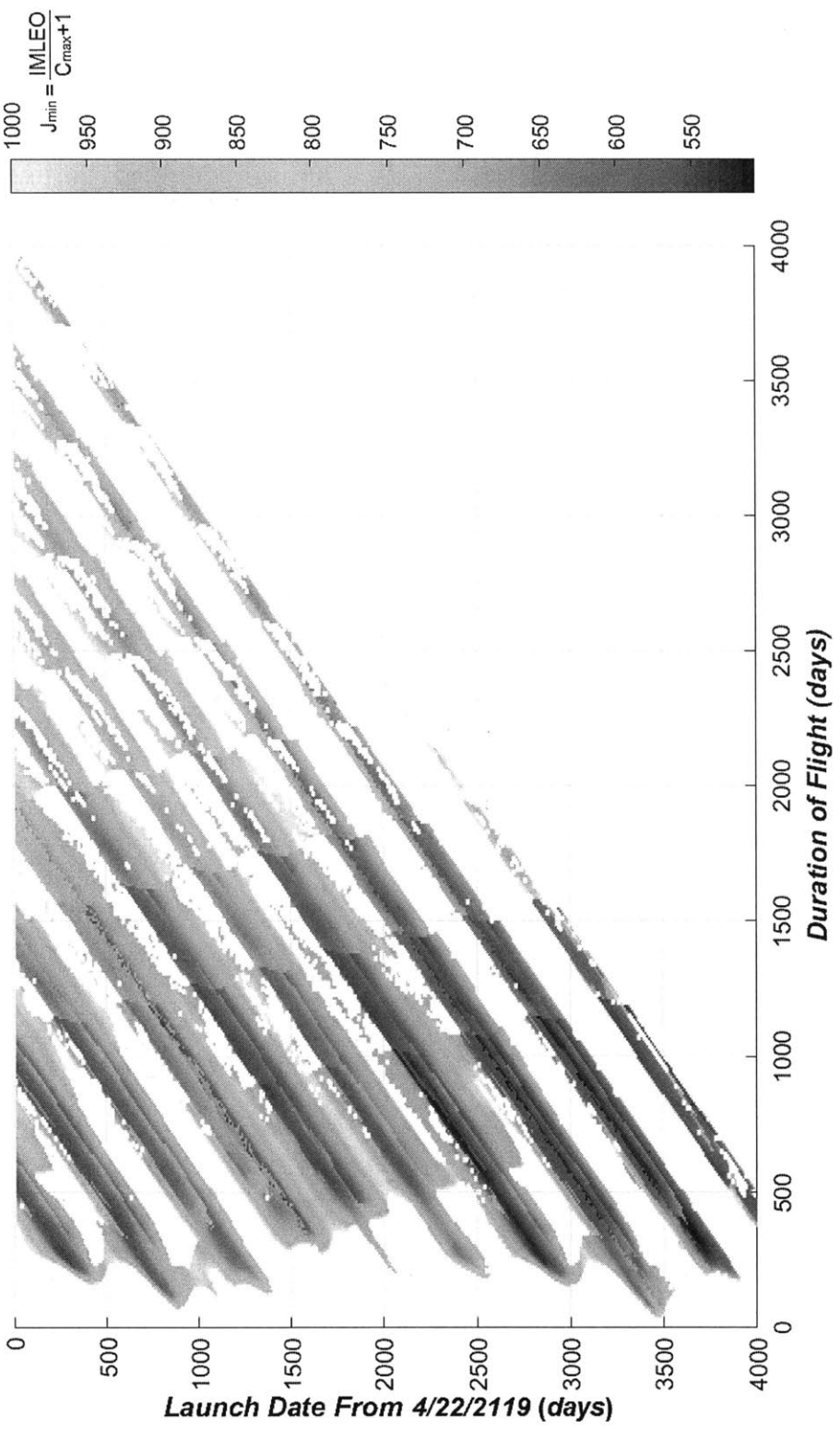


Figure 6-15: Balanced objective ($\frac{IMLEO}{C_{max}+1}$) of Type 0 campaigns (PoS=99.99%)

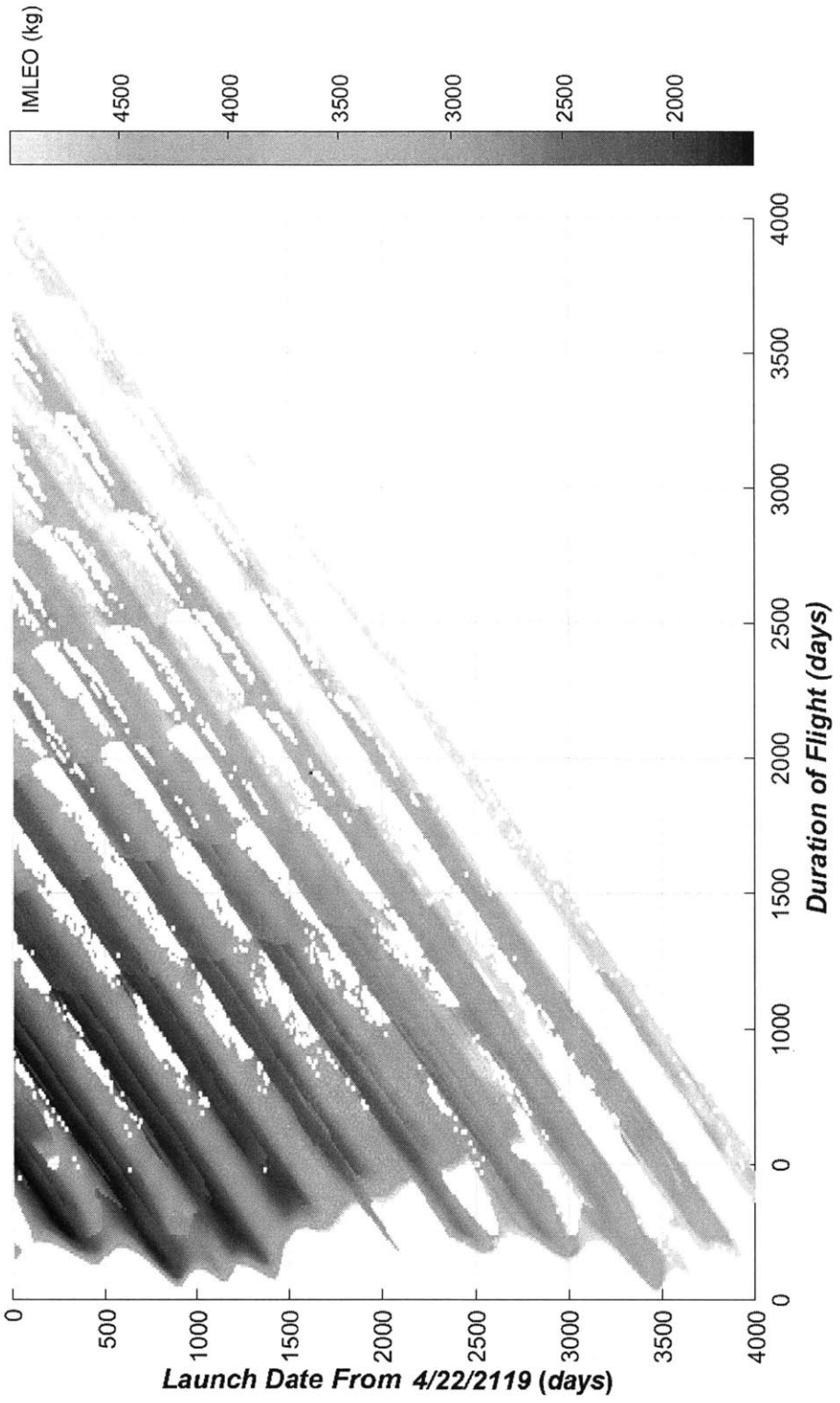


Figure 6-16: Mass (IMLEO[kg]) of Type 0 campaigns (PoS=99.99%)

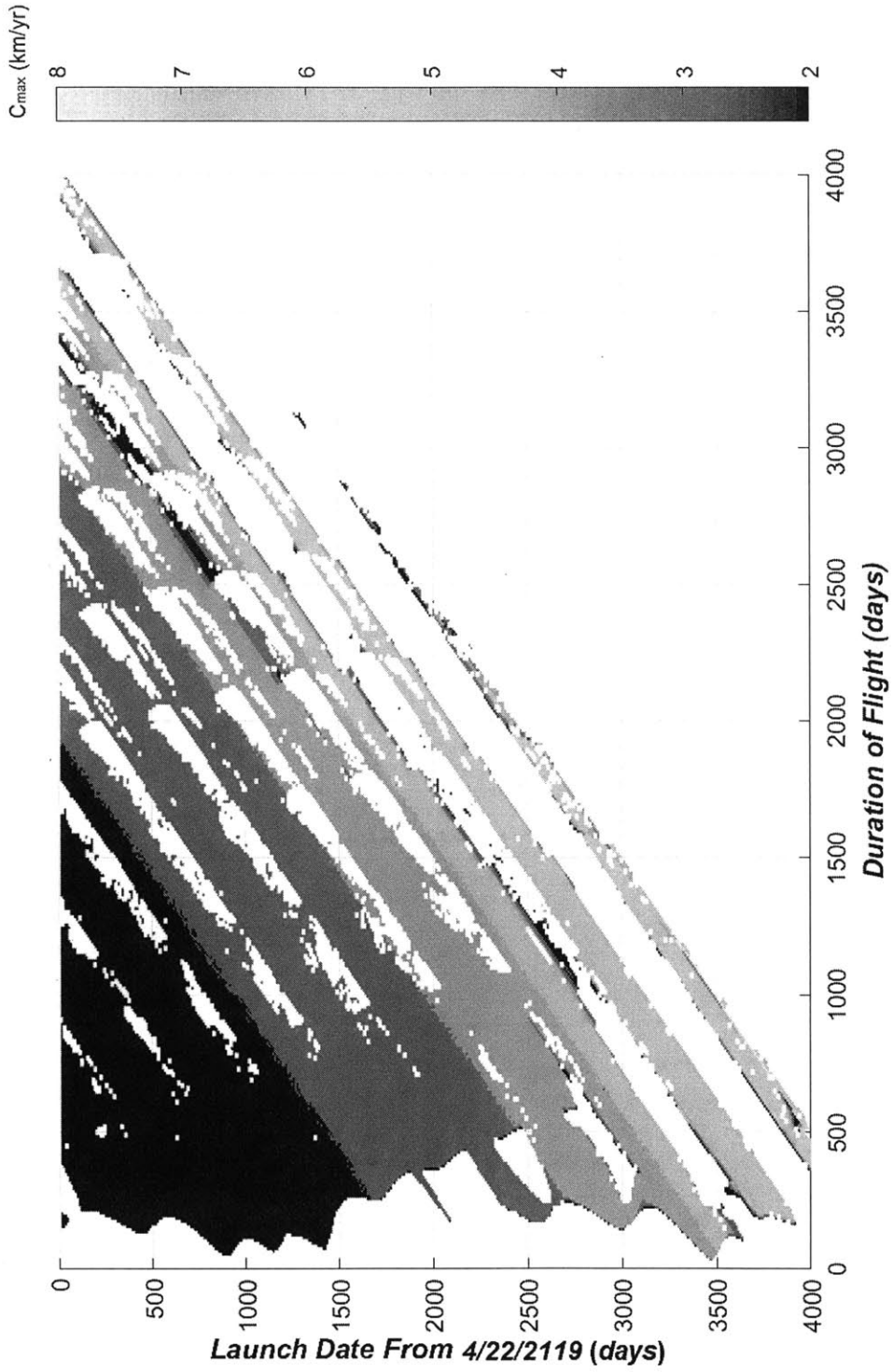


Figure 6-17: Robustness coefficient ($C_{max}$) of Type 0 campaigns (PoS=99.99%)

In these *carpet plots*, the values of $J$ tend to increase for higher threshold levels. This trend is visible from their dominant colors: dark blue ($J \sim 200$) for 90% in Fig. 6-6, light blue ($J \sim 400$) for 99% in Fig. 6-9, green ($J \sim 650$) for 99.9% in Fig. 6-12, yellow ($J \sim 900$) for 99.99% in Fig. 6-15. We can confirm this further by extracting the minimum $J$ values on each launch date with optimal flight time ($J_{min}$), as described earlier in Fig. 5-7 and Algorithm 6. The results of applying these procedures are presented in Fig. 6-18. For all threshold levels, $J_{min}$ does not change much until just before the end of solution. Except for the sharp increase at the end, the value of $J_{min}$ does not change by more than 20%, whose variation level is similar to those in the Apophis case. In Apophis, threshold values of 90% and 99% produce the same plots, but Bennu has different curves for all threshold levels, implying a greater sensitivity to them.

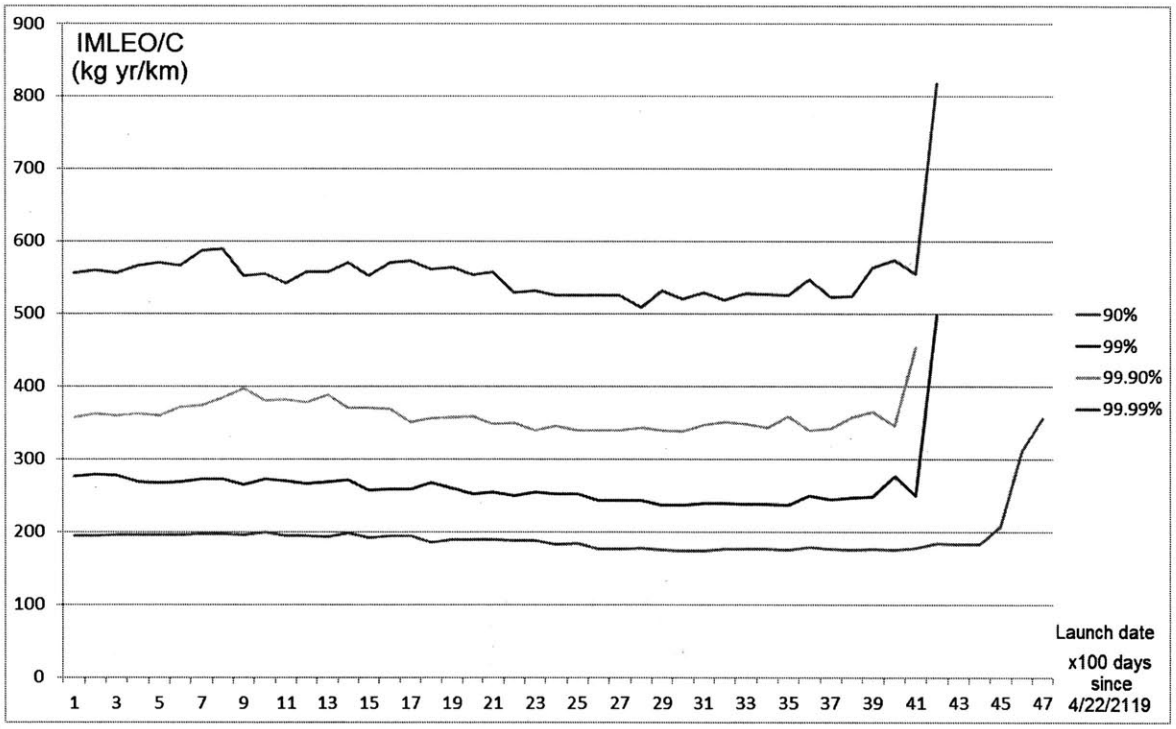


Figure 6-18: Type 0 performance for various reliability levels

The plateaus in the time histories of $J_{min}$ suggest that IMLEO and $C_{max}$ move together in the same direction at similar paces. This can be confirmed in Figures 6-19 and 6-20, where IMLEO and $C_{max}$ are both increasing at similar relative rates.

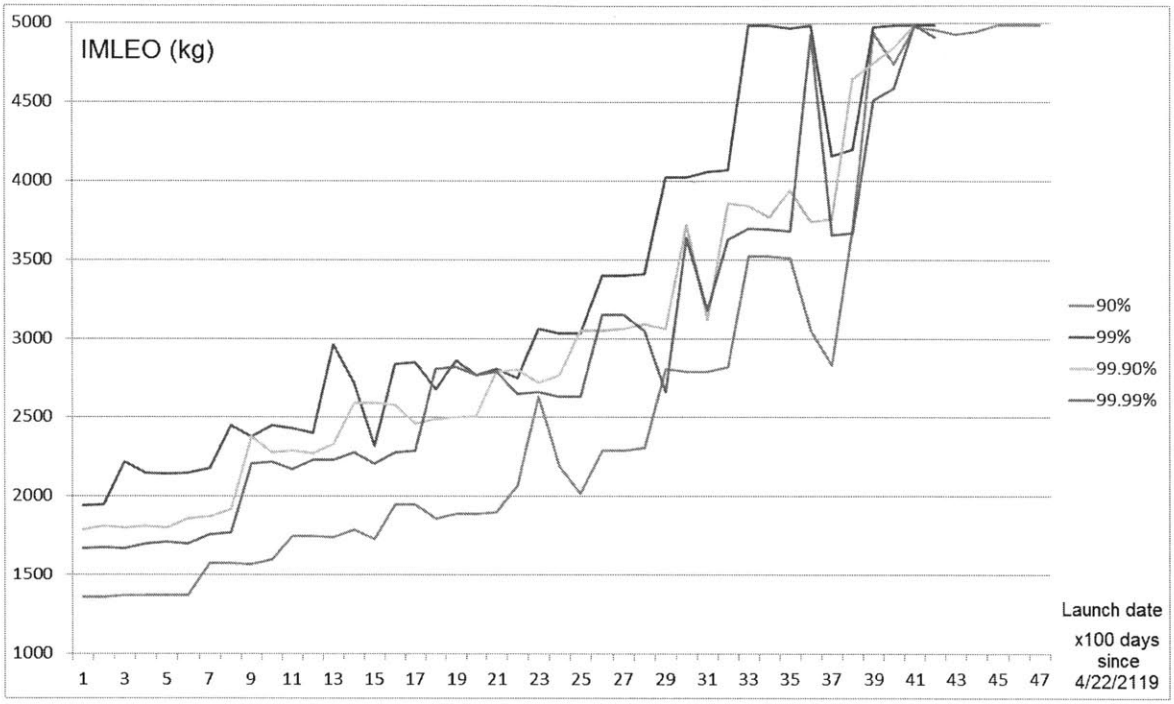


Figure 6-19: Type 0 IMLEO for various reliability levels

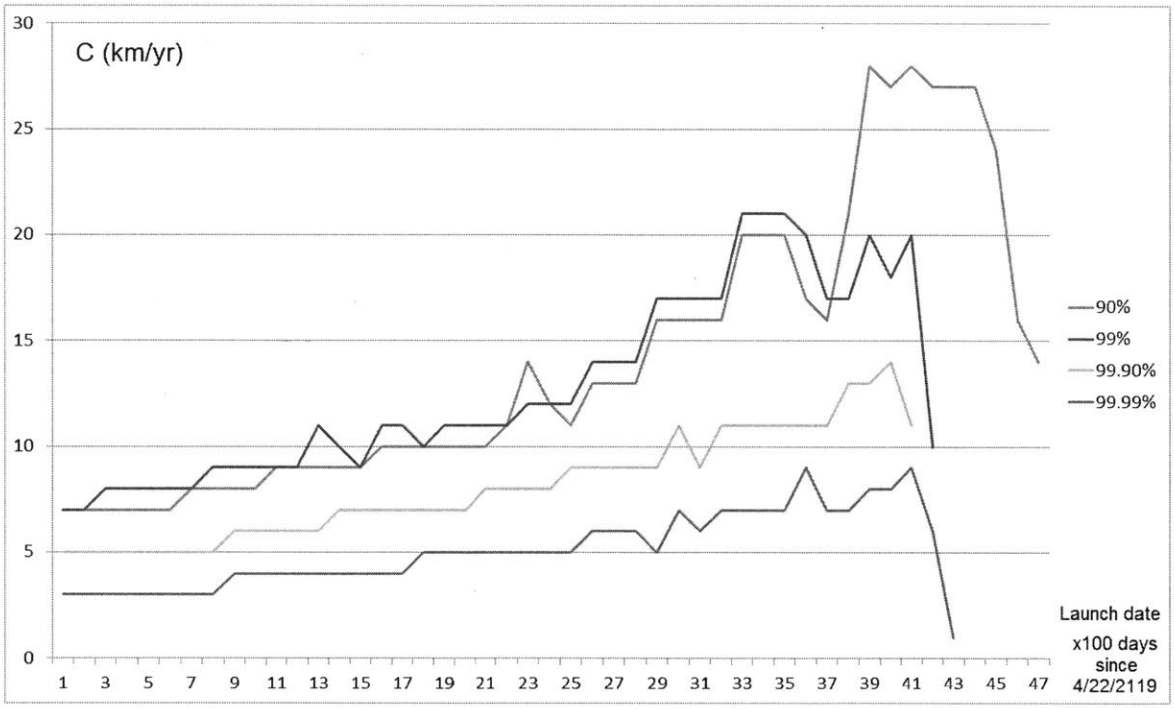


Figure 6-20: Type 0 $C_{max}$ for various reliability levels

Consequently, the $J_{min}$ does not change significantly for the greater part of a time interval considered. However, when $C_{max}$ drops at the end of interval, with IMLEO still increasing, the value of $J_{min}$ sharply increases. Based on the finite values of $J_{min}$ available, the last date when Bennu may be deflected using a Type 0 campaign is 4,200 days since the epoch or 1,800 days (5 years) prior to the keyhole passage if a likelihood-of-success level of 99% is targeted. If this threshold is lowered to 90%, the last date is extended by 400 days and Bennu may be deflected approximately 4 years prior to its keyhole passage at the latest.

To conclude, there are more options for selecting different Type 0 missions trading off IMLEO and C for asteroid Bennu than asteroid Apophis, 6-19 as shown in Fig. and Fig. 6-20. This is a benefit of having more knowledge (or less uncertanity) in the asteroid mass and beta.

## 6.2 Type 1 Campaign

Figure 6-21 summarizes the time histories of $J_{min}$, IMLEO, and $C_{max}$ of Type 1 campaigns for Bennu. The horizontal axis shows launch dates in terms of how many days have elapsed since April 22, 2119. The start date has been set such that a time span of 6,000 days will end at the keyhole passage date on September 23, 2135. The plots for 90%, 99%, and 99.9% thresholds are identical and have higher $J_{min}$ values than Type 0 campaigns. Because Bennu has a mass uncertainty level much lower than Apophis,[4] Type 1 precursors, which only reduce the mass uncertainty and cannot reduce the $\beta$ uncertainty, are not a superior option compared to the no-precursor, Type 0 campaigns. Furthermore, the marginal improvement in mass knowledge is offset by additional precursor mass and later departure dates, making Type 1 campaigns less effective in terms of both IMLEO and $C_{max}$. In addition to its low effectiveness, the launch window for Type 1 terminates much earlier than Type 0: 2,500 days since the epoch or 3,500 days prior to the keyhole passage.

[4]The mass uncertainty level of Apophis is 50%, whereas the mass uncertainty level of Bennu is less than 10%. This difference comes from the uncertainty levels of the mean (bulk) density of the two asteroids.

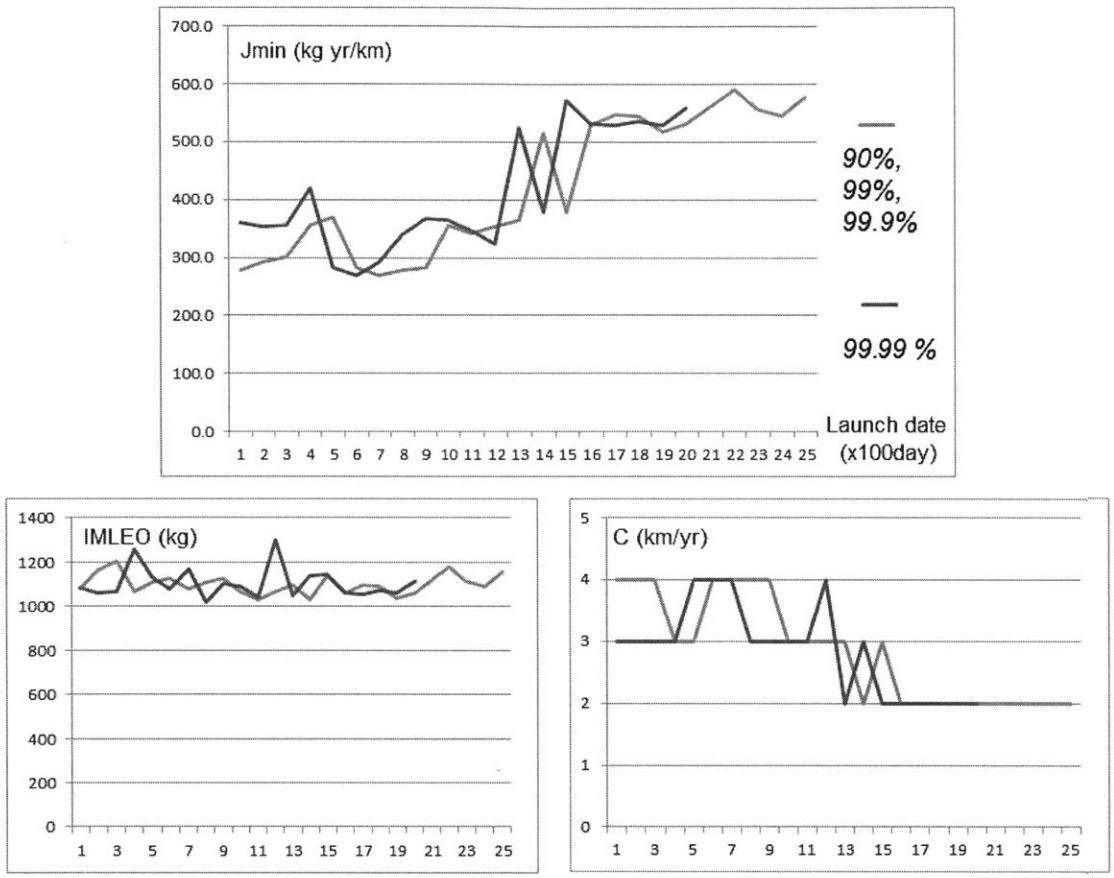


Figure 6-21: $J_{min}$, IMLEO, and $C_{max}$ for Type 1 campaigns

## 6.3 Type 2 Campaign

Figures 6-22, 6-23, and 6-24 delineate the time histories of $J_{min}$, IMLEO, and $C_{max}$ for Type 2 campaigns to deflect Bennu. The most outstanding feature is the "keep-out zone" where Type 2 campaigns are impossible to execute, for which the orbital alignments of Earth and Bennu could be a reason. In this band, $C_{max}$ is not zero, so it is still possible to execute a campaign. However, campaigns in this band has been ruled out during post-processing because their impactor arrive at Bennu too late. A Type 2 campaign must have its last impact no later than 5 years from keyhole passage in order to track the deflected orbit and calculate the $\beta$ with high accuracy. Entering this time interval, the arrival dates of the main impactor are delayed by 2 years at

least, possibly due to the relative orbital alignments of Earth and Bennu. After the time passes, out of this interval, the main impactor's arrival dates are recovered to earlier dates, and post-processing does not preclude these campaigns.

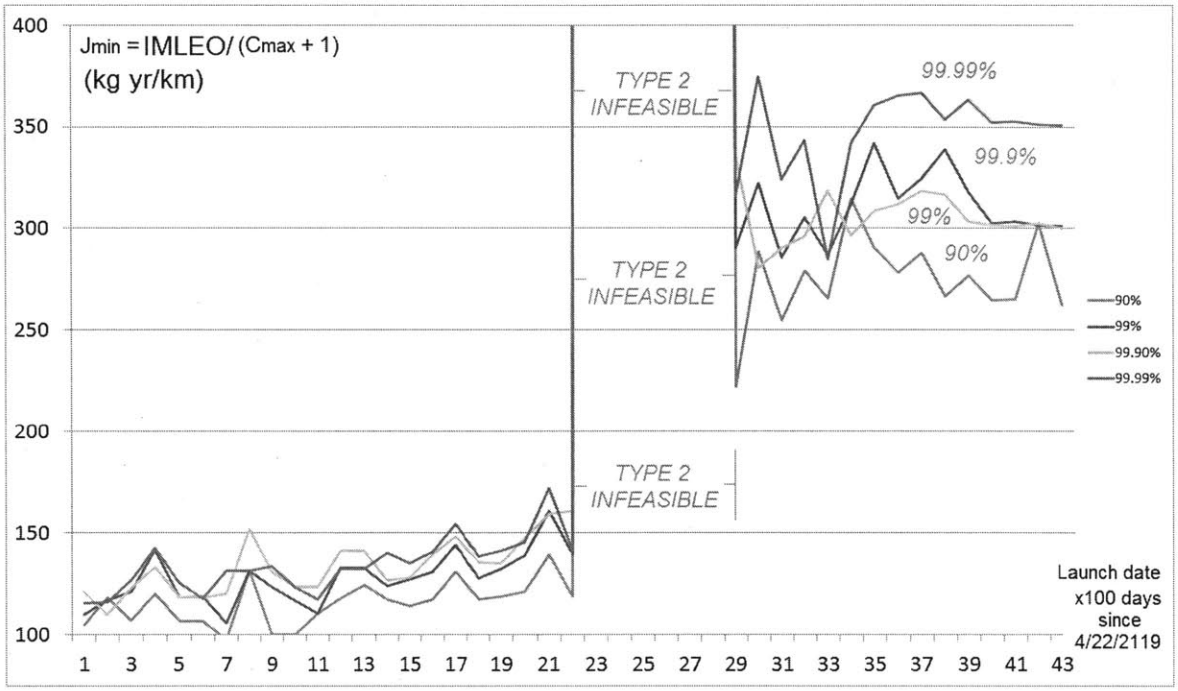


Figure 6-22: Type 2 performance for various reliability levels

The IMLEO in Fig. 6-23 does not differ among four POS levels before entering the infeasible band, but the difference is clearer after coming out of the band. The $C_{max}$ values differ by similar amounts before and after the infeasile band, but the relative difference is larger toward the end where $C_{max}$ values are lower. For the two reasons, $J_{min}$ exhibits more distinct stratification after the infeasible band.

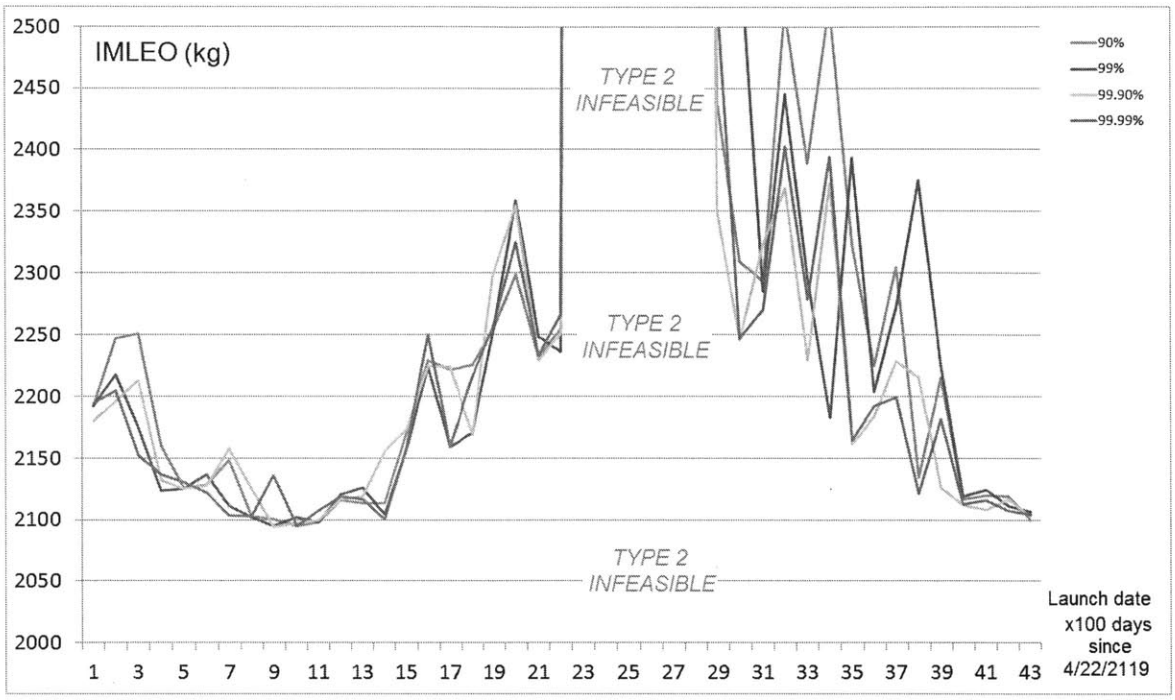


Figure 6-23: Type 2 IMLEO for various reliability levels

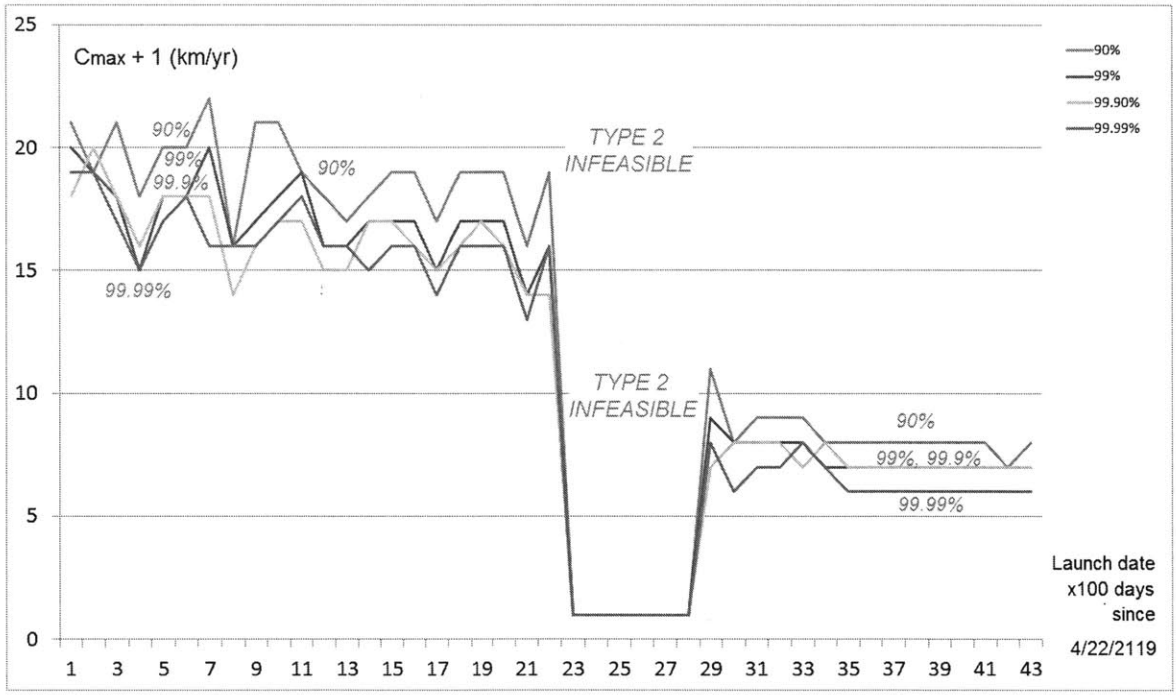


Figure 6-24: Type 2 robustness for various reliability levels

## 6.4 Type S Map and Type M Map

Figure 6-25 summarizes the optimization results of all types of campaigns. The vertical axis denotes launch dates in terms of how many days have elapsed since April 22, 2119. The start date (0 days since epoch) is at the top, and the later launch dates are listed at the bottom. The epoch has been set such that a time span of 6000 days will end at the keyhole passage date on September 23, 2135. With 100-day intervals, a total of 60 time grid points are generated. The horizontal axis shows different levels for the likelihood of success.

### 6.4.1 Type S Map

The left figure shows a single dominant solution (in terms of $J_{min}$ in each case. The decision map shows that Type 2 campaigns dominate the choice of optimal campaign type up to 2,500 days. After that a mixed of Type 0 and Type 1 campaigns can be selected. Before Type 2 campaigns dominate again as time gets closers to the keyhole passage, there are a few cases where no solution is feasible.

### 6.4.2 Type M Map

The right figure lists all non-dominated solutions in each case. The Type 2 regime in the previous map can be further divided into two regions, before and after the keep-out zone. For earlier launch dates prior to the keep-out zone, Type 0 and Type 1 campaigns are non-dominated in most of the cases. For later launch dates after the keep-out zone, Type 2 is the one and only possible solution. Type 0 and Type 1 campaigns inside the keep-out zone tend to be the only feasible solutions as well.

| days | 90% | 99% | 99.90% | 99.99% |
|---|---|---|---|---|
| 0 | 2 | 2 | 2 | 2 |
| 100 | 2 | 2 | 2 | 2 |
| 200 | 2 | 2 | 2 | 2 |
| 300 | 2 | 2 | 2 | 2 |
| 400 | 2 | 2 | 2 | 2 |
| 500 | 2 | 2 | 2 | 2 |
| 600 | 2 | 2 | 2 | 2 |
| 700 | 2 | 2 | 2 | 2 |
| 800 | 2 | 2 | 2 | 2 |
| 900 | 2 | 2 | 2 | 2 |
| 1000 | 2 | 2 | 2 | 2 |
| 1100 | 2 | 2 | 2 | 2 |
| 1200 | 2 | 2 | 2 | 2 |
| 1300 | 2 | 2 | 2 | 2 |
| 1400 | 2 | 2 | 2 | 2 |
| 1500 | 2 | 2 | 2 | 2 |
| 1600 | 2 | 2 | 2 | 2 |
| 1700 | 2 | 2 | 2 | 2 |
| 1800 | 2 | 2 | 2 | 2 |
| 1900 | 2 | 2 | 2 | 2 |
| 2000 | 2 | 2 | 2 | 2 |
| 2100 | 2 | 2 | 2 | 2 |
| 2200 | 2 | 2 | 2 | 2 |
| 2300 | 2 | 2 | 2 | 2 |
| 2400 | 1 | 1 | 1 | 2 |
| 2500 | 0 | 1 | 2 | 0 |
| 2600 | 0 | 1 | 1 | 0 |
| 2700 | 0 | 1 | 1 | 0 |
| 2800 | 0 | 1 | 1 | 0 |
| 2900 | 0 | 1 | 1 | 0 |
| 3000 | 0 | 1 | 1 | 0 |
| 3100 | 0 | 1 | 1 | 0 |
| 3200 | 0 | 0 | 0 | 0 |
| 3300 | 0 | 0 | 0 | 0 |
| 3400 | 0 | 0 | 0 | 0 |
| 3500 | 0 | 0 | 0 | 0 |
| 3600 | 0 | 0 | 0 | 0 |
| 3700 | 0 | 0 | 0 | 0 |
| 3800 | 0 | 1 | 1 | 0 |
| 3900 | 0 | 0 | 0 | 0 |
| 4000 | 0 | 0 | 0 | 0 |
| 4100 | 0 | 0 | 1 | 0 |
| 4200 | 0 | 1 | 1 | -1 |
| 4300 | 0 | -1 | -1 | -1 |
| 4400 | 0 | -1 | -1 | -1 |
| 4500 | 2 | 2 | 2 | 2 |
| 4600 | 2 | 2 | 2 | 2 |
| 4700 | 2 | 2 | 2 | 2 |
| 4800 | 2 | 2 | 2 | 2 |
| 4900 | 2 | 2 | 2 | 2 |
| 5000 | 2 | 2 | 2 | 2 |
| 5100 | 2 | 2 | 2 | 2 |
| 5200 | 2 | 2 | 2 | 2 |
| 5300 | 2 | 2 | 2 | 2 |
| 5400 | 2 | 2 | 2 | 2 |
| 5500 | 2 | 2 | 2 | 2 |
| 5600 | 2 | 2 | 2 | 2 |
| 5700 | 2 | 2 | 2 | 2 |
| 5800 | 2 | 2 | 2 | 2 |
| 5900 | 2 | 2 | 2 | 2 |

| 90% | 99% | 99.90% | 99.99% |
|---|---|---|---|
| 210 | 21 | 210 | 210 |
| 210 | 21 | 210 | 210 |
| 210 | 21 | 210 | 210 |
| 210 | 21 | 210 | 210 |
| 210 | 21 | 210 | 210 |
| 210 | 21 | 210 | 210 |
| 210 | 21 | 210 | 210 |
| 210 | 21 | 210 | 210 |
| 210 | 21 | 21 | 21 |
| 210 | 21 | 21 | 21 |
| 210 | 21 | 21 | 21 |
| 210 | 21 | 21 | 21 |
| 210 | 21 | 21 | 21 |
| 210 | 21 | 21 | 21 |
| 210 | 21 | 21 | 21 |
| 210 | 21 | 21 | 21 |
| 210 | 21 | 21 | 21 |
| 210 | 21 | 21 | 21 |
| 210 | 21 | 21 | 21 |
| 210 | 21 | 21 | 21 |
| 210 | 21 | 21 | 21 |
| 20 | 20 | 2 | 2 |
| 21 | 21 | 21 | 21 |
| 210 | 21 | 21 | 21 |
| 1 | 1 | 1 | 21 |
| 0 | 1 | 21 | 0 |
| 0 | 1 | 1 | 0 |
| 0 | 1 | 1 | 0 |
| 0 | 1 | 1 | 0 |
| 0 | 10 | 1 | 0 |
| 0 | 10 | 10 | 0 |
| 0 | 10 | 10 | 0 |
| 0 | 0 | 0 | 0 |
| 0 | 0 | 0 | 0 |
| 0 | 0 | 0 | 0 |
| 0 | 0 | 0 | 0 |
| 0 | 0 | 0 | 0 |
| 0 | 0 | 0 | 0 |
| 0 | 1 | 1 | 0 |
| 0 | 0 | 0 | 0 |
| 0 | 0 | 0 | 0 |
| 0 | 0 | 1 | 0 |
| 0 | 1 | 1 | -1 |
| 0 | -1 | -1 | -1 |
| 0 | -1 | -1 | -1 |
| 2 | 2 | 2 | 2 |
| 2 | 2 | 2 | 2 |
| 2 | 2 | 2 | 2 |
| 2 | 2 | 2 | 2 |
| 2 | 2 | 2 | 2 |
| 2 | 2 | 2 | 2 |
| 2 | 2 | 2 | 2 |
| 2 | 2 | 2 | 2 |
| 2 | 2 | 2 | 2 |
| 2 | 2 | 2 | 2 |
| 2 | 2 | 2 | 2 |
| 2 | 2 | 2 | 2 |
| 2 | 2 | 2 | 2 |
| 2 | 2 | 2 | 2 |

Figure 6-25: Decision Map of Bennu : Single Option (Left) and Multiple Options (Right)

## 6.5 Conclusion

Bennu share a number of common physical characteristics with Apophis, except the estimated distributions of its mass and beta factor. Bennu is a C-type (carbonaceous) asteroid, whose beta distribution is assumed to be narrower and more left-skewed than Apophis which is an S-type (siliceous or stony) asteroid. The mass uncertainty of Bennu is much lower than that of Apophis,[5] which renders Type 1 campaigns capable of only reducing mass uncertainty somewhat less useful, as shown in the single-option decision map. Nevertheless, Type 1 campaigns also exhibited as high flexibility as Type 2 campaigns in the multiple-option decision map, so Type 1 may still be considered if the program uncertainty is high.

[5] For Bennu, the average mass is $7.8 \times 10^{10}$ kg and the standard deviation is $1.0 \times 10^{10}$ kg, yielding the coefficient of variation (COV) of 0.13. Apophis has a much higher COV of 0.61 because its mass standard deviation ($2.5 \times 10^{10}$ kg) is large compared to its mass average ($4.1 \times 10^{10}$ kg).

# Chapter 7

# Conclusions

In this thesis, a new methodology for designing and assessing asteroid deflection campaigns is proposed. This methodology comprehensively incorporates multiple sources of epistemic uncertainty. Reducing their uncertainty levels is critical to the robustness of the resulting campaigns. The following sections present contributions and conclusions of this thesis, along with several areas of future research.

## 7.1 Thesis Summary

The goal of this thesis is robustification of asteroid deflection campaigns. The term "robustification" here means that campaigns are optimized to be less sensitive to the effects of stochastic perturbation or random variability that are inherent in the physical properties of an asteroid and the process of deflecting it. There are three distinct approaches for robustification: experimental , analytical, and numerical [111].[1] Experimental data is scarce in asteroid deflection techniques. The analytic approach is inappropriate owing to the complexity of deflection dynamics and nonlinearity of uncertainty propagation. Therefore, this thesis takes a numerical approach, relying on Monte Carlo simulations in particular. This enables us to predict variability in

[1]These approaches have in common that the random variability of inputs is controlled and reduced, such that the system can exhibit improved quality. They may also be applied to the policy-making aspect of asteroid mitigation, as well as to engineering system optimization, which is beyond the scope of this research.

outputs and find the optimum nominal values for the design inputs, which are two pillars of probabilistic design.

To identify the research gaps in previous studies, Chapter 1 provides a brief literature review in the related fields including astrodynamics, planetary defense, and campaign design. Located at the intersection of these three fields, the proposed framework, *asteroid deflection integrating epistemic uncertainties* (ADIEU), contributes not only to the asteroid mitigation research, but also promises spin-offs to each of these fields.

Chapter 2 details the latest developments in approaches towards the asteroid hazards problem. Detection of near-Earth objects has been progressing successfully through the *Spaceguard* program. Determination of asteroid impact risks is carried out by highly automated collision-monitoring systems, which catalogue the potential hazards over the next century. The most hazardous asteroids are ranked in the Sentry List, and this thesis thesis selected two of the top ten asteroids as case studies. Asteroid deflection techniques are still at the level of theoretical development or laboratory experiments, with a technology readiness level lower than 4, which motivated the following research questions: (1) Is it necessary to use a precursor to reduce deflection uncertainty? (2) If a precursor is needed, what type should we use?

Chapter 3 introduces the ADIEU framework, which designs optimally customized campaigns for asteroid deflection. Even using the same deflection technique, the deflection results differ from one asteroid to another because of asteroid-specific characteristics unknown a priori. Therefore, the framework explicitly considers comprehensive sources of uncertainty, in both the asteroid's position and physical characteristics. The framework should be implemented as flexibly as possible, however, so that it can be applied to a wide population of potentially hazardous asteroids.

Chapter 4 provides a mathematical formulation of optimizing asteroid deflection campaigns. Solving a numerical robustification problem often uses evolutionary algorithms to find the optimum nominal values for inputs. This chapter shows how a genetic algorithm is incorporated into the outer loop or front-end of the ADIEU framework. This chapter also explains spacecraft trajectory optimization using Chebyshev

polynomials, which work in the inner loop or back-end. The two algorithms complete the dual-loop optimization architecture.

Chapters 5 and 6 present the results from case studies of deflecting Apophis and Bennu, respectively. These asteroids have similar masses and impose nearly identical deflection requirements in terms of keyhole distributions. The difference in their momentum multiplication distributions, however, does result in distinct precursor choices, but the results show that multi-stage campaigns with any type of precursor outperform a single-stage mission in most cases. The only exception to this may be bery late launches before keyhole passages hwen there is no time to act on the information obtained by a precursor mission.

## 7.2 Limitations

Despite the aforementioned contributions of the ADEIU framework, it is still in its early design stages, with much room for improvement. The following are the current limitations of the ADIEU framework.

**(1) Fixed impact speed and impactor mass** The impact speed is fixed at 10 km/s, but it can be optimized to increase the probability of success and the robustness coefficient. For this fixed value, the CHEBYTOP program tends to produce a spacecraft trajectory whose terminal velocity vector is nearly collinear with the asteroid. This is no longer true for higher speeds, and the oblique angle between the two velocity vectors must be taken into account. Also, the beta distribution changes as the speed increase, which necessitates further updates in the current ADIEU framework. Also, the impactor mass was fixed to 500 kg in a Type 2 campaign due to optimization convergence issues. Because the current level of $\beta$ uncertainty reduction in Type 2 campaigns is somewhat optimistic, more refinements are necessary.

**(2) Single deflection method (kinetic impactor only)** This thesis only considered a kinetic impactor method because it has the highest level of technology readiness. However, this limits other choices such as a gravity tractor or nuclear det-

onation. Introducing a gravity tractor option would require a minimum amount of effort because it doesn not require any knowledge about the asteroid's $\beta$. In contrast, nucleaer detonation would require extra knowledge about the asteroid's internal structures to predict whether the asteroid would break and where the fragments would go if it breaks.

**(3) Single propulsion method (electric propulsion only** The CHEBTYOP program can only optimize low-thrust trajectories. However, chemical propulsion is much faster than electric propulsion while providing as flexible launch windows as electric propulsion.

**(4) Issues of unnecessary precursors or redundancy** The current framework assumes that the ephemeris uncertainty has been reduced to be conclusive of 100% probability of impact. However, it is also possible that additional measurements by a preliminary orbiter completely preclude this impact probability. In this case, the value of the precursor itself may be questionable becasue it does not have to support the subsequent impactor anymore. Another possible, opposite scenario is when the entire campaign is jeopardized because of one single mission failure. These two extreme cases are not taken into account in the current framework.

## 7.3 Future Work

The ADIEU framework is still in its early development stage. Therefore, the framework requires further refinement in its the simulation model. For example, the future work could focus on sizing the spacecraft subsystems n more detail, beyond the system-level architecture considered in this thesis. Another possible direction to improve the ADIEU framework is expansion of the design space, which can be done in the following ways.

**(1) Variable impact velocity and launch dates (for limitation 1)** The impact velocity is fixed at 10 km/s in the current ADIEU framework. Varying the impact velocity changes the dynamics of momentum transfer, and hence the $\beta$ distri-

bution). Another potential improvement is to consider launch capabiilties for more realistic missions. The current framework assumes that the preliminary impactor and the preliminary orbiter are launched at the same time onboard the identical launch vehicle. This approach saves launch costs, but launching the two precursors on different dates may lead to faster transfer orbits and more favorable impact velocities. The trade studies of launch opportuniteis are left for future work.

**(2) Other deflection methods (for limitation 2)** Since the 2006 release of the NASA report which did not acknowledge the effectiveness of "slow-push" methods, there have been attempts to improve the effectiveness of these methods. For example, Mazanek et al. (2015) proposed a concept called *enhanced gravity tractor*, which may shorten the deflection time by orders of magnitude. In this scheme, the spacecraft grasps boulders on the asteroid surface, takes off the asteroid, and stays close to it. Because the spacecraft mass is augmented with the boulder mass, the gravitational forces coming from mutual attraction between the asteroid and the spacecraft will be multiplied by several factors. Electromagetic forces also exert force on metallic asteroids, orders of magnitude greater than pure gravity. Solar-sails or albedo alteraton methods [96] may also be considered.

**(3) Chemical propulsion (for limitation 3)** The ballistic trajectories with chemical propulsion can be easily optimized by solving Lambert's problem. Considering both chemical propulsion and electric propulsion would create more campaign architectures, such as hybrid schemes with mixed propulsion choise among different mission phases.

**(4) Modular or distributed architectures (for limtation 4)** The current ADIEU framework implement temporal distribution in the form of multiple stages in a deflection campaign, but each stage is considered as a monolithic spacecraft in the current framework. Increasing the degree of distribution further, the framework may consider modular or fractionated architectures of the impactor spacecraft. Equipped with modular and adjustable impact mass, the impactor spacecraft no longer needs to wait until the precursor spacecraft returns the in-situ information of the target as-

teroid. With this spatial distribution, it is also conceivable to launch extra impactors between launch windows in case of a mission failure

**(5) Astronomical measurement (for limitation 4)**

The ADIE framework should incorporate astronomical measurements (space based telescopes discussed in 2.1.1) which might give the definitive ephemeris knowledge (0 or 100% chance of impact) at a fraction the cost of a spacecraft to the asteroid.

**(6) Precursor to visit multiple asteroids (for limitation 4)** The cost of a Type 1 precursor might be saved by means of amortization. The precursor spacecraft does not need to be bound to one asteroid. It can fly by the asteroid to visit other asteroids, as long as its propellant allows, and can even be used as an impactor at the end of its life. In contrast to the dedicated orbiter case, the error in the asteroid position will grow again after a fly-by, but the mass uncertainty can still be reduced significantly, unless a "beacon" is deployed by the precursor. Consideration of the multiple-visits option may result in a multiple-asteroid mitigation campaign, which could decrease the mitigation cost per asteroid, at the cost of increasing overall campaign complexity. Fig. 7-1 illustrates that the mass of precursors may be reduced if one precursor visits 2 to 4 asteroids, assuming a IMLEO-to-dry-mass ratio of 1.5 (or mass ratio of 2/3) for each flight leg via electric propulsion. The mass for a one-spacecraft tour increase exponentially, exceeding the mass of dedicated sorties if the number of visited asteroid is greater than 4.

One can easily imagine that incorporating these expansions will lead to an explosion of the design space as well as the objective space. The genetic algorithm used in this thesis should be adapted to this, necessitating the use of a multi-objective genetic algorithm.

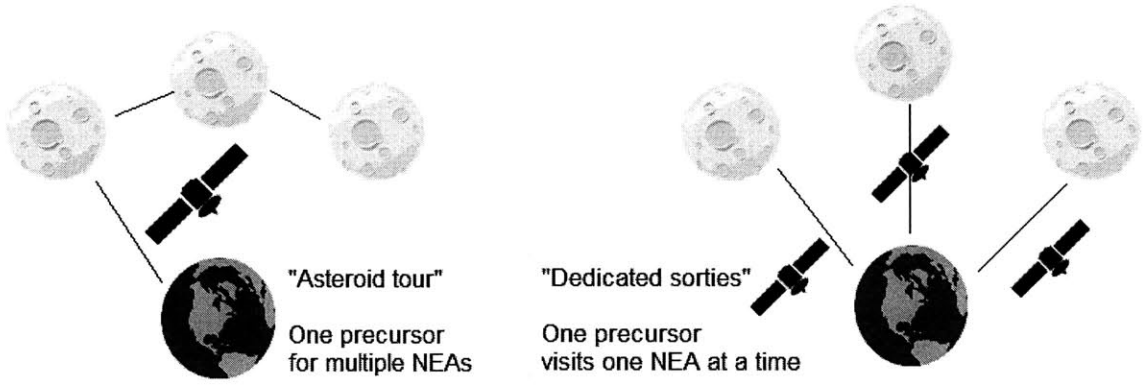


| Asteroids | Tour | Dedicated | (T-D)/D*100 |
|---|---|---|---|
| 1 | 1.5 | 1.5 | 0 |
| 2 | 2.25 | 3 | 25 |
| 3 | 3.375 | 4.5 | 25 |
| 4 | 5.0625 | 6 | 15.625 |
| 5 | 7.59375 | 7.5 | -1.25 |
| 6 | 11.39063 | 9 | -26.5625 |
| 7 | 17.08594 | 10.5 | -62.7232 |
| 8 | 25.62891 | 12 | -113.574 |

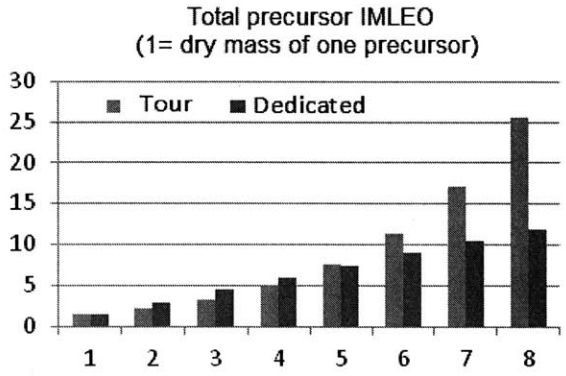


Figure 7-1: Comparison of dedicated sorties and asteroid tour as precursor options

## 7.4 More Applications

Another research direction, besides improving the framework itself, could be application of the framework to other disciplines. This chapter concludes with two examples, one for updating the Sentry List and the other for terrestrial medical applications.

- **Deflection Campaigns for Comets**

From its beginning, the ADIEU framework was conceived to be applicable to any population of near-Earth asteroids so long as they have gravitational keyholes near Earth. However, the framework may be applied to near-Earth comets as well, by

varying the target body's mass. For example, the following function may be used to describe the mass loss of a comet [112].

$$M(t) = \frac{1}{2}(M_i + M_f) - (M_i - M_f)\tanh\frac{2t}{T} \tag{7.1}$$

where $M_i$ is the initial mass, $M_f$ is the final mass, and $T$ is the mass-loss interval. Considering both asteroids and comets, the framework can now tell us which near-Earth object is more difficult to deal with.

- **Modification of the Sentry List**

In difficult cases, the probability for a campaign to succeed is low, or the object remains hazardous even after deflection is made. Therefore, it is conceivable to come up with a *post-deflection* Sentry List that accounts for remaining risks after reducing them through mitigation efforts.

- **Medical Applications**

In the medical practice of treating cancers, biopsy and surgical resection act as Type 1 and Type 2 precursors in asteroid deflection campaigns. Biopsy minimizes the mortality risks associated with the diagnostic surgery, but its accuracy and reliability may be questionable, highly influenced by individual surgeon's expertise [113]. In contrast to biopsy, surgical resection minimizes the likelihood of sampling error by providing considerably more tissue for histological analysis. However, the process exposes the patient to greater risk. The same problem associated with "value of information" may be applied to vaccine manufacturing as well.

# Appendix A

# Terminology

A *minor planet* is an object in the solar system that is neither a planet nor a comet. Minor planets can be dwarf planets, asteroids, trojans, centarus, Kuiper belt object, and other trans-Neptunian objects. The term *planetoid* is also used, especially for larger objects. In 2006, the International Astronomical Union (IAU) reclassified minor planets and comets into *dwarf planets* and *small Solar System bodies* (SSSB) [114]. Dwarf planets are objects whose gravity is sufficient to form an ellipsoidal shape. All other minor planets and comets are called SSSB. Figure A-1 shows the different types of bodies in the Solar System. Note the different boundaries in old classification and new classification. Figure A-2 illustrates SSSBs and their products.

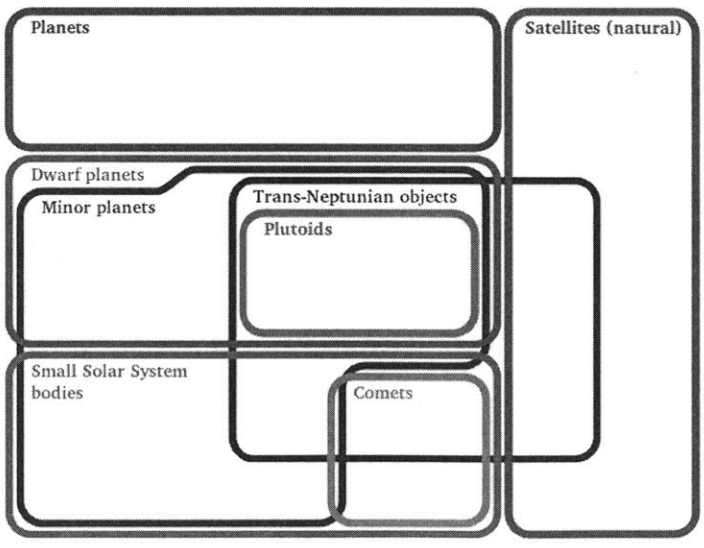


Figure A-1: Types of boies in the Solar System [40]

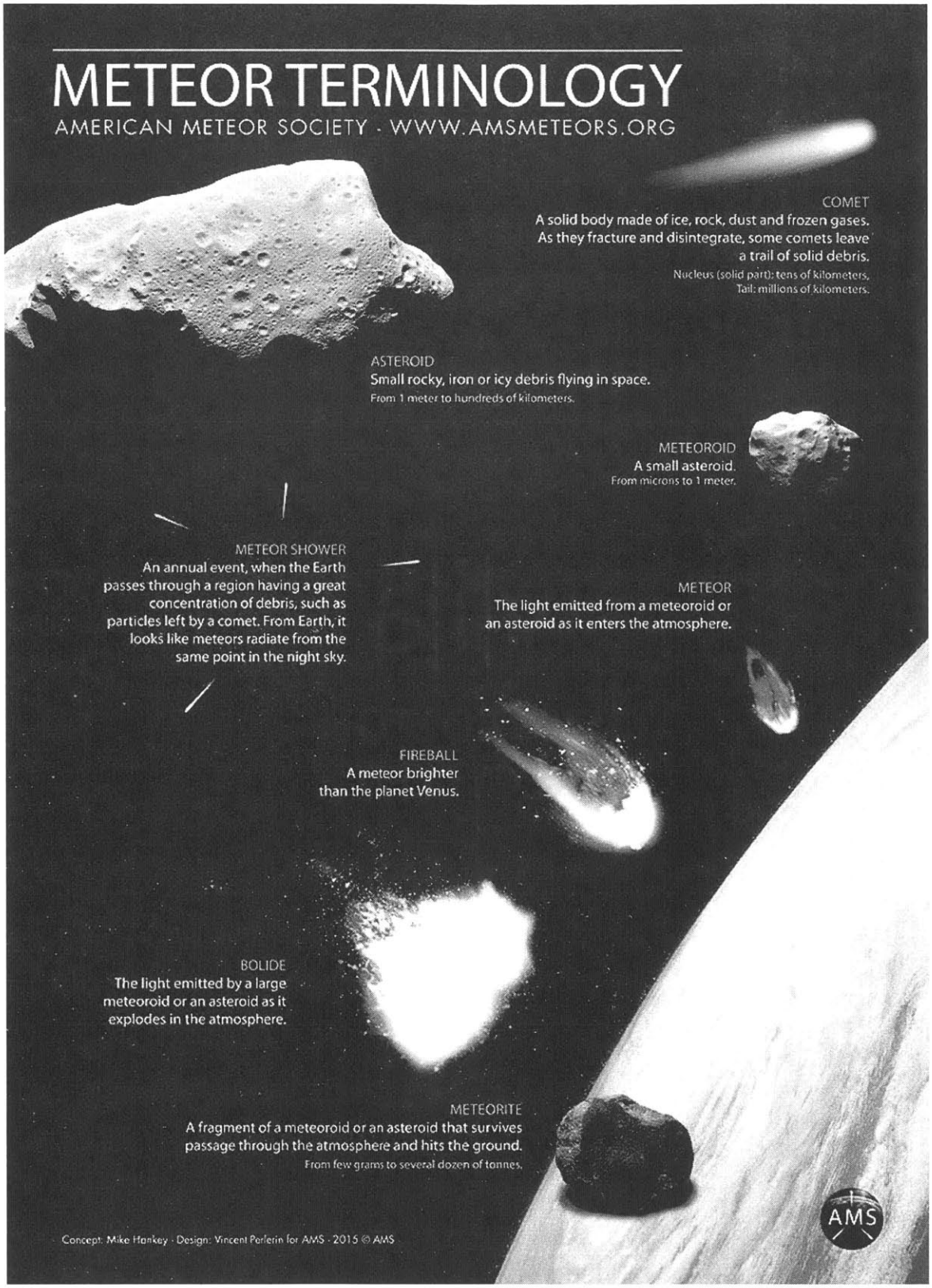


Figure A-2: Meteor Terminology [40]

The IAU defines *meteoroids*[1] as objects "of a size considerably smaller than an asteroid and considerably larger than an atom," between 10 microns and 1 meter in diameter [115,116]. Objects maller than meteoroids are classified as micrometeoroids (several microns) and space/cosmic dust (less than 0.1 micron). The streak of light created by a meteoroid entering the Earth's atmosphere is called a *meteor.*[2] If the meteoroid survives the atmospheric re-entry to reach the ground, then these remnants are called *meteorites.* A *fireball* is another term for a very bright meteor, generally brighter than magnitude -4, which is about the same magnitude of the planet Venus in the morning or evening sky. A *bolide* is a special type of fireball which explodes in a bright flash. Its apparent magnitude could be -14 or brighter, which is more than twice as bright as the full moon [117]. A *superbolide* is a bolide which reaches an apparent magnitude of -17 or brighter.

In terms of orbital elements, NEOs are asteroids and comets with perihelion distance q less than 1.3 AU. Near-Earth Comets (NECs) are further restricted to include only short-period comets (i.e orbital period P less than 200 years). The vast majority of NEOs are asteroids, referred to as Near-Earth Asteroids (NEAs). NEAs are divided into groups (Aten, Apollo, Amor) according to their perihelion distance ($r_p$), aphelion distance ($r_a$) and their semi-major axes ($a$). An Earth-crosser is a near-Earth asteroid whose orbit crosses that of Earth as observed from the ecliptic pole of Earth's orbit.

[1]This term is not being used by the Minor Planet Center.

[2]Meteors were once thought to be a purely atmospheric phenomena, and the study of these and other atmospheric effects, especially weather, spawned the science of meteorology. It was not until the mid-1800s that the extra-terrestrial nature of meteors was widely recognized [40].

| Group | Description | Definition |
|---|---|---|
| **NEC** | Near-Earth Comets | $r_a$< 1.3 AU, $P$<200 years |
| **NEA** | Near-Earth Asteroids | $r_a$< 1.3 AU |
| **Aitra(s)** | NEAs whose orbits are contained entirely within the orbit of the Earth, also known as Apohele(s) or Inner-Earth objects (IEOs) | $a$< 1.0 AU, $r_a$< 0.983 AU |
| **Aten(s)** | Earth-crossing NEAs with semi-major axes *smaller* than Earth's | $a$< 1.0AU, $r_a$> 0.983 AU |
| **Apollo(s)** | Earth-crossing NEAs with semi-major axes *larger* than Earth's | $a$> 1.0AU, $r_p$> 1.017 AU |
| **Amor(s)** | NEAs with orbits exterior to Earth's but interior to Mars' | $a$> 1.0AU, 1.017 AU <$r_p$<1.3 AU |

Table A.1: Classification of Near-Earth Objects

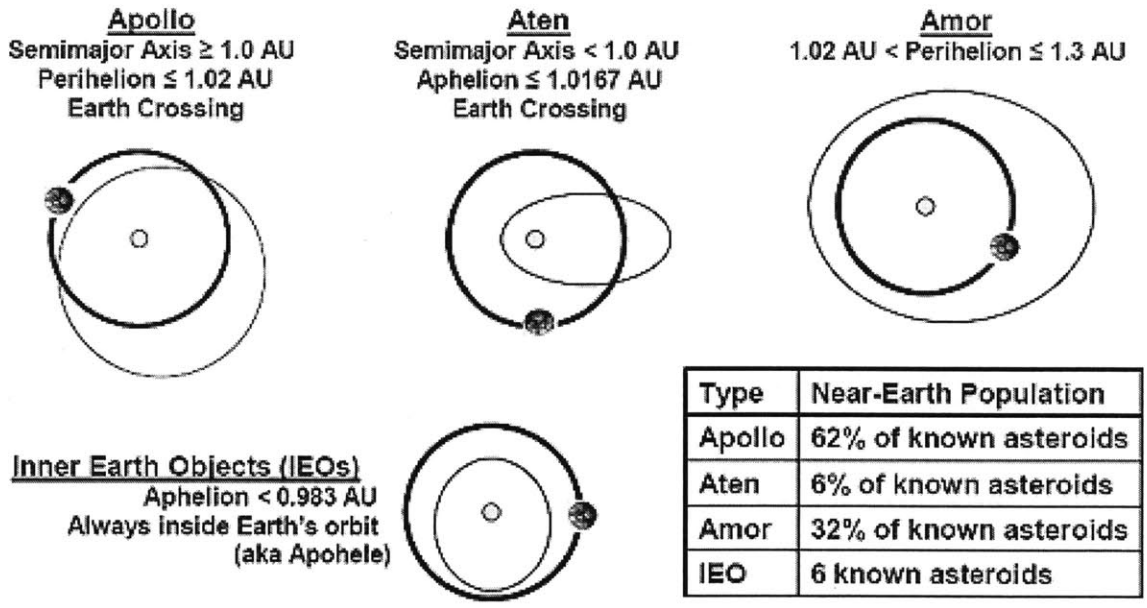


Figure A-3: Near-Earth Asteroid Orbit Types [6]

More generally, asteroid orbits can be categorized with regard to other planets as well. Fig. A-4 shows six categories of asteroid orbits relative to the perihelion and aphelion of a planet. The minor planets discovered so far include Mercury-crossers, Venus-crossers, Mars-crossers, Jupiter-crossers, Saturn-crossers, and so forth. Apollo and Aten are special cases of Earth-crossers.

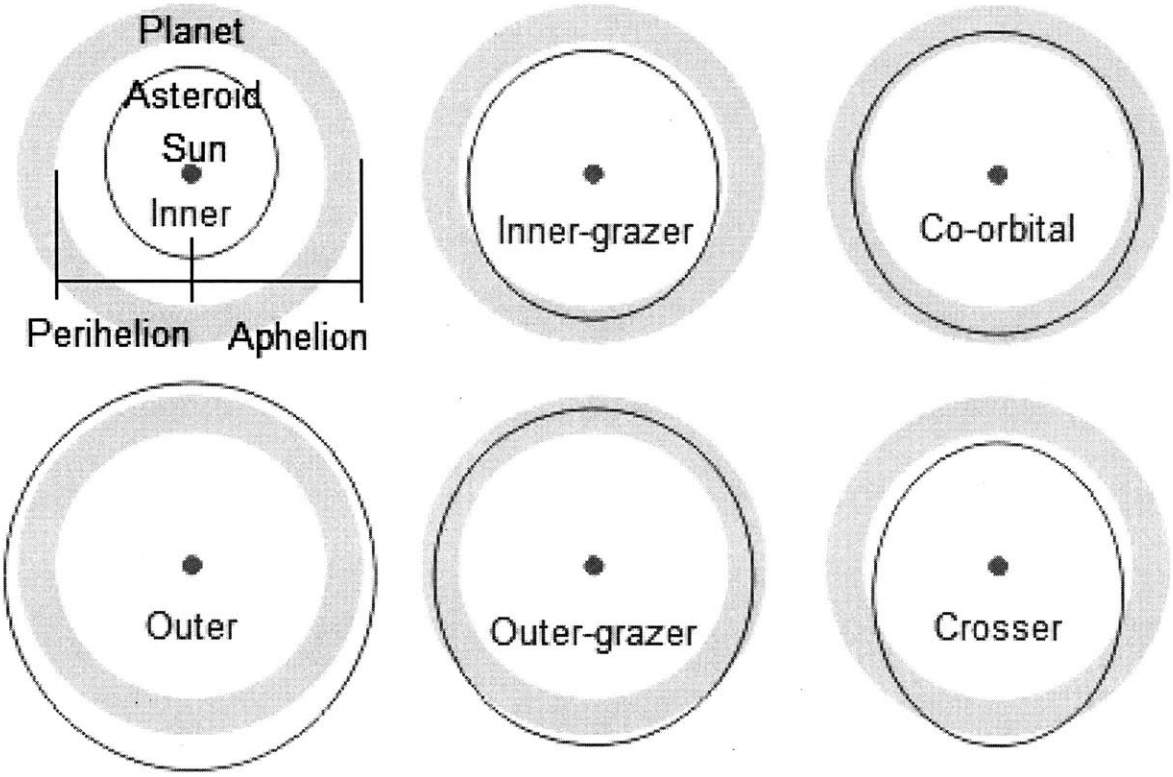


Figure A-4: General Orbit Types [41]

# Appendix B

# B Plane Derivation

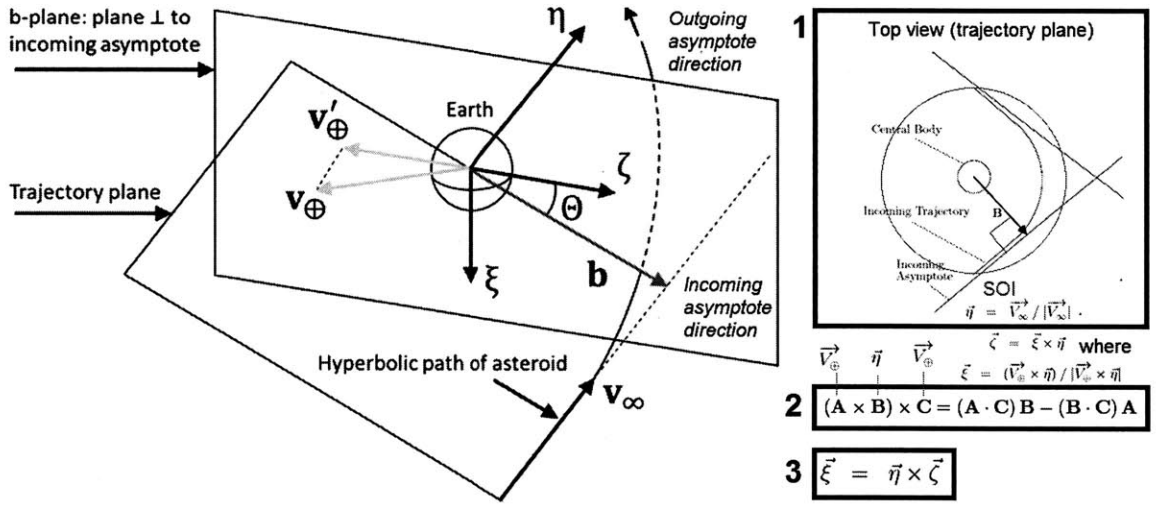


Figure B-1: Definition of B-plane Axes [20]

The equations described in 2.2.1 were used in the ADIEU framework, but there is an alternative derivation which closely follows the coordinate geometry definitions more closely.

(1) The positive $\eta$-axis is obtained from the asteroid's velocity relative to Earth. That is, $\overrightarrow{V_\infty} = \overrightarrow{V}_{asteroid} - \overrightarrow{V_\oplus}$. The asteroid velocity is taken right before it enters the EarthâĂŹs sphere of influence (Fig. B-1, box 1).

(2) Next, the negative $\zeta$-axis is aligned with the b-plane projection of the Earth's heliocentric velocity. This can be done by replacing $\overrightarrow{A}, \overrightarrow{B}, \overrightarrow{C}$ in the vector identity (Fig. B-1, box 2) with $\overrightarrow{V_\oplus}, \overrightarrow{\eta}, \overrightarrow{V_\oplus}$.

(3) Obtain $\overrightarrow{\xi}$ by vector-crossing $\overrightarrow{\eta}$ and $\overrightarrow{\zeta}$.

Figure B-2 illustrates difference between the deflection distance before the B-plane coordinates transformation ($\delta$) and the deflection distance after coordinates transformation ($\zeta$). The difference is less than 10 % for Bennu but may be significantly higher for other asteroid cases. Also, $\delta$ contains the magnitude of deflection but does not contain information about the direction of deflection ($\delta$ is always positive). The $\zeta$ coordinate on the b-plane contains both kinds of information. If the deflection increases the orbit energy (spacecraft faster than asteroid), its sign is positive. If the deflection decreases the orbit energy (spacecraft slower than asteroid), then its sign is negative because the $\theta$ angle in Fig. B-1 (or the $\psi$ angle in 2.2.1) is 180 degrees.

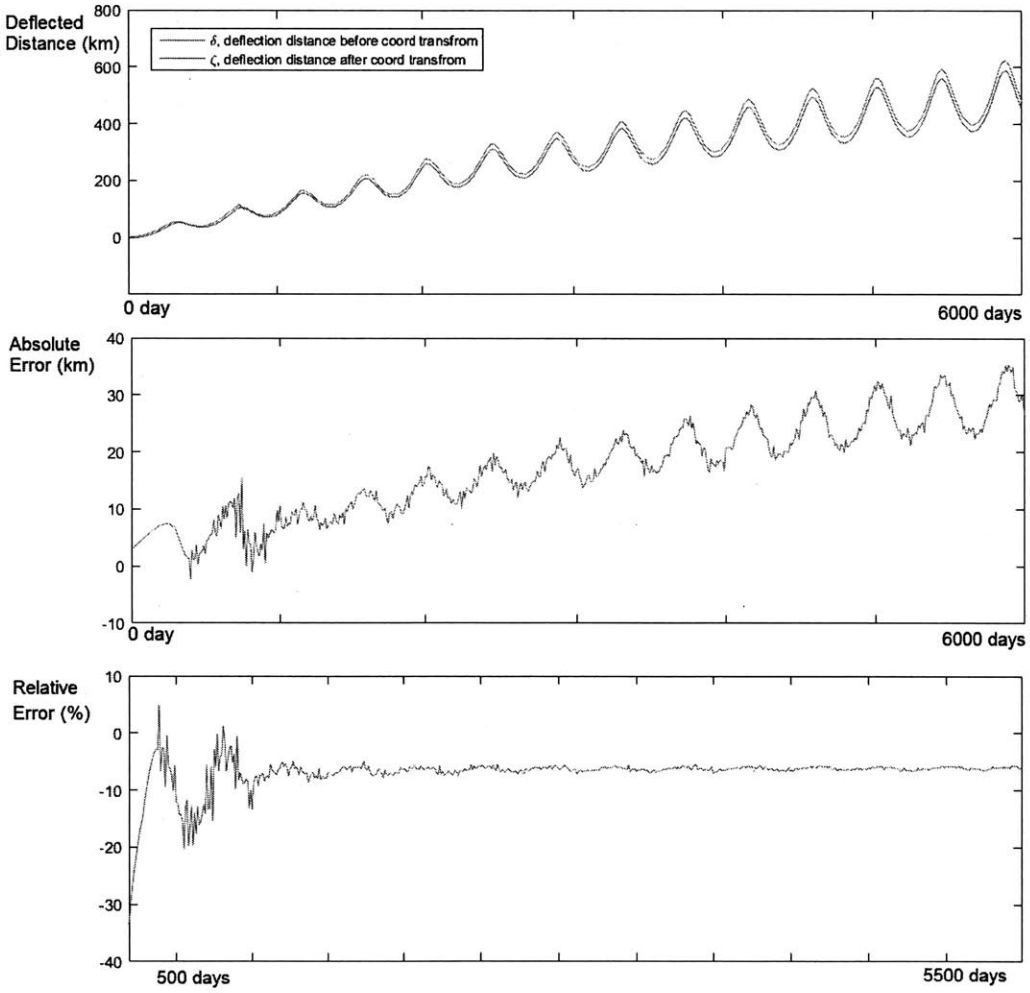


Figure B-2: Deflection distance of Bennu ($\Delta v = 0.37$ mm/s)

# Appendix C

# Chebyshev Polynomials and CHEBYTOP

Chebyshev polynomials (of the first kind), denoted as $T_n(x)$, are defined as the solutions to the Chebyshev differential equation

$$(1-x^2)y'' - xy' + n^2 y = 0 \tag{C.1}$$

They are defined using the following recurrence relationship:

$$T_0(x) = 1, T_1(x) = x \tag{C.2}$$

$$T_{n+1}(x) = 2xT_n(x) - T_{n-1}(x) \tag{C.3}$$

where $T_2(x) = 2x^2-1$, $T_2(x) = 4x^3-3x$, $T_3(x) = 8x^4-8x^2+1$, $T_4(x) = 16x^5-20x^3+5$, and so forth, can be obtained, as shown in Fig. C-1.

Chebyshev polynomials are important in approximation theory because the roots of the Chebyshev polynomials of the first kind, which are also called Chebyshev nodes, are used as nodes in polynomial interpolation:

$$x_k = \cos\frac{2k-1}{2n}\pi \tag{C.4}$$

where $k = 1, 2, ..., n$. Figure C-2 illustrates that the non-uniform distribution of

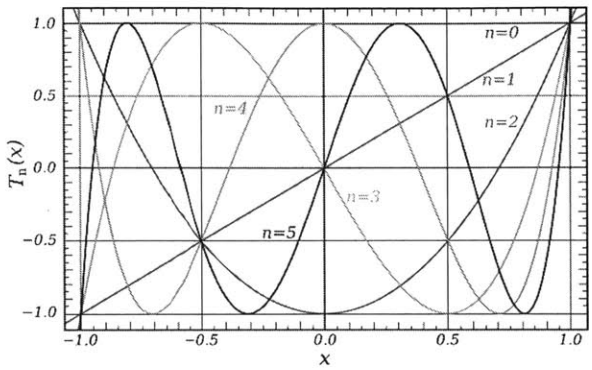


Figure C-1: Chebyshev polynomials with degree $n = 1, .., 5$ [42]

Chebyshev nodes on interval [-1,1] comes from the uniform angular distribution on the unit circle.

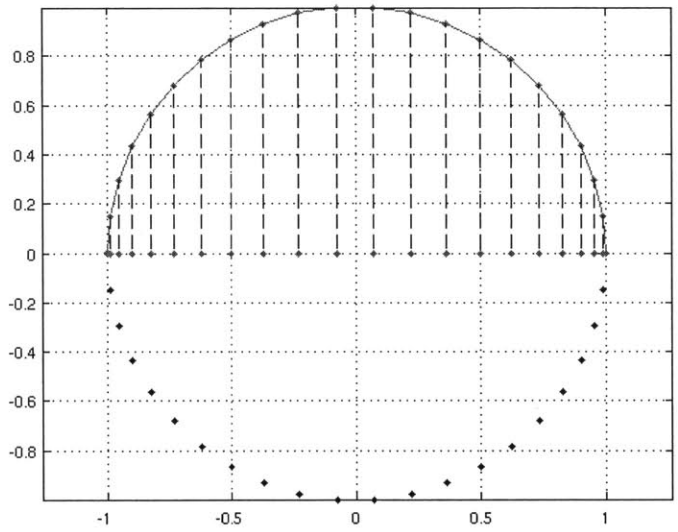


Figure C-2: Chebyshev nodes with $n = 10$ [43]

This is because the coefficients of Chebyshev polynomials are identical to those of $(\cos\theta)^n$ terms expanded from $\cos(n\theta)$. In other words, Chebyshev polynomials can also be defined using a trigonometric relation.

$$T_n(x) = \cos(n \arccos(x)) \tag{C.5}$$

$$T_n(\cos\theta) = T_n(n\theta) \tag{C.6}$$

The CHEBYTOP program was chosen because it is easy to use and not subject to ITAR restrictions, but there are many other low-thrust trajectory design tools, as shown in Fig. C-3. The user-friendliness was rated for each from 1 to 10, with 10 being the easiest to use. The BOLD fontmeans the "Best in Category" for each feature [44].

**Low Thrust Software/Code/Tool Comparison/Summary Table**

**Bold entry is "Best in Category"**

| Feature: / Code: | Direct/ Indirect | Method / submethod: | User-Friendly | Appli-cation | Turn-around Capability | Easily Converged | Self-starting | Fide-lity |
|---|---|---|---|---|---|---|---|---|
| **CHEBYTOP** | Indirect | Chebyshev polynomial approx. for traj. segments | 4 | Narrow | Small | Yes | Yes | Low |
| **CHEBYTOP / ss** | Indirect | Chebyshev polynomial approx. for traj. segments | 5 | Narrow | **VeryLarge** | **Yes** | **Yes** | Low |
| **CHEBYTOP/MdIC** | Indirect | Chebyshev polynomial approx. for traj. segments | 5 | Very Narrow | Large | Yes | Yes | Low |
| **QT2 (QuickTOP II** | Indirect | Chebyshev polynomial approx. for traj. segments | 5 | Narrow | Medium | Sometimes | Yes | Low |
| **CHEBYTOP/func/s** | Indirect | Chebyshev polynomial approx. for traj. segments | 5 | Very Narrow | Large | Yes | Yes | Low |
| **SEPSPOT** | Indirect | Averaging techniques for planetocentric problems | **6** | Narrow | Large | Yes | No | Med |
| **VARITOP** | Indirect | Variational & optimal control using 2PBVP solution | 3 | Broad | ~Large | Sometimes | No | Med |
| **VARITOP/Jupiter** | Indirect | Variational & optimal control using 2PBVP solution | 3 | ~broad | ~Large | Sometimes | No | Med |
| **SEPTOP** | Indirect | Variational & optimal control using 2PBVP solution | 2 | Mid | ~Large | Sometimes | No | Med |
| **NEWSEP** | Indirect | Variational & optimal control using 2PBVP solution | 2 | Narrow | ~Large | No | No | Med |
| **Sail** | Indirect | Variational & optimal control using 2PBVP solution | 2 | Narrow | ~Large | Sometimes | No | Med |
| **GALLOP** | Direct | Parameter optimization(NPOPT | 4 | Broad | Large | Sometimes | Maybe | Med |
| **Mystic** | Direct | Static / Dynamic Control | **6,w/ GUI** | **Very Broad** | ~medium | Sometimes | No | **High** |
| **OTIS** | Direct | Collocation (Hermite-Simpson nodes) | 4 | Broad | Large | No | No | Med |
| **SNAP** (Num. Integr.) | N/A | Not Applicable | 5 | Mid | Large | Not App | Not App | **High** |
| **ESPAS** environment | N/A | Gradient based optimization | 5 | Broad | Large | Sometimes | Yes | Med |
| **RAPTOR** (Earth-Mars) | Indirect | Variational & optimal control using 2PBVP solution w/ a GA to initiate guesses | 6 | Narrow | Small | Yes | Yes | Low |
| **Copernicus** | Direct/ Indirect /Hybrid | Constrained Parameter Optimization (SQP)/Optimal Control using Multi-PBVP | 3 | very broad | ~Large | Sometimes | No | High |

Figure C-3: Low thrust trajectory tools [44]

Figure C-3 compares the fidelity levels of the low-thrust tools. As can be seen, the low fidelity tools (including CHEBYTOP) have greater turn-around capability at the expense of being applicable to fewer types of missions and analyses. Incorporating state-of-the-art tools with higher fidelity into the ADIEU framework is left as future work.

JPL GRC JSC

Bold entry is "Best in Category"

| Feature: / Code: | Direct/ Indirect | Method / submethod: | 3-body, N-body | Multi-Leg, Int Bdy Flyby | Tour Capability | Out-of-Plane? | Documentation |
|---|---|---|---|---|---|---|---|
| CHEBYTOP | Indirect | Chebyshev polynomial approx. for traj. segments | No / No | No / No | No | No | ~3 pg UG/X |
| CHEBYTOP / ss | Indirect | Chebyshev polynomial approx. for traj. segments | No / No | No / No | No | No | ~3 pg UG/X |
| CHEBYTOP/MdlC | Indirect | Chebyshev polynomial approx. for traj. segments | No / No | Yes/Yes, 1 | No | No | ~3 pg UG/X |
| QT2 (QuickTOP II | Indirect | Chebyshev polynomial approx. for traj. segments | No / No | No / No | No | No | Ug/Xmp/Thry |
| CHEBYTOP/func/s | Indirect | Chebyshev polynomial approx. for traj. segments | No / No | No / No | No | No | ~3 pg UG/X |
| SEPSPOT | Indirect | Averaging techniques for planetocentric problems | NotAppl. | Not Appl. | No | Yes | ~200pg |
| VARITOP | Indirect | Variational & optimal control using 2PBVP solution | No / No | Yes/Yes, <3 | No | Yes | U/X/T |
| VARITOP/Jupiter | Indirect | Variational & optimal control using 2PBVP solution | No / No | Yes/Yes, <3 | ~Yes | Yes | 0 pg |
| SEPTOP | Indirect | Variational & optimal control using 2PBVP solution | No / No | Yes/Yes, <3 | No | Yes | ?? |
| NEWSEP | Indirect | Variational & optimal control using 2PBVP solution | No / No | Yes/Yes, <3 | No | Yes | 0 pg |
| Sail | Indirect | Variational & optimal control using 2PBVP solution | No / No | No? / No? | No | Yes | UG |
| GALLOP | Direct | Parameter optimization(NPOPT | No / No | Yes/Yes, N | Yes | Yes | UG/X |
| **Mystic** | Direct | Static / Dynamic Control | **Yes/Yes** | **Yes/Yes** | **Yes** | **Yes** | **U/X/T** |
| OTIS | Direct | Collocation (Hermite-Simpson nodes) | Yes?/ No | Yes/Yes, n | Yes | Yes | Ug/Xm/Th |
| SNAP (Num. Integr.) | N/A | Not Applicable | Yes / Yes | Yes/Yes, n | Yes | Yes | u/x/t |
| ESPAS environment | N/A | Gradient based optimization | Yes?/ No | yes/yes, n | Yes | Yes | UG/X |
| RAPTOR (Earth-Mars) | Indirect | Variational & optimal control using 2PBVP solution w/ a GA to initiate guesses | *No / No* | No / No | No | Yes | Ug/Xmp/Thry |
| Copernicus | Direct/ Indirect /Hybrid | Constrained Parameter Optimization (SQP)/Optimal Control using Multi-PBVP | Yes / Yes | Yes / Yes, ? | Yes | Yes | 90 pg, Theory (2 pprs) |

Figure C-4: Low thrust trajectory tools (continued) [44]

# Appendix D

# Results (Apophis)

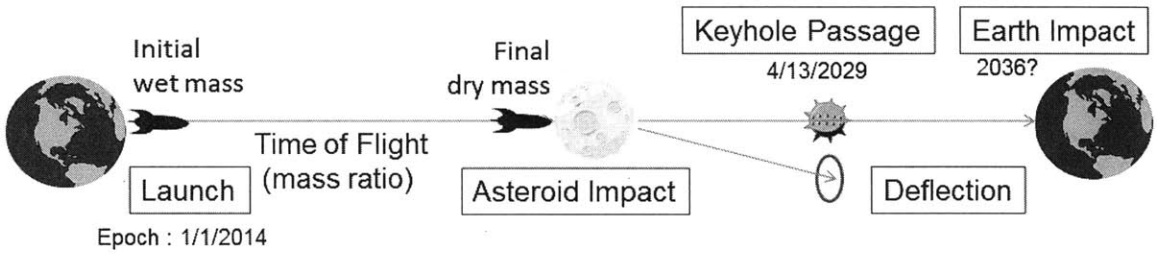


Figure D-1: Overview of an Apophis deflection campaign (max duration = 5,500 days

## D.1 Apophis, Type 0 Campaigns (90% and 99%)

Table D.1: Type 0 Campaign Parameters (POS = 90% and POS = 99%)

| $t^1_{start}$ *days* | $IMLEO$ *kg* | $C_{max}+1$ *km/yr* | $\frac{IMLEO}{C_{max}+1}$ *kg yr/km* | $\Delta t^1$ *days* | $\frac{m_{impactor}}{IMLEO}$ - | $m_{impactor}$ *kg* |
|---|---|---|---|---|---|---|
| 0 | 910 | 9 | 101.1 | 1200 | 0.7082 | 644 |
| 100 | 910 | 9 | 101.1 | 1090 | 0.6911 | 629 |
| 200 | 910 | 9 | 101.1 | 990 | 0.6906 | 628 |
| 300 | 920 | 9 | 102.2 | 890 | 0.6843 | 630 |
| 400 | 990 | 10 | 99 | 1120 | 0.7096 | 702 |
| 500 | 990 | 10 | 99 | 1020 | 0.7077 | 701 |
| 600 | 990 | 10 | 99 | 920 | 0.7076 | 700 |
| 700 | 1040 | 11 | 94.5 | 1150 | 0.7270 | 756 |
| 800 | 1060 | 11 | 96.4 | 1050 | 0.7186 | 762 |
| 900 | 1050 | 11 | 95.5 | 950 | 0.7188 | 755 |
| 1000 | 1030 | 11 | 93.6 | 840 | 0.7149 | 736 |
| 1100 | 1130 | 12 | 94.2 | 1080 | 0.7317 | 827 |
| 1200 | 1140 | 12 | 95.0 | 980 | 0.7295 | 832 |
| 1300 | 1100 | 12 | 91.7 | 870 | 0.7262 | 799 |
| 1400 | 1100 | 12 | 91.7 | 770 | 0.7267 | 799 |
| 1500 | 1110 | 12 | 92.5 | 670 | 0.7225 | 802 |
| 1600 | 1140 | 12 | 95.0 | 580 | 0.7272 | 829 |
| 1700 | 1190 | 13 | 91.5 | 800 | 0.7352 | 875 |
| 1800 | 1150 | 13 | 88.5 | 690 | 0.7342 | 844 |
| 1900 | 1140 | 13 | 87.7 | 580 | 0.7187 | 819 |
| 2000 | 1520 | 16 | 95.0 | 1130 | 0.6600 | 1003 |
| 2100 | 1130 | 13 | 86.9 | 370 | 0.7167 | 810 |
| 2200 | 1130 | 13 | 86.9 | 280 | 0.7303 | 825 |
| 2300 | 1120 | 13 | 86.2 | 180 | 0.7316 | 819 |
| 2400 | 1660 | 18 | 92.2 | 1060 | 0.6752 | 1121 |
| 2500 | 1660 | 18 | 92.2 | 910 | 0.6629 | 1100 |
| 2600 | 1900 | 21 | 90.5 | 1190 | 0.6922 | 1315 |
| 2700 | 1900 | 21 | 90.5 | 1080 | 0.6824 | 1297 |
| 2800 | 1860 | 21 | 88.6 | 980 | 0.6836 | 1272 |

Table D.2: Type 0 Campaign Parameters (POS = 90% and 99%, continued)

| $t^1_{start}$ | $IMLEO$ | $C_{max}+1$ | $\frac{IMLEO}{C_{max}+1}$ | $\Delta t^1$ | $\frac{m_{impactor}}{IMLEO}$ | $m_{impactor}$ |
|---|---|---|---|---|---|---|
| *days* | *kg* | *km/yr* | *kg yr/km* | *days* | - | *kg* |
| 2900 | 2280 | 26 | 87.7 | 1210 | 0.7107 | 1620 |
| 3000 | 2290 | 26 | 88.1 | 1110 | 0.6980 | 1599 |
| 3100 | 2320 | 26 | 89.2 | 1010 | 0.6983 | 1620 |
| 3200 | 2160 | 26 | 83.1 | 880 | 0.6881 | 1486 |
| 3300 | 2930 | 33 | 88.8 | 1140 | 0.7191 | 2107 |
| 3400 | 2970 | 33 | 90.0 | 1040 | 0.7133 | 2118 |
| 3500 | 2960 | 33 | 89.7 | 940 | 0.7129 | 2110 |
| 3600 | 2850 | 32 | 89.1 | 790 | 0.6540 | 1864 |
| 3700 | 3920 | 46 | 85.2 | 1060 | 0.7195 | 2820 |
| 3800 | 3920 | 46 | 85.2 | 960 | 0.7190 | 2818 |
| 3900 | 3920 | 46 | 85.2 | 860 | 0.7185 | 2817 |
| 4000 | 4150 | 47 | 88.3 | 770 | 0.7249 | 3008 |
| 4100 | 4210 | 47 | 89.6 | 670 | 0.7124 | 2999 |
| 4200 | 4110 | 45 | 91.3 | 540 | 0.6283 | 2582 |
| 4300 | 3890 | 45 | 86.4 | 450 | 0.6967 | 2710 |
| 4400 | 4990 | 55 | 90.7 | 620 | 0.6095 | 3042 |

## D.2 Apophis, Type 1 Campaigns (90% and 99%)

Table D.3: Type 1 Campaign Parameters (POS = 90% and POS = 99%)

| $t^1_{start}$ *days* | $m$ *kg* | $C_{max}+1$ *km/yr* | $\frac{m}{C_{max}+1}$ *kg yr/km* | $\Delta t^1$ *days* | $t^2_{start}$ *days* | $\Delta t^2$ *days* |
|---|---|---|---|---|---|---|
| 0 | 1070 | 24 | 44.6 | 1080 | 2656 | 770 |
| 100 | 1204 | 23 | 52.3 | 1479 | 2698 | 416 |
| 200 | 1219 | 27 | 45.2 | 890 | 2810 | 914 |
| 300 | 1100 | 25 | 44.0 | 968 | 2845 | 583 |
| 400 | 1008 | 23 | 43.8 | 624 | 2850 | 1231 |
| 500 | 992 | 23 | 43.1 | 881 | 2982 | 762 |
| 600 | 1149 | 21 | 54.7 | 1149 | 1336 | 2965 |
| 700 | 1067 | 22 | 48.5 | 1064 | 2990 | 798 |
| 800 | 1045 | 22 | 47.5 | 780 | 3080 | 411 |
| 900 | 1039 | 23 | 45.2 | 1090 | 3106 | 962 |
| 1000 | 1285 | 27 | 47.6 | 902 | 3188 | 595 |
| 1100 | 994 | 21 | 47.3 | 859 | 3202 | 1220 |
| 1200 | 1023 | 23 | 44.5 | 785 | 3271 | 470 |
| 1300 | 1035 | 19 | 54.5 | 860 | 3390 | 1220 |
| 1400 | 999 | 19 | 52.6 | 838 | 3378 | 1059 |
| 1500 | 1025 | 21 | 48.8 | 839 | 3480 | 1225 |
| 1600 | 982 | 22 | 44.6 | 909 | 3520 | 574 |
| 1700 | 1025 | 21 | 44.8 | 1059 | 3560 | 820 |
| 1800 | 1198 | 26 | 46.1 | 505 | 3560 | 550 |
| 1900 | 1034 | 25 | 41.4 | 537 | 3662 | 430 |
| 2000 | 1011 | 22 | 46.0 | 988 | 3640 | 767 |
| 2100 | 1028 | 19 | 54.1 | 847 | 3800 | 890 |
| 2200 | 1155 | 23 | 50.2 | 591 | 3747 | 603 |
| 2300 | 1044 | 25 | 41.8 | 510 | 3815 | 260 |
| 2400 | 1213 | 23 | 52.7 | 758 | 3877 | 603 |
| 2500 | 1075 | 23 | 46.7 | 1191 | 3965 | 755 |
| 2600 | 1094 | 28 | 39.1 | 840 | 3970 | 410 |
| 2700 | 1139 | 22 | 51.8 | 1061 | 4097 | 347 |
| 2800 | 988 | 19 | 54.9 | 1054 | 4130 | 606 |

Table D.4: Type 1 Campaign Parameters (POS = 90% and POS = 99%, continued)

| $t^1_{start}$ *days* | $m$ *kg* | $C+1$ *km/yr* | $\frac{m}{C_{max}+1}$ *kg yr/km* | $\Delta t^1$ *days* | $t^2_{start}$ *days* | $\Delta t^2$ *days* |
|---|---|---|---|---|---|---|
| 2900 | 1195 | 26 | 46.0 | 890 | 4162 | 202 |
| 3000 | 1097 | 24 | 45.7 | 1150 | 4188 | 216 |
| 3100 | 1138 | 20 | 56.9 | 1084 | 4255 | 445 |
| 3200 | 1072 | 17 | 63.1 | 730 | 4311 | 730 |
| 3300 | 1040 | 21 | 49.5 | 449 | 4291 | 110 |
| 3400 | 1193 | 24 | 49.7 | 710 | 4371 | 311 |
| 3500 | 1025 | 13 | 78.9 | 890 | 4430 | 644 |
| 3600 | 1222 | 22 | 55.5 | 780 | 4460 | 240 |
| 3700 | 1016 | 19 | 53.5 | 715 | 4550 | 171 |
| 3800 | 1123 | 13 | 86.4 | 440 | 4614 | 382 |
| 3900 | 1047 | 13 | 80.5 | 670 | 4605 | 441 |
| 4000 | 1233 | 17 | 72.5 | 267 | 4710 | 341 |
| 4100 | 1086 | 21 | 51.7 | 569 | 4780 | 229 |
| 4200 | 1291 | 17 | 75.9 | 451 | 4755 | 300 |
| 4300 | 1309 | 18 | 72.7 | 478 | 4805 | 190 |
| 4400 | 1203 | 18 | 66.8 | 180 | 4940 | 128 |
| 4500 | 1240 | 6 | 206.6 | 463 | 4995 | 307 |
| 4600 | 2152 | 3 | 717.4 | 183 | 4950 | 376 |
| 4700 | 1350 | 5 | 269.9 | 290 | 5096 | 214 |
| 4800 | 1022 | 3 | 340.7 | 310 | 5141 | 199 |

## D.3 Apophis, Type 1 Campaigns (99.9%+)

Table D.5: Type 1 Campaign Parameters (POS = 99.9% and POS = 99.99%)

| $t^1_{start}$ *days* | $m$ *kg* | $C_{max}+1$ *km/yr* | $\frac{m}{C_{max}+1}$ *kg yr/km* | $\Delta t^1$ *days* | $t^2_{start}$ *days* | $\Delta t^2$ *days* |
|---|---|---|---|---|---|---|
| 0 | 1790 | 17 | 105.3 | 1861 | 2687 | 430 |
| 100 | 910 | 12 | 75.8 | 862 | 2710 | 980 |
| 200 | 1100 | 11 | 100.0 | 1249 | 2750 | 838 |
| 300 | 1542 | 16 | 96.4 | 1159 | 2840 | 930 |
| 400 | 1524 | 14 | 108.8 | 854 | 2920 | 480 |
| 500 | 1553 | 17 | 91.4 | 704 | 2972 | 771 |
| 600 | 1472 | 13 | 113.2 | 984 | 3000 | 788 |
| 700 | 988 | 12 | 82.4 | 766 | 3009 | 899 |
| 800 | 1428 | 12 | 119 | 374 | 3150 | 936 |
| 900 | 1496 | 14 | 106.8 | 911 | 3100 | 651 |
| 1000 | 1267 | 12 | 105.6 | 1543 | 3210 | 659 |
| 1100 | 1544 | 14 | 110.3 | 1167 | 3281 | 430 |
| 1200 | 1034 | 11 | 94.0 | 1177 | 3321 | 1150 |
| 1300 | 1504 | 13 | 115.7 | 710 | 3369 | 744 |
| 1400 | 1645 | 15 | 109.7 | 478 | 3367 | 1060 |
| 1500 | 1552 | 13 | 119.4 | 894 | 3450 | 639 |
| 1600 | 1700 | 15 | 113.3 | 1678 | 3470 | 580 |
| 1700 | 1797 | 15 | 119.8 | 1623 | 3507 | 870 |
| 1800 | 1820 | 17 | 107.1 | 1100 | 3550 | 480 |
| 1900 | 1725 | 19 | 90.8 | 600 | 3662 | 453 |
| 2000 | 1016 | 10 | 101.6 | 1310 | 3700 | 462 |
| 2100 | 1749 | 15 | 116.6 | 747 | 3780 | 952 |
| 2200 | 1584 | 13 | 121.9 | 570 | 3745 | 968 |
| 2300 | 1627 | 13 | 125.1 | 1370 | 3872 | 232 |
| 2400 | 1616 | 13 | 124.3 | 711 | 3940 | 790 |
| 2500 | 1498 | 11 | 136.2 | 758 | 3917 | 440 |
| 2600 | 1003 | 11 | 91.2 | 1085 | 4010 | 93 |
| 2700 | 1583 | 12 | 131.9 | 898 | 4000 | 430 |
| 2800 | 1550 | 12 | 129.2 | 974 | 4119 | 610 |

Table D.6: Type 1 Campaign Parameters (POS = 99.9% and POS = 99.99%, continued)

| $t^1_{start}$ *days* | $IMLEO$ *kg* | $C_{max}+1$ *km/yr* | $\frac{IMLEO}{C_{max}+1}$ *kg yr/km* | $\Delta t^1$ *days* | $t^2_{start}$ *days* | $\Delta t^2$ *days* |
|---|---|---|---|---|---|---|
| 2900 | 939 | 7 | 134.2 | 480 | 4160 | 310 |
| 3000 | 1530 | 15 | 102.0 | 861 | 4170 | 220 |
| 3100 | 1001 | 11 | 91.0 | 669 | 4264 | 397 |
| 3200 | 1575 | 10 | 157.5 | 892 | 4250 | 456 |
| 3300 | 1594 | 14 | 113.8 | 399 | 4323 | 86 |
| 3400 | 1531 | 11 | 139.2 | 900 | 4420 | 276 |
| 3500 | 1577 | 7 | 225.3 | 879 | 4460 | 619 |
| 3600 | 1580 | 10 | 158.0 | 817 | 4496 | 180 |
| 3700 | 1746 | 12 | 145.5 | 708 | 4540 | 480 |
| 3800 | 954 | 4 | 238.5 | 723 | 4560 | 401 |
| 3900 | 1032 | 4 | 258.1 | 697 | 4620 | 218 |
| 4000 | 1591 | 7 | 227.3 | 450 | 4650 | 433 |
| 4100 | 1476 | 6 | 246.0 | 590 | 4793 | 255 |

## D.4 Apophis, Type 2 Campaigns (90%)

Table D.7: Type 2 Campaign Parameters (POS = 90%)

| $t^1_{start}$ *days* | $m$ *kg* | $C_{max}+1$ *km/yr* | $\frac{m}{C_{max}+1}$ *kg yr/km* | $\Delta t^1$ *days* | $t^2_{start}$ *days* | $\Delta t^2$ *days* | $t^3_{start}$ *days* | $\Delta t^3$ *days* |
|---|---|---|---|---|---|---|---|---|
| 0 | 2049 | 43 | 47.7 | 504 | 0 | 880 | 1932 | 830 |
| 100 | 2077 | 43 | 48.3 | 761 | 100 | 990 | 1972 | 780 |
| 200 | 2160 | 44 | 49.1 | 691 | 200 | 920 | 1880 | 960 |
| 300 | 2108 | 43 | 49.0 | 785 | 300 | 905 | 1968 | 790 |
| 400 | 2213 | 41 | 54.0 | 792 | 400 | 990 | 1930 | 871 |
| 500 | 2276 | 43 | 52.9 | 623 | 500 | 956 | 1877 | 851 |
| 600 | 2222 | 44 | 50.5 | 760 | 600 | 926 | 1819 | 961 |
| 700 | 2115 | 41 | 51.6 | 770 | 700 | 865 | 1968 | 820 |
| 800 | 2478 | 44 | 56.3 | 385 | 800 | 989 | 1810 | 979 |
| 900 | 2133 | 44 | 48.5 | 793 | 900 | 928 | 1951 | 830 |
| 1000 | 2212 | 44 | 50.3 | 629 | 1000 | 840 | 2000 | 810 |
| 1100 | 2243 | 43 | 52.2 | 695 | 1100 | 1000 | 2043 | 730 |
| 1200 | 2181 | 45 | 48.5 | 540 | 1200 | 919 | 2080 | 980 |
| 1300 | 2046 | 47 | 43.5 | 750 | 1300 | 850 | 2130 | 998 |
| 1400 | 2108 | 42 | 50.2 | 787 | 1400 | 980 | 2399 | 980 |
| 1500 | 2096 | 49 | 42.8 | 730 | 1500 | 980 | 2441 | 993 |
| 1600 | 2043 | 50 | 40.9 | 773 | 1600 | 840 | 2506 | 950 |
| 1700 | 2045 | 41 | 49.9 | 772 | 1700 | 810 | 2510 | 640 |
| 1800 | 2043 | 47 | 43.5 | 780 | 1800 | 962 | 2580 | 876 |
| 1900 | 2040 | 51 | 40 | 711 | 1900 | 841 | 2783 | 956 |
| 2000 | 2061 | 50 | 41.2 | 513 | 2000 | 811 | 3005 | 742 |

## D.5 Apophis, Type 2 Campaigns (99%)

Table D.8: Type 2 Campaign Parameters (POS = 99%)

| $t^1_{start}$ *days* | $m$ *kg* | $C_{max}+1$ *km/yr* | $\frac{m}{C_{max}+1}$ *kg yr/km* | $\Delta t^1$ *days* | $t^2_{start}$ *days* | $\Delta t^2$ *days* | $t^3_{start}$ *days* | $\Delta t^3$ *days* |
|---|---|---|---|---|---|---|---|---|
| 0 | 2048 | 38 | 53.9 | 480 | 0 | 880 | 1935 | 825 |
| 100 | 2197 | 38 | 57.8 | 663 | 100 | 830 | 1807 | 981 |
| 200 | 2262 | 40 | 56.5 | 720 | 200 | 940 | 1930 | 920 |
| 300 | 2173 | 40 | 54.3 | 580 | 300 | 838 | 1883 | 1000 |
| 400 | 2224 | 39 | 57.0 | 750 | 400 | 815 | 1910 | 850 |
| 500 | 2178 | 38 | 57.3 | 669 | 500 | 930 | 1781 | 950 |
| 600 | 2218 | 39 | 56.9 | 620 | 600 | 910 | 1920 | 933 |
| 700 | 2090 | 38 | 55.0 | 796 | 700 | 801 | 1909 | 810 |
| 800 | 2215 | 39 | 56.8 | 705 | 800 | 980 | 1916 | 879 |
| 900 | 2154 | 39 | 55.2 | 741 | 900 | 907 | 1940 | 865 |
| 1000 | 2191 | 39 | 56.2 | 680 | 1000 | 800 | 1990 | 833 |
| 1100 | 2259 | 38 | 59.4 | 588 | 1100 | 1000 | 2080* | 681 |
| 1200 | 2198 | 43 | 51.1 | 635 | 1200 | 920 | 2120 | 968 |
| 1300 | 2060 | 43 | 47.9 | 763 | 1300 | 821 | 2309 | 780 |
| 1400 | 2141 | 36 | 59.5 | 761 | 1400 | 1000 | 2144* | 610 |
| 1500 | 2096 | 45 | 46.6 | 730 | 1500 | 944 | 2437* | 981 |
| 1600 | 2071 | 45 | 46.0 | 687 | 1600 | 838 | 2525 | 929 |
| 1700 | 2042 | 43 | 47.5 | 735 | 1700 | 800 | 2700 | 1000 |
| 1800 | 2070 | 41 | 50.5 | 570 | 1800 | 999 | 2402 | 1000 |
| 1900 | 2043 | 48 | 42.6 | 700 | 1900 | 880 | 2871 | 880 |
| 2000 | 2205 | 46 | 47.9 | 680 | 2000 | 800 | 2816 | 962 |
| 2100 | 2045 | 45 | 45.4 | 532 | 2100 | 980 | 2766 | 998 |
| 2200 | 2047 | 44 | 46.5 | 788 | 2200 | 920 | 2940 | 802 |
| 2300 | 2058 | 44 | 46.8 | 470 | 2300 | 810 | 3112 | 660 |

## D.6 Apophis, Type 2 Campaigns (99.9%)

Table D.9: Type 2 Campaign Parameters (POS = 99.9%)

| $t^1_{start}$ *days* | $m$ *kg* | $C_{max}+1$ *km/yr* | $\frac{m}{C_{max}+1}$ *kg yr/km* | $\Delta t^1$ *days* | $t^2_{start}$ *days* | $\Delta t^2$ *days* | $t^3_{start}$ *days* | $\Delta t^3$ *days* |
|---|---|---|---|---|---|---|---|---|
| 0 | 2051 | 35 | 58.6 | 535 | 0 | 880 | 1884 | 846 |
| 100 | 2198 | 36 | 61.1 | 730 | 100 | 983 | 1930 | 900 |
| 200 | 2160 | 35 | 61.7 | 691 | 200 | 880 | 1885 | 959 |
| 300 | 2194 | 37 | 59.3 | 550 | 300 | 850 | 1903 | 979 |
| 400 | 2254 | 35 | 64.4 | 420 | 400 | 990 | 1867 | 922 |
| 500 | 2298 | 35 | 65.6 | 756 | 500 | 960 | 1809 | 898 |
| 600 | 2222 | 36 | 61.7 | 731 | 600 | 889 | 1890 | 978 |
| 700 | 2138 | 36 | 59.4 | 781 | 700 | 807 | 1890 | 980 |
| 800 | 2187 | 35 | 62.5 | 700 | 800 | 959 | 1842 | 940 |
| 900 | 2171 | 36 | 60.3 | 701 | 900 | 855 | 1940 | 889 |
| 1000 | 2187 | 36 | 60.7 | 750 | 1000 | 838 | 1981 | 845 |
| 1100 | 2287 | 36 | 63.5 | 660 | 1100 | 1000 | 2110 | 695 |
| 1200 | 2124 | 40 | 53.1 | 780 | 1200 | 926 | 2200 | 900 |
| 1300 | 2094 | 39 | 53.7 | 630 | 1300 | 802 | 2260 | 890 |
| 1400 | 2102 | 32 | 65.7 | 590 | 1400 | 970 | 2159* | 895 |
| 1500 | 2119 | 41 | 51.7 | 680 | 1500 | 950 | 2503 | 980 |
| 1600 | 2052 | 41 | 50.1 | 727 | 1600 | 874 | 2450* | 959 |
| 1700 | 2021 | 37 | 54.6 | 680 | 1700 | 821 | 2426* | 995 |
| 1800 | 2069 | 44 | 47.0 | 663 | 1800 | 980 | 2777* | 970 |
| 1900 | 2081 | 42 | 49.6 | 444 | 1900 | 840 | 2872 | 941 |
| 2000 | 2207 | 41 | 53.8 | 695 | 2000 | 820 | 2894 | 960 |
| 2100 | - | 1 | - | - | - | - | - | - |
| 2200 | 2064 | 41 | 50.3 | 410 | 2200 | 919 | 2841 | 910 |
| 2300 | - | 1 | - | - | - | - | - | - |
| 2400 | 2044 | 38 | 53.8 | 762 | 2400 | 996 | 3074 | 718 |

## D.7 Apophis, Type 2 Campaigns (99.99%)

Table D.10: Type 2 Campaign Parameters (POS = 99.99%)

| $t^1_{start}$ *days* | $m$ *kg* | $C_{max}+1$ *km/yr* | $\frac{m}{C_{max}+1}$ *kg yr/km* | $\Delta t^1$ *days* | $t^2_{start}$ *days* | $\Delta t^2$ *days* | $t^3_{start}$ *days* | $\Delta t^3$ *days* |
|---|---|---|---|---|---|---|---|---|
| 0 | 2052 | 32 | 64.1 | 511 | 0 | 880 | 1750 | 792 |
| 100 | 2076 | 31 | 67.0 | 769 | 100 | 970 | 1735 | 760 |
| 200 | 2160 | 34 | 63.5 | 664 | 200 | 870 | 1840 | 979 |
| 300 | 2207 | 35 | 63.0 | 544 | 300 | 880 | 1929 | 963 |
| 400 | 2204 | 34 | 64.8 | 800 | 400 | 810 | 1820 | 905 |
| 500 | 2326 | 34 | 68.4 | 730 | 500 | 897 | 1949 | 850 |
| 600 | 2246 | 34 | 66.1 | 560 | 600 | 860 | 1874 | 998 |
| 700 | 2239 | 33 | 67.8 | 650 | 700 | 860 | 1972 | 800 |
| 800 | 2220 | 33 | 67.3 | 704 | 800 | 1000 | 1971 | 740 |
| 900 | 2136 | 35 | 61.0 | 780 | 900 | 930 | 1950 | 883 |
| 1000 | 2144 | 34 | 63.0 | 691 | 1000 | 810 | 2004 | 990 |
| 1100 | 2244 | 34 | 66.0 | 749 | 1100 | 990 | 2010 | 810 |
| 1200 | 2196 | 36 | 61.0 | 660 | 1200 | 948 | 2130 | 930 |
| 1300 | 2065 | 35 | 59.0 | 713 | 1300 | 830 | 2265 | 780 |
| 1400 | 2127 | 31 | 68.6 | 750 | 1400 | 990 | 2131* | 918 |
| 1500 | 2119 | 37 | 57.3 | 677 | 1500 | 960 | 2235* | 980 |
| 1600 | 2052 | 39 | 52.6 | 729 | 1600 | 830 | 2449 | 959 |
| 1700 | 2085 | 37 | 56.4 | 548 | 1700 | 805 | 2505 | 995 |
| 1800 | 2050 | 38 | 53.9 | 791 | 1800 | 995 | 2651* | 779 |
| 1900 | 2067 | 38 | 54.4 | 588 | 1900 | 903 | 2907 | 800 |
| 2000 | 2038 | 37 | 55.1 | 673 | 2000 | 800 | 2640* | 780 |

# Appendix E

# Results (Bennu)

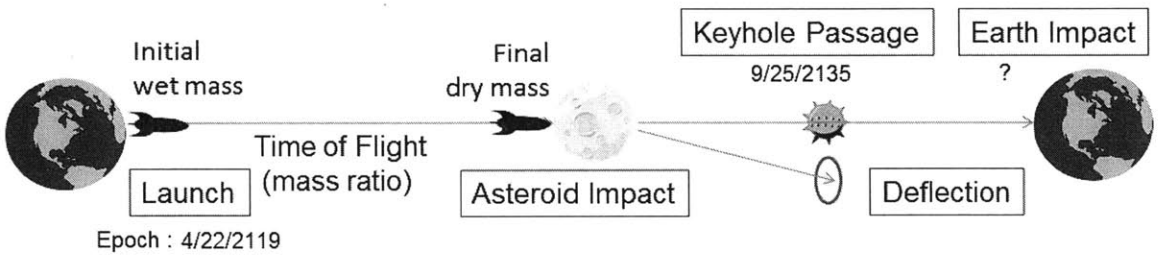


Figure E-1: Overview of a Bennu deflection campaign

## E.1 Bennu, Type 0 Campaigns (90%)

Table E.1: Type 0 Campaign Parameters (POS = 90%)

| $t^1_{start}$ *days* | $IMLEO$ *kg* | $C_{max}+1$ *km/yr* | $\frac{IMLEO}{C_{max}+1}$ *kg yr/km* | $\Delta t^1$ *days* | $\frac{m_{impactor}}{IMLEO}$ - | $m_{impactor}$ *kg* |
|---|---|---|---|---|---|---|
| 0 | 1360 | 7 | 194.3 | 940 | 0.7100 | 644 |
| 100 | 1360 | 7 | 194.3 | 850 | 0.6745 | 629 |
| 200 | 1370 | 7 | 195.7 | 750 | 0.6365 | 628 |
| 300 | 1370 | 7 | 195.7 | 630 | 0.6703 | 630 |
| 400 | 1370 | 7 | 195.7 | 540 | 0.6527 | 702 |
| 500 | 1370 | 7 | 195.7 | 450 | 0.5381 | 701 |
| 600 | 1580 | 8 | 197.5 | 1200 | 0.6356 | 700 |
| 700 | 1580 | 8 | 197.5 | 1100 | 0.6923 | 756 |
| 800 | 1570 | 8 | 196.3 | 990 | 0.6345 | 762 |
| 900 | 1600 | 8 | 200.0 | 890 | 0.7155 | 755 |
| 1000 | 1750 | 9 | 194.4 | 1230 | 0.6235 | 736 |
| 1100 | 1750 | 9 | 194.4 | 1130 | 0.6589 | 827 |
| 1200 | 1740 | 9 | 193.3 | 1030 | 0.6058 | 832 |
| 1300 | 1790 | 9 | 198.8 | 950 | 0.6825 | 799 |
| 1400 | 1730 | 9 | 192.2 | 850 | 0.5667 | 799 |
| 1500 | 1950 | 10 | 195.0 | 1170 | 0.6163 | 802 |
| 1600 | 1950 | 10 | 195.0 | 1050 | 0.7130 | 829 |
| 1700 | 1860 | 10 | 186.0 | 950 | 0.6674 | 875 |
| 1800 | 1890 | 10 | 189.0 | 850 | 0.5739 | 844 |
| 1900 | 1890 | 10 | 189.0 | 760 | 0.5899 | 819 |
| 2000 | 1900 | 10 | 190.0 | 650 | 0.7147 | 1003 |
| 2100 | 2070 | 11 | 188.2 | 970 | 0.6316 | 810 |
| 2200 | 2630 | 14 | 187.9 | 1410 | 0.5914 | 825 |
| 2300 | 2190 | 12 | 182.5 | 830 | 0.5808 | 819 |
| 2400 | 2020 | 11 | 183.6 | 680 | 0.6968 | 1121 |
| 2500 | 2290 | 13 | 176.2 | 1010 | 0.6035 | 1100 |
| 2600 | 2290 | 13 | 176.2 | 910 | 0.5800 | 1315 |
| 2700 | 2310 | 13 | 177.7 | 810 | 0.5898 | 1297 |
| 2800 | 2810 | 16 | 175.6 | 1120 | 0.6930 | 1272 |

Table E.2: Type 0 Campaign Parameters (POS = 90%, continued)

| $t^1_{start}$ *days* | $IMLEO$ *kg* | $C_{max}+1$ *km/yr* | $\frac{IMLEO}{C_{max}+1}$ *kg yr/km* | $\Delta t^1$ *days* | $\frac{m_{impactor}}{IMLEO}$ - | $m_{impactor}$ *kg* |
|---|---|---|---|---|---|---|
| 2900 | 2280 | 26 | 174.4 | 1050 | 0.6969 | 1620 |
| 3000 | 2290 | 26 | 174.4 | 950 | 0.6209 | 1599 |
| 3100 | 2320 | 26 | 176.3 | 850 | 0.5830 | 1620 |
| 3200 | 2160 | 26 | 176.0 | 1150 | 0.6689 | 1486 |
| 3300 | 2930 | 33 | 176.0 | 1050 | 0.6853 | 2107 |
| 3400 | 2970 | 33 | 175.5 | 980 | 0.6490 | 2118 |
| 3500 | 2960 | 33 | 179.4 | 410 | 0.5557 | 2110 |
| 3600 | 2850 | 32 | 176.9 | 540 | 0.6496 | 1864 |
| 3700 | 3920 | 46 | 175.7 | 380 | 0.5535 | 2820 |
| 3800 | 3920 | 46 | 176.4 | 740 | 0.6430 | 2818 |
| 3900 | 3920 | 46 | 175.6 | 900 | 0.7245 | 2817 |
| 4000 | 4150 | 47 | 177.9 | 830 | 0.5426 | 3008 |
| 4100 | 4210 | 47 | 183.7 | 700 | 0.6155 | 2999 |
| 4200 | 4110 | 45 | 182.6 | 600 | 0.5882 | 2582 |
| 4300 | 3890 | 45 | 183.3 | 530 | 0.6746 | 2710 |
| 4400 | 4990 | 55 | 207.9 | 510 | 0.7092 | 3042 |
| 4500 | 4990 | 55 | 311.9 | 300 | 0.4565 | 3042 |
| 4600 | 4990 | 55 | 356.4 | 630 | 0.7047 | 3042 |

## E.2 Bennu, Type 0 Campaigns (99%)

Table E.3: Type 0 Campaign Parameters (POS = 99%)

| $t^1_{start}$ *days* | $IMLEO$ *kg* | $C_{max}+1$ *km/yr* | $\frac{IMLEO}{C_{max}+1}$ *kg yr/km* | $\Delta t^1$ *days* | $\frac{m_{impactor}}{IMLEO}$ - | $m_{impactor}$ *kg* |
|---|---|---|---|---|---|---|
| 0 | 1940 | 6 | 277.1 | 520 | 0.6763 | 644 |
| 100 | 1950 | 6 | 278.6 | 410 | 0.6029 | 629 |
| 200 | 2220 | 7 | 277.5 | 1140 | 0.4415 | 628 |
| 300 | 2150 | 7 | 268.8 | 1070 | 0.6734 | 630 |
| 400 | 2140 | 7 | 267.5 | 970 | 0.6527 | 702 |
| 500 | 2150 | 7 | 268.8 | 870 | 0.5381 | 701 |
| 600 | 2180 | 7 | 272.5 | 770 | 0.4606 | 700 |
| 700 | 2450 | 8 | 272.2 | 1150 | 0.5573 | 756 |
| 800 | 2380 | 8 | 264.4 | 1040 | 0.6812 | 762 |
| 900 | 2450 | 8 | 272.2 | 950 | 0.6190 | 755 |
| 1000 | 2430 | 8 | 270.0 | 840 | - | - |
| 1100 | 2400 | 8 | 266.7 | 790 | 0.6589 | 827 |
| 1200 | 2960 | 10 | 269.1 | 1480 | 0.6435 | 832 |
| 1300 | 2720 | 9 | 272.0 | 1030 | 0.6063 | 799 |
| 1400 | 2320 | 8 | 257.8 | 440 | 0.5502 | 799 |
| 1500 | 2840 | 10 | 258.2 | 1170 | 0.6163 | 802 |
| 1600 | 2850 | 10 | 259.1 | 1080 | 0.7130 | 829 |
| 1700 | 2680 | 9 | 268.0 | 950 | 0.6674 | 875 |
| 1800 | 2860 | 10 | 260.0 | 880 | 0.5901 | 844 |
| 1900 | 2770 | 10 | 251.8 | 770 | 0.5827 | 819 |
| 2000 | 2810 | 10 | 255.5 | 680 | 0.6931 | 1003 |
| 2100 | 2750 | 10 | 250.0 | 570 | 0.5638 | 810 |
| 2200 | 3060 | 11 | 255.0 | 870 | 0.5897 | 825 |
| 2300 | 3030 | 11 | 252.5 | 780 | 0.5890 | 819 |
| 2400 | 3030 | 11 | 252.5 | 680 | 0.6968 | 1121 |
| 2500 | 3400 | 13 | 242.9 | 1010 | 0.6035 | 1100 |
| 2600 | 3400 | 13 | 242.9 | 910 | 0.5800 | 1315 |
| 2700 | 3410 | 13 | 243.6 | 810 | 0.5898 | 1297 |
| 2800 | 4020 | 16 | 236.5 | 1120 | 0.6930 | 1272 |

Table E.4: Type 0 Campaign Parameters (POS = 99%, continued)

| $t^1_{start}$ *days* | $IMLEO$ *kg* | $C_{max}+1$ *km/yr* | $\frac{IMLEO}{C_{max}+1}$ *kg yr/km* | $\Delta t^1$ *days* | $\frac{m_{impactor}}{IMLEO}$ - | $m_{impactor}$ *kg* |
|---|---|---|---|---|---|---|
| 2900 | 4020 | 16 | 236.5 | 1020 | 0.5885 | 1620 |
| 3000 | 4060 | 16 | 238.8 | 950 | 0.6209 | 1599 |
| 3100 | 4070 | 16 | 239.4 | 830 | 0.5820 | 1620 |
| 3200 | 4990 | 20 | 237.6 | 1170 | 0.6485 | 1486 |
| 3300 | 4990 | 20 | 237.6 | 1070 | 0.6986 | 2107 |
| 3400 | 4970 | 20 | 236.7 | 980 | 0.6853 | 2118 |
| 3500 | 4990 | 19 | 249.5 | 880 | 0.5629 | 2110 |
| 3600 | 4160 | 16 | 244.7 | 380 | 0.5535 | 1864 |
| 3700 | 4200 | 16 | 247.1 | 290 | 0.0602 | 2820 |
| 3800 | 4980 | 19 | 249.0 | 550 | 0.6366 | 2818 |
| 3900 | 4990 | 17 | 277.2 | 470 | 0.5454 | 2817 |
| 4000 | 4990 | 19 | 249.5 | 420 | 0.6290 | 3008 |
| 4100 | 4990 | 9 | 499.0 | 720 | 0.6592 | 2999 |

## E.3 Bennu, Type 0 Campaigns (99.9%)

Table E.5: Type 0 Campaign Parameters (POS = 99.9%)

| $t^1_{start}$ *days* | $IMLEO$ *kg* | $C_{max}+1$ *km/yr* | $\frac{IMLEO}{C_{max}+1}$ *kg yr/km* | $\Delta t^1$ *days* | $\frac{m_{impactor}}{IMLEO}$ - | $m_{impactor}$ *kg* |
|---|---|---|---|---|---|---|
| 0 | 1790 | 4 | 358.0 | 940 | 0.7100 | 644 |
| 100 | 1790 | 4 | 358.0 | 850 | 0.6745 | 629 |
| 200 | 1810 | 4 | 362.0 | 750 | 0.6365 | 628 |
| 300 | 1800 | 4 | 360.0 | 640 | 0.6703 | 630 |
| 400 | 1810 | 4 | 362.0 | 540 | 0.6527 | 702 |
| 500 | 1800 | 4 | 360.0 | 450 | 0.5381 | 701 |
| 600 | 1860 | 4 | 372.0 | 330 | 0.4606 | 700 |
| 700 | 1870 | 4 | 374.0 | 220 | 0.5573 | 756 |
| 800 | 1920 | 4 | 384.0 | 570 | 0.6186 | 762 |
| 900 | 2380 | 5 | 396.7 | 1030 | 0.5860 | 755 |
| 1000 | 2280 | 5 | 380.0 | 1230 | 0.6235 | 736 |
| 1100 | 2290 | 5 | 381.7 | 1130 | 0.6589 | 827 |
| 1200 | 2270 | 5 | 378.3 | 1030 | 0.6058 | 832 |
| 1300 | 2330 | 5 | 388.3 | 950 | 0.6825 | 799 |
| 1400 | 2590 | 6 | 370.0 | 1270 | - | - |
| 1500 | 2590 | 6 | 370.0 | 1140 | 0.6498 | 802 |
| 1600 | 2580 | 6 | 368.6 | 1050 | 0.7130 | 829 |
| 1700 | 2460 | 6 | 351.4 | 950 | 0.6674 | 875 |
| 1800 | 2490 | 6 | 355.7 | 860 | 0.5786 | 844 |
| 1900 | 2500 | 6 | 357.1 | 760 | 0.5899 | 819 |
| 2000 | 2510 | 6 | 358.6 | 660 | 0.7131 | 1003 |
| 2100 | 2790 | 7 | 348.8 | 1010 | 0.6175 | 810 |
| 2200 | 2800 | 7 | 350.0 | 910 | - | - |
| 2300 | 2720 | 7 | 340.0 | 780 | 0.5890 | 819 |
| 2400 | 2770 | 7 | 346.3 | 700 | 0.6218 | 1121 |
| 2500 | 3050 | 8 | 338.9 | 1010 | 0.6035 | 1100 |
| 2600 | 3050 | 8 | 338.9 | 910 | 0.5800 | 1315 |
| 2700 | 3060 | 8 | 340.0 | 810 | 0.5898 | 1297 |
| 2800 | 3090 | 8 | 343.3 | 710 | 0.6599 | 1272 |

Table E.6: Type 0 Campaign Parameters (POS = 99.9%, continued)

| $t^1_{start}$ *days* | $IMLEO$ *kg* | $C_{max}+1$ *km/yr* | $\frac{IMLEO}{C_{max}+1}$ *kg yr/km* | $\Delta t^1$ *days* | $\frac{m_{impactor}}{IMLEO}$ - | $m_{impactor}$ *kg* |
|---|---|---|---|---|---|---|
| 2900 | 3060 | 8 | 340.0 | 610 | 0.6357 | 1620 |
| 3000 | 3720 | 10 | 338.2 | 960 | 0.6278 | 1599 |
| 3100 | 3120 | 8 | 346.7 | 410 | 0.3961 | 1620 |
| 3200 | 3860 | 10 | 350.9 | 770 | 0.6034 | 1486 |
| 3300 | 3840 | 10 | 349.1 | 670 | 0.6867 | 2107 |
| 3400 | 3770 | 10 | 342.7 | 560 | 0.6260 | 2118 |
| 3500 | 3940 | 10 | 358.2 | 540 | 0.6493 | 2110 |
| 3600 | 3740 | 10 | 340.0 | 380 | 0.5535 | 1864 |
| 3700 | 3760 | 10 | 341.8 | 290 | 0.7195 | 2820 |
| 3800 | 4650 | 12 | 357.7 | 550 | 0.7190 | 2818 |
| 3900 | 4750 | 12 | 365.4 | 490 | 0.5710 | 2817 |
| 4000 | 4850 | 13 | 346.4 | 440 | 0.5145 | 3008 |
| 4100 | 4990 | 10 | 453.6 | 390 | 0.6044 | 2999 |
| 4200 | 4980 | 5 | 830.0 | 600 | 0.5882 | 2999 |

## E.4 Bennu, Type 0 Campaigns (99.99%)

Table E.7: Type 0 Campaign Parameters (POS = 99.99%)

| $t^1_{start}$ *days* | $IMLEO$ *kg* | $C_{max}+1$ *km/yr* | $\frac{IMLEO}{C_{max}+1}$ *kg yr/km* | $\Delta t^1$ *days* | $\frac{m_{impactor}}{IMLEO}$ - | $m_{impactor}$ *kg* |
|---|---|---|---|---|---|---|
| 0 | 1670 | 2 | 556.7 | 940 | 0.7100 | 644 |
| 100 | 1680 | 2 | 560.0 | 850 | 0.6745 | 629 |
| 200 | 1670 | 2 | 556.7 | 750 | 0.6365 | 628 |
| 300 | 1700 | 2 | 556.7 | 640 | 0.6703 | 630 |
| 400 | 1710 | 2 | 570.0 | 540 | 0.6527 | 702 |
| 500 | 1700 | 2 | 556.7 | 450 | 0.5381 | 701 |
| 600 | 1760 | 2 | 586.7 | 330 | 0.4606 | 700 |
| 700 | 1770 | 2 | 590.0 | 220 | 0.5573 | 756 |
| 800 | 2210 | 3 | 552.5 | 570 | 0.6186 | 762 |
| 900 | 2220 | 3 | 555.0 | 1030 | 0.5860 | 755 |
| 1000 | 2170 | 3 | 542.5 | 1230 | 0.6235 | 736 |
| 1100 | 2230 | 3 | 557.5 | 1130 | 0.6589 | 827 |
| 1200 | 2230 | 3 | 557.5 | 1030 | 0.6058 | 832 |
| 1300 | 2280 | 3 | 570.0 | 950 | 0.6825 | 799 |
| 1400 | 2210 | 3 | 552.5 | 1270 | - | - |
| 1500 | 2280 | 3 | 570.0 | 1140 | 0.6498 | 802 |
| 1600 | 2290 | 3 | 572.5 | 1050 | 0.7130 | 829 |
| 1700 | 2810 | 4 | 562.0 | 950 | 0.6674 | 875 |
| 1800 | 2820 | 4 | 564.0 | 860 | 0.5786 | 844 |
| 1900 | 2770 | 4 | 554.0 | 760 | 0.5899 | 819 |
| 2000 | 2790 | 4 | 558.0 | 660 | 0.7131 | 1003 |
| 2100 | 2650 | 4 | 530.0 | 1010 | 0.6175 | 810 |
| 2200 | 2660 | 4 | 532.0 | 910 | - | - |
| 2300 | 2630 | 4 | 526.0 | 780 | 0.5890 | 819 |
| 2400 | 3630 | 4 | 526.0 | 700 | 0.6218 | 1121 |
| 2500 | 3150 | 5 | 525.0 | 1010 | 0.6035 | 1100 |
| 2600 | 3150 | 5 | 525.0 | 910 | 0.5800 | 1315 |
| 2700 | 3050 | 5 | 508.3 | 810 | 0.5898 | 1297 |
| 2800 | 2660 | 4 | 532.0 | 710 | 0.6599 | 1272 |

Table E.8: Type 0 Campaign Parameters (POS = 99.99%, continued)

| $t^1_{start}$ *days* | $IMLEO$ *kg* | $C_{max}+1$ *km/yr* | $\frac{IMLEO}{C_{max}+1}$ *kg yr/km* | $\Delta t^1$ *days* | $\frac{m_{impactor}}{IMLEO}$ - | $m_{impactor}$ *kg* |
|---|---|---|---|---|---|---|
| 2900 | 3640 | 6 | 520.0 | 610 | 0.6357 | 1620 |
| 3000 | 3180 | 5 | 530.0 | 960 | 0.6278 | 1599 |
| 3100 | 3630 | 6 | 518.6 | 410 | 0.3961 | 1620 |
| 3200 | 3700 | 6 | 528.6 | 770 | 0.6034 | 1486 |
| 3300 | 3690 | 6 | 527.1 | 670 | 0.6867 | 2107 |
| 3400 | 3680 | 6 | 525.7 | 560 | 0.6260 | 2118 |
| 3500 | 4930 | 8 | 547.8 | 540 | 0.6493 | 2110 |
| 3600 | 3660 | 6 | 522.9 | 380 | 0.5535 | 1864 |
| 3700 | 3670 | 6 | 524.3 | 290 | 0.7195 | 2820 |
| 3800 | 4510 | 7 | 563.8 | 550 | 0.7190 | 2818 |
| 3900 | 4590 | 7 | 573.8 | 490 | 0.5710 | 2817 |
| 4000 | 4990 | 8 | 554.4 | 440 | 0.5145 | 3008 |
| 4100 | 4910 | 5 | 818.3 | 600 | 0.5875 | 2999 |

## E.5 Bennu, Type 1 Campaigns (90%, 99%, 99.9%)

Table E.9: Type 1 Campaign Parameters (POS = 90%, POS = 99%, POS = 99.9%)

| $t^1_{start}$ *days* | $m$ *kg* | $C_{max}+1$ *km/yr* | $\frac{m}{C_{max}+1}$ *kg yr/km* | $\Delta t^1$ *days* | $t^2_{start}$ *days* | $\Delta t^2$ *days* |
|---|---|---|---|---|---|---|
| 0 | 1118 | 4 | 279.5 | 1016 | 2983 | 547 |
| 100 | 1165 | 4 | 291.1 | 1519 | 3030 | 517 |
| 200 | 1205 | 4 | 301.4 | 1284 | 3075 | 457 |
| 300 | 1067 | 3 | 355.5 | 827 | 3160 | 390 |
| 400 | 1107 | 3 | 368.9 | 728 | 3240 | 731 |
| 500 | 1129 | 4 | 282.3 | 1170 | 3230 | 330 |
| 600 | 1079 | 4 | 269.8 | 1050 | 3267 | 301 |
| 700 | 1110 | 4 | 277.5 | 425 | 3289 | 230 |
| 800 | 1129 | 4 | 282.3 | 1135 | 3433 | 143 |
| 900 | 1068 | 3 | 356.0 | 990 | 3449 | 572 |
| 1000 | 1029 | 3 | 343.0 | 1102 | 3467 | 477 |
| 1100 | 1064 | 3 | 354.8 | 1057 | 3521 | 441 |
| 1200 | 1095 | 3 | 365.1 | 917 | 3608 | 340 |
| 1300 | 1031 | 2 | 515.3 | 685 | 3670 | 229 |
| 1400 | 1137 | 3 | 379.0 | 1069 | 3640 | 357 |
| 1500 | 1060 | 2 | 530.0 | 1188 | 3710 | 708 |
| 1600 | 1098 | 2 | 548.8 | 1291 | 3827 | 580 |
| 1700 | 1092 | 2 | 546.1 | 1281 | 3803 | 650 |
| 1800 | 1034 | 2 | 517.2 | 1150 | 3850 | 560 |
| 1900 | 1062 | 2 | 530.8 | 1105 | 3915 | 510 |
| 2000 | 1123 | 2 | 561.6 | 889 | 3940 | 470 |
| 2100 | - | - | - | - | - | - |
| 2200 | 1182 | 2 | 590.9 | 841 | 4040 | 420 |
| 2300 | 1113 | 2 | 556.3 | 884 | 4090 | 341 |
| 2400 | 1090 | 2 | 544.8 | 810 | 4130 | 251 |
| 2500 | 1155 | 2 | 577.3 | 1011 | 4200 | 205 |

## E.6 Bennu, Type 1 Campaigns (99.99%)

Table E.10: Type 1 Campaign Parameters (POS = 99.99%)

| $t^1_{start}$ *days* | $m$ *kg* | $C_{max}+1$ *km/yr* | $\frac{m}{C_{max}+1}$ *kg yr/km* | $\Delta t^1$ *days* | $t^2_{start}$ *days* | $\Delta t^2$ *days* |
|---|---|---|---|---|---|---|
| 0 | 1118 | 4 | 284.5 | 1016 | 2979 | 520 |
| 100 | 1165 | 3 | 361.5 | 1485 | 3071 | 423 |
| 200 | 1205 | 3 | 352.8 | 939 | 3127 | 445 |
| 300 | 1067 | 3 | 355.9 | 668 | 3180 | 774 |
| 400 | 1107 | 3 | 418.9 | 1972 | 3225 | 700 |
| 500 | 1129 | 4 | 283.3 | 883 | 3220 | 323 |
| 600 | 1079 | 4 | 270.0 | 1200 | 3240 | 289 |
| 700 | 1110 | 4 | 292.5 | 425 | 3304 | 217 |
| 800 | 1129 | 3 | 339.7 | 1555 | 3384 | 135 |
| 900 | 1068 | 3 | 367.8 | 765 | 3434 | 520 |
| 1000 | 1029 | 3 | 364.3 | 575 | 3448 | 517 |
| 1100 | 1064 | 3 | 348.0 | 314 | 3552 | 398 |
| 1200 | - | - | - | - | - | - |
| 1300 | 1031 | 2 | 526.0 | 2383 | 3580 | 432 |
| 1400 | 1137 | 3 | 379.2 | 855 | 3643 | 350 |
| 1500 | 1060 | 2 | 572.2 | 1080 | 3720 | 740 |
| 1600 | 1098 | 2 | 531.2 | 978 | 3768 | 620 |
| 1700 | 1092 | 2 | 528.9 | 960 | 3791 | 628 |
| 1800 | 1034 | 2 | 537.2 | 1165 | 3890 | 510 |
| 1900 | 1062 | 2 | 530.3 | 1133 | 3900 | 490 |
| 2000 | 1123 | 2 | 558.7 | 1444 | 3964 | 458 |

## E.7 Bennu, Type 2 Campaigns (90%)

Table E.11: Type 2 Campaign Parameters (POS = 90%)

| $t^1_{start}$ *days* | $m$ *kg* | $C_{max}+1$ *km/yr* | $\frac{m}{C_{max}+1}$ *kg yr/km* | $\Delta t^1$ *days* | $t^2_{start}$ *days* | $\Delta t^2$ *days* | $t^3_{start}$ *days* | $\Delta t^3$ *days* |
|---|---|---|---|---|---|---|---|---|
| 0 | 2192 | 21 | 104.4 | 650 | 0 | 980 | 2497 | 970 |
| 100 | 2247 | 19 | 118.3 | 732 | 100 | 900 | 1884 | 789 |
| 200 | 2250 | 21 | 107.2 | 783 | 200 | 803 | 2515 | 943 |
| 300 | 2160 | 18 | 120.0 | 695 | 300 | 990 | 2523 | 975 |
| 400 | 2125 | 20 | 106.3 | 720 | 400 | 984 | 2230 | 926 |
| 500 | 2128 | 20 | 106.4 | 587 | 500 | 920 | 2284 | 869 |
| 600 | 2149 | 22 | 97.7 | 416 | 600 | 837 | 2550 | 1000 |
| 700 | 2103 | 16 | 131.4 | 778 | 700 | 997 | 2223 | 939 |
| 800 | 2100 | 21 | 100.0 | 640 | 800 | 994 | 2551 | 980 |
| 900 | 2095 | 21 | 99.8 | 730 | 900 | 910 | 2541 | 977 |
| 1000 | 2098 | 19 | 110.4 | 695 | 1000 | 820 | 2458 | 668 |
| 1100 | 2116 | 18 | 117.5 | 626 | 1100 | 810 | 2530 | 979 |
| 1200 | 2114 | 17 | 124.3 | 540 | 1200 | 990 | 2252 | 848 |
| 1300 | 2113 | 18 | 117.4 | 460 | 1300 | 930 | 2402 | 712 |
| 1400 | 2169 | 19 | 114.2 | 715 | 1400 | 852 | 2516 | 960 |
| 1500 | 2229 | 19 | 117.3 | 655 | 1500 | 803 | 2535 | 975 |
| 1600 | 2221 | 17 | 130.7 | 585 | 1600 | 981 | 2599 | 970 |
| 1700 | 2225 | 19 | 117.1 | 693 | 1700 | 955 | 2615 | 939 |
| 1800 | 2254 | 19 | 118.6 | 640 | 1800 | 880 | 2680 | 903 |
| 1900 | 2298 | 19 | 121.0 | 795 | 1900 | 810 | 2600 | 948 |
| 2000 | 2231 | 16 | 139.5 | 798 | 2000 | 850 | 2990 | 978 |
| 2100 | 2254 | 19 | 118.7 | 795 | 2100 | 999 | 3043 | 924 |
| 2200 | 2273 | 19 | 119.7 | 797 | 2200 | 926 | 3132 | 827 |
| 2300 | 2290 | 20 | 114.5 | 778 | 2300 | 880 | 3014 | 961 |

Table E.12: Type 2 Campaign Parameters (POS = 90%, continued)

| $t^1_{start}$ *days* | $m$ *kg* | $C_{max}+1$ *km/yr* | $\frac{m}{C_{max}+1}$ *kg yr/km* | $\Delta t^1$ *days* | $t^2_{start}$ *days* | $\Delta t^2$ *days* | $t^3_{start}$ *days* | $\Delta t^3$ *days* |
|---|---|---|---|---|---|---|---|---|
| 4700 | 2294 | 9 | 254.8 | 745 | 4700 | 930 | 3138 | 860 |
| 4800 | 2514 | 9 | 279.3 | 720 | 4800 | 931 | 3352 | 640 |
| 4900 | 2388 | 9 | 265.4 | 780 | 4900 | 820 | 3199 | 391 |
| 5000 | 2517 | 8 | 314.7 | 525 | 5000 | 830 | 3219 | 731 |
| 5100 | 2323 | 8 | 290.4 | 555 | 5100 | 949 | 2926 | 606 |
| 5200 | 2224 | 8 | 278.0 | 709 | 5200 | 878 | 2620 | 500 |
| 5300 | 2305 | 8 | 288.1 | 510 | 5300 | 960 | 2779 | 366 |
| 5400 | 2134 | 8 | 266.8 | 760 | 5400 | 938 | 2860 | 705 |
| 5500 | 2216 | 8 | 277.0 | 605 | 5500 | 855 | 3090 | 449 |
| 5600 | 2116 | 8 | 264.6 | 741 | 5600 | 800 | 2982 | 551 |
| 5700 | 2119 | 8 | 264.9 | 568 | 5700 | 990 | 2862 | 682 |
| 5800 | 2119 | 7 | 302.7 | 500 | 5800 | 935 | 3016 | 477 |
| 5900 | 2099 | 8 | 262.4 | 609 | 5900 | 920 | 2753 | 371 |

## E.8 Bennu, Type 2 Campaigns (99%)

Table E.13: Type 2 Campaign Parameters (POS = 99%)

| $t^1_{start}$ *days* | $m$ *kg* | $C_{max}+1$ *km/yr* | $\frac{m}{C_{max}+1}$ *kg yr/km* | $\Delta t^1$ *days* | $t^2_{start}$ *days* | $\Delta t^2$ *days* | $t^3_{start}$ *days* | $\Delta t^3$ *days* |
|---|---|---|---|---|---|---|---|---|
| 0 | 2193 | 20 | 109.6 | 650 | 0 | 985 | 2509 | 970 |
| 100 | 2218 | 19 | 116.7 | 720 | 100 | 851 | 2200 | 981 |
| 200 | 2174 | 18 | 120.8 | 761 | 200 | 830 | 2220 | 883 |
| 300 | 2124 | 15 | 141.6 | 776 | 300 | 970 | 2218 | 855 |
| 400 | 2125 | 18 | 118.1 | 668 | 400 | 990 | 2380 | 741 |
| 500 | 2137 | 18 | 118.7 | 617 | 500 | 871 | 2410 | 768 |
| 600 | 2112 | 20 | 105.6 | 772 | 600 | 820 | 2559 | 967 |
| 700 | 2102 | 16 | 131.4 | 761 | 700 | 993 | 2555 | 991 |
| 800 | 2095 | 17 | 123.2 | 785 | 800 | 1000 | 2300 | 798 |
| 900 | 2102 | 18 | 116.8 | 486 | 900 | 950 | 2495 | 993 |
| 1000 | 2098 | 19 | 110.4 | 698 | 1000 | 858 | 2550 | 988 |
| 1100 | 2121 | 16 | 132.5 | 593 | 1100 | 810 | 2483 | 615 |
| 1200 | 2126 | 16 | 132.8 | 774 | 1200 | 994 | 2420 | 698 |
| 1300 | 2104 | 17 | 123.8 | 726 | 1300 | 925 | 2310 | 804 |
| 1400 | 2157 | 17 | 126.9 | 630 | 1400 | 860 | 2448 | 650 |
| 1500 | 2224 | 17 | 130.8 | 688 | 1500 | 830 | 2535 | 995 |
| 1600 | 2159 | 15 | 143.9 | 786 | 1600 | 801 | 2600 | 960 |
| 1700 | 2170 | 17 | 127.7 | 730 | 1700 | 960 | 2700 | 870 |
| 1800 | 2252 | 17 | 132.4 | 648 | 1800 | 910 | 2810 | 720 |
| 1900 | 2358 | 17 | 138.7 | 610 | 1900 | 820 | 2604 | 924 |
| 2000 | 2249 | 17 | 160.6 | 763 | 2000 | 990 | 2742 | 810 |
| 2100 | 2236 | 14 | 139.7 | 780 | 2100 | 963 | 3089 | 980 |
| 2200 | 2331 | 16 | 145.7 | 798 | 2200 | 875 | 2915 | 680 |
| 2300 | 2278 | 18 | 126.5 | 791 | 2300 | 825 | 2995 | 959 |
| 2400 | 2278 | 18 | 163.8 | 791 | 2400 | 830 | 2684 | 900 |

Table E.14: Type 2 Campaign Parameters (POS = 99%, continued)

| $t^1_{start}$ *days* | $m$ *kg* | $C_{max}+1$ *km/yr* | $\frac{m}{C_{max}+1}$ *kg yr/km* | $\Delta t^1$ *days* | $t^2_{start}$ *days* | $\Delta t^2$ *days* | $t^3_{start}$ *days* | $\Delta t^3$ *days* |
|---|---|---|---|---|---|---|---|---|
| 4500 | 2512 | 9 | 290.2 | 750 | 4500 | 838 | 2610 | 507 |
| 4600 | 2579 | 8 | 322.4 | 692 | 4600 | 889 | 2646 | 511 |
| 4700 | 2285 | 8 | 285.6 | 640 | 4700 | 990 | 3058 | 952 |
| 4800 | 2445 | 8 | 305.6 | 733 | 4800 | 853 | 3860 | 540 |
| 4900 | 2296 | 8 | 287.0 | 747 | 4900 | 830 | 2642 | 934 |
| 5000 | 2183 | 7 | 311.8 | 790 | 5000 | 910 | 2747 | 805 |
| 5100 | 2394 | 7 | 342.0 | 620 | 5100 | 900 | 3101 | 440 |
| 5200 | 2204 | 7 | 314.9 | 779 | 5200 | 975 | 2760 | 783 |
| 5300 | 2273 | 7 | 324.7 | 694 | 5300 | 890 | 2583 | 580 |
| 5400 | 2375 | 7 | 339.3 | 342 | 5400 | 810 | 2739 | 392 |
| 5500 | 2225 | 7 | 317.9 | 789 | 5500 | 971 | 3185 | 328 |
| 5600 | 2119 | 7 | 302.7 | 580 | 5600 | 948 | 2980 | 576 |
| 5700 | 2125 | 7 | 303.5 | 588 | 5700 | 990 | 2833 | 712 |
| 5800 | 2111 | 7 | 301.6 | 694 | 5800 | 920 | 2757 | 379 |
| 5900 | 2107 | 7 | 301.0 | 794 | 5900 | 930 | 3136 | 442 |

## E.9 Bennu, Type 2 Campaigns (99.9%)

Table E.15: Type 2 Campaign Parameters (POS = 99.9%)

| $t^1_{start}$ *days* | $m$ *kg* | $C_{max}+1$ *km/yr* | $\frac{m}{C_{max}+1}$ *kg yr/km* | $\Delta t^1$ *days* | $t^2_{start}$ *days* | $\Delta t^2$ *days* | $t^3_{start}$ *days* | $\Delta t^3$ *days* |
|---|---|---|---|---|---|---|---|---|
| 0 | 2180 | 18 | 121.1 | 687 | 0 | 1000 | 2167 | 960 |
| 100 | 2196 | 20 | 109.8 | 770 | 100 | 835 | 2549 | 999 |
| 200 | 2213 | 18 | 123.0 | 723 | 200 | 810 | 2298 | 818 |
| 300 | 2132 | 16 | 133.2 | 750 | 300 | 980 | 2522 | 980 |
| 400 | 2125 | 18 | 118.0 | 712 | 400 | 980 | 2522 | 980 |
| 500 | 2128 | 18 | 118.2 | 770 | 500 | 860 | 2519 | 980 |
| 600 | 2158 | 18 | 119.9 | 406 | 600 | 802 | 2305 | 830 |
| 700 | 2125 | 14 | 151.8 | 630 | 700 | 857 | 2318 | 780 |
| 800 | 2094 | 16 | 130.9 | 780 | 800 | 960 | 2139 | 979 |
| 900 | 2097 | 17 | 123.4 | 707 | 900 | 950 | 2266 | 864 |
| 1000 | 2099 | 17 | 123.5 | 710 | 1000 | 814 | 2393 | 740 |
| 1100 | 2116 | 15 | 141.1 | 640 | 1100 | 819 | 2179 | 924 |
| 1200 | 2119 | 15 | 141.3 | 510 | 1200 | 990 | 2300 | 820 |
| 1300 | 2155 | 17 | 126.8 | 369 | 1300 | 929 | 2556 | 973 |
| 1400 | 2173 | 17 | 127.8 | 587 | 1400 | 829 | 2516 | 989 |
| 1500 | 2225 | 16 | 139.1 | 680 | 1500 | 838 | 2550 | 999 |
| 1600 | 2224 | 15 | 148.3 | 579 | 1600 | 980 | 2570 | 994 |
| 1700 | 2169 | 16 | 135.6 | 792 | 1700 | 950 | 2685 | 832 |
| 1800 | 2298 | 17 | 135.2 | 629 | 1800 | 880 | 2720 | 821 |
| 1900 | 2355 | 16 | 147.2 | 665 | 1900 | 840 | 2770 | 785 |
| 2000 | 2229 | 14 | 159.2 | 798 | 2000 | 801 | 2655 | 883 |
| 2100 | 2251 | 14 | 160.8 | 791 | 2100 | 920 | 2773 | 775 |
| 2200 | 2261 | 17 | 133.0 | 790 | 2200 | 920 | 3099 | 872 |
| 2300 | 2347 | 17 | 138.0 | 725 | 2300 | 800 | 2990 | 973 |
| 2400 | 2269 | 15 | 151.3 | 756 | 2400 | 801 | 3130 | 863 |
| 2500 | 2189 | 15 | 146.0 | 741 | 2400 | 979 | 3110 | 879 |

Table E.16: Type 2 Campaign Parameters (POS = 99.9%, continued)

| $t^1_{start}$ *days* | $m$ *kg* | $C_{max}+1$ *km/yr* | $\frac{m}{C_{max}+1}$ *kg yr/km* | $\Delta t^1$ *days* | $t^2_{start}$ *days* | $\Delta t^2$ *days* | $t^3_{start}$ *days* | $\Delta t^3$ *days* |
|---|---|---|---|---|---|---|---|---|
| 4500 | 2350 | 7 | 335.7 | 749 | 4500 | 960 | 2859 | 741 |
| 4600 | 2245 | 8 | 280.6 | 784 | 4600 | 820 | 3070 | 910 |
| 4700 | 2323 | 8 | 290.4 | 739 | 4700 | 957 | 2844 | 711 |
| 4800 | 2369 | 8 | 296.1 | 759 | 4800 | 818 | 3040 | 534 |
| 4900 | 2229 | 7 | 318.5 | 758 | 4900 | 805 | 2639 | 858 |
| 5000 | 2373 | 8 | 296.6 | 739 | 5000 | 800 | 2775 | 730 |
| 5100 | 2162 | 7 | 308.8 | 740 | 5100 | 990 | 2564 | 980 |
| 5200 | 2184 | 7 | 311.9 | 632 | 5200 | 920 | 2567 | 970 |
| 5300 | 2228 | 7 | 318.3 | 791 | 5300 | 840 | 2820 | 748 |
| 5400 | 2215 | 7 | 316.5 | 649 | 5400 | 860 | 2900 | 639 |
| 5500 | 2126 | 7 | 303.6 | 670 | 5500 | 850 | 2790 | 748 |
| 5600 | 2112 | 7 | 301.7 | 511 | 5600 | 950 | 2631 | 467 |
| 5700 | 2108 | 7 | 301.2 | 790 | 5700 | 900 | 2955 | 564 |
| 5800 | 2117 | 7 | 302.4 | 298 | 5800 | 976 | 3044 | 511 |
| 5900 | 2103 | 7 | 300.4 | 559 | 5900 | 978 | 2570 | 570 |

## E.10 Bennu, Type 2 Campaigns (99.99%)

Table E.17: Type 2 Campaign Parameters (POS = 99.99%)

| $t^1_{start}$ *days* | $m$ *kg* | $C_{max}+1$ *km/yr* | $\frac{m}{C_{max}+1}$ *kg yr/km* | $\Delta t^1$ *days* | $t^2_{start}$ *days* | $\Delta t^2$ *days* | $t^3_{start}$ *days* | $\Delta t^3$ *days* |
|---|---|---|---|---|---|---|---|---|
| 0 | 2194 | 19 | 115.5 | 687 | 0 | 938 | 2547 | 962 |
| 100 | 2204 | 19 | 116.0 | 770 | 100 | 850 | 2538 | 990 |
| 200 | 2152 | 17 | 126.6 | 723 | 200 | 810 | 2140 | 930 |
| 300 | 2137 | 15 | 142.5 | 750 | 300 | 1000 | 2145 | 940 |
| 400 | 2131 | 17 | 125.3 | 712 | 400 | 962 | 2210 | 939 |
| 500 | 2122 | 18 | 117.9 | 770 | 500 | 907 | 2511 | 989 |
| 600 | 2104 | 16 | 131.5 | 406 | 600 | 819 | 1690 | 990 |
| 700 | 2103 | 16 | 131.4 | 630 | 700 | 801 | 2517 | 996 |
| 800 | 2136 | 16 | 133.5 | 780 | 800 | 978 | 2250 | 879 |
| 900 | 2095 | 17 | 123.2 | 707 | 900 | 940 | 2558 | 940 |
| 1000 | 2107 | 18 | 117.1 | 710 | 1000 | 860 | 2556 | 990 |
| 1100 | 2119 | 16 | 132.4 | 640 | 1100 | 811 | 2527 | 997 |
| 1200 | 2117 | 16 | 132.3 | 510 | 1200 | 997 | 2530 | 1000 |
| 1300 | 2101 | 15 | 140.0 | 369 | 1300 | 920 | 2320 | 751 |
| 1400 | 2157 | 16 | 134.8 | 587 | 1400 | 850 | 2458 | 679 |
| 1500 | 2250 | 16 | 140.6 | 680 | 1500 | 800 | 2550 | 980 |
| 1600 | 2159 | 14 | 154.2 | 579 | 1600 | 970 | 2600 | 917 |
| 1700 | 2216 | 16 | 138.5 | 792 | 1700 | 970 | 2630 | 939 |
| 1800 | 2256 | 16 | 141.0 | 629 | 1800 | 900 | 2679 | 900 |
| 1900 | 2325 | 16 | 145.3 | 665 | 1900 | 803 | 2690 | 855 |
| 2000 | 2233 | 13 | 171.8 | 798 | 2000 | 840 | 2585 | 943 |
| 2100 | 2266 | 16 | 141.7 | 791 | 2100 | 990 | 2990 | 1000 |
| 2200 | 2267 | 17 | 133.4 | 790 | 2200 | 901 | 3133 | 853 |
| 2300 | 2247 | 16 | 140.4 | 725 | 2300 | 830 | 3232 | 810 |
| 2400 | 2258 | 14 | 161.3 | 756 | 2400 | 806 | 3232 | 716 |

Table E.18: Type 2 Campaign Parameters (POS = 99.99%, continued)

| $t^1_{start}$ *days* | $m$ *kg* | $C_{max}+1$ *km/yr* | $\frac{m}{C_{max}+1}$ *kg yr/km* | $\Delta t^1$ *days* | $t^2_{start}$ *days* | $\Delta t^2$ *days* | $t^3_{start}$ *days* | $\Delta t^3$ *days* |
|---|---|---|---|---|---|---|---|---|
| 4500 | 2350 | 7 | 316.2 | 675 | 4500 | 800 | 3235 | 674 |
| 4600 | 2245 | 8 | 374.4 | 795 | 4600 | 870 | 2949 | 965 |
| 4700 | 2323 | 8 | 324.3 | 790 | 4700 | 930 | 3472 | 932 |
| 4800 | 2369 | 8 | 343.2 | 668 | 4800 | 955 | 3050 | 942 |
| 4900 | 2229 | 7 | 284.9 | 761 | 4900 | 810 | 2564 | 977 |
| 5000 | 2373 | 8 | 342.0 | 625 | 5000 | 807 | 2750 | 830 |
| 5100 | 2162 | 7 | 360.7 | 700 | 5100 | 860 | 2570 | 985 |
| 5200 | 2184 | 7 | 365.4 | 580 | 5200 | 930 | 2619 | 908 |
| 5300 | 2228 | 7 | 366.5 | 850 | 5300 | 870 | 2730 | 773 |
| 5400 | 2215 | 7 | 353.6 | 747 | 5400 | 890 | 3140 | 847 |
| 5500 | 2126 | 7 | 363.6 | 667 | 5500 | 851 | 2680 | 473 |
| 5600 | 2112 | 7 | 352.1 | 540 | 5600 | 958 | 2604 | 933 |
| 5700 | 2108 | 7 | 352.6 | 480 | 5700 | 851 | 2579 | 955 |
| 5800 | 2117 | 7 | 351.2 | 700 | 5800 | 945 | 2990 | 570 |
| 5900 | 2103 | 7 | 350.7 | 610 | 5900 | 977 | 2764 | 319 |

# Bibliography


[1] NASA, "Planetary Science Archieve [online]," 2014. http://www.nasa.gov/jpl/bolide-events-1994-2013/ [Cited: Dec 11th, 2015].

[2] NASA, "Near-Earth Asteroid Discovery Statistics - Near-Earth Object Program." URL:http://neo.jpl.nasa.gov/stats/ [Cited: Aug 9th, 2015].

[3] ESA, "Asteroid Impact Deflection Assessment - Asteroid Impact Mission - Our Activities." http://www.esa.int/spaceinimages/Images/2015/10/AIDA_mission_concept_infographic [Cited: Mar 6th, 2016].

[4] NASA, "Asteroid Redirect Mission Reference Concept Description," tech. rep., 2006.

[5] Wikipedia, "Kirkwood gap." [Cited: Mar 19th, 2016].

[6] NASA Near-Earth Object Survey and Deflection Study, 2006.

[7] J. Lesurf, "Sky noise." University of St Andrews, School of Physics and Astronomy, 2013. https://www.st-andrews.ac.uk/~www_pa/Scots_Guide/RadCom/part8/page3.html [Cited: Jan 20th, 2016].

[8] S. Montanari, "Fabrication and characterization of planar gunn diodes for Monolithic Microwave Integrated Circuits.." Forschungszentrum Julich, 2005. http://juser.fz-juelich.de/record/49632/files/Informationstech_9.pdf [Cited: Jan 20th, 2016].

[9] NASA, "Wise Revises Numbers of Asteroids Near Earth." [Online], September 2011. http://www.jpl.nasa.gov/spaceimages/ [Cited: Feb 16th, 2016].

[10] T. Yanagisawa, H. Kurosaki, H. Banno, Y. Kitazawa, M. Uetsuhara, and T. Hanada, "Comparison between four detection algorithms for geo objects," in *Proceedings of the Advanced Maui Optical and Space Surveillance Technologies Conference, Maui, HI, USA*, vol. 1114, p. 9197, 2012.

[11] Wikipedia, "Earth's atmospheric transmittance (or opacity) to various wavelengths of electromagnetic radiation." [Original:NASA], December 2008. [Cited: Feb 16th, 2016].

[12] D. Yeomans, S. Bhaskaran, S. Broschart, S. Chesley, P. Chodas, T. H. Sweetser, and R. Schweickart., "Deflecting a hazardous near-earth object," in *The 1st IAA Planetary Defense Conference.*, 2009.

[13] Elementy, "Japanese probe Hayabusa has almost reached its goal." `http://elementy.ru/novosti_nauki/164801/Yaponskiy_zond_Khayabusa_pochti_nastig_svoyu_tsel`, 2005. [Online; accessed 20-Apr-2016].

[14] JAXA, "Research plan of the asteroid explorer Hayabusa." `http://www.isas.jaxa.jp/e/special/2003/kawaguchi/02.shtml`, 2003. [Online; accessed 20-Apr-2016].

[15] D. J. Scheeres, S. Broschart, S. J. Ostro, and L. A. Benner, "The dynamical environment about asteroid 25143 itokawa: Target of the hayabusa mission," (Providence, RI), AIAA/AAS Astrodynamics Specialist Conference and Exhibit, 2004.

[16] T. G. Muller, T. Sekiguchi, M. Kaasalainen, M. Abe, and S. Hasegawa, "Thermal infrared observations of the hayabusa spacecraft target asteroid 25143 itokawa," *Astronomy & Astrophysics*, 2005.

[17] S. Abe, T. Mukai, N. Hirata, O. S. Barnouin-Jha, and A. F. Cheng, "Mass and local topography measurements of itokawa by hayabusa," *Science*, vol. 312, pp. 1344–1347, 2006.

[18] JAXA, "Official approval of names on itokawa by iau." `http://www.jaxa.jp/press/2009/03/20090303_itokawa_e.html`, 2013. [Online; accessed 24-Dec-2013].

[19] ESO, "The anatomy of an asteroid." `http://www.eso.org/public/news/eso1405/`, 2014. [Online; accessed 20-Apr-2016].

[20] G. Vardaxis and B. Wie, "Impact probability analysis for near-earth objects in earth resonant orbits," in *AIAA Conferences*, 2014.

[21] A. Bourdoux and D. Izzo, "Characterization and hazard mitigation of resonant returning near earth objects," final stage report, European Space Agency, Oct. 2005. ACT internal report: ACT-RPT-4100-AB-CHMRRNEO05.

[22] G. B. Valsecchi, "Resonant returns to close approaches: Analytical theory," *Astronomy and Astrophysics*, vol. 408, no. 3, pp. 1179–1196, 2003. DOI: 10.1051/0004-6361:20031039.

[23] S. R. Chesley, J. Baer, and D. G. Monet, "Treatment of star catalog biases in asteroid astrometric observations," *Icarus*, vol. 210, no. 1, pp. 158–181, 2010.

[24] P. Chodas, "Impact risk assessment: An introduction." NASA Near Earth Object Program [Online], 2013. `http://neo.jpl.nasa.gov/risk/doc/sentry.html` [Cited: Sep 15th, 2015].

[25] R. S. Margulieux, "Avoiding earth impacts using albedo modification as applied to 99942 apophis," Master's thesis, TAMU, 2010.

[26] G. F. Gronchi and G. T. Williams, "NEODyS-2 : Proper Elements." Near Earth Objects Dynamic Site2 [Online], 2011. `http://newton.dm.unipi.it/neodys/` [Cited: Sep 25th, 2015].

[27] T. J. Ahrens and A. W. Harris, *Hazards due to comets and asteroids: deflection and fragmentation of near-Earth asteroids*, pp. 897–927. The University of Arizona Press, 1994.

[28] H. E. Edgerton and J. R. Killian, *Flash!: Seeing the unseen by ultra high-speed photography.*

[29] M. Jutzi, E. Asphaug, P. Gillet, J. Barrat, and W. Benz, "The structure of the asteroid 4 Vesta as revealed by models of planet-scale collisions.," *Nature*, vol. 494, no. 7436, pp. 207–210, 2013.

[30] T. J. Ahrens and A. W. Harris, "Deflection and fragmentation of near-earth asteroids," *Nature*, vol. 360, no. 6403, pp. 429–433, 1992.

[31] B. Wie, "Dynamics and control of gravity tractor spacecraft for asteroid deflection.," *Journal of Guidance, Control, and Dynamics*, vol. 31, no. 5, pp. 1413–1423, 2008.

[32] NASA, "Final Environmental Assessment for the Origins, Spectral Interpretation, Resource Identification, and Security-Regolith Explorer Mission," technical report, 2013.

[33] Wikipedia, "Hayabusa." [Online].

[34] Wikipedia, "Don Quijote (spacecraft)." [Online].

[35] D. Farnocchia, S. Chesley, P. Chodas, M. Micheli, D. Tholen, A. Milani, G. Elliott, and F. Bernardi, "Yarkovsky-driven impact risk analysis for asteroid (99942) Apophis.," *Icarus*, vol. 224, pp. 192–220, 2013.

[36] David Farnocchia, "Trajectory analysis of the potentially hazardous asteroid bennu." `http://postdocs.jpl.nasa.gov/files/ura/Trajectory_analysis_of_the_potentially_hazardous_asteroid_Bennu.pdf` [Cited: May 17th, 2016].

[37] S. W. Paek, "Reconfigurable satellite constellations for geo-spatially adaptive earth observation missions," Master's thesis, Massachusetts Institute of Technology, 2012.

[38] F. T. Johnson, "Approximate finite-thrust trajectory optimization," *AIAA Journal*, vol. 7, no. 6, pp. 993–997, 1969.

[39] A. Alfaris, "Multiobjective optimization." MIT Open Courseware.

[40] "American Meteor Society," 2016. http://www.amsmeteors.org.

[41] Wikipedia, "List of Mars-crossing minor planets." [Cited: May 17th, 2016].

[42] Wikipedia, "Chebyshev polynomials." [Cited: Mar 26th, 2016].

[43] M. Central, "Fle exchange - the fft in chebfun." [Cited: Mar 26th, 2016].

[44] NASA, "Low thrust (LT) tool capability gap analysis and state-of-the-art tools assessment," tech. rep., 2006. Report by the intercenter low thrust trajectory tool (LTTT) Team.

[45] S. W. Paek and O. L. de Weck, "A two-stage asteroid deflection campaign consisting of precursor and mission and impactor mission," in *65th International Astronaut-ical Congress*, 2014.

[46] S. A. Stewart and P. J. Allen, "3D seismic reflect-ion mapping of the silverpit multi-ringed crater, north sea," *Geological Society of America Bulletin*, vol. 117, no. 3–4, pp. 354–368, 2005.

[47] C. D. Murray and S. F. Dermott, *Solar system dynamics*. Cambridge university press, 1999.

[48] P. Nicholson, "Physics of the planets," 2015. http://astro.cornell.edu/ [Cited: Mar 29th, 2016].

[49] M. Showalter and D. Hamilton, "Resonant interactions and chaotic rotation of pluto/'s small moons," *Nature*, vol. 522, no. 7554, pp. 45–49, 2015.

[50] J. Mula, R. Poler, J. Garcia-Sabater, and F. C. Lario, "Models for production planning under uncertainty: A review," *International journal of production economics*, vol. 103, no. 1, pp. 271–285, 2006.

[51] ESA, "Herschel intercepts asteroid Apophis." Space Science Activities, January 2013. http://www.esa.int/Our_Activities/Space_Science/Herschel_intercepts_asteroid_Apophis[Accessed 29-Dec-2013].

[52] NASA, "Near-Earth Asteroid Delta-V for Spacecraft Rendezvous." http://echo.jpl.nasa.gov/~lance/delta_v/delta_v.rendezvous.html. [Accessed 29-Dec-2013].

[53] P. K. Chodas and D. K. Yeomans, "Predicting close approaches and estimating impact probabilities for near earth objects," in *AAS-AIAA Astrodynamics Specialist Conference*, 1999.

[54] O. P. Popova, "Chelyabinsk airburst, damage assessment, meteorite recovery, and characterization.," *Science*, vol. 342, no. 6162, pp. 1069–1073, 2013.

[55] D. K. Yeomans, *Near-Earth objects: finding them before they find us*. Princeton University Press, 2013.

[56] B. W. Barbee and J. A. Nuth III, "Asteroid impact threats: Advancements in asteroid science to enable rapid and effective deflection missions," *Journal of Cosmology*, vol. 2, pp. 386–410, 2009.

[57] JPL, "NASA team finds riches in meteorite treasure hunt," 2009. `http://neo.jpl.nasa.gov/news/news163.html` [Cited: May 18th, 2016].

[58] Paul Chodas, "Personal communication." [Cited: May 4th, 2016].

[59] D. D. Mazanek, D. M. Reeves, J. B. Hopkins, D. W. Wade, M. Tantardini, and H. Shen, "Enhanced gravity tractor technique for planetary defense," 2015.

[60] L. S. Pontryagin, *Mathematical theory of optimal processes*. CRC Press, 1987.

[61] A. E. Bryson, *Applied optimal control: optimization, estimation and control*. CRC Press, 1975.

[62] B. J. Griffin, *Improvements to an analytical multiple-shooting approach for optimal burn-coast-burn ascent guidance*. ProQuest, 2007.

[63] D. Williams and W. Tucker, "Computation of quasi-optimal reentry trajectories using the simplex algorithm of linear programming," Report M-240-1208 7, Northrop Services, Inc., Huntsville, Alabama, Apr. 1973.

[64] E. J. Rivera, G. Laughlin, R. P. Butler, S. S. Vogt, N. Haghighipour, and S. Meschiari, "The lick-carnegie exoplanet survey: A uranus-mass fourth planet for gj 876 in an extrasolar laplace configurationbased on observations obtained at the wm keck observatory, which is operated jointly by the university of california and the california institute of technology.," *The Astrophysical Journal*, vol. 719, no. 1, p. 890, 2010.

[65] M. Moons and A. Morbidelli, "Secular resonances in mean motion commensurabilities: The 4/1, 3/1, 5/2, and 7/3 cases," *Icarus*, vol. 114, no. 1, pp. 33–50, 1995.

[66] P. W. Chodas and D. K. Yeomans, "Predicting close approaches and estimating impact probabilities for near earth objects," *Astrodynamics 1999*, pp. 2531–2550, 2000.

[67] Paul Chodas, "E-mail correspondence." [Cited: May 18th, 2016].

[68] Wikipedia, "Campaign plan." [Cited: Mar 19th, 2016].

[69] J. Ahn, O. de Weck, and J. Hoffman, "An optimization framework for global planetary surface exploration campaigns," *Journal of the British Interplanetary Society*, vol. 61, no. 12, p. 487, 2008.

[70] R. H. Nyström, R. Franke, I. Harjunkoski, and A. Kroll, "Production campaign planning including grade transition sequencing and dynamic optimization," *Computers & chemical engineering*, vol. 29, no. 10, pp. 2163–2179, 2005.

[71] R. de Neufville, "Real options: dealing with uncertainty in systems planning and design," *Integrated Assessment*, vol. 4, no. 1, pp. 26–34, 2003.

[72] C. Carlsson and R. Fullér, "A fuzzy approach to real option valuation," *Fuzzy sets and systems*, vol. 139, no. 2, pp. 297–312, 2003.

[73] J. Lin, O. de Weck, and D. MacGowan, "Modeling epistemic subsurface reservoir uncertainty using a reverse wiener jump–diffusion process.," *Journal of Petroleum Science and Engineering*, vol. 84, pp. 8–19, 2012.

[74] S. W. Paek, P. Egger, O. de Weck, and R. Polany, "Asteroid deflection campaign design integrating epistemic uncertainties," in *IEE Aerospace Conference*, March 2016.

[75] S. R. Chesley and P. W. Chodas, "Asteroid close approaches: analysis and potential impact detection," in *Asteroids III* (W. F. Bottke, ed.), pp. 179–183, University of Arizona Press, 2002.

[76] D. Morrison, "The Spaceguard Survey," report of the International Near-Earth-object Detection Workshop, NASA, 1993.

[77] A. W. Harris, "What spaceguard did," *Nature*, vol. 453, no. 7199, pp. 1178–1179, 2008.

[78] L. Johnson, "Finding near earth objects: In the context of an agency grand challenge." Near Earth Object Program Executive [Online], Sep 2014. `http://science.nasa.gov/media/medialibrary/2014/10/01/NEO_Update_to_PSS-CAPsTAGGED.pdf`.

[79] E. Bowell and K. Muinonen, "Earth-crossing asteroids comets: Groundbased search strategies," in *Hazards Due to Comets and Asteroids* (T. Gehrels, ed.), pp. 149–197, Tuscon: University of Arizona, 1994.

[80] P. W. Chodas, "Estimating the impact probability of a minor planet with the earth," *Bull. Am. Astron. Soc.*, vol. 25, no. 1236, 1993.

[81] D. K. Yeoman and P. W. Chodas, "Periodic comet Shoemaker-Levy 9," *IAU Circular*, vol. 5807, 1993.

[82] P. W. Chodas and D. K. Yeoman, "The orbital motion and impact circumstances of comet shoemaker-levy 9," in *The Collision of Comet Shoemaker-Levy 9 and Jupiter* (K. S. Noll, ed.), vol. 15, pp. 1–130, IAU Colloq., 1996.

[83] H. Yoon, S. W. Paek, Y. Lim, B.-H. Lee, and H. Lee, "New star pattern identification with vector pattern matching for attitude determination," *Aerospace and Electronic Systems, IEEE Transactions on*, vol. 49, no. 2, pp. 1108–1118, 2013.

[84] S. J. Ostro, L. A. M. Benner, M. C. Nolan, and C. Magri, "Radar observations of asteroid 25143 itokawa (1998 SF36)," *Meteoritics & Planetary Science*, vol. 39, no. 3, pp. 407–424, 2004.

[85] D. R. Williams, "Sun fact sheet." NASA Space Science Data Coordinated Archive[Online], 2013. `URL: http://nssdc.gsfc.nasa.gov/planetary/factsheet/sunfact.html` [Cited: May 8th, 2015].

[86] A. Carusi, G. B. Valsecchi, and R. Greenberg, "Planetary close encounters: Geometry of approach and post-encounter orbital parameters," *Celestial Mechanics and Dynamanics in Astronomy*, vol. 49, pp. 111–131, 1990.

[87] R. S. Park, "99942 Apophis Close-Approach Data." JPL Small-Body Database Browser [Online], 2015. `http://ssd.jpl.nasa.gov/sbdb.cgi?sstr=apophis` [Cited: May 11th, 2015].

[88] S. Yabushita and J. Henrard, eds., *Dynamics of Comets and Asteroids and Their Role in Earth History*, vol. 61. Springer Science & Business Media, 1998.

[89] G. F. Gronchi and A. Milani, "Proper elements for earth-crossing asteroids," *Icarus*, vol. 152, no. 1, pp. 58–69, 2001.

[90] J. C. Solem, "Interception of comets and asteroids on collision course with earth," *Journal of Spacecraft and Rockets*, vol. 30, no. 2, pp. 222–228, 1993.

[91] L. Kleiman, "Project icarus," MIT Report, MIT Press, 1968.

[92] L. Alvarez, W. Alvarez, F. Asaro, and H. Michel, "Extraterrestrial cause for the cretaceous-tertiary extinction," *Science*, vol. 208, no. 4448, pp. 1095–1108, 1980.

[93] R. A. Hyde, "Cosmic bombardment," technical report, Univ. of California Lawrence Livermore National Lab., 1984.

[94] L. Wood, R. Hyde, and M. Ishikawa, "Cosmic Bombardment II, intercepting the Bomblet Cost-Efficiently," technical report, Univ. of California Lawrence Livermore National Lab., 1990.

[95] C. D. Hall and I. M. Ross, "Dynamics and control problems in the deflection of near-earth objects," *Advances in the Astronautical Sciences, Astrodynamics*, vol. 97, no. 1, pp. 613–631, 1997.

[96] S. W. Paek, "A multi-functional paintball cloud for asteroid deflection," in *63rd International Astronaut-ical Congress*, 2012.

[97] M. Y. Louge and M. E. Adams, "Anomalous behavior of normal kinematic restitution in the oblique impacts of a hard sphere on an elastoplastic plate," *Physical review E*, vol. 65, no. 2, 2002.

[98] J. Yang, "Materials and Heat Transport : Thermal Expansion." `http://kasap13.usask.ca/ee271`, 2008. [Accessed 25-Feb-2016].

[99] D. Yeomans, S. Bhaskaran, S. Chesley, P. Chodas, D. Grebow, D. Landau, S. Petropoulos, and J. Sims, "Report on asteroid 2011 ag5 hazard assessment and contingency planning," 2012.

[100] B. Wie, "Kinetic Impactors and Gravity Tractors for Asteroid Deflection." `https://www.adrc.iastate.edu/files/2015/02/Bong-Wie.pdf`, 2008. [Accessed 24-Feb-2016].

[101] H. Li and K. Zhang, "Development of a fuzzy-stochastic nonlinear model to incorporate aleatoric and epistemic uncertainty," *Journal of contaminant hydrology*, vol. 111, no. 1, pp. 1–12, 2010.

[102] P. C. Egger, "Efficient computational approaches to trajectory prediction for future earth-asteroid impact mitigation," Master's thesis, EPFL, 2014.

[103] D. Rapp, *Human Missions to Mars.* Springer, 2007.

[104] M. Matsumoto and T. Nishimura, "Mersenne twister: a 623-dimensionally equidistributed uniform pseudo-random number generator," *ACM Transactions on Modeling and Computer Simulation (TOMACS)*, vol. 8, no. 1, pp. 3–30, 1998.

[105] R. S. L. Jr, *Optimization and valuation of recongurable satellite constellations under uncertainty.* PhD thesis, Massachusetts Institute of Technology, 2014.

[106] P. G. Rowe, *Design thinking.* MIT Press, 1991.

[107] E. W. Weisstein, "Interpolation from mathworld - a wolfram web resource.." `http://mathworld.wolfram.com/Interpolation.html`. [Cited: Mar 26th, 2016].

[108] J. Horsewood, "99942 apophis rendezvous mission opportunities."

[109] O. L. De Weck and M. B. Jones, "Isoperformance: Analysis and design of complex systems with desired outcomes," *Systems engineering*, vol. 9, no. 1, pp. 45–61, 2006.

[110] I. Y. Kim and O. de Weck, "Adaptive weighted sum method for multiobjective optimization: a new method for pareto front generation," *Structural and multidisciplinary optimization*, vol. 31, no. 2, pp. 105–116, 2006.

[111] Wikipedia, "Robustification." [Cited: Mar 23rd, 2016].

[112] J. Parriott and C. Alcock, "On the number of comets around white dwarf stars: orbit survival during the late stages of stellar evolution," *The Astrophysical Journal*, vol. 501, no. 1, p. 357, 1998.

[113] N. Pouratian, A. Asthagiri, J. Jagannathan, M. E. Shaffrey, and D. Schiff, "Surgery insight: the role of surgery in the management of low-grade gliomas," *Nature Clinical Practice Neurology*, vol. 3, no. 11, pp. 628–639, 2007.

[114] D. W. Hughes and B. G. Marsden, "Planet, asteroid, minor planet: a case study in astronomical nomenclature," *Journal of Astronomical History and Heritage*, vol. 10, pp. 21–30, 2007.

[115] R. A. S. of Canada, *Journal of the Royal Astronomical Society of Canada*, vol. 46. Royal Astronomical Society of Canada., 1952.

[116] A. E. Rubin and J. N. Grossman, "Meteorite and meteoroid: New comprehensive definitions," *Meteoritics & Planetary Science*, vol. 45, no. 1, pp. 114–122, 2010.

[117] M. J. Belton, *Mitigation of hazardous comets and asteroids*. Cambridge University Press, 2004.